Probing Gravity and the Neutrinos with Cosmology

Shaun Anthony Thomas

Thesis submitted for the Degree of Doctor of Philosophy
of the University College London

Department of Physics & Astronomy
UNIVERSITY COLLEGE LONDON

October 2009

I, Shaun Thomas, confirm that the work presented in this thesis is my own. Where information has been derived from other sources, I confirm that this has been indicated in the thesis. Specifically:

- In Chapter 3, which I present in Thomas, Abdalla and Lahav 2009a (In prep), the running of ANNz to convert galaxy photometry to galaxy redshift was performed by the second author Filipe Abdalla.
- Figure 1.1, Figure 1.3 (left panel), Figure 1.4 (left panel), Figure 2.4, Figure 3.1 and Figure 4.1 can be found from external sources and are credited to Hubble (1929)**,** Blanton and the SDSS [*http://www.sdss.org*] **,** the WMAP science team [*http://lambda.gsfc.nasa.gov*] and NASA [*http://hubblesite.org/gallery*]**,** Padmanabhan *et al.* (2007) and Lesgourgues & Pastor (2006)**,** respectively.

To my mum, for everything...

”If my calculations are correct, when this baby hits eighty-eight miles per hour... you’re gonna see some serious shit.”

— Dr. Emmett Brown

Back to the Future (1985)

ABSTRACT

This thesis is related to the growth of structure in the late-time Universe. It addresses both the measurement of this structure and the use of such information in constraining fundamental underlying physics. This includes the gravitational framework and the sum of the three neutrinos' mass.

The thesis starts by using weak gravitational lensing data (CFHTLS) to constrain a modification of gravity that is invoked to provide the observed accelerated expansion in the Universe. This is shown to disfavour the model in question. It is, however, incapable of placing any bounds on the growth parameter that represents extensions to gravity. The future of weak lensing in probing general relativity is illustrated with forecasts on the growth signature and power spectrum parameter using the proposed Euclid probe.

A measurement is made on the clustering of Luminous Red Galaxies (LRGs) in the Universe. This represents a new photometric galaxy clustering angular power spectrum: MegaZ LRG Data Release 7 (DR7). The cosmological constraints are demonstrated to be competitive with spectroscopic surveys and complementary to the WMAP5 data. Specifically, bounds of $f_b \equiv \Omega_b/\Omega_m = 0.173 \pm 0.046$ and $\Omega_m = 0.260 \pm 0.035$ are placed. Potential systematics in the data are discussed and examined.

The work concludes by placing one of the most stringent constraints available of the sum of the three neutrino masses. By combining cosmic microwave background information, distance measures from supernovae and baryon acoustic oscillations with growth from the MegaZ LRG galaxy clustering data, produced earlier, the limit is found to be $\sum m_\nu < 0.281$ eV at the 95% confidence level.

CONTENTS

LIST OF FIGURES

LIST OF TABLES

CHAPTER 1

INTRODUCTION

Cosmology is one of the boldest of all intellectual endeavors. It seeks to describe the origin, evolution and fate of the Universe. It also aspires to provide a complete census of its contents. Indeed, it is not only with this shameless ambition that it stands in stark contrast to other scientific fields; for example, it is not, in terms of the scientific method, reproducible. Moreover, it is a field that seems to most closely border the metaphysical with its furthest advancing outposts represented by a new philosophy: *precision cosmology*.

This recent deluge of data, from the tiny fluctuations in the afterglow of the Big Bang to the positions of millions of galaxies, is revealing a fascinating and dynamic Universe. As we will see in the rest of the *introduction*, it is expanding (Section 1.1.1) and is best described by a theory where the fabric of space-time and mass intimately manipulate one another (Section 1.1.2). However, this requires the existence of new physics with unseen dark matter (Section 1.1.4.4) and dark energy (Section 1.1.4.5) necessarily being invoked to explain both the *accelerated* expansion (Section 1.1.4) and the statistics of fluctuations in the mass distribution (Section 1.2.2). In fact, it forces us to consider the very notion of a *model* and its fundamental relation–through a choice in the statistical approach–to the data (Section 1.3).

In addition, the vast wealth of data still being mined from our surroundings is capable of providing a fertile testbed for fundamental and underlying physics such as gravity, the neutrino, dark energy or the discrete nature of space-time. This is a theme throughout the thesis and subsequently the rest of the chapter outlines are described in Section 1.4.

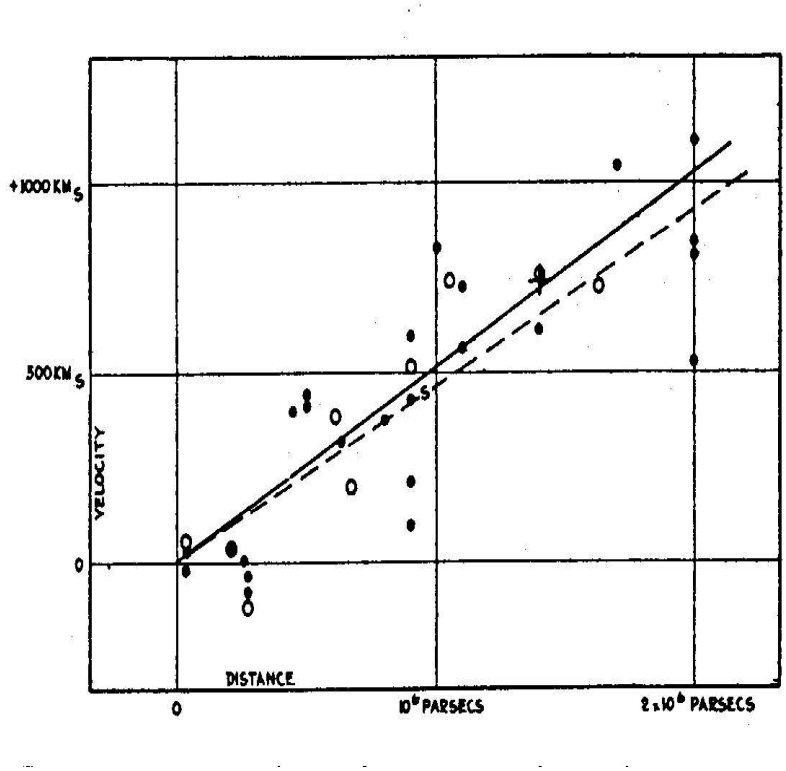

Figure 1.1: The first Hubble diagram where the plot of velocity against distance demonstrates that distant galaxies are receding from us. The solid line and points correspond to an analysis corrected for the sun's movement. CREDIT: *Hubble (1929)*.

1.1 The smooth and expanding Universe

This subsection describes the smooth first order Universe associated with the concept of a dynamic cosmos. It highlights the surprising link between this evolution and the stamp collecting-like quest to quantify its energy contents (1.1.4), through both the concept of distance (1.1.5) and the theory of gravity (1.1.2).

1.1.1 The expansion

The expansion of the Universe is perhaps one of the most startling yet central concepts in all of modern cosmology. There are a number of direct and indirect methods to infer this expansion with the clearest being through the Doppler effect.

Elements and their atoms have characteristic energy levels governed by quantum theory. A transition between these energy levels is the result of an emission or absorption of a discrete and specific packet of light energy. This definite energy has a fixed corresponding wavelength known for each element and their energy levels in the rest frame. However, for a moving object, such

as a galaxy containing the element, this wavelength will be shifted, or *Doppler shifted*, towards one end of the spectrum. For an object moving away from an observer the succession of peaks from an emitted wavelength $\lambda_{\rm em}$ will become more sparse thus shifting the observed wavelength $\lambda_{\rm obs}$ towards the red end of the spectrum; that is, *red*shifting the light. Conversely, an object approaching the observer suffers a crowding of its light's peaks and troughs and subsequently it is *blue*shifted.

Similarly, Vesto Slipher and Edwin Hubble, after years of observation, discovered that distant galaxies tend to recede from every observer with a velocity $\bar{v}$ proportional to the relative distance $\bar{d}$ (Hubble 1929). This has been enthusiastically referred to as Hubble's law,

$$\bar{v} = H_0 \bar{d} \tag{1.1}$$

where H_0 is the Hubble constant. The early emergence of this trend can be seen in Figure 1.1. Since then determining H_0 has been a challenging but tantalising task with recent *Hubble Space Telescope* measurements proposing $H_0 = 72 \pm 8 \ \mathrm{kms}^{-1}\mathrm{Mpc}^{-1}$ (Freedman *et al.* 2001) and $H_0 = 74.2 \pm 3.6 \ \mathrm{kms}^{-1}\mathrm{Mpc}^{-1}$ (Riess *et al.* 2009). This overall recession of distant objects–the expansion of the Universe–has led us to define the redshift z,

$$1 + z \equiv \frac{\lambda_{\rm obs}}{\lambda_{\rm em}} = \frac{a_{\rm obs}}{a_{\rm em}} \tag{1.2}$$

where $a = a(t)$, the scale factor, literally describes a relative scale for the expansion. Most remarkably we might now presuppose that any Universe that is expanding must have at some point been arbitrarily small. Indeed, we now have complementary and consistent evidence of a Universe with a beginning (within the bounds of everyday language), where recent data insists on a present age of 13.69 ± 0.13 billion years (Dunkley *et al.* 2009).

1.1.2 General Relativity

In order to accurately describe the expansion of the previous section it is essential to have a fully viable and working theory of gravity. Conventionally this is fulfilled by general relativity.

Originally underlined by Bernhard Riemann and later expanded by Albert Einstein the theory uses the concept of gravity not as a force but as a representation of the geometry, or the curvature, of space-time. This geometry is described by an entity known as the metric that relates distances between coordinate points. Any test particle moving through such a geometry will follow a geodesic (a generalisation of a 'straight' line in a curved space) and have its motion subsequently affected. Specifically, general relativity associates gravity to the metric and pertains the existence

of mass or energy to the distortion of the surrounding spacetime. This is encapsulated in Einstein's field equations,

$$R^{\mu\nu} - \frac{1}{2}g^{\mu\nu}R = -\frac{8\pi G}{c^4}T^{\mu\nu} \tag{1.3}$$

where $R^{\mu\nu}$ and R, which describe the curvature, are the Ricci tensor and scalar, respectively, and $T^{\mu\nu}$ is the energy-momentum tensor. Also present, and implicit within $R^{\mu\nu}$ and R, is the 4×4 symmetric metric $g^{\mu\nu}$. The Greek indices run from the temporal (0) to the three spatial components (1, 2, 3).

To retrieve our expanding cosmology we might start with a metric such as,

$$\mathrm{d}s^2 = -c^2\,\mathrm{d}t^2 + g_{ij}\,\mathrm{d}x^i\,\mathrm{d}x^j \tag{1.4}$$

where the spatial metric (for a constant time slice) is given by g_{ij}. The form of this metric is heavily restrained by the fact that observers perceive the cosmic microwave background (CMB) to be astonishingly isotropic. Different parts of the background, which are now separated by large fractions of the observable Universe, are virtually identical to several parts in 10^5 after subtracting the dipole contribution. Therefore for any constant time slice the Universe should be remarkably homogeneous. Likewise g_{ij}, which describes the geometry of the space, should also be close to homogeneity. Indeed, if there exists both isotropy and homogeneity the full metric can be described at all times by the Friedmann-Robertson-Walker metric,

$$\mathrm{d}s^2 = -c^2\,\mathrm{d}t^2 + a(t)^2\Big(\frac{\mathrm{d}r^2}{1-kr^2} + r^2\,\mathrm{d}\theta^2 + r^2\sin^2\theta\,\mathrm{d}\phi^2\Big) \tag{1.5}$$

where k is the curvature of the current time slice and I set $c = 1$ from here on.

The evolution of the metric (Eq. 1.5) is governed by Einstein's equations (Eq. 1.3) and depends on the contents of the energy-momentum tensor. For a perfect and isotropic fluid this can be detailed by,

$$T^{\mu\nu} = \begin{pmatrix} \rho & 0 & 0 & 0 \\ 0 & P & 0 & 0 \\ 0 & 0 & P & 0 \\ 0 & 0 & 0 & P \end{pmatrix} \tag{1.6}$$

where P is the pressure and ρ is the energy/mass density. This configuration yields two independent equations. The time-time ($\mu = \nu = 0$) part of the Einstein equation provides the Friedmann

equation,

$$H^2 \equiv \left(\frac{\dot{a}}{a}\right)^2 = \frac{8\pi G}{3}\rho_{\rm total} - \frac{k}{a^2}. \tag{1.7}$$

with $\rho_{\rm total} = \rho(a)$ containing contributions from all the energy components. Secondly, the space-space ($\mu = \nu = 1, 2, 3$) part of the Einstein equations (with the above Friedmann equation subtracted) gives the acceleration equation,

$$\frac{\ddot{a}}{a} = -\frac{4\pi a}{3}\Big(\rho + 3P\Big). \tag{1.8}$$

Remembering that the scale factor gives us a measure of the Universe's expansion one can see that its very evolution and dynamics depend on the energy contents. This is a powerful reason therefore to quantify and understand the energy contents within the cosmos; to understand how it started, how it is evolving and ultimately what might happen inexorably in the future. Viewed another way, if we examine the expansion history in detail we might be able to *infer* the properties of any known, or unknown, matter constituents. Accordingly, to interpret an equation such as (Eq. 1.7) we must understand the evolution of any fluids $\rho(a)$ with expansion (Section 1.1.4).

1.1.3 Geometry

In the aforementioned Friedmann equation (Eq. 1.7) there is a certain value of $\rho_{\rm total}$ that results in $k = 0$ for a set H. This is widely known as the *critical density*,

$$\rho_c(t) = \frac{3H^2}{8\pi G}. \tag{1.9}$$

It is therefore enormously convenient to express any matter densities as a fraction of this critical density $\Omega(t) \equiv \rho/\rho_c$. In this way if the total matter density $\Omega_{\rm total} = 1$ then $k = 0$ and the Universe will have a flat geometry. Physically this is represented by Euclidean geometry and states, for example, that angles within a triangle add to 180 degrees. If we have more matter $\Omega_{\rm total} > 1$ we find $k > 0$ and we acquire spherical geometry. Interestingly in this case the internal angles of a triangle are greater than 180 degrees. Alternatively if there is less matter, $\Omega_{\rm total} < 1$, we find the three angles are smaller than 180 degrees. This is embodied by hyperbolic geometry and subsequently $k < 0$. Note that it is this k that features in the metric of Equation 1.5. These three geometries are displayed clearly in Figure 1.2.

Observationally the Universe is seen to be very close to flat with Komatsu *et al.* (2009) finding $\Omega_k = 1 - \Omega_{\rm total} = -0.0049^{+0.0066}_{-0.0064}$. It is commonly thought that sufficient evidence for a flat Universe arises solely from the main acoustic peak in the CMB (Section 1.2.2.2 and Figure 1.4).

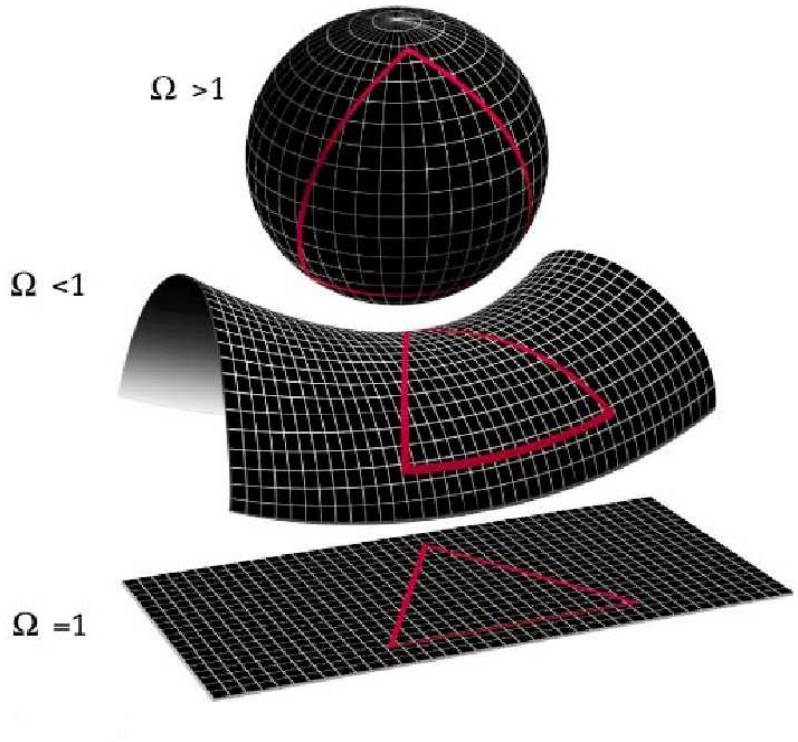

Figure 1.2: The three possible geometries for the Universe and their relation to the total density Ω. For $\Omega > 1$ the geometry is described as spherical and $k > 0$ similarly to the surface of the Earth (top). When the density is sub-critical $\Omega < 1$, hyperbolic geometry ensues and $k < 1$ (middle). Finally, when $\Omega = 1$ the Universe is said to be flat ($k = 0$) and correspondingly follows flat, or Euclidean, geometry (bottom). Also shown is the relation between an apparent angle and geometry as described in the text. CREDIT: *http://map.gsfc.nasa.gov/media* [*Gary Hinshaw and Nasa*].

This is the scale of the most prominent fluctuations. A spherical (hyperbolic) geometry will act to increase (decrease) the apparent angular size[1] of characteristic temperature fluctuations thus shifting the position of the first peak on a scale of size. However, as the CMB effectively measures the angular diameter distance (Section 1.1.5) to an isolated redshift and the position of the first peak is also dependent on the sound horizon at decoupling it is degenerate with other parameters that influence the expansion history and horizon (pressure) scale at that time, including Ω_m and Ω_Λ. By introducing probes of this history it is possible to break the degeneracy and retrieve the tight bound as illustrated above. It is therefore common to assume flatness in many cosmological analyses and similarly I follow this procedure for simplicity and clarity.

[1] As can be seen in Figure 1.2.

1.1.4 The Energy Contents

A simple rearrangement of Equation 1.7 and 1.8 allows us to produce a third, but dependent, Einstein equation for the density evolution. This is known as the fluid equation,

$$\dot{\rho} + 3\frac{\dot{a}}{a}\Big(\rho + P\Big) = 0. \tag{1.10}$$

Alternatively one can derive this directly by ensuring mass-energy conservation in the field equations. This is obtained by forcing the covariant derivative of the energy-momentum tensor to be zero[2]: $\nabla_\mu T^\mu_\nu = 0$. The derivative arises from a generalisation of the Euler $\partial P/\partial x^j = 0$ and continuity equations $\partial\rho/\partial t + \nabla.(\rho\mathbf{u}) = \mathbf{0}$. Moreover, the covariant part allows us to see whether a quantity has changed along a curve, say, independent to the change from a non-inertial coordinate system.

We can now solve for ρ provided we know how to treat the pressure term. This is different for the different forms of matter.

1.1.4.1 Baryons

In terms of *familiarity* the primary form of matter is baryonic. Strictly speaking this is matter composed of three quark particles. However, for the purposes of cosmology this is extended to include the electron. Therefore all atoms, all of ourselves and all of the structures in our surroundings are baryonic.

We can quantify the energy E of these baryons if we know both the rest mass m and their momenta p by $E^2 = m^2 + p^2$. Generally speaking, in the later stages of the Universe's evolution matter tends to be less energetic and has small momenta relative to its rest mass. In this case we say that it behaves non-relativistically and subsequently it is a good approximation to assume it exerts negligible pressure $P \approx 0$.

Inserting this into the fluid equation (Eq. 1.10) we can solve for ρ first finding $\dot{\rho}+3\frac{\dot{a}}{a}\rho = 0$ and finally $\rho \propto 1/a^3$. This implies, as we might have guessed, that the density drops in proportion to the volume. Despite the apparent abundance of baryons recent studies suggest that $\Omega_b = 0.0441 \pm 0.0030$ (Dunkley *et al.* 2009), i.e. baryons comprise only $\approx 5\%$ of the entire energy contents.

1.1.4.2 Radiation

Again in terms of its apparent ubiquitousness radiation is an important constituent in the cosmos. In the electromagnetic form it is literally our primary tool for observing the Universe. Observations

[2]Note that there is a summation over the repeated μ index.

in the visible, infrared, X-ray, radio and microwave allow us to infer the expansion highlighted in Section 1.1.1, the properties of galaxies such as star formation and their mergers, the properties of clusters and their gas, and the small fluctuations in thermal equilibrium present in the very early Universe – to name a few.

The pressure of radiation is given by $P = \rho/3$. Entering this into the fluid equation once more (Equation 1.10) renders $\dot{\rho} + 4\frac{\dot{a}}{a}\rho = 0$ and finally $\rho \propto 1/a^4$. This implies, as one might not have guessed, that the energy density for radiation falls faster than matter. Physically the extra factor can be attributed to a redshifting of the radiation's wavelength with expansion. Furthermore, via the Stefan-Boltzmann law, which states that the energy density of black body radiation is given by $\epsilon \propto T^4$, the temperature of the CMB, for example, is seen to decrease in accordance with $T \propto 1/a$. It is expected therefore that the early and energetic Universe was dominated by radiation with the faster decrease in density later giving rise to matter domination. This density Ω_R is monopolised by the energy in the microwave background and is inferred from its temperature ($T_0 = 2.728\ K$) giving $\Omega_R \approx 5 \times 10^{-5}$.

1.1.4.3 Neutrinos

First postulated by Wolfgang Pauli in 1930 to conserve energy and momenta in beta decay the neutrino was long thought to be massless. However, it was later observed by the Super-Kamiokande experiment that there are oscillations between the neutrino flavours (Fukuda *et al.* 1998). This indicates that the neutrino species must have finite mass eigenstates. Furthermore, the thermal equilibrium that briefly occurred between the early primordial plasma and the cosmic neutrino background ensures the neutrino to be particularly abundant. One might suggest therefore that neutrinos could account for a large fraction of the missing energy density, giving $\Omega_{\rm total} \sim 1$. Quantifying Ω_ν or equivalently $\sum m_\nu$, the sum of the individual masses, is considered in detail in Chapter 4. Unfortunately it is found that while the neutrino contributes significantly to cosmological phenomena it does not contribute sufficiently to the total energy density $\Omega_\nu \sim 0.01$.

The neutrino is not only of great cosmological interest but also an astrophysical one. For example, in the process of a core collapse supernova $\sim 99\%$ of the energy released is via neutrinos. These are produced both thermally and in the formation of a neutron star: $p + e^- \rightarrow n + \nu_e$. The photons formed can take considerable time to diffuse through the extreme density of the collapsing material. On the contrary the neutrinos barely interact with the infalling matter and free-stream away from the object. This allows the possibility of using neutrino burst detections as an early warning system in order to observe an entire supernova intensity profile with time.

1.1.4.4 Dark Matter

It is now becoming increasingly apparent that in order to have a flat Universe, as stated in Section 1.1.3, there must be a previously *unknown* contribution to the energy density. Explicitly speaking, if we add up all the baryons Ω_b, photons Ω_R and neutrinos Ω_ν described above we can not account for $\sim 95\%$ of the cosmos.

One potential insight concerns the dynamics of galaxies. It has long been noted that their high rotation velocities require an inordinate amount of mass relative to that observed as visible matter (in any part of the electromagnetic spectrum). Put simply: there must be large quantities of extra matter. This is known as *dark matter* and by definition it is not expected to interact electromagnetically. It is often assumed to be collisionless and non-relativistic (and so $P \approx 0$) and is therefore frequently referred to as *cold* dark matter (CDM). Subsequently its density Ω_c evolves like baryonic matter $\propto 1/a^3$ and so too comes to dominance over the early radiation era. A host of independent cosmological probes from the CMB to the clustering of galaxies (Chapter 3) all agree on a consistent value of $\Omega_c + \Omega_b = \Omega_m \approx 0.25$.

As the existence of dark matter in galaxies has been deduced purely on gravitational grounds it has been suggested that the effect could be the result of a modification to gravity. For example, Milgrom (1983) has proposed an acceleration scale a_0 below which Newtonian dynamics are modified to explain the galactic rotation curves. This is called Modified Newtonian Dynamics (MOND). On the other hand recent data from a merging cluster system–the *Bullet Cluster*–has cast some doubt on this (Clowe *et al.* 2006). The cluster system appears to show a distinct separation in baryonic and dark matter caused by electromagnetic collisions in the former. This dissociation is not present in MOND and the theory seems to require neutrinos with ≈ 2 eV mass to remain viable. I undertake a cosmological constraint of the neutrino in Chapter 4 and show this mass range to be unlikely–consistent with the community.

1.1.4.5 Dark Energy

Despite the fact that the energy budget is increasing there is still $\approx 75\%$ that is completely unaccounted for. This additional form of missing matter is called *dark energy* and it is expected to have the most peculiar of properties.

Just over a decade ago it was empirically found that the expansion of the Universe is not slowing down, as one would expect under the attraction of the aforementioned matter, but instead accelerating! This was achieved by probing the luminosity distance-redshift relation (see Sec-

tion 1.1.5) with observations of type 1a supernovae (E.g. Riess *et al.* (1998) and Perlmutter *et al.* (1999)).

By looking at the acceleration equation (Eq. 1.8) it is possible to see the unusual condition under which this acceleration might occur. For this phenomenon we require that $\ddot{a} > 0$ and so $(\rho + 3P) < 0$. Now given that we know nothing about this hypothetical fluid we have very little chance of guessing its pressure term. Instead we can simply parameterise the pressure in terms of the density $P = w\rho$, where the constant of proportionality w is known as the equation of state. Under this terminology $w = 1/3$ for radiation and $w = 0$ for the baryons and dark matter. Inserting this expression into the condition above we find $\rho(1 + 3w) < 0$. After some rearrangement this can be reduced to $w < -1/3$; the missing energy component must have a negative pressure.

The Cosmological Constant

The cosmological constant Λ was initially introduced by Einstein as a modification to the original general relativity theory in order to accomplish a balanced and stationary Universe,

$$R^{\mu\nu} - \frac{1}{2}g^{\mu\nu}R + \Lambda g^{\mu\nu} = 8\pi G T^{\mu\nu}. \tag{1.11}$$

This idea temporarily vanished with the evidence of the Hubble expansion but has since reappeared as a way of explaining dark energy. In this specific case the equation of state is constant and is exactly equal to -1. The resulting solution to the fluid equation gives $\rho = \text{constant}$. As a result the density does not fall off with expansion and will come to dominate over matter. Together with dark matter this has become a popular, although theoretically unfulfilled, paradigm and is often referred to as ΛCDM. Complementary estimates indicate $\Omega_\Lambda \approx 0.75$ thus fulfilling the missing energy budget.

Similarly to dark matter the existence of dark energy has been invoked assuming an underlying theory of gravity: general relativity. It could be that under the circumstances of interest this theory is a poor description of gravitational phenomena and that a modification to this theory will explain the acceleration naturally. This is the subject of Chapter 2.

1.1.5 Distance

Throughout the introduction of the metric and of the scale factor we have not explicitly addressed the idea of distance in an expanding background. Clearly, measuring distance in such a setting could be a challenging yet subtle task and accordingly there are several forms to consider:

Comoving Distance

Any observer that perceives the CMB to be isotropic[3] is a *comoving* observer. They are comoving in the sense that their motion is determined entirely by the Hubble flow and expansion. Imagine now that earlier in the Universe's expansion history we had placed a grid over comoving observers such that it too was carried along with the expansion. Therefore on a given grid axis the distance between two observers would not change. This is the *comoving distance*.

One coordinate system that does not expand with the Hubble flow is that associated with the physical distance. The physical (r) and comoving (x) scales are related simply by $r = a(t)x$. Therefore, the comoving distance between a distant object and ourselves can be calculated as,

$$\chi(a) = \int_{t_a}^{t_o} \frac{\mathrm{d}t}{a(t)} = \int_a^1 \frac{\mathrm{d}a}{a^2 H(a)} \tag{1.12}$$

where the scale factor today is defined to be unity ($a_0 = 1$) but becomes vanishingly small ($a \to 0$) towards the Big Bang. The $H(a)$ factor is the solution to the Friedmann equation (Eq. 1.7) depending on all the constituent matter densities.

If we increase the lower limit in the above integral such that $t_a = a = 0$ this will represent the comoving limit of causality. As such it is often referred to as the *comoving horizon* (η).

Luminosity Distance

A pragmatic approach to inferring distance in cosmology is to consider an object for which the intrinsic luminosity L is known. One can then make an estimate of the distance d by taking a measurement of its observed flux F. For an isotropic source the energy is spread evenly over the surface of a sphere and so the quantities of interest are related by,

$$F = \frac{L}{4\pi d^2}. \tag{1.13}$$

This is valid in a static or comoving space ($d = \chi(a)$ and $L = L(\chi)$) but needs to be generalised for an expanding one.

Working from a comoving coordinate system the observed luminosity in the physical coordinates L_o is diminished relatively by both the Doppler shift of emission and a relativistic redshift. Both of these decrease L_o by a factor of $(1 + z)$ giving,

$$F = \frac{L_o}{4\pi\chi^2(1+z)^2}. \tag{1.14}$$

[3]Obviously only an observer with poor instrumentation can observe the CMB to be truely isotropic on all scales. This refers to a redshifting and blueshifting of the entire CMB produced by relative motion thus resulting in a *dipole* anisotropy.

Equating this expression to the earlier flux equation (Eq. 1.13), the *luminosity distance* d_L can be interpreted as,

$$d_L \equiv \chi(1+z) = \frac{\chi}{a}. \tag{1.15}$$

In practise, this distance measure is applicable to type 1a supernovae. These are a specific form of thermonuclear explosion resulting in the death of a star. In particular they are thought to arise from the accretion of matter onto a white dwarf in a binary system. At a definite mass (the Chandrasekhar mass) the star is unable to support itself and collapses thus increasing its temperature. At this moment the star becomes capable of carbon fusion and obliterates itself in a runaway process releasing large quantities of stellar material, photons and neutrinos.

The prominent point is that as this is expected to occur at the same mass each supernova might be expected to have the same intrinsic luminosity. In fact, the intrinsic luminosity is dependent on the observed intensity profile of the exploding star. In this way by measuring the observed brightness of supernovae in the sky it is possible to examine the luminosity distance-redshift relation and hence probe models of the expansion history in the process. This is performed in Section 2.5.2 and 4.3 in order to reduce the parameter degeneracies of the model in question.

Angular Diameter Distance

Alternatively, one can measure the *angular diameter distance* d_A. This is defined as the ratio of a body's (potentially known or theorised) projected magnitude on the sky l to its angular size θ[4], i.e.,

$$d_A = l/\theta. \tag{1.16}$$

In comoving space the projected scale of the object is l/a and the comoving distance *to* the object is $\chi(a)$. As the subtended angle is the ratio of the transverse and radial distances, $\theta = (l/a)/\chi(a)$. Inserting this into Equation 1.16 enables a calculation of the angular diameter distance,

$$d_A = \frac{\chi}{1+z} = a\chi. \tag{1.17}$$

This can therefore be applied whenever we know or whenever we can theorise the extent of something in the sky. This includes, for example, the characteristic scale of acoustic fluctuations in the CMB or their remnants in the galaxy clustering pattern known as baryon acoustic oscillations (BAOs). Again, this is encountered in Section 2.5.2 and 4.3 to relate the available data to proposed cosmological parameters, such as Ω_m and H_0, sequentially through $d_A(a)$, $\chi(a)$ and $H(a)$.

[4] In radians.

In addition, it should be noted that in the potential presence of curvature (Section 1.1.3) the angular diameter distance is generalised to,

$$d_A = \frac{a}{H_0\sqrt{|\Omega_k|}} \begin{cases} \sin[\sqrt{-\Omega_k}H_0\chi] & \Omega_k < 0 \\ \sinh[\sqrt{\Omega_k}H_0\chi] & \Omega_k > 0 \end{cases}$$

with $\Omega_k = 1 - \Omega_{\rm total}$.

1.1.6 Inflation

Except for the nature of dark matter and dark energy there are several other major issues that face the Big Bang model we have built up so far. These can be summarised as the flatness, horizon, structure and monopole problems:

Flatness

Using the expression for the critical density ρ_c (Eq. 1.9), the Friedmann equation (Eq. 1.7) can be recast succinctly into,

$$|\Omega(a) - 1| = \frac{|k|}{a^2H^2}. \tag{1.18}$$

From this it is clear that if the total density $\Omega(a)$ is identical to one then it persists as equal to one for the entire evolution of the Universe. However, it is also clear that this is an unstable solution; for in the presence of matter or radiation, say, $|\Omega(a) - 1|$ grows with evolution. Therefore, any deviation from a flat geometry will give rise to an ever more curved geometry. Indeed, under the assumption of matter domination $|\Omega(a) - 1| \propto t^{\frac{2}{3}}$.

With the above reasoning and the empirical evidence that $\Omega_k \approx 0$ one can argue that the early Universe ($t \approx 10^{17}$ seconds ago) must have been *exceptionally* flat! This can be interpreted as rather fine-tuned given that even a slight change in the early value leads to wild differences in today's observable cosmology.

Horizon

When deducing the form of a cosmological metric in Section 1.1.2 we noted that the Universe, and thus the metric, are extremely isotropic even on large scales. Evident in the CMB temperature we can attribute this to an early Universe that was hot and in thermal equilibrium. However, as light from widely separate regions has been traveling to us from the edges of our observable horizon, since this equilibrium epoch, we must conclude that these areas are not causally connected!

For this reason they could not have been in thermal equilibrium to produce the uniformity.

Structure

The small fluctuations in the CMB thermal bath are believed to be the progenitors of galaxies, clusters and voids we observe now. Although, to obtain the current large scale structure there must have been fluctuations in the density spectrum on scales that previously were outside the horizon. Again, causal processes could not have caused these perturbations.

Monopoles

A magnetic monopole is a hypothetical particle with only *one* pole. These have been predicted by a number of Grand Unified Theories (GUTs) and are expected to be particularly numerous and massive. Therefore these particles would have been non-relativistic far earlier than ordinary baryonic matter giving them, on average, a much slower density reduction with regards to radiation or any other matter component. However, the problem is that these particles are at least rare enough not to have been observed to date–unless of course, they do not exist at all.

The solution:

A period of prodigious and extreme expansion in the very early Universe ($t \sim 10^{-34}$ seconds), called Inflation, has since been invoked to explain these issues and yet preserve the successful features of the Big Bang model.

The enormous increase in the scale factor with time blows up the denominator in Equation 1.18 thus driving the geometry decisively towards flatness. If there is ample increase at these early times this can be sufficient to keep Ω_k close to zero as observed today, despite all the consequent departure from flatness in $|\Omega - 1|$. Furthermore, this rapid period of inflation takes a region of causally connected and thermalised space and amplifies it beyond the boundaries of our current observable Universe. In this way widely separated regions on the sky *have* been in causal contact. The observed large scale homogeneity is then a result of smaller scale homogeneity being frozen across the sky with post-inflation mechanisms incapable of altering it in a causal way. The inflation also allows for the inhomogeneous structure we observe today as the inflationary period enables primordially generated quantum fluctuations to grow to cosmological scales. Many theories of inflation predict these fluctuations to be Gaussian and this is seen to be consistent with the CMB. Finally, if the aforementioned magnetic monopoles are produced at an energy above that corresponding to the end of inflation their observed density will be diminished resulting from a

dilution with inflationary expansion.

1.2 The not-so-smooth and expanding Universe

This subsection describes the departures from isotropy and homogeneity associated with the growth of structure in the Universe. It illustrates the growth of over-densities (1.2.1), the statistical quantities that describe them (1.2.2) and finally the probes that are sensitive to these fluctuations (1.2.2.1 and 1.2.2.2).

1.2.1 Inhomogeneities

In our earlier treatment of the Friedmann-Robertson-Walker metric (Eq. 1.5) we observed that the Universe was close to homogeneous on large scales–effectively pervaded by a smooth homogeneous fluid. However, the field of astronomy is interesting because our present and local environment is decidedly inhomogeneous; it is filled with clusters, galaxies and a whole host of astrophysical entities.

Earlier I alluded to the notion that inflation takes primordial quantum fluctuations and amplifies them to astrophysical and cosmological size. These and the resulting irregularities in the CMB are the seeds of this fascinating structure. It is important to notice though that there is a large discrepancy in the magnitude of these perturbations. As stated before, the CMB fluctuations are very small, whereas a galaxy cluster, for example, can be of order a hundred times the mean density of the Universe. The mechanism that provides this growth, from seed to structure, is *gravitational instability*.

An initially over-dense region can be considered to have two competing forces acting on it. Firstly, a mutual gravitational attraction will act towards the centre of the mass attempting to increase the overdensity. This is contested by a pressure force acting against gravity. The pressure can be provided, for example, by the thermal motion of the gravitating particles under consideration. This can be seen prominently in the plasma of the very early Universe. In the radiation dominated Universe the photons will have a small mean free path due to regular Thomson scattering with free electrons. The entirety of the electron population will be free because the mean thermal energy exceeds the hydrogen binding energy. Therefore, the electron and photon fluids are tightly coupled, forming in the process a photon-baryon plasma. Due to the domination of the radiation energy density in this epoch the photons dominate the bulk of the gravitational force. Collapsing under this force the photons, and therefore the baryon fluid, will eventually oscillate

due to the radiation's pressure. Over large scales this pressure is unable to act due to a finite sound speed and as a result the perturbation can continue to increase with gravity.

Mathematically this can be derived from perturbed energy-momentum conservation in the Einstein Equations. This is equivalent to utilising the Euler and continuity (conservation) equations on the first order perturbed quantities ($\delta\rho$, δP, $\delta\vec{v}$ and $\delta\psi$) and substituting for the Poisson equation,

$$k^2\psi = -4\pi G a^2 \rho\delta. \tag{1.19}$$

Here P, $\vec{v}$ and ψ are the pressure, velocity and potential, respectively. The over-density ρ can be further written in terms of the mean density in the Universe $\bar{\rho}$ and is referred to as the density contrast δ,

$$\delta(\vec{r}) = \frac{\rho(\vec{r}) - \bar{\rho}}{\bar{\rho}}. \tag{1.20}$$

Combining this all together yields Equation (1.21). This expression is analogous to the physical explanation above concerning radiation pressure and gravitational instability. The k^2 term is a consequence of writing the density contrast in Fourier space and c_s^2 describes the sound speed of the fluid.

$$\ddot{\delta} + 2H\delta = (-\frac{c_s^2}{a^2}k^2 + 4\pi G\rho_0)\delta. \tag{1.21}$$

Whether the perturbation grows or not therefore depends on the overall sign of the right hand side. The associated scale ($\lambda_J = 2\pi/k_J$) for this is called the Jeans length and is given by,

$$\lambda_J = c_s\Big(\frac{\pi}{G\rho_0}\Big)^{\frac{1}{2}}. \tag{1.22}$$

In line with the physical interpretation (in the radiation dominated era) when $\lambda > \lambda_J$ gravitational collapse dominates and the perturbation can increase. Otherwise, when $\lambda < \lambda_J$, the pressure remains substantial and the perturbations do not grow.

During matter domination, on the other hand, the radiation is incapable of governing the gravitational dynamics. This role is taken over by the dark matter which, as we noted earlier (Section 1.1.4.4), has negligible pressure ($P \approx 0 \implies c_s^2 \approx 0$). As a result the gravitational attraction becomes uncontested and the perturbations grow on all scales; evolving eventually to become a galaxy, pulsar or even Earth-like planet.

1.2.2 The Power Spectrum

A given model for cosmology is not expected to make an exact prediction as to the specific location of an over-density or the precise temperature of a CMB fluctuation at a point in the sky. It is, however, expected to make a prediction for the statistical distribution of these fluctuations.

In cosmology a valuable statistical entity (and the one most commonly adopted) is the power spectrum (Blackman & Tukey (1959), Yu & Peebles (1969) and Peebles (1973)). This effectively describes how much a field changes on varying scales. Specifically, if a field has fluctuations that are changing significantly over fixed separations, such that the variance of these fluctuations are large, the power spectrum would be sizable over this scale too. Conversely, if the field is not varying on a given scale the power spectrum will be small. Accordingly, the power spectrum is defined through,

$$< \tilde{\delta}(\vec{k})\tilde{\delta}^{*}(\vec{k}^{\prime}) >= (2\pi)^{3}P(k)\delta^{n}(\vec{k}-\vec{k}^{\prime}) \tag{1.23}$$

where δ^n is the Dirac delta function, $P(k)$ is the power spectrum and $< .. >$ is the ensemble average of a realisation of the field δ. The ensemble average is over many realisations of the field each with identical statistical properties. Propitiously, if the underlying field is a random Gaussian field then the power spectrum succeeds in describing and encapsulating the whole of the field. Indeed, if a superposition of many independent random processes produced the fluctuations in the early Universe, the resulting field would be Gaussian as a consequence of the Central Limit Theorem. Such a mechanism could be provided by quantum fluctuations during inflation, for example.

1.2.2.1 Matter Power Spectrum

The matter power spectrum can be calculated theoretically by considering the growth of structure on different scales as described in Section 1.2.1. We can get insight into the shape of this function by first noting that most theories of inflation predict the initial (post-inflation) power spectrum to be in the form of a power law,

$$P_i(k) \propto k^n. \tag{1.24}$$

As the matter power spectrum is usually plotted in log-log space this initial power spectrum is a diagonal straight line. From the earlier discussion we know that on the smallest scales (large k) the perturbations are unable to grow. However, large scales (small k) are beyond the influence of the radiation pressure and are free to evolve. The extra growth leads to a more clustered field and so the power spectrum subsequently increases (at that scale). The net result is for the straight line power law to bend, or turnover, at the interface of these two conditions.

With time the pressure/sound wave propagates to the larger perturbations. Obviously this halts any evolution at this scale and so the amplitude of the power spectrum stabilises, shifting the

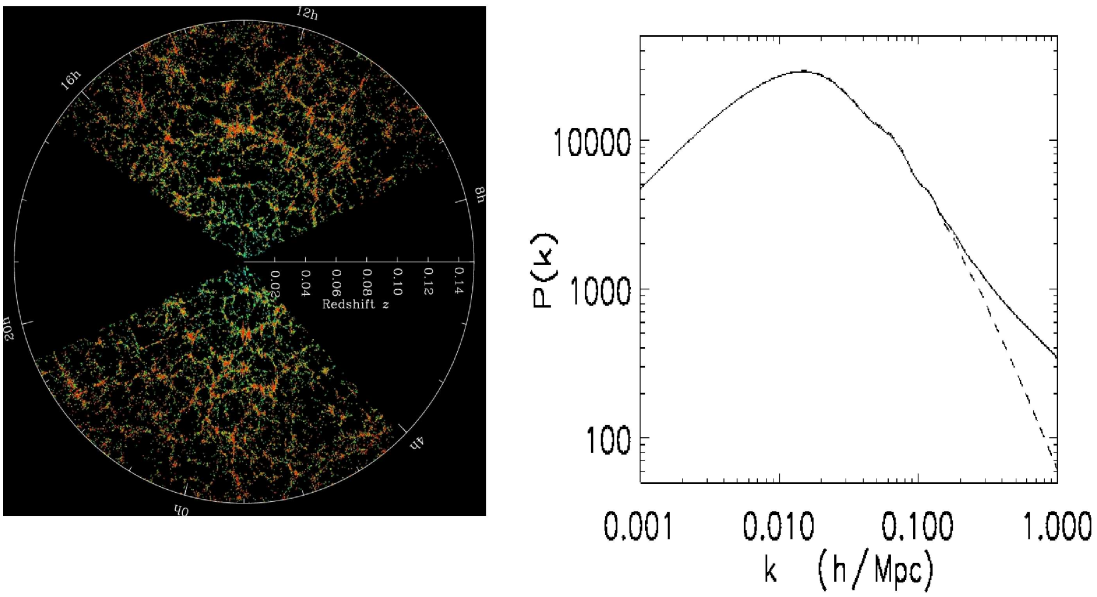

Figure 1.3: **Left panel:** The distribution of nearly one million galaxies in the local Universe as seen by the Sloan Digital Sky Survey (SDSS). The dark wedges result from dust obscuration from our own Galaxy. CREDIT: *http://www.sdss.org* [*M. Blanton and the SDSS*]. **Right panel:** The present day matter power spectrum $P(k)$, calculated using CAMB (Lewis *et al.* 2000), quantifies how the underlying mass distribution varies across different scales. The turnover of the power spectrum, the baryonic wiggles and the non-linear evolution (linear evolution is dashed) are clearly evident at progressively smaller scales.

turnover of the spectrum to larger and larger scales (smaller and smaller k). Finally, at the onset of matter domination, when all the scales are able to evolve, the shape of the power spectrum becomes fixed. The resultant present day power spectra is illustrated in the right panel of Figure 1.3. To reiterate, the x-axis is expressed in the wavenumber k and hence small scales appear to the right of the plot.

Clearly evident in Figure 1.3 are a succession of wiggles at slightly smaller scales than the turnover. This is a consequence of the photon-baryon fluid set up in the early Universe. In the absence of pressure later in the matter dominated era the baryons will be left in a shell at a fixed radius from the original centre of the over-density. As the dark matter is not coupled electromagnetically to either photon nor baryon it will still reside mainly at this centre. These two regions will subsequently attract matter gravitationally, eventually forming into galaxies over this preferential scale. The resulting signatures in the power spectrum are befittingly referred to as the baryon acoustic oscillations (BAOs). In addition, their calculable scale on the sky enables a clean measurement of the angular diameter distance d_A (Section 1.1.5).

The matter power spectrum can be observed by measuring the angular and radial positions of galaxies. The radial position is necessarily a redshift observation and hence a series of galaxy measurements is often referred to as a galaxy or redshift survey. One such survey–the Sloan Digital Sky Survey (SDSS)–is illustrated in the left panel of Figure 1.3. Strictly speaking such a measurement is a measurement of the *galaxy* power spectrum as we observe, by definition, only the luminous matter. If these galaxies linearly trace the dark matter distribution it is possible to relate the two spectra,

$$P_g(k,z) = b^2\ P_m(k,z) \tag{1.25}$$

where $P_g(k,z)$ is the galaxy power spectrum, $P_m(k,z)$ is the matter power spectrum and b is called the bias. Our ignorance with respect to this bias represents one of the major uncertainties in a galaxy survey measurement and, at the very least, b must be included and marginalised (Section 1.3.1) over in any cosmological analysis. Generally this biasing is expected to be a function of redshift and of scale $b = b(k,z)$.

In Chapter 3 I construct a new measurement of the power spectrum based on the most recent SDSS galaxy catalogue (DR7) and use this to place constraints on the matter Ω_m and baryon $f_b = \Omega_b/\Omega_m$ densities.

Non-linear Matter Power Spectrum

As a given over-density continues to collapse the density contrast (Eq. 1.20) will eventually become of order unity $|\delta| \sim 1$. This is particularly common over smaller scales in the late time Universe. At this point linear perturbation theory ceases to be valid. One could calculate successively higher order perturbations although it inevitably fails to converge. Instead a pragmatic approach to this issue is to reproduce the non-linear evolution with N-body simulations for a range of parameters. With this methodology Peacock & Dodds (1996) and Smith *et al.* (2003), for example, have provided a fitting function to map the linearly evolved power spectrum into the non-linear. The non-linear growth causes an additional increase in the clustering of the matter field, thus boosting the power spectrum on small scales. The difference in the linear and non-linear power spectra can be seen distinctively in Figure 1.3 as the dashed and solid lines, respectively. Some of the issues pertaining to the use and applicability of these universally implemented fitting functions are discussed in Chapter 5.

Weak Gravitational Lensing

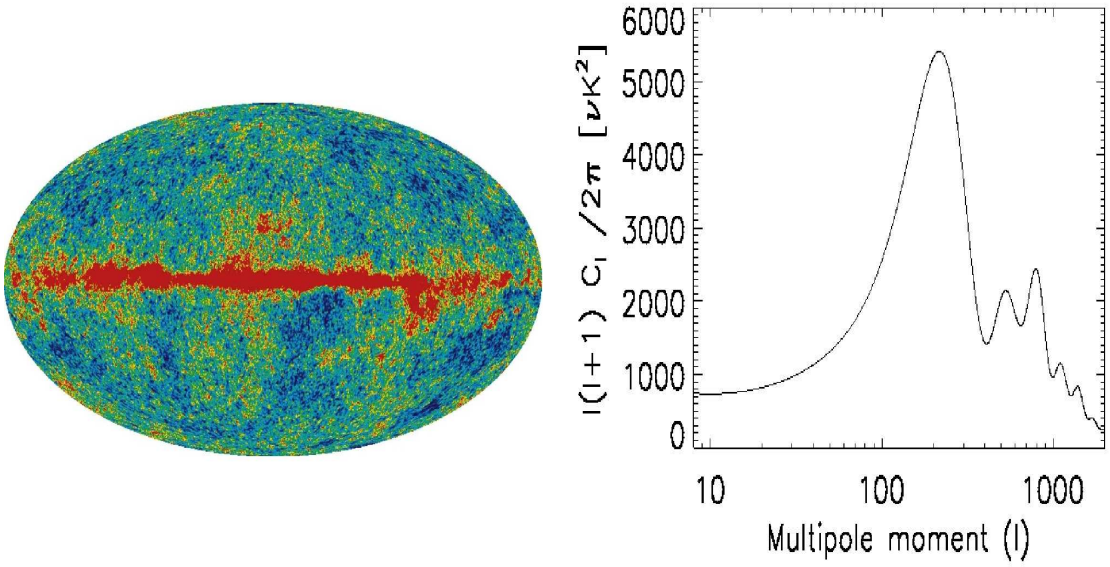

Figure 1.4: **Left panel:** The temperature fluctuations in the cosmic microwave background radiation as seen by WMAP. This full-sky map is observed in the V-band (61 Ghz) where the galactic foreground across the centre (red) is minimal. The linear temperature scale ranges from $-200\mu K$ to $200\mu K$. CREDIT: *http://lambda.gsfc.nasa.gov* [*wmap science team*] **Right panel:** The CMB angular power spectrum C_ℓ quantifies how these temperature fluctuations vary across different scales. The C_ℓ values have been calculated using CAMB (Lewis *et al.* 2000) and can be matched to the data points to infer an underlying model as in Dunkley *et al.* (2009) and Section 4.2.

Weak gravitational lensing provides an alternative and powerful method to probe the matter power spectrum. This involves measuring the shapes of galaxies, which have been distorted by the intervening mass distribution, on route to the observer. Even though this distortion, or *shearing*, is a small effect significant cosmological information can be extracted with a statistical analysis. A more thorough introduction to this cosmological probe is left to Chapter 2 where it is used extensively.

1.2.2.2 The CMB Power Spectrum

The observed temperature fluctuations in the cosmic microwave background are shown in the left panel of Figure 1.4. This is quantified statistically by the angular power spectrum and is illustrated for a representative cosmology in the right panel. The current best fit cosmology has been inferred in Dunkley *et al.* (2009) and is explored also Section 4.2. The underlying mechanisms for these anisotropies can be categorised into those that happened at the time of last scattering (*primary*

anisotropies) and those that have acted since (*secondary* anisotropies).

Primary Anisotropies

Acoustic Oscillations

The main physical process in the formation of the anisotropies is once again the oscillation of the photon-baryon fluid described copiously in Sections 1.2.1 and 1.2.2.1, but with the focus on the conclusion to the photon perturbations.

While the matter over-densities are collapsing freely during the onset of matter domination the photons will continue to oscillate in the potential governed by the dark matter. Finally, when the mean thermal energy is considerably lower than the hydrogen binding energy there is a cessation of Thomson scattering enabling the photons to free stream. It is this pattern of acoustic oscillations, at the time of recombination, that we observe today. One particular scale will correspond to an over-density that has collapsed and is on the verge of oscillating for the first time. As this is replicated over the entire sky we can expect the power spectrum at this scale to be large. This is the main acoustic peak in the CMB as seen in Figure 1.4.

Over successively smaller distances there will be perturbations having undergone multiple oscillations. These have had time to expand and contract back to maximum density and represent the series of acoustic peaks to the right of the main bump.

The Sachs-Wolfe effect

A photon observed from an over-dense region will have to climb out of its surrounding potential well in order to escape. In an under-dense region the photon will instead roll down its local potential. The overall effect of this is to provide power to the CMB over large scales (small multipole moment ℓ). This is known as the Sachs-Wolfe effect.

Silk Damping

At very small scales ($\ell \gtrsim 800$) the anisotropies suffer an exponential damping called Silk Damping. This is a consequence of an extended period of recombination. During this time photons diffuse from the denser and therefore hotter regions to the colder less dense areas. In doing so the electrons too are displaced, dragging protons with them through the Coulomb force. This effectively smoothes out the perturbations on small scales and so suppresses the associated power spectrum.

Secondary Anisotropies

The Integrated Sachs-Wolfe effect (ISW)

Photons that are propagating through the late-time Universe are inevitably incident on some gravitational potential. As they descend into the potential the photon is gravitationally blueshifted due to an increase in energy. On departure the photon is redshifted resulting from a loss of energy in climbing from the potential well. The net effect would seem to be zero. However, this is only the case for a time independent potential. If it were to decay, for example, the photon would suffer a net blueshifting; it would have less of a hill to climb out of, than it rolled down in the first place. Such a decay is expected to occur in the presence of curvature or dark energy.

The overall effect for a photon is the sum from all contributions along the line-of-sight and is in this sense the *Integrated* Sachs-Wolfe effect. The ISW contributes to the CMB power on large scales but is sub-dominant to the normal Sachs-Wolfe effect. Evidence for the ISW has been claimed in a number of sources, such as Rassat *et al.* (2007), and can be found through a cross correlation of the CMB signal with large scale structure.

The Sunyaev-Zeldovich effect

The Sunyaev-Zeldovich (SZ) effect is caused by the inverse Compton scattering of CMB photons by hot cluster electrons. It has a specific frequency dependence and can therefore be detected through observations in multiple wavelength bands. Most importantly, as the SZ effect is caused by scattering its magnitude is redshift independent. This is particularly useful for the SZ as a cluster finding tool given that it can detect clusters at high redshift just as easily as it can at low redshift. Accounting for this distortion is particularly important for any CMB analysis at small scales (high ℓ).

Gravitational Lensing of the CMB

In the same way that images of distant galaxies are expected to be distorted by large scale structure so too are the anisotropies of the CMB, e.g. Seljak (1996) and Lewis & Challinor (2006). This is a small effect which occurs mainly at high ℓ. The overall contribution slightly smoothes the anisotropic peaks while adding power to the smallest of scales ($\ell \sim 3000$).

As the secondary anisotropies occur at a different point in cosmic evolution and often are the

result of different physics, they provide a self-contained procedure for breaking the parameter degeneracies implicit within any isolated cosmological probe. Furthermore, they contain important information on the late-time Universe, such as the era of dark energy domination $z \sim 1$. In this way they are a welcome consistency check with galaxy clustering and weak lensing, for example.

1.3 The Cosmological Model

This subsection describes the role of the statistical method in inferring physical components or parameters in the cosmological model. It highlights how we relate data to a model given any prior information we might have (1.3.1) and specifically the notion of a best fit and its error (1.3.2).

1.3.1 Bayes' Theorem

We start with what initially appears to be an abstract exercise in rearranging probabilities but is, in fact, a powerful method for statistical inference:

If there are two quantities X and Y then the product rule within probability simply states that the probability of X and Y both being true–given some other background information B–is equal to the probability that X is true *given* that Y is true, multiplied by the probability that Y is true,

$$P(X, Y|B) = P(X|Y, B) \times P(Y|B). \tag{1.26}$$

Obviously we can interchange the labels for X and Y without altering the truthfulness of this statement, i.e., there is a simple symmetry,

$$P(Y, X|B) = P(Y|X, B) \times P(X|B). \tag{1.27}$$

Even more apparent is that the probability of X and Y being true $P(Y, X|B)$ does not depend on the order we say or write them either. Therefore, the two expressions above are equivalent. This enables us to derive the far-reaching Bayes' theorem,

$$P(X|Y, B) = \frac{P(Y|X, B) \times P(X|B)}{P(Y|B)}. \tag{1.28}$$

In its present guise Bayes' theorem certainly does not seem so instrumental. However, we can write this in the slightly more provocative manner,

$$P(\Theta|\{d_i\}, B) \propto P(\{d_i\}|\Theta, B) \times P(\Theta|B) \tag{1.29}$$

if we call Y the data ($\{d_i\}$) and X the hypothesis (Θ). This new form of Bayes' theorem now states that the probability that an hypothesis is true given the data is proportional to the probability of obtaining the data assuming the hypothesis! This is particularly potent because it is our intention as cosmologists to derive the former probability (the posterior). For example, what is the probability that $\Omega_m = 0.25$ (hypothesis) given an angular power spectrum (data)? Moreover, it allows an estimate of this quantity because we can often calculate the second probability (the likelihood). In this case, what is the probability of getting that angular power spectrum given $\Omega_m = 0.25$?

Notice that the hypothesis does not have to be a single proposition, like X, but is free to represent a variable, parameter or series of parameters in a model. The probability is therefore a probability density function.

The second term in Equation 1.29 is known as the prior $P(\Theta|B)$. This contains any information that we might know (or not know) about the chosen variable *before* the analysis. This might be a parameter range introduced via common sense or physical reasoning. For example,

$$P(\Omega_m|B) = \begin{cases} 1 & \Omega_m \geq 0 \\ 0 & \text{otherwise} \end{cases} \tag{1.30}$$

where the background information B is that there is *some* matter in the Universe. By itself the prior encapsulates our level of knowledge about the hypothesis with no (extra) data. The shape of this function is subsequently altered in the light of more empirical information by the likelihood function.

The constant of proportionality in Bayes' theorem (Eq. 1.29) was introduced above because we neglected the evidence term $P(\{d_i\})$. This will not alter an estimate of the probability for a parameter as it does not depend on the hypothesis; it merely changes the normalisation scale. It can, however, be vital in differentiating between models.

Marginalisation

In general there may be a model with several parameters for which it is possible to calculate the posterior distribution. However, it may be that we are really only interested in one of them. Using a two parameter example, we could be interested in some physical entity X, that is necessarily associated with another parameter Y (a nuisance parameter). To understand the physics entailed by X it would be desirable to obtain the posterior just for this parameter. Obviously we can not fix the value of Y as this is tantamount to taking an arbitrary slice through the 2D posterior. A less biased 1D posterior treats the probability of X *irrespective* of Y, allowing it to vary through a

range of values. This procedure is marginalisation and can be derived with a little more algebra.

If the probability that X is true and Y is *not* true $P(X, \bar{Y}|B)$ is added to Equation 1.27 it is possible to obtain the expression,

$$P(X, Y|B) + P(X, \bar{Y}|B) = [P(Y|X, B) + P(\bar{Y}|X, B)] \times P(X|B). \tag{1.31}$$

Obviously the term in the square brackets is equal to one because in the discrete case Y is either true or not true. However, if instead Y represents a series of different outcomes one is free to simply add more terms, like $P(X, Y_1|B)$ or $P(X, Y_2|B)$, to the equation above. If the exhaustive range of possibilities for Y are added, the term in the square brackets will expand, becoming eventually equal to one again. Therefore,

$$\sum_{i=1}^{N} P(X, Y_i|B) = P(X|B). \tag{1.32}$$

In the circumstance that Y is a variable or parameter and is not discrete, the left hand expression in Equation 1.32 tends to an integral of the joint posterior distribution $\int P(X, Y|B)\,\mathrm{d}Y$. The distribution $P(X|B)$ is thus the posterior of the relevant quantity X having been marginalised over Y.

1.3.2 Parameter Estimation

1.3.2.1 The Best Fit

The best fit is the parameter value we most believe to be true. It can therefore be found by locating the value of the parameter for which the posterior distribution is largest. If the posterior is a continuous function of a parameter X this best fit point is the value for which the derivative, with respect to X, is zero. In the case of a flat prior this is equivalent to finding the *maximum likelihood*.

The probability of making a single observation o_1 given some signal s and measurement error σ_1 (e.g. the likelihood) is often assumed to take the Gaussian form,

$$P(o_1|s, \sigma_1, B) = \frac{1}{\sqrt{2\pi\sigma_1^2}} \exp\Big(- \frac{(o_1 - s)^2}{2\sigma_1^2}\Big). \tag{1.33}$$

For a multitude of measurements the likelihood generalises to $P(\{o_i\}|s, \sigma_i, B)$ for the set of data points $\{o_i\}$. However, two quantities are independent if $P(X, Y) = P(X) \times P(Y)$. Therefore, if the series of measurements are also independent (i.e. they do not affect one another) the joint likelihood can be expressed as a product of the individual Gaussians,

$$P(\{o_i\}|s, \sigma_i, B) = \frac{1}{(2\pi)^{\frac{N}{2}} \prod_{i=1}^{N} \sigma_i} \exp\Big(- \sum_{i=1}^{N} \frac{(o_i - s)^2}{2\sigma_i^2}\Big) \tag{1.34}$$

where N is the number of data points. It is common, however, to work with the logarithm of the likelihood and so this can be written,

$$\ln L = \text{constant} - \sum_{i=1}^{N} \frac{(o_i - s)^2}{2\sigma_i^2}. \tag{1.35}$$

The second term on the right is often referred to as the χ^2. Finding the best fit parameters by maximising the likelihood is thus the equivalent to minimising χ^2. This seems rather logical because we want the value of s to be such that the net difference between itself and the data is small. Evaluating $\mathrm{d}\chi^2/\,\mathrm{d}s = 0$ results in the rather intuitive, $s = \sum_i^N o_i/N$.

1.3.2.2 Uncertainty in the Estimate

The precision of any best fit value depends on the behaviour of the posterior in the local environment of the most likely value. A sharply peaked function simply states that there is little chance of the parameter taking a value too far from the best fit. A wide posterior assigns closely matched probabilities to all the values under consideration. The error bar corresponding to the first distribution should therefore be small; the second large.

To investigate the log likelihood in the vicinity of the best fit ($X = a$) one can take the Taylor expansion,

$$\ln L = \ln L(a) + \ln L'(a)(X-a) + \frac{\ln L''(a)}{2}(X-a)^2 + \frac{\ln L^3(a)}{3!}(X-a)^3 + \dots . \tag{1.36}$$

The first thing to notice is that the second term on the right hand side vanishes. This is because the best fit value has been found by requiring the first derivative to be zero. Also, we are free to ignore orders greater than or equal to 3 due to their diminishing contribution. This implies that the log likelihood can be detailed mainly by the constant first term and the shape determining quadratic term,

$$\ln L \approx \ln L(a) + \frac{\ln L''(a)}{2}(X-a)^2. \tag{1.37}$$

This equation has the same form as Equation 1.35 and can be equated. For the specific case of having one observation (i.e. $N = 1$) this reduces to,

$$\ln L''(a) = -\frac{1}{\sigma^2} \quad \Longrightarrow \quad \sigma_0 = \Big(\frac{-1}{\ln L''(a)}\Big)^{\frac{1}{2}} \tag{1.38}$$

Therefore, one can associate the uncertainty in the best fit (parameter) σ_0 as being related to the square root of minus the inverse of the second derivative in the log likelihood. When more data exists we expect our uncertainty to decrease, with the estimate of the posterior becoming

more sharply peaked about the best fit value. This can be quantified by increasing the value of N above–resulting in the summation $\sum_1^N 1/\sigma^2 = N/\sigma^2$ in Equation (1.38). The corresponding error σ, on the parameter, is subsequently reduced by the square root of the number of data points: $\sigma = \sigma_0/\sqrt{N}$.

Compared with most other scientific fields this last point results in a fundamental issue for cosmology: *cosmic variance*. The problem is that we only observe one Universe with a finite number of realisations or observations. For example, if we wish to observe the power spectrum over several large patches of sky, there are only several large patches of sky to observe. In this way cosmic variance affects any statistical analysis over small ℓ or k most severely and would be present even in the circumstance of having a noiseless instrument.

It is important to stress that much of the above reasoning has assumed a model with one parameter X. This can be expanded to an arbitrary number of dimensions with one or two extra generalisations:

- Best fit: The best fit parameters are derived by maximising the likelihood as before. However, in this case the solutions are from a set of *simultaneous* equations.

- Error bar: The exploration of the local likelihood as in Equation (1.36) will include extra derivatives with respect to the other variables. Therefore, the notion of the variance σ^2 resulting from the second derivative terms is generalised to a *covariance matrix*. The diagonal terms correspond to the variance for each parameter in question and the off-diagonal terms are associated with the mixed parameter derivatives. These cross terms describe the degree of correlation and degeneracy present between two parameters and is usually illustrated as a contour plot.

Practical Parameter Estimation

In order to sample the posterior space of n parameters one could envisage sampling a regularly spaced grid of parameter values. This method is highly inefficient though as the number of calculations, and hence computation time, scales with the power of n. In addition, it is most likely that more samples will be needed nearer and nearer to the best fit point. With limitations in computing time and patience in mind, alternative methods in parameter exploration have been developed.

- Markov Chain Monte Carlo (MCMC)

This is a general class of algorithms for sampling a probability distribution that rely on building a Markov chain. This chain is Markov in the sense that a new sample relies only on the current point and not on the history of points. It is intended that the desired posterior distribution is the equilibrium distribution of the Markov chain.

One specific algorithm that allows the user to construct such a Markov chain is the *Metropolis-Hastings* algorithm. In this procedure one can draw samples from the probability distribution $P(x)$, where at each time step a candidate point Y is chosen from a proposal distribution $Q(Y; x^t)$[5]. This proposal is accepted as the next point in the chain x^{t+1} if α, which is drawn from a random uniform distribution $U(0, 1)$, satisfies,

$$\alpha < \frac{P(Y)Q(x^t; Y)}{P(x^t)Q(Y; x^t)}. \tag{1.39}$$

The chain is implemented at a set of starting points $\mathbf{x}^{t=0}$ and run past a number of samples known as the *burn-in*. The number of samples in the burn-in correspond to the amount of time for the system to forget its starting point. These values are removed and all subsequent accepted points form a sample from $P(x)$. This is the procedure implemented by the industry standard code COSMOMC (Lewis & Bridle 2002) that is used throughout this thesis.

1.4 The Thesis Structure

This thesis is based mainly on the work in Thomas *et al.* (2009); Thomas, Abdalla and Lahav 2009a (In prep.) and Thomas, Abdalla and Lahav 2009b (In prep.). It is primarily concerned with using and providing data on the growth of structure in our Universe in order to test the underlying physics of our cosmology. In general, I assume that the geometry of the Universe is flat throughout with Gaussian and adiabatic primordial fluctuations and no running of the spectral index ($\alpha_s = 0$). However, explicit or implicit parameter choices, assumptions and values are stated within each chapter.

Chapter Overview

- Chapter 2: underlines the role of weak lensing in probing modifications to gravity. These departures from general relativity are invoked to explain dark energy and the corresponding

[5]For example, this might be a multivariate Gaussian at x^t.

accelerated expansion of distant galaxies. I use new CFHTLS weak lensing data to constrain a modified gravity theory motivated by a large extra dimension. Similarly, I use this data to test a more general parameterisation of gravity. Finally, I look to the proposed space-based Euclid weak lensing mission and forecast its potential constraining power with respect to these two models.

- Chapter 3: I construct a new angular power spectrum based on the final photometric Luminous Red Galaxy (LRG) Sloan Digital Sky Survey (SDSS II) data release–MegaZ LRG DR7. I use this data to place cosmological constraints on Ω_m, Ω_b, b and σ_8; the matter and baryon densities, the galaxy bias and the normalisation of the powerspectrum, respectively. The cosmological implications are tested against a number of potential systematics. Furthermore, I test for complementarity with the CMB.

- Chapter 4: I use a succession of cosmological probes to place a combined constraint on the cosmological model and the mass of the neutrino species. This includes data from the cosmic microwave background, supernovae, baryon acoustic oscillations, the HST prior and the new galaxy clustering data presented in Chapter 3.

- Chapter 5: includes a discussion of the issues, systematics, limitations and implications raised in the preceding chapters. This includes, for example, a consideration of the non-linear power spectrum and its application to a study of both modified gravity and the neutrinos. I also illustrate potential areas and avenues for fruitful work in the future. Finally, I conclude the work presented in this Thesis.

CHAPTER 2

CONSTRAINING MODIFIED GRAVITY AND GROWTH WITH WEAK LENSING

Abstract

The idea that we live in a Universe undergoing a period of acceleration is a new, yet strongly held, notion in cosmology. As this can *potentially* be explained with a modification to General Relativity I look at current cosmological data with the intention of testing gravity. Firstly, I constrain a phenomenological model (mDGP) motivated by a possible extra dimension. This is characterised by a parameter α that interpolates between $\alpha = 0$ (LCDM) and $\alpha = 1$ (the Dvali-Gabadadze-Porrati (DGP) 5D braneworld model). In addition, I analyse more *general* signatures of modified gravity given by the growth parameter γ and power spectrum parameter Σ. I utilise large angular scale ($\theta > 30$ arcminutes) Weak Lensing data (CFHTLS-wide) in order to work in the more linear regime and then add, in combination, Baryon Acoustic Oscillations (BAOs) and Type 1a Supernovae (SNe). I demonstrate that the bounds inferred are insensitive to potential systematics in the lensing data such as an underestimation of the CFHTLS shear at high redshift. Finally, I look beyond these present capabilities and demonstrate that Euclid, a future weak lensing survey, will deeply probe the nature of gravity.

This work is presented originally in Thomas, S.A., Abdalla, F.B. & Weller, J., 2009, *MNRAS*, **395**, 197. Also, my Euclid predictions for the standard cosmological model in Section 2.6.2 have been used by the Euclid Weak Lensing Working group for probe forecasting and detailed code comparisons.

2.1 Introduction

General relativity, a cornerstone of physics, is arguably one of our greatest intellectual achievements. It is not only elegant and physically motivated, but it makes a whole host of predictions including gravitational waves, the anomalous precession of Mercury and the deflection of light–all of which have been verified.

Considering this, today's cosmologists have been posed the most tantalising problem: given that recent precision data from Supernovae, the Cosmic Microwave Background and large scale structure (E.g. Astier *et al.* (2006), Dunkley *et al.* (2009), Percival *et al.* (2007) and Chapter 3) all indicate that the Universe is undergoing a period of cosmic acceleration, do we stand by this successful theory and invoke some new unseen matter component (*Dark Energy* - Section 1.1.4.5) to explain it? Or, more radically, do we treat this as evidence that Einstein's theory of gravitation, or the manner in which we implement it, is incomplete?

In this chapter I focus on the latter and investigate the idea that General Relativity is not general enough. We do not attempt to motivate a new theory of gravity but instead aim towards testing existing theories and aspects of general theories with current and future data. In Section 2.2 I review the concept of modified gravity, including a phenomenological model I go on to constrain, and touch upon some of its interesting features. One example feature, and thus potential signature of modified gravity, concerns the growth of structure. In Section 2.3 I look deeper at this characteristic and attempts to parameterise it analogous to the equation of state for dark energy. I highlight how this extra richness in modified gravity can break the observational degeneracy with dark energy models and discuss the ensuing limitations. In addition, it is noted how modified gravity alters the relationship, relative to GR, between the power spectrum of the potentials and the matter power spectrum which is implicit within weak lensing. Section 2.4 introduces weak gravitational lensing and its particular importance to modified gravity. This section also details the survey and data that is used (CFHTLS-wide: Fu *et al.* (2008) - From here on F08) and follows with a discussion of the working caveats, including non-linearities, and how this data circumvents the issue. Section 2.5.1 subsequently contains the analysis and constraints of the phenomenological model and parameterisation of growth through lensing. It is promptly followed in Section 2.5.2 by the addition of BAOs and Supernovae data to improve upon these constraints and break the parameter degeneracies. For all the analyses in Section 2.5.1 and Section 2.5.2 I implement a Monte Carlo Markov Chain (MCMC) approach (Section 1.3.2.2) with COSMOMC[1] (Lewis & Bridle 2002),

[1] http://cosmologist.info/cosmomc/

where the resulting plots have been produced with COSMOLOGUI[2]. In Section 2.5.3 I highlight potential systematics in the data and quantify any effect on the constraints. I also look beyond present day constraints on gravity in Section 2.6 and see how the highly exciting future weak lensing probe Euclid (Refregier *et al.* (2008) and Cimatti *et al.* (2009)) will be able to distinguish between GR and other models of cosmic acceleration and growth. I finish in Section 2.7 with a summary of the chapter including a discussion of the caveats and limitations as well as suggestions for future work.

2.2 Modified Gravity

General relativity itself is a modification of gravity. It superseded the previous established theory of gravity, Newton's Law of Gravitation, with a breathtaking physical principle for gravitational phenomena (Section 1.1.2). Although an elegant change in how we think about gravity it was quite simply necessary: The previous framework did not explain all gravitational processes. For example, it did not account for the anomalous precession of Mercury. Given the success of Newton's theory many attempts were made to understand this effect within its framework. In fact, even a form of dark matter was invoked (an unseen planet) to cause the required procession.

Today we face a similar choice with the evidence of accelerated expansion in the Universe. Again early attempts have tried to incorporate some new matter component within the formalism of our current theory. The simplest procedure has been to introduce a cosmological constant– *perhaps* arising from vacuum energy–to the usual Einstein field equations (Eq. 1.3 and Eq. 1.11). However, an observed disagreement of 120 orders of magnitude in the event of it resulting from the vacuum expectation represents a severe fine tuning problem. Other similar avenues have included the introduction of a dynamical scalar field which is either trapped within a false vacuum or slowly rolling down a potential (E.g. Wetterich (1988), Peebles & Ratra (1988), Frieman *et al.* (1995), Ferreira & Joyce (1998) and Albrecht & Skordis (2000)). These Quintessence or dark energy models can potentially lead to the desired acceleration.

2.2.1 Modifications

Alternatively, the more controversial, but historically successful, route is with another modification to gravity. Starting from the assumption that any viable theory should be described by a Lagrangian one might consider adding terms to the Ricci scalar (R) in the Einstein-Hilbert action

[2]http://www.sarahbridle.net/cosmologui/

for GR given by,

$$I_G \equiv -\frac{1}{16\pi G}\int \sqrt{-g}R\,\mathrm{d}^4x. \tag{2.1}$$

This procedure was first performed by Weyl and later in the context of inflation by Starobinskii (1980) but has more recently been analysed for the late-time low curvature universe, in e.g. Carroll *et al.* (2004), where the term $1/R$ was added. It was found to have the desired effect of acceleration but is ultimately unfeasible as a realistic alternative due to its failure to comply with solar system constraints (Chiba *et al.* 2006). A generalised modification could assume the underlying theory to be some general function of the Ricci scalar. These models, called $f(R)$ models, are being studied extensively in the literature (Durrer & Maartens (2008) and references therein). One could generalise this even further to functions of the Ricci tensor $R_{\mu\nu}$ and curvature tensor $R_{\mu\nu\rho\sigma}$, resulting in $f(R,R_{\mu\nu}R^{\mu\nu},R_{\mu\nu\rho\sigma}R^{\mu\nu\rho\sigma})$ gravity. However, this more general gravity suffers from higher order instabilities, through Ostrogradski's theorem (Woodard 2007), and so analysis has tended to focus on $f(R)$. It is not exclusively this subset of theoretical space that suffers theoretical problems however. Healthy theories of gravity seem to be particularly rare with most suffering from a whole host of theoretical afflictions; from ghost negative energy states to tachyonic behaviour (Durrer & Maartens 2007).

2.2.2 The Dvali-Gabadadze-Porrati (DGP) model

Beyond these general Lagrangians one could also look to higher dimensional models. Within the context of cosmology this *braneworld* scenario can somewhat be described as string theory inspired. Normal matter might be confined to a 4-dimensional brane, where the conservation equation $\dot{\rho}+3H(\rho+p)=0$ holds firm, but gravity is free to roam into a higher dimensional bulk. For late time acceleration we desire a model that will change over large distances and low energy scales. The DGP model[3] of Dvali-Gabadadze-Porrati (Dvali *et al.* 2000), described by the Lagrangian in Equation (2.2), is exactly this.

$$I_G \equiv \frac{-1}{16\pi G}\Big[\frac{1}{r_c}\int_{\mathrm{bulk}}\mathrm{d}^5x\sqrt{-g^{(5)}}R^{(5)}+\int_{\mathrm{brane}}\mathrm{d}^4x\sqrt{-g}R\Big] \tag{2.2}$$

It was originally created consisting of a 4-dimensional Minkowski brane within a 5-dimensional Minkowski bulk and with no motivation to explain dark energy. However the generalisation (Deffayet 2001) to a Friedmann-Robertson-Walker brane gave rise to a self-accelerating solution. Gravity leaking from this 4D brane into the bulk over large scales gives rise to the acceleration

[3] See Lue (2006) for an extensive review.

through a weakening effect. The resulting Friedmann equation represents a correction to the GR equation (Eq. 1.7) and is given by Equation (2.3) with r_c, the cross over scale, specified in Equation (2.4).

$$H^2 - \frac{H}{r_c} = \frac{8\pi G\rho}{3} \tag{2.3}$$

$$r_c = \frac{1}{H_0(1-\Omega_m)} \tag{2.4}$$

With this modification one has a full description of the expansion history. This also allows us to work towards understanding the growth of large scale structure giving two observational signatures that enable a cosmological study. The difference in the background acceleration is itself enough to produce a difference in the growth of structure. This can be seen in the second term, the Hubble drag, in the growth of density perturbations δ for in Equation (2.5). This is the same form as Eq. 1.21 that was motivated in Section 1.2.1, but instead with no pressure or sound speed term.

$$\ddot{\delta} + 2H\dot{\delta} = 4\pi G\rho_m\delta \tag{2.5}$$

However, assuming that the only modification is via changes in H is *fortunately* incorrect. It is fortunate because it is the extra modification that allows us to break the degeneracy between some general dark energy within GR, which can replicate any desired expansion history, and this modified gravity model (to be addressed in more detail in Section 2.3). The correct approach regarding the evolution of perturbations in this gravitational framework is particularly difficult and was tackled by Koyama & Maartens (2006). It was found that treating gravity as 4-dimensional, which leads to Equation (2.5), induces an inconsistency in the 4-dimensional Bianchi identities. Instead with the full five-dimensional analysis, and assumptions of a quasi-static regime and sub-horizon scales, they found the metric perturbations on the brane to be,

$$k^2\phi = -4\pi Ga^2(1 - \frac{1}{3\beta})\rho_m\delta \tag{2.6}$$

$$k^2\psi = -4\pi Ga^2(1 + \frac{1}{3\beta})\rho_m\delta \tag{2.7}$$

with the extra β factor given by,

$$\beta = 1 - 2r_cH(1 + \frac{\dot{H}}{3H^2}). \tag{2.8}$$

ϕ is the spatial and ψ the Newtonian potential seen within the perturbed metric in the Newtonian gauge,

$$\mathrm{d}s^2 = -(1+2\psi)\mathrm{d}t^2 + a^2(1-2\phi)\mathrm{d}x^2. \tag{2.9}$$

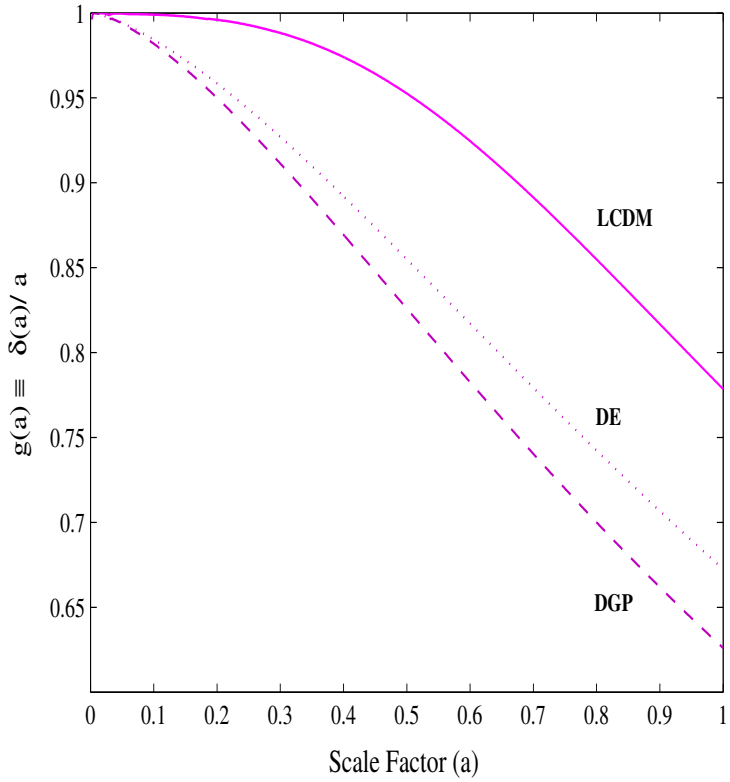

Figure 2.1: $\mathrm{g(a)} \equiv \delta(a)/a$, the linear growth, is plotted for a range of late time acceleration models. The solid line demonstrates the growth for LCDM, the dashed for the 5D braneworld model DGP and the dotted for a dark energy model with identical expansion history to DGP ($w_0 = -0.78$ and $w_a = 0.32$ where $w(a) = w_0 + (1-a)w_a$). The difference in the expansion history gives a significant suppression in growth relative to a pure cosmological constant. The effect, however, of the 5D perturbations not only adds to the suppression for DGP but breaks the degeneracy between itself and the smooth dark energy model.

It is the β factor within Equation (2.7) that breaks the expansion degeneracy and modifies Equation (2.5) becoming rather (Lue *et al.* (2004) and Koyama & Maartens (2006)),

$$\ddot{\delta} + 2H\dot{\delta} = 4\pi G\Big(1 + \frac{1}{3\beta}\Big)\rho_m\delta. \tag{2.10}$$

One can see this effect by looking at Figure 2.1. I have plotted the linear growth factor for LCDM, DGP and a dark energy model with the same expansion history as DGP. It is evident that the expansion history has considerable influence on the linear growth of structure with a suppression in the dark energy model relative to a cosmological constant. The effect of the five-dimensional modified gravity perturbations adds to this suppression and acts to clarify the deviation between the dark energy and DGP model.

With the modified Friedmann equation and the correct linear growth equation it is now possible to perform tests on the expansion history and/or large scale structure for this particular modifica-

tion to gravity. Some of these tests already exist and it has been found that DGP is under tension from the recent influx of cosmological data (E.g. Fang *et al.* (2008) and Song *et al.* (2007) and references therein). It is also worth noting that this model is potentially not without some of the theoretical problems alluded to above with notions of a ghost (Koyama (2005) and Gorbunov *et al.* (2006)) and a strong coupling problem (Rubakov 2003). The model is still a good example theory, however, and an excellent benchmark to test new methods, data or concepts.

2.2.3 The Phenomenological Model

I consequently go beyond DGP as an isolated theory and examine a phenomenological model that is motivated by the concept of an extra dimension with infinite extent. This model, first introduced by Dvali & Turner (2003), interpolates between LCDM and DGP and corrects the Friedmann equation with the addition of the parameter α shown in Equation (2.11) and r_c in Equation (2.12).

$$H^2 - \frac{H^\alpha}{r_c^{2-\alpha}} = \frac{8\pi G\rho}{3} \tag{2.11}$$

$$r_c = (1-\Omega_m)^{\frac{1}{\alpha-2}} H_0^{-1}. \tag{2.12}$$

It is clear that in this case LCDM is recovered when $\alpha = 0$ and DGP when $\alpha = 1$. Furthermore, it is worth noting that $\alpha < 0$ leads to effective equation of states less than -1, whereas $\alpha \gtrsim 1$ acts to disrupt both the long matter era needed for structure formation and the limits set by Big Bang Nucleosynthesis (Dvali & Turner 2003). Also, $\alpha > 2$ is capable of describing early universe braneworld modifications.

It is possible to detail the entire background behaviour of this model with an effective equation of state w_{eff} that I derived generally in Equation 2.13. This reduces to Equation 2.14 for DGP as in Lue (2006).

$$w_{DE}^{\text{eff}}(a) = -\frac{(2-\alpha)}{2-\alpha(1-\Omega_m(a))} \tag{2.13}$$

$$w_{DE}^{\text{eff}}(a) = \frac{-1}{1+\Omega_m(a)} \tag{2.14}$$

From Equation (2.11) it is possible to test the model with probes of expansion history and indeed this has already been performed by Yamamoto *et al.* (2006) with BAOs. If one wants to go beyond this and include tests of large scale structure then a formalism is needed for the growth of density perturbations analogous to Equations (2.7), (2.8) and (2.10). The problem in this scenario is that in order to deduce the growth of perturbations one needs an underlying covariant theory and all that exists in this modified DGP model (mDGP) is a parameterisation. Koyama (2006)

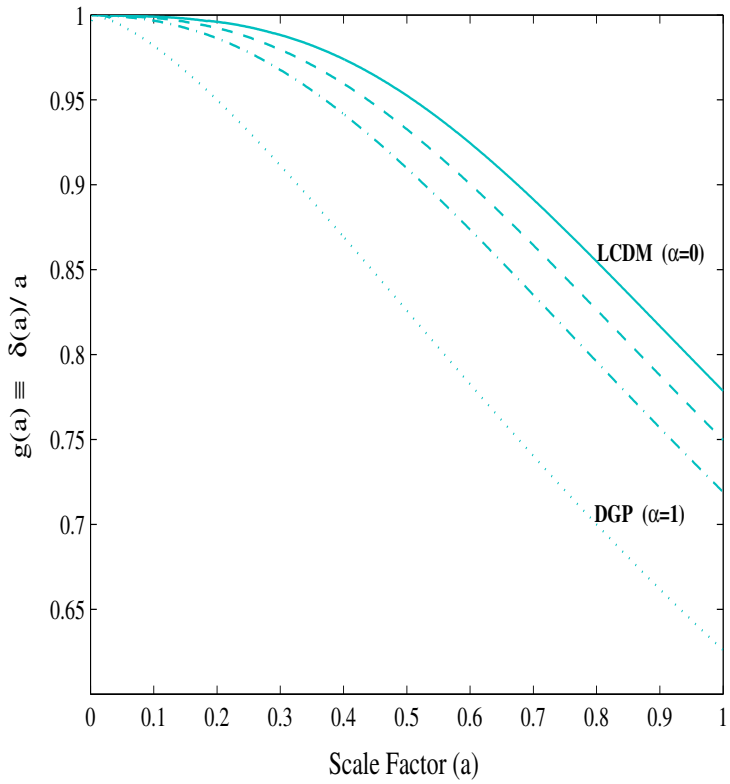

Figure 2.2: $\mathrm{g(a)} \equiv \delta(a)/a$, the linear growth, is plotted for various values of α that characterise the phenomenological LCDM-DGP interpolation (mDGP) model. The solid line demonstrates the growth for $\alpha = 0$ (LCDM), the dashed for $\alpha = 0.25$, the dash-dotted for $\alpha = 0.5$ and the dotted for $\alpha = 1$ (DGP). Once again it is evident that the more DGP-like end of the α spectrum experiences more suppression in the growth of density perturbations.

introduced such an analysis based on a covariant generalisation of the DGP perturbations (a limit in the model). It was subsequently found that the metric perturbations take the same form as Equations (2.6) and (2.7) but instead with (Koyama 2006),

$$\beta = 1 - \frac{2}{\alpha}(Hr_c)^{2-\alpha}\Big(1 + \frac{(2-\alpha)\dot{H}}{3H^2}\Big). \tag{2.15}$$

Figure 2.2 demonstrates how the growth of density perturbations alter within the mDGP model– from LCDM to DGP. As in the previous figure it is clear that there is a suppression of growth at the more DGP end of the α spectrum.

Although phenomenological, the mDGP model now has a definite Friedmann equation that governs the expansion history, a set of metric perturbation equations and a corresponding density perturbation equation. One can therefore treat this as a specific model and I choose to constrain it as an example of modified gravity later in the paper. It is worth noting that using this as a measure

of deviation from GR or as a parameterisation of general modified gravity is not the aim. This would constitute a poor choice of parameter given the severe lack of generalness. I touch upon the idea of parameterising modified gravity in the next section. This model has, however, been extremely illustrative with regards to the extra richness that can occur in modified gravity. Not only does it have varying expansion histories but a range of perturbation equations which alters the growth of structure and the relationship to the power spectrum. This is useful when attempting to distinguish between LCDM, general dark energy and modified gravity, and insightful to the probes that will be most adept at detecting them.

2.3 Growth

The alteration in the growth of structure within the mDGP model demonstrated an additional observational characteristic that allows us to further constrain the model and potentially break the degeneracy with a general dark energy. It also highlights the possibility of searching for *signatures* of modified gravity in current data by looking for changes in the growth of structure. It may be desirable, therefore, to parameterise this extra growth.

The notion of this parameterisation is analogous to the familiar parameterisation of the background expansion into w_0 and w_a. This is sufficient in describing and restricting the multitude of possible dark energy models and expansion histories. It is now common procedure to examine data and convert it into constraints on various cosmological parameters including the w_0 and w_a. One might therefore like to extend this parameter space and allow for the signatures of gravity. One possible parameterisation for growth is given by γ in Equation (2.16) and was first introduced by Peebles (1980) and Lahav *et al.* (1991) and later discussed in Wang & Steinhardt (1998), Linder (2005), Huterer & Linder (2007) and Linder & Cahn (2007).

$$\frac{\delta}{a} \equiv g(a) = \exp\Big(\int_0^a (\Omega_{\rm m}(a)^\gamma - 1)\, {\rm dln}a \Big) \tag{2.16}$$

By again looking at Figure 2.1 we can see that the growth factor g(a) is affected by the expansion history and by the gravitational framework. It is worth noting that the γ parameterisation attempts to distinguish the two contributions, encapsulating the latter in isolation. This is due to the effect of the expansion being absorbed into $\Omega_m(a)$ thus leaving γ to pick out any remaining remaining contribution. It is in this way that γ has become known as a modified gravity or beyond-Einstein parameter. It is easy to see why given that it detects changes to the growth not associated with expansion. This could be down to a change in the force law acting on matter represented, for

example, by the extra factor in Equation (2.10). And as we alluded to earlier, evident in Figure 2.1, this allows us to distinguish between dark energy and modified gravity.

However, as highlighted in Kunz & Sapone (2007) there exists an interesting caveat. They found that contrary to Figure 2.1 one could force some generic dark energy to replicate the growth of DGP. This is achieved by allowing for dark energy models with low sound speeds ($c_s^2 \neq 1$) which in turn induces a clustering in the fluid. The clustering instigates a deepening of the gravitational potential wells thus leading to a magnification in the metric perturbations and subsequently an increase in the growth. In addition, the existence of anisotropic stress is permitted which has the effect of suppressing growth. With a balance between stress and sound speed it is possible to replicate g(a) for DGP. Now although highly fine tuned it is worth keeping in mind that observationally detecting some non-LCDM growth factor, or γ, would not necessarily constitute modified gravity. Unless one allows only non-clustering dark energy the growth parameter is not just a modified gravity parameter. It has the ability to pick up on clustered dark energy and modified gravity both of which are interesting. Given this it is therefore my intention to test the growth parameter and see whether current data or a future probe can pick out this subtle but potentially important effect. There exist a few other attempts, including constraints from peculiar velocity measurements in low redshift Supernovae (Abate & Lahav 2008) as well as future survey forecasts from Amendola *et al.* (2007), Huterer & Linder (2007) and Heavens *et al.* (2007).

Figure 2.3 demonstrates the result of varying this parameter on the linear growth factor. The growth for standard LCDM corresponds to $\gamma = 0.55$ whereas for flat DGP $\gamma = 0.68$. It is clear that a higher growth parameter results in a suppression of growth.

2.3.1 Extra Signatures

It is worthwhile noting that other attempts at parameterising modified gravity have been made which aspire to encapsulate the properties of gravity similar to the Parameterised Post-Newtonian (PPN) parameters for local gravity constraints (Will 1993). For example, these include parameterising the relationship between the two metric potentials (ϕ and ψ) and/or quantifying any modification to the Poisson equation (E.g. Amendola *et al.* (2007), Hu & Sawicki (2007), Ishak *et al.* (2006), Jain & Zhang (2007), Daniel *et al.* (2008) and Bertschinger & Zukin (2008)). These parameterisations help illustrate the final modified gravity signature I consider before the analysis with weak lensing.

Any deviation in the Poisson equation or between the metric potentials causes a deviation in the relationship between the power spectrum of the potentials and the power spectrum of the

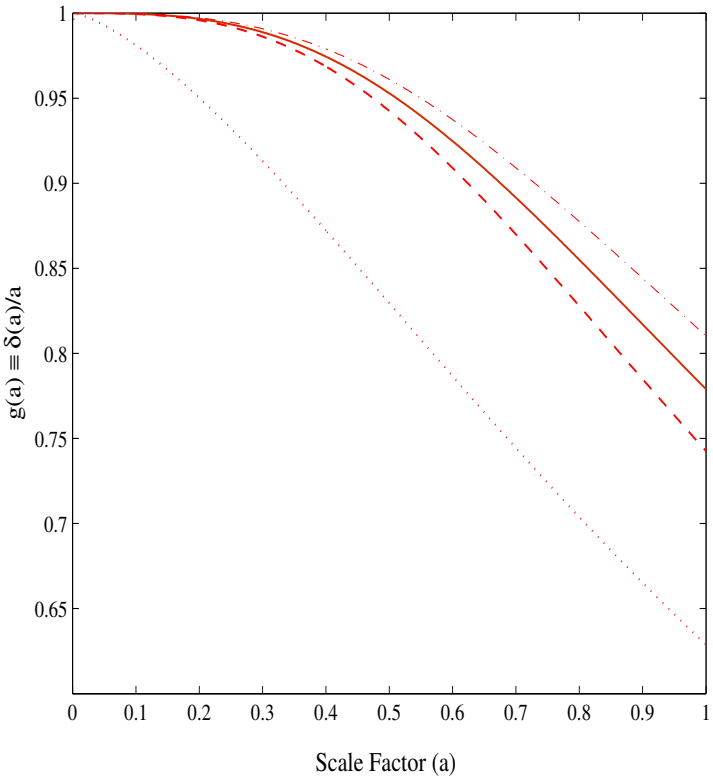

Figure 2.3: $\mathrm{g(a)} \equiv \delta(a)/a$, the linear growth, is plotted for various values of γ, the growth parameter, resulting potentially from a change in force law. The solid line represents the growth for LCDM ($w_0 = -1, \quad w_a = 0$) with the corresponding growth parameter $\gamma = 0.55$. The dashed line shows the growth for $\gamma = 0.68$ which is the same as flat DGP but with the same expansion as in LCDM. The dotted line also has $\gamma = 0.68$ but now with $w_0 = -0.78$ and $w_a = 0.32$, thus completely specifying the growth of the example DGP model. Finally the dot-dashed line shows the growth for a LCDM expansion but $\gamma = 0.45$. It is clear that a high value of the growth parameter corresponds to a suppression of growth. This potentially arises from a weakening of gravity.

density contrast. Failure to account for this by not modifying the corresponding lensing equations will render any analysis incomplete. To understand this I use the notation of Amendola *et al.* (2007) but in doing so note the equivalence of their Q and η (defined in Equations (2.17) and (2.18)) to $\tilde{\mathrm{G}}_{\mathrm{eff}}$ and η given in the other thorough consideration by Jain & Zhang (2007).

Firstly, as will be further detailed in the following section, let us notice that in weak lensing the deflection of light is sensitive primarily to the sum of the metric *potentials* $\phi + \psi$. Therefore, we require the power spectrum within the lensing statistic (Equation (2.26)) to actually be the power spectrum of $\phi + \psi$, written $P_{(\phi+\psi)}$. This is *then* related to the matter power spectrum P_δ. Defining the matter power spectrum in Equation (2.19) and the potential power spectrum similarly it is obvious that a general relationship between P_δ and $P_{(\phi+\psi)}$ relies on the relationship between

$\phi + \psi$ and δ. In turn this depends on the Poisson equation and the relationship between ϕ and ψ. This is where the parameters Q and η are particularly illustrative. Here Q parameterises any modification in the Poisson equation relating the metric variable ϕ to the matter density δ. η on the other hand, also defined below, describes the relationship between ϕ and ψ.

$$k^2\phi = -4\pi G Q \rho a^2 \delta \tag{2.17}$$

$$\psi \equiv (1+\eta)\phi \tag{2.18}$$

If one now adds the two metric potentials together and substitutes ψ for η and ϕ, it is possible to transform the combined Poisson equation, as given in the definition of the matter power spectrum below,

$$< \delta(\vec{k_1}, z)\delta(\vec{k_2}, z) >= (2\pi)^3 \delta(\vec{k_1} + \vec{k_2}) P_\delta(k, z), \tag{2.19}$$

and similarly for the potential, to see the general relationship between the power spectra,

$$P_{(\phi+\psi)}(k, z) = \frac{(8\pi G)^2 \rho^2 a^4 [Q(1 + \frac{\eta}{2})]^2 P_\delta(k, z)}{k^4}. \tag{2.20}$$

I then, following the notation of Amendola *et al.* (2007), define $\Sigma \equiv Q(1 + \frac{\eta}{2})$, giving the modification to the power spectrum more succinctly as,

$$P_{(\phi+\psi)}(k, z) = \frac{(8\pi G)^2 \rho^2 a^4 \Sigma^2 P_\delta(k, z)}{k^4}. \tag{2.21}$$

In a standard cosmological scenario, such as LCDM for example, $\eta = 0$ and $Q = 1$ leaving $\Sigma = 1$. This results in the standard relation between the power spectra assumed in the literature. It is clear therefore that neglecting Σ is tantamount to constraining the subset of modified gravity models that do not alter the power spectrum relation from GR. The mDGP model studied earlier is one such model. This can be seen by adding Equations (2.6) and (2.7) and observing the cancellation in β. Therefore, for this model $\Sigma = 1$. Generally, however, if one strives to include general models Σ should be allowed to vary. Note that it modifies the amplitude of the power spectrum and so a constant value is degenerate with σ_8. Accordingly and more generally, as introduced in Amendola *et al.* (2007), I consider the general parameterisation,

$$\Sigma(a) = 1 + \Sigma_0 a. \tag{2.22}$$

It is my intention therefore to constrain and forecast for the specific mDGP gravity model and then, separately, constrain the general characteristics of modified gravity. For the latter I choose

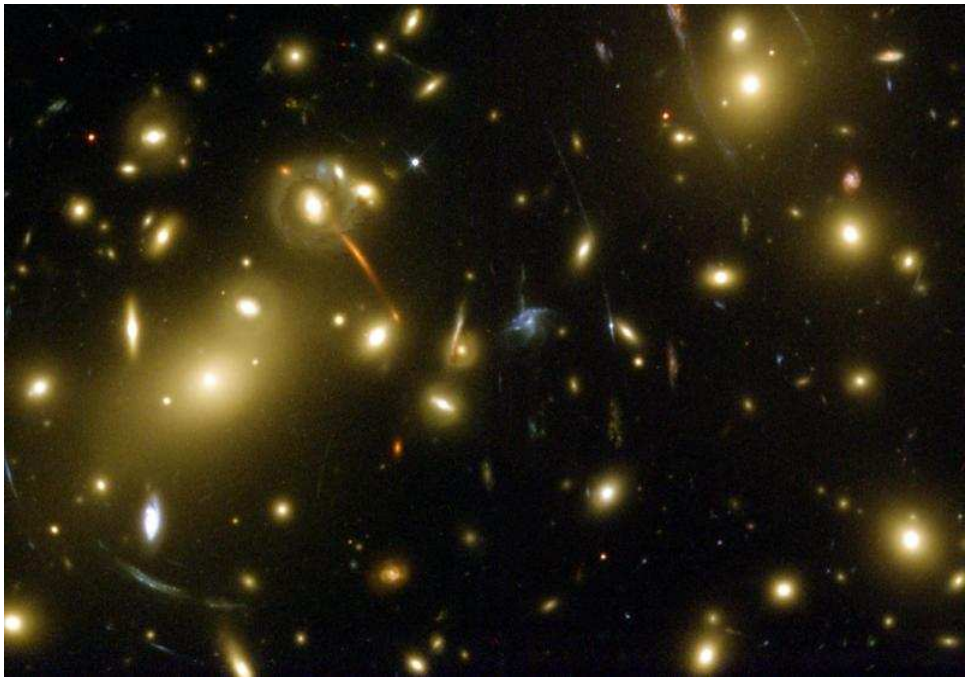

Figure 2.4: The distortion of background galaxies caused by the intervening mass distribution is particularly vivid in the vicinity of galaxy cluster Abell 2218. The images are stretched out, or sheared, becoming more elliptical and in this scenario represents a more exaggerated version of weak lensing. In this latter case the underlying information resulting from a more subtle deformation is deduced statistically over many galaxies. CREDIT: *http:hubblesite.org/gallery* [*NASA*].

to set $\Sigma = 1$ (or $\Sigma_0 = 0$) due to limitations in data and constrain w_0 and γ signatures only. I later include $\Sigma_0 \neq 0$ for the Euclid forecasts (Section 2.6).

γ and Σ are *functions*, optimised for weak lensing, of the more fundamental Q and η. These parameters themselves are, most generally, $Q(k, a)$ and $\eta(k, a)$. The assumption that γ is constant and the ansatz placed on Σ could be restrictive (Gannouji *et al.* 2008) with regards to the range of modified gravities available (including normal DGP and some $f(R)$ models (Durrer & Maartens 2008)) but have been enforced again due to limitations in current data.

2.4 Weak Lensing as a Cosmological Probe

The deflection of light by mass is given by the transverse gradient of the metric potentials integrated along the path length,

$$\vec{\varphi} = -\int \partial(\psi + \phi)\mathrm{d}s. \tag{2.23}$$

This acts to not only change the apparent position of some point source but, in turn, distort the shape of distant source galaxies. In fact, one can relate the observed position of the image $\vec{\theta}_I$ to

the true position of the source $\vec{\theta}_S$, in the plane of the sky by,

$$\vec{\theta}_I = \vec{\theta}_S + \frac{D(\chi_s - \chi)}{D(\chi)}\vec{\varphi}, \tag{2.24}$$

where $D(\chi)$ is given by the comoving angular diameter distance (Eq. 1.17). The subsequent image distortion is given by the differential of this lens equation resulting in the Jacobian,

$$\vec{A} = \frac{\mathrm{d}\vec{\theta}_S}{\mathrm{d}\vec{\theta}_I} = \begin{pmatrix} 1-\kappa-\gamma_1 & \gamma_2 \\ \gamma_2 & 1-\kappa+\gamma_1 \end{pmatrix}$$

where the convergence κ is reconstructed from the shear γ (with $\gamma = \gamma_1 + i\gamma_2$) measured from galactic ellipticities (Refregier 2003). An extreme example of this distortion can be seen in Figure 2.4.

With regards to the analysis of a cosmological model one may choose to examine the convergence quantity. This convergence, which represents a weighted projected mass distribution on the plane of the sky, is given (Bartelmann & Schneider 2001) for a general mass distribution by,

$$\kappa = \frac{3\Omega_m H_0^2}{2c^2}\int_0^{\chi_s} \mathrm{d}\chi \frac{D(\chi)D(\chi_s-\chi)}{\chi_s}(1+z)\delta(\chi). \tag{2.25}$$

Given that it is desirable to analyse this distribution in a statistical way it is possible to use the definition of the power spectrum–analogous to Equation (2.19) and Equation (1.23)–to find the expression for the *convergence* power spectrum,

$$P_\kappa(l) = \frac{9\Omega_m^2 H_0^4}{4c^4}\int_0^{\chi_H} \mathrm{d}\chi \Big[\frac{g(\chi)}{a(\chi)}\Big]^2 P_\delta\Big(\frac{l}{\chi},\chi\Big), \tag{2.26}$$

where the geometric comoving angular diameter distance terms ($D(\chi)D(\chi_s-\chi)/\chi_s$) have been absorbed into $g(\chi)$. It is therefore now clear, given the earlier discussion, how weak lensing is particularly useful in studies of modified gravity; this statistic is sensitive to the growth of structure via the presence of the linear growth factor in the matter power spectrum P_δ; it is also sensitive to the expansion history through the terms in the square brackets and through the Hubble drag in the growth terms; and finally, as discussed at the end of Section 2.3.1, it is sensitive to the relation between the power spectrum of the potentials and density. In the equation above the relation from $P_{\phi+\psi}$ to P_δ has been performed assuming GR as given routinely in the literature. Again, it is worth reiterating that if there is a modification to the Poisson equation and/or to the anisotropic stress one must augment this power spectrum with the appropriate prefactor given, for example, in Equation (2.20). Furthermore, in addition to these sensitivities, as the deflection of light is given by the gradient of the potentials, which are sourced by mass irrespective of being baryonic or dark, weak lensing does not suffer from any unknown bias (as in Eq. 1.25). That is, it probes the entirety of the mass distribution.

2.4.1 Issues and Caveats

While this probe, in principle, is excellent for the chosen study the shear signal is a small 1% distortion on the already existing intrinsic ellipticity. This provides a thorough technical challenge that is being combated with a combination of large galaxy number analyses and refined shear measurement techniques (Heymans *et al.* (2006), Massey *et al.* (2007), Bridle *et al.* (2008) and Bridle *et al.* (2009)). Further still, the first detections of weak lensing are particularly recent (Bacon *et al.* (2000), Kaiser *et al.* (2000), Wittman *et al.* (2000) and Van Waerbeke *et al.* (2000)) and so lensing is very much a highly promising, yet developing, cosmological probe. Despite this there are already a number of papers that have addressed the relationship between weak lensing and modified gravity/dark energy, such as Uzan & Bernardeau (2001), Schimd *et al.* (2005), Doré *et al.* (2007), Schimd *et al.* (2007), Amendola *et al.* (2007), Jain & Zhang (2007) and Tsujikawa & Tatekawa (2008). With these studies and potential modified gravity attributes it is imperitive to realise that there does exist a severe caveat. This is due to the fact that weak lensing probes the non-linear regime.

Usually one is able to use a fitting function (E.g. Peacock & Dodds (1996) and Smith *et al.* (2003)) for the non-linearities in standard gravity. These have been calibrated by detailed N-body simulations. However, despite some early work to quantify the changes that arise in other models with simulations (E.g. Laszlo & Bean (2008) and Oyaizu *et al.* (2008)) no such prescription is currently available. The uncertainty is exacerbated by the potentially environment and scale dependent modifications that can arise in gravity, such as those through the chameleon effect. The current fitting functions map the linear regime into the non-linear domain and subsequently fail to include such behaviour. I therefore strive to work in the linear regime where possible in this study. Obviously further effort is needed to explore these changes with N-body simulations but since this work new methods have started to arise. I leave a discussion of this recent progress to Chapter 5.

There are, in addition, other benefits in avoiding the inclusion of small scales such as the evasion of intrinsic ellipticity correlations (Crittenden *et al.* 2001), shear-shape correlations (Hirata & Seljak 2004) and the presence of non-Gaussianity in the error (Semboloni *et al.* 2007). I therefore utilise the data provided by F08 based on the CFHTLS-wide survey which, due to its range of large angular scales (up to 230 arcminutes) probing the linear regime, is ideal for work on non-LCDM cosmology such as this.

2.4.2 CFHTLS

The Canada-France-Hawaii Telescope Legacy Survey [4] (CFHTLS), based on the MEGAPRIME / MEGACAM instrument, is an ongoing survey with a target of 450 nights extending over 5 years. The recent analysis by Benjamin *et al.* (2007) has gone beyond the initial releases and investigations by Semboloni *et al.* (2006) and Hoekstra *et al.* (2006) which themselves were successful in deriving constraints on the $\Omega_m - \sigma_8$ degeneracy and demonstrating the evolution of the shear signal with redshift. This was achieved in Benjamin *et al.* (2007) through a better understanding of the redshift distribution and having an increased area. This, while marking significant progress, is still not the most optimal lensing analysis for this work. This is because they are potentially sensitive to the growth of structures on non-linear scales which, as I emphasised above, is undesirable for a current study of beyond-Einstein cosmology and weak lensing.

I therefore look to the 3rd year CFHTLS-wide release (T0003) given by Fu *et al.* (2008) (F08). Although having a smaller field of view than Benjamin *et al.* (2007) it utilises much larger angular scales (into the linear regime) also avoiding many of the potential systematics mentioned at the end of the last section. It is because of this that both works reveal approximately equivalent cosmological constraints and little constraining power is lost. The current sky coverage of $57\mathrm{deg}^2$, approximately 35% of the final CFHTLS target area, is reduced to $34.2\mathrm{deg}^2$ after masking and the removal of various contaminants. Eventually including five bands this i' band study stretches to a magnitude of $i'_{AB} = 24.5$ and encapsulating nearly 1.7 million galaxies has an effective galaxy number density of $n = 13.3\ \mathrm{gal}/\mathrm{arcmin}^2$. The data (F08) comes in the form of several two point statistics which are relevant to this study. I choose to utilise the E correlation function (ξ_E) which is shown in Equation (2.27) and displayed along with the cosmological best fit in Figure 2.5.

$$\xi_E = \frac{1}{2\pi}\int_0^\infty l P_\kappa(l) J_0(l\theta)\,\mathrm{d}l \tag{2.27}$$

As for the aperture mass $< M_{\mathrm{ap}}^2 >$ and shear top hat variance $< |\gamma|^2 >$ two point statistics this is a weighted transform of the convergence power spectrum. In this case it is given by a zeroth order Bessel function of the first kind J_0. It is in this way that the two point functions vary in their sensitivity to various aspects of the power spectrum and systematics. ξ_E suffers from a constant offset resulting from a mixing of E and B-modes. A finite survey size introduces a maximum angular scale which prevents a complete calculation of the shear correlation function over larger ranges. This is needed for a separation of E and B (Kilbinger *et al.* 2006). To alleviate this I alter the statistic ξ_E to $\xi_E + c'$ including the constant offset c' as an extra parameter. An expression can

[4] http:/www.cfht.hawaii.edu/Science/CFHTLS/

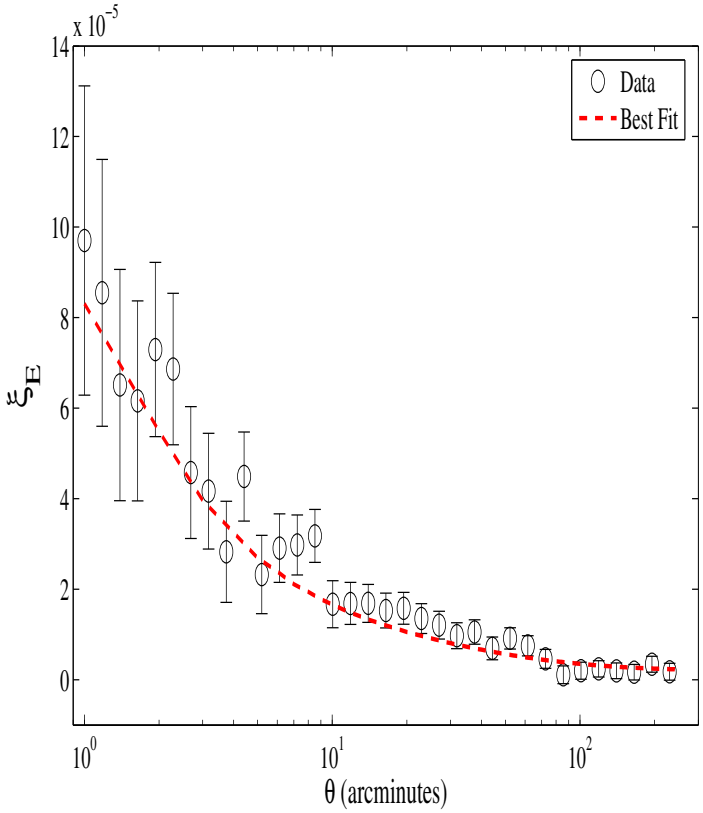

Figure 2.5: The open circles with associated error bars represent the ξ_E two-point statistic as a function of θ (arcminutes) for the CFHTLS-wide survey used in this paper. I selectively use scales greater than 30 arcminutes to remove the unknown non-linear effects. The red dashed line shows the best fit values as found with the combined probes mDGP analysis (Section 2.5.2).

then be obtained for the offset given by the best fit offset ($\mathrm{d}\chi^2/\mathrm{d}c' = 0$) for each parameter choice. This constitutes an analytic marginalisation[5] over c' (Lewis & Bridle 2002). I subsequently find the expression for c' to be,

$$c' = \frac{\sum_{i,j}(C^{-1})_{ij}(\xi_i - D_i)}{\sum_{i,j}(C^{-1})_{ij}}, \tag{2.28}$$

where the element ξ_i is the model correlation function, D_i the data and C the full covariance matrix between all elements. Furthermore, the B correlation function ξ_B which describes the curl component of the shear field, as opposed to ξ_E which measures the curl-free component, is expected to be non-zero only for non-lensing contributions to the shear (Crittenden *et al.* 2002). It is because of this that ξ_B is an excellent check on any contamination of the lensing signal. F08

[5]The concept of which is introduced in Section 1.3.1.

found no real B-mode contribution except for the presence of a very small signal at large angular scales. They find however that their cosmological conclusions are not affected by this potential mode.

It was shown in F08 that there is no significant deviation in cosmological constraints across any of the aforementioned two point statistics. Doré *et al.* (2007), also looking at a form of modified gravity in the context of this CFHTLS data, came to a similar conclusion. It is worth noting that other cosmological studies of this data set include a phenomenological modified gravity analysis (Daniel *et al.* 2008) and more recently an early study of the neutrino mass (Tereno *et al.* 2009). I therefore choose, for simplicity, to use the one ξ_E statistic.

The redshift distribution of the source galaxies, which weak lensing is critically sensitive to, has been calibrated for the CFHTLS study using Ilbert *et al.* (2006). I decide to follow F08 and model this distribution using the function,

$$n(z) = A\frac{z^a + z^{ab}}{z^b + c} \quad \text{with} \quad A = \Big(\int_0^{z_{\max}} \frac{z^a + z^{ab}}{z^b + c}\, \mathrm{d}z \Big)^{-1} \tag{2.29}$$

where A is the normalisation and a, b and c are three extra parameters to be varied and marginalised over in the cosmological fit. It is found that Equation (2.29) enables a closer fit to the distribution data that other common n(z) fitting formulae. The observed normalised redshift distribution and the fitting function evaluated at the best fit points found in the mDGP combined probes cosmological run (Section 2.5.2) are shown in Figure 2.6.

2.5 Constraints

2.5.1 Lensing

Having earlier discussed the characteristics of certain late-time acceleration models in Section 2.2 and Section 2.3, and having chosen a probe that is potentially capable of picking out these particular behaviours with weak lensing, we are now in a position to make cosmological constraints based on the data which was decided, in Section 2.4.2, to be the most suitable. That is, I start by making an analysis of the mDGP cosmological model and then separately the parameterisation of growth with the F08 CFHTLS-wide lensing data.

I perform a full likelihood analysis using a Monte Carlo Markov Chain (MCMC) approach (refer to Section 1.3.2.2) on a set of 7 cosmological parameters for the mDGP analysis and 8 for the growth parameterisation study. I vary Ω_m, h, σ_8, a, b, c which are common to both models, in addition to α for mDGP and w_0 and γ for the growth. The w_0 is not included for the former model

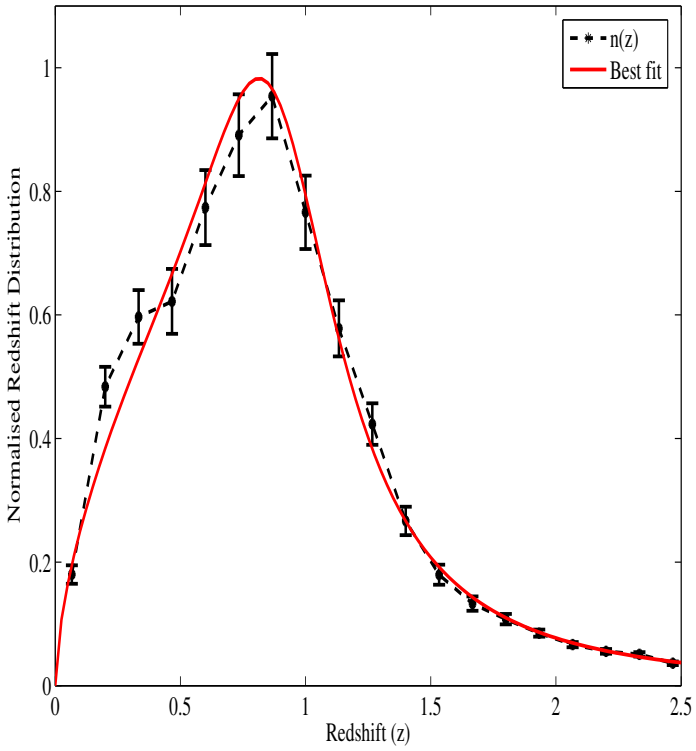

Figure 2.6: The black dashed line represents the source redshift distribution with associated error in the bins. The red solid line is given by the fitting function in Equation (2.29). The fit is drawn for the function evaluated at the best-fit points as deduced by the combined probes analysis for mDGP (Section 2.5.2). This corresponded to best fit values: $a = 0.614 \pm 0.034$, $b = 8.11 \pm 0.681$, $c = 0.627 \pm 0.0610$ and $A = 0.6462$ consistent with F08.

as α uniquely specifies its own expansion history as it does for the evolution of perturbations– from GR to DGP. I do not vary the spectral index n_s because the data needed at large angular scales is insufficient for any constraint. Instead I set $n_s = 0.963$ consistent with the best fit five-year WMAP result (Dunkley *et al.* 2009). Likewise I neglect varying w_a and Σ_0 for the growth model due to limitations in data. Instead both w_a and Σ_0 are set to 0 and a flat universe is assumed throughout. This might represent a limitation and a restriction of parameter space. However, given the recent analysis by Fang *et al.* (2008) with the CMB where they find a slight but insignificant change in constraint with a non-flat Universe, the effect is considered to be small.

For the lensing analysis the Gaussian log-likelihood is given by,

$$\chi^2 = \frac{1}{2}\sum_{\rm ij}(D_{\rm i} - T_{\rm i})(C^{-1})_{\rm ij}(D_{\rm j} - T_{\rm j}) \tag{2.30}$$

where the data vector $\vec{D}$ is given by the measured $\xi_E(\theta_i)$. The theoretical predictions deduced at

the corresponding angular scale θ_i are represented by $\vec{T}$ and, finally, C^{-1} is the inverse covariance matrix provided by the CFHTLS collaboration[6]. At present variation in either a, b or c in the redshift distribution is detected implicitly through a modification in the model power spectrum. However, in implementing the MCMC approach regions of parameter space will be sampled that correspond to configurations of a, b and c incompatible with knowledge of just the redshift distribution in isolation. I therefore follow the procedure in F08 and multiply the likelihood above by the likelihood of the redshift distribution given by,

$$\chi^2_{\mathrm{n(z)}} = \frac{1}{2}\sum_{\mathrm{i}} \frac{(n_i - n(z_i))^2}{\sigma_{\mathrm{i}}^2}, \tag{2.31}$$

where n_i, the observed number of galaxies in a bin, are shown in Figure 2.6. $n(z_i)$ represent the values of the fitting function in Equation (2.29) evaluated at the bin centred redshifts. While ignoring cross-correlations in the bins I include σ_i which is the error in n_i. This error includes Poisson noise, sample variance and the associated redshift uncertainty. In addition, an HST prior (Freedman *et al.* 2001) is included for h as given by,

$$\chi^2_{\mathrm{HST}} = \frac{1}{2}\frac{(h - 0.72)^2}{0.08^2}. \tag{2.32}$$

Before the analysis in different gravitational frameworks I first test for consistency with the Fu *et al.* (2008) ΛCDM analysis. In order to do so I vary six parameters (Ω_m, σ_8, h, a, b, c) and include all angular scales from 1 to 230 arcminutes. The resulting likelihood contours are displayed in Figure 2.7. The Hubble parameter h has been marginalised with a, b and c in this plot. The HST prior is left out however. The bounds are exactly equivalent to those derived in the original data release.

Returning to the modified gravity study the data is cut for the lensing only analysis such that only angular scales greater than 30 arcminutes are used. I reiterate, this is to avoid the unknown non-linear contribution to the lensing constraint. The analysis for the mDGP model is shown in Figure 2.8. It shows the marginalised Ω_m and α contours where, as detailed in Section 2.2, α parameterises corrections to the Friedmann and growth equations. The mDGP model interpolates between LCDM ($\alpha = 0$) and the DGP braneworld model ($\alpha = 1$). It is clear therefore that a lensing only analysis is presently not capable of constraining mDGP–at least in the context of physically more viable models ($\alpha \lesssim 1$).

I find a similar difficulty in constraining γ with no bound possible for any reasonable physical values given weak lensing in isolation. This should not be too surprising as I have used a relatively

[6]With thanks to Martin Kilbinger and Liping Fu for distribution.

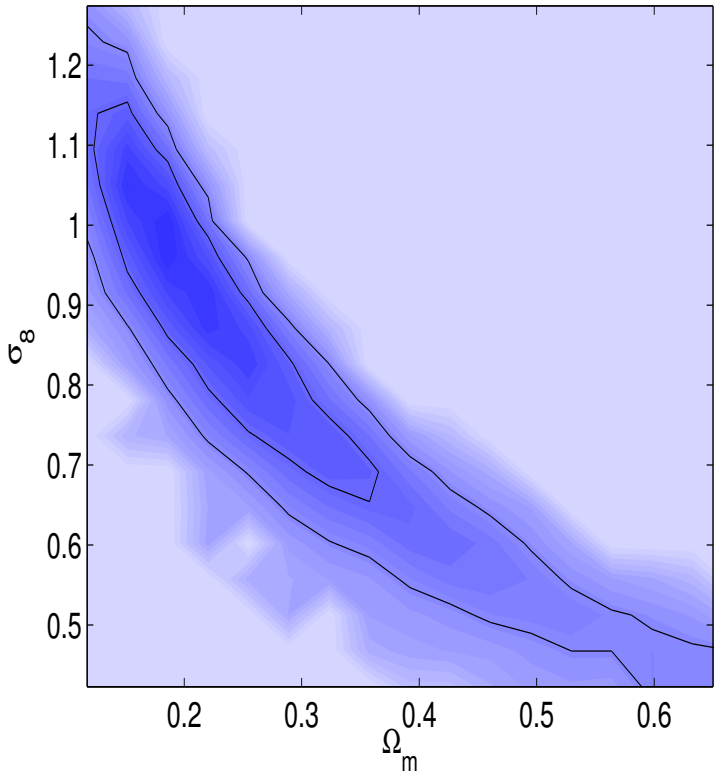

Figure 2.7: To test for consistency I include the 68% and 95% contours for a ΛCDM analysis with all angular scales (1 - 230 arcminutes) as in Fu *et al.* (2008). 6 parameters are varied in total (Ω_m, σ_8, h, a, b, c). Similarly I do not include the HST prior or the residual offset ($c' = 0$) for this analysis. The baryon fraction is also fixed to $\Omega_b = 0.044$. The degeneracy between Ω_m and σ_8 is clearly visible.

new cosmological probe and have, in neglecting the non-linear scales, used only a third of the data. Tomographic, or redshift binned, information is not yet currently available for this either and will act to vastly improve information on the expansion history and hence α. I have also allowed significant cosmological freedom with the variation of 7 parameters. However, this does not mean that lensing, even with a current analysis, is not useful with regards to the late-time acceleration models. In order to see this we now look at BAOs, Supernovae and weak lensing in combination in the next section. Then in Section 2.6 we see how the future space-based weak lensing survey Euclid will improve upon today's lensing only constraining power.

2.5.2 Supernovae and Baryon Acoustic Oscillations

In the previous section I performed a preliminary analysis based on linear to quasi-linear weak lensing data alone. This probe, while having characteristics significant for the discrimination of

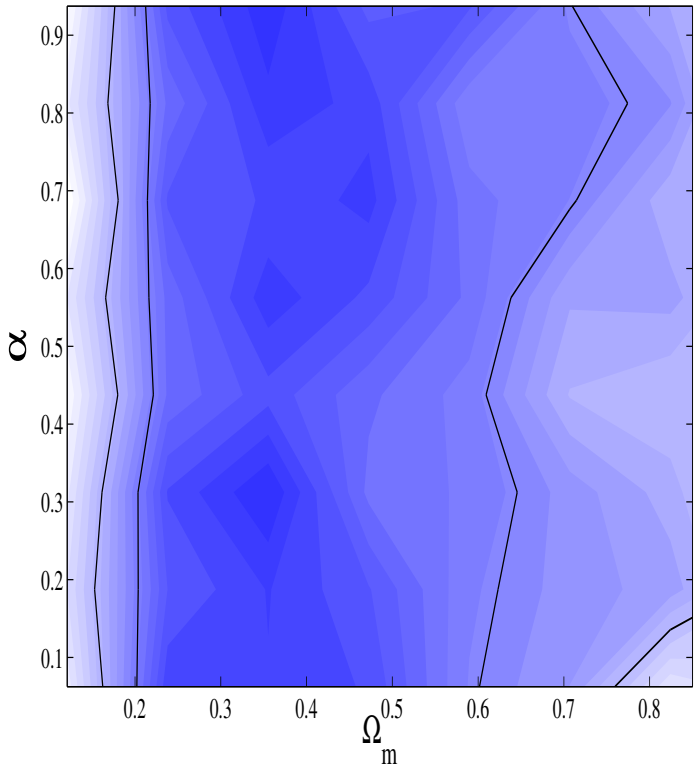

Figure 2.8: The diagram above demonstrates the attempted constraint on a parameterised gravitational model that is motivated by the concept of a large extra dimension (mDGP). The contours are for Ω_m and α (the modified gravity parameter) where 5 other cosmological parameters (h, σ_8, a, b and c) have been marginalised. Here only angular scales greater than 30 arcminutes have been used in order to avoid the non-linear regime. The data is from the CFHTLS-wide (F08) survey using the E correlation two point statistic $\xi_E + c'$. For mDGP, $\alpha = 0$ corresponds to LCDM, whereas $\alpha = 1$ is equivalent to DGP.

late time acceleration, was unable to constrain either the mDGP model or the growth parameterisation. As such it is desirable to combine it with other probes in order to improve potential constraints. Moreover, it is most beneficial to combine weak lensing, an indicator of growth and expansion, with distance indicators. This is because of the particular degeneracies that exist following an isolated study. For example, there is a degeneracy between w and γ and so tighter constraints on the expansion history will act to aid any constraint on γ. Furthermore, inclusion of additional expansion data will aid the constraint of mDGP given that different α correspond to different late time accelerations. I therefore choose to include both Supernovae and BAOs which, due to their vastly different $\Omega_m - w$ degeneracies, are also extremely complementary to one another.

BAOs

BAOs are used as standard rulers and are observed in the galaxy distribution (Section 1.2.2.1), testing cosmology through the distance-redshift relation. Using the data and notation of Percival *et al.* (2007) I look to utilise the distance measure given by,

$$D_V(z) = [(1+z)^2 D_A^2 cz/H(z)]^{\frac{1}{3}} \tag{2.33}$$

where D_A is the angular diameter distance (Eq. 1.17) and $H(z)$ is the Hubble parameter. Specifically, it is the ratio $r_s/D_V(z)$ that I examine where r_s is the comoving sound horizon at recombination. Percival *et al.* (2007) detects the BAO in the clustering of 2dFGRS and SDSS galaxy samples and the clustering of SDSS LRGs to quantify this measure at $z = 0.2$ and $z = 0.35$, respectively. For each likelihood evaluation I compare this data to $r_s/D_V(z)$ calculated with $D_V(z)$ from Equation (2.33) and the varying comoving sound horizon r_s evaluated using the formulae in Eisenstein & Hu (1998).

Supernovae

For the inclusion of Supernovae (Section 1.1.5) I use the data provided from the first year Supernova Legacy Survey (SNLS) (Astier *et al.* 2006). This data set includes 71 type 1a Supernovae also detected at the Canada-France-Hawaii Telescope. Here the distance modulus μ_0, a measure of the luminosity distance d_l (Eq. 1.15), is used as the observable,

$$\mu_0 = 5\log 10(d_L(z)) + 25. \tag{2.34}$$

This is given in the log-likelihood in Equation (2.35), where μ_B is the observed value. $\sigma_{\rm int}$ is given by the intrinsic dispersion of the absolute magnitudes and $\sigma(\mu_B)$ by peculiar velocity and light curve parameter information.

$$\chi^2 = \sum_{\rm objects} \frac{(\mu_B - 5\log_{10}(d_L(\theta, z)) - 25)^2}{\sigma^2(\mu_B) + \sigma_{\rm int}^2} \tag{2.35}$$

With this machinery in place it is now possible to perform additional tests on the mDGP model. I do not constrain the γ parameterisation with these probes in isolation as in this format they have no growth information. I do, however, attempt to constrain the growth with a combined analysis at the end of this section.

By looking at the top left hand panel of Figure 2.9 one can see that it is feasible to place a constraint on α with a BAO only analysis. It should be noted that the disfavouring of DGP ($\alpha = 1$) is not as promising as it first appears because I have, replicating the work of Yamamoto

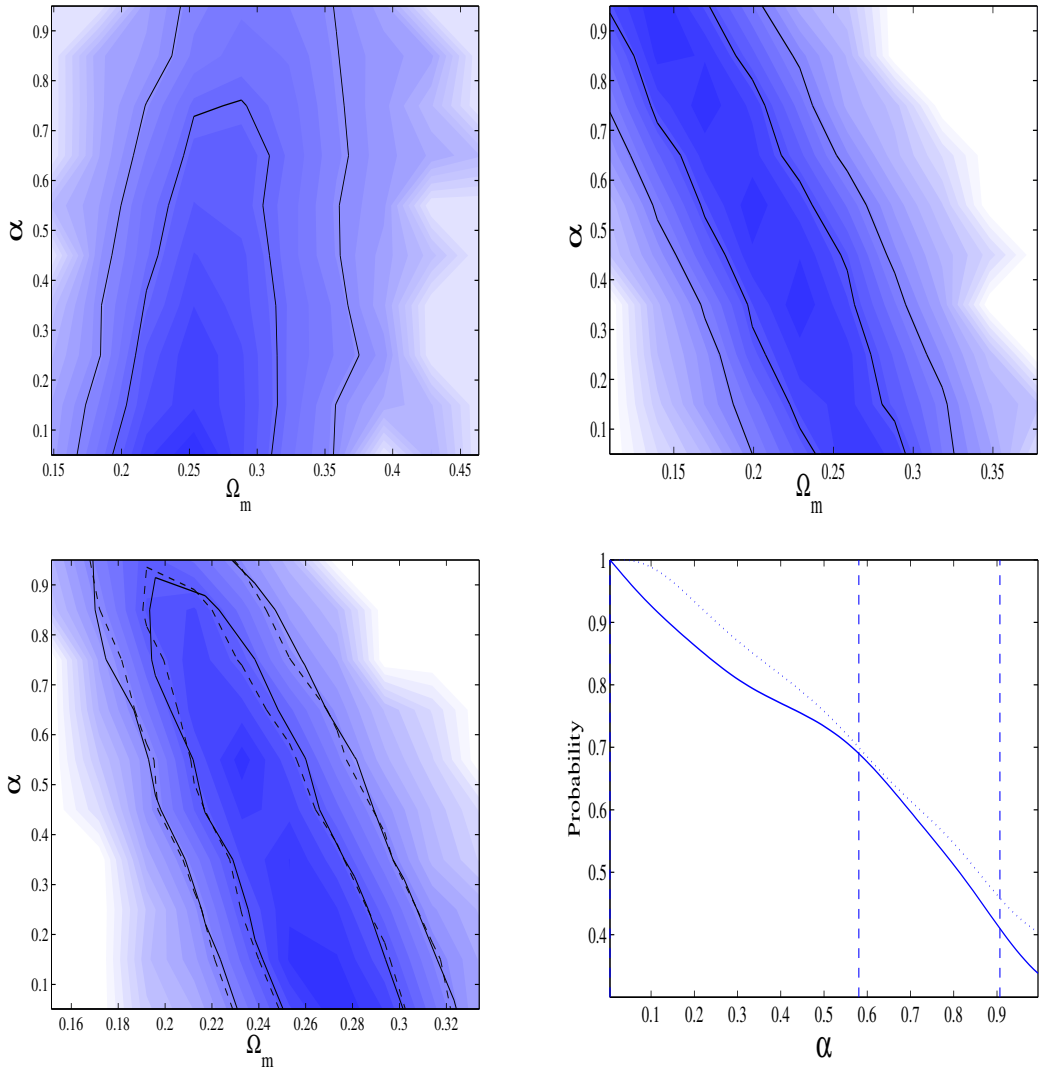

Figure 2.9: The plot in the top left panel shows the constraint on Ω_m and α. Although appearing to disfavour DGP ($\alpha = 1$) as in the analysis by Yamamoto *et al.* (2006) the remaining parameters Ω_b and h have been fixed at 0.044 and 0.66, respectively. I go beyond this in the top right panel which contains constraints given on the same parameters but when Supernovae data is added and Ω_b and h are allowed to vary. One can now see that the 1σ contour is beyond the bounds of the plot and so no constraint can be inferred. The benefit of the weak lensing data is seen in the bottom left panel where once again I use angular scales greater than 30 arcminutes from the CFHTLS-wide (F08) lensing survey. I also vary Ω_m, h, σ_8, Ω_b, a, b, c and α whilst keeping $n_s = 0.963$. With this addition it is evident that there is a visible improvement in constraint and that DGP is marginally disfavoured. This is exemplified in the bottom right panel where I include the 1D marginalised probability distribution (solid line). I find that the joint analysis gives constraints on mDGP of $\alpha < 0.58$ and $\alpha < 0.91$ at the 68% and 95% confidence levels, respectively. The dotted line represents the mean likelihood of the samples. Finally, the dashed contours in the bottom left hand panel show that the constraints are insensitive to any systematics in the data such as an over or underestimation in the CFHTLS shear at high redshift (Section 2.5.3).

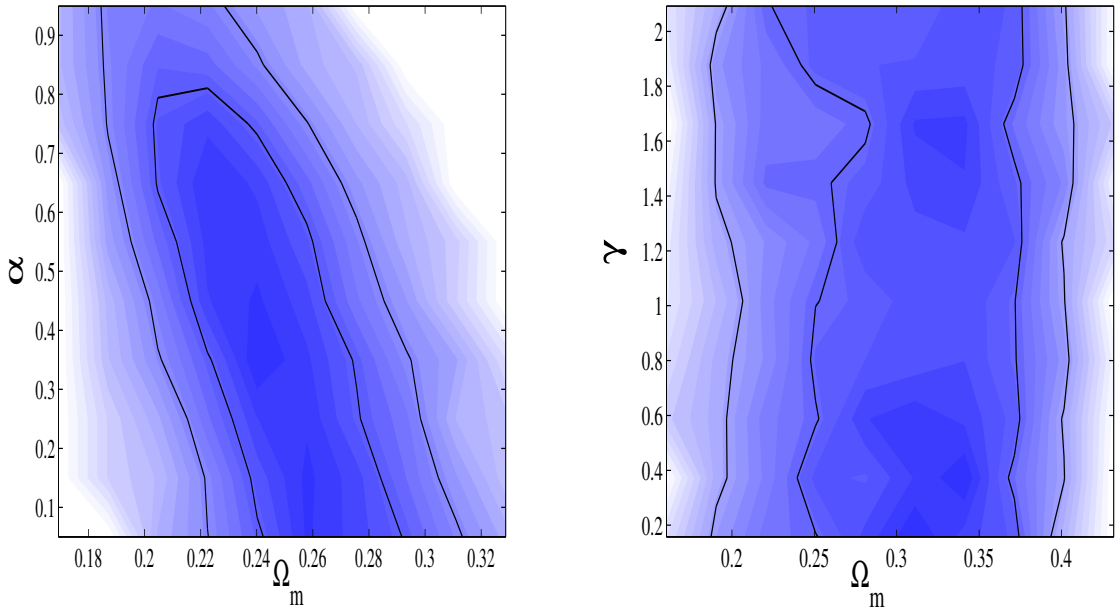

Figure 2.10: The left panel is an analysis of the mDGP model with weak lensing, BAO and Supernovae, as before, but with the full range of angular scales (1-230 arcminutes). There is a slight, but not significant, improvement compared to the more linear analysis. Here I find $\alpha < 0.56$ and $\alpha < 0.86$ at the 68% and 95% confidence levels, respectively. It should be noted that this analysis includes data from the unknown non-linear regime. The right panel demonstrates the current challenge in constraining the gravitational–as opposed to the expansion's–contribution to the growth of structure. I find that with current data it is unfeasible to put any bounds on reasonable values of the γ parameter. This plot contains an analysis with weak lensing, Supernovae and BAOs. Implicit in this plot is the variation of also h, σ_8, Ω_b, a, b, c and w_0.

et al. (2006) with BAO only, varied just Ω_m and α with Ω_b and h held fixed at 0.044 and 0.66, respectively. The top right hand panel of the same figure demonstrates the need for caution as I go beyond the Yamamoto *et al.* (2006) analyses. By allowing more cosmological freedom (i.e. varying Ω_b and h) and including the Supernovae data the two probes are in fact incapable of disfavouring DGP. This is in contrast to other Supernovae and BAO studies by Fairbairn & Goobar (2006) and Maartens & Majerotto (2006) where, as in Yamamoto *et al.* (2006), they either fix Ω_b fixing the BAO scale or use CMB data as a prior on Ω_b. I allow a more general variation as I, nor the aforementioned papers, have calculated the influence of DGP on the CMB. This is the main difference in this aspect of the work and is otherwise consistent.

One can now see how, even at present, the weak lensing data is useful in the study of this modified gravity. The $\Omega_m - \alpha$ contours for a joint analysis with all three combined probes is displayed in the bottom left hand panel. Once again I use only angular scales greater than 30

arcminutes to avoid the unknown non-linear regime. I also vary a large number of cosmological parameters: Ω_m, h, σ_8, Ω_b, a, b, c and α. It is evident that the addition of the weak lensing analysis is beneficial with a mild disfavouring of the DGP end of the α spectrum. Indeed, I include in the bottom right hand panel the 1D probability distribution for α, in the process demonstrating that $\alpha < 0.58$ at the 68% confidence level and $\alpha < 0.91$ at the 95% confidence level. This corresponds to a disfavouring of DGP at over 2σ. Furthermore, I include for interest in the left panel of Figure 2.10 the same analysis but with all angular scales (1-230 arcminutes). There is a noticeable but not significant improvement in the constraint leading to $\alpha < 0.56$ and $\alpha < 0.86$ at the 68% and 95% confidence levels, respectively.

Having had success with a combination of the three cosmological probes it is worth investigating whether they can aid the determination of the far more subtle growth parameterisation γ. While the BAO and Supernovae will not add growth information explicitly they will help reduce the parameter degeneracies. I find however, by looking at the right panel of Figure 2.10, that at present and for meaningful values of γ there is still insufficient constraining power. This is understandable given that for mDGP α contained growth *and* expansion information. In this way the Supernovae and the BAO actively contributed to the constraint, while the lensing constrained it through the comoving diameter distances $D(\chi)$ in the convergence power spectrum, through expansion terms within the growth via the Hubble drag and finally through the pure growth contribution as seen in the addition of β (Eq. 2.10). Constraining γ, on the other hand, is equivalent to just changes in β and is therefore far more subtle. However, just because we do not have the current data to pick out this effect it should not deter us from continuing to pursue these signatures of modified gravity. In fact, future cosmological probes, such as the weak lensing, will be able to extract this contribution and tighten constraints on beyond-Einstein cosmology. I look to the future in Section 2.6.

2.5.3 Accounting for systematics

Despite the absence of any significant B-modes in the CFHTLS data there exists a potential underestimation of the shear at high redshift (Kilbinger *et al.* 2009). In order to account for this effect I use the model introduced in Kilbinger *et al.* (2009) and multiply the redshift distribution at high redshift ($z > 1$) by some constant c_0; where $c_0 < 1$ constitutes underestimation, $c_0 > 1$ overestimation and $c_0 = 1$ no alteration in the shear. I vary c_0 and marginalise over the parameter in an additional cosmological run, thus accounting for any such systematic. No additional prior is placed on c_0 other than that it is flat with the parameter varying from 0 to 2. I consequently find

little change in the constraint on mDGP as shown by the dashed contour in the bottom left hand panel of Figure 2.9. In this way the constraint is limited by *statistical* rather than systematic error.

The 68% confidence interval is subsequently shifted only from $\alpha < 0.58$ to $\alpha < 0.61$ with systematic treatment. With the cut in angular scales at $\theta = 30$ arcminutes it has not been possible to meaningfully constrain c_0 itself. It should be noted that further systematics might also affect this data however one would expect, as above, to be limited instead by statistical information. Further treatment and causes of potential systematics in the data are detailed in van Waerbeke et al. in prep. and Kilbinger *et al.* (2009).

2.6 Future Probes - Euclid

Within the foreseeable future the age of precision cosmology looks likely to get ever more precise. The field of weak lensing is most definitely no exception and it is perhaps set to be one of the most promising areas of development. One striking reason, among others, is the planned Euclid mission (Refregier *et al.* (2008) and Cimatti *et al.* (2009)).

Euclid is a proposed space-based wide-field imager that will carry out an all-sky survey in one visible and three Near-Infrared (NIR) bands. It will accomplish this as a medium class mission carrying a 1.2m telescope. It is intended to launch $\sim$ 2017 with a major requirement over a ground-based mission being the need for a stable point spread function (PSF) in weak gravitational lensing at this precision. The primary science goals are focused on the *Dark Universe*[7], such as dark matter, dark energy and the nature of gravity. However, it will also shed light on many other areas of astronomy such as galaxy evolution and extrasolar planets.

It is of great interest to see how this future survey will probe the nature of the cosmological model and the nature of gravity, whatever that may be. I therefore firstly undertake a Fisher matrix analysis with the intention of forecasting, for lensing only, how Euclid will constrain the standard cosmological model (Section 2.6.2). I then extend this model to include deviations from Einstein-cosmology with the mDGP model (α) as well as the more general parameterisation for gravity (γ and Σ) in Section 2.6.3.

2.6.1 The Fisher Matrix

In Section 1.3.2.2 I touched upon the idea that the uncertainty in a quantity can be found by investigating the neighbourhood and therefore the derivatives of a probability density function

[7] Hence its previous name DUNE as the Dark UNiverse Explorer.

about the best fit point. This culminated in associating a type of error to the second derivative of the log likelihood (Eq. 1.38). In the particular scenario when the likelihood/posterior is Gaussian this is not an approximation but an exact case. One can imagine therefore that a quick method for examining a parameter space X is to examine the second derivative at an assumed point. This can be thought of as a curvature of the space and is given by,

$$F = -\frac{\partial^2 \ln L}{\partial X^2}. \tag{2.36}$$

For a set of parameters the *multivariate* version of this is called the *Fisher Information Matrix* F_{ij},

$$F_{ij} \equiv \Big\langle -\frac{\partial^2 \ln L}{\partial X_i \partial X_j} \Big\rangle. \tag{2.37}$$

This is a powerful concept not just because of its speed but also because it can be calculated without current data. Instead it is possible to use a planned survey design, as described below, to forecast the potential constraints for a probe given a fiducial input cosmology.

The errors are found simply as $\sigma^2_{X_i} = (F^{-1})_{ii}$ (marginalised) and $\sigma^2_{X_i} = 1/F_{ii}$ (fixed/conditional). This fits intuitively with the curvature concept of the likelihood space. For a highly 'curved' distribution the likelihood will fall off more quickly from the best fit point and thus give a smaller error.

2.6.2 Forecast: The standard Cosmological Model

The Fisher matrix formalism for weak lensing is subsequently given as,

$$F_{ij} = \sum_l \frac{\partial C}{\partial p_i} \mathrm{Cov}^{-1} \frac{\partial C}{\partial p_j} \tag{2.38}$$

where C is the weak lensing observable shown by,

$$C_{ij}(l) = P^k_{ij} + <\gamma^2_{\rm int}> \delta_{ij}/\bar{n_i} \tag{2.39}$$

and P^k_{ij} is a convergence power spectrum similar to Equation (2.26), hence the k superscript, but with indices i and j denoting tomographic bins. Further still, $\bar{n}_i$ is the average galaxy number per steradian in bin i and $<\gamma^2_{\rm int}>^{\frac{1}{2}}$ is the rms intrinsic shear in each component, that here is equal to 0.22. ∂p_i denotes the derivative with respect to a parameter p and Cov is the covariance matrix given by,

$$\mathrm{Cov}[C^k_{ij}(l), C^k_{kl}(l')] = \frac{\delta_{ll'}}{(2l+1) f_{\rm sky} \Delta l} [C^k_{ik}(l) C^k_{jl}(l) + C^k_{il}(l) C^k_{jk}(l)]. \tag{2.40}$$

For the following analyses I take the effective sky coverage to be $\mathrm{f_{sky}} = 20,000$ square degrees, while probing the galaxy distribution with a median redshift $z_m = 0.9$ and having an effective galaxy density of $40\ \mathrm{gal/arcmin^2}$. I assume the redshift distribution given in Equation (2.41) where $z_0 = z_m/1.412$, $\alpha = 2$ and $\beta = 1.5$. I allow for five redshift bins with divisions such as to give approximately equal galaxy number in each bin (0.0, 0.56, 0.79, 1.01, 1.32 and 3.0). The photometric error (see Section 3.2.1 for more information on photometric redshifts) is accounted for by using the parameterisation $\sigma_z = \sigma_p(1+z)$, with $\sigma_p = 0.03$. To impart this error the binned redshift distribution is convolved with a Gaussian, characterised by a width of σ_z. I use the transfer function as described in Eisenstein & Hu (1998) and the non-linear prescription of Smith *et al.* (2003).

$$n(z) \propto z^{\alpha}\mathrm{exp}(-(z/z_0)^{\beta}) \tag{2.41}$$

For the standard cosmology I vary 7 parameters about their fiducial values. These are given by: $\Omega_\mathrm{m} = 0.3$, $h = 0.7$, $\sigma_8 = 0.8$, $\Omega_\mathrm{b} = 0.05$, $n_s = 1.0$, $w_0 = -0.95$ and $w_a = 0.0$. The resulting 2D marginalised contours are given for each parameter combination in Figure 2.11. I use no extra priors on any of the parameters and so the derived bounds represent a true and conservative *Euclid-only* capability[8].

Assuming this underlying cosmological model Euclid would find 1σ marginalised bounds of $\Omega_\mathrm{m} = 0.3 \pm 0.003$, $h = 0.7 \pm 0.0832$, $\sigma_8 = 0.8 \pm 0.0041$, $\Omega_\mathrm{b} = 0.05 \pm 0.0140$, $n_s = 1.0 \pm 0.0158$, $w_0 = -0.95 \pm 0.0357$ and $w_a = 0.0 \pm 0.1326$.

2.6.3 Forecast: Modified Gravity

I now extend the above analysis further to include modified gravity. I use the same survey design, requirements, noise and parameters as for the standard model but now include γ and Σ as extra parameters for the general parameterisation (see Section 2.3) and instead α for the mDGP model. Note that this LCDM-DGP interpolation model specifies its own w_0, w_a, γ and Σ_0. The fiducial values are taken to be $\gamma = 0.55$, $\Sigma_0 = 0$ and $\alpha = 0$.

The resulting forecasts for this proposed project can be seen clearly in Figure 2.12. The left panel shows that Euclid will be able to put considerable strain on any braneworld-like gravity scenario that resembles the mDGP model. The solid (1σ) and dashed (2σ) contours are significantly

[8]For a code comparison or consistency check my fisher matrix and the associated parameter derivatives, as a function of ℓ, can be found at: http://zuserver2.star.ucl.ac.uk/∼sat/DUNE_working_group/**X**, with **X**=fisher, deriv_omega_m, deriv_h_0, deriv_sigma_8, deriv_omega_b, deriv_w_0, deriv_w_a or deriv_n_s. These have been calculated with the exact specification as described above.

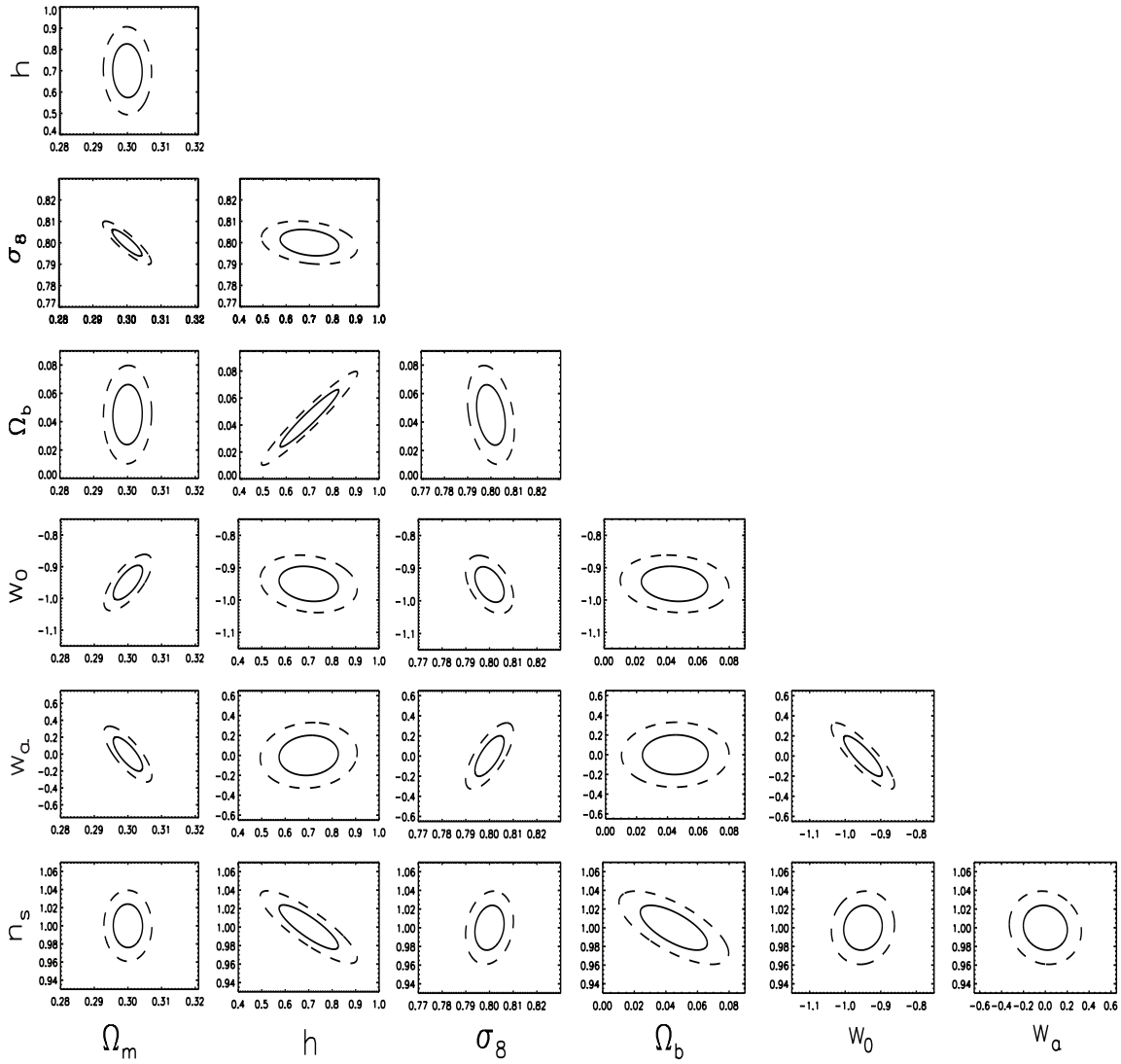

Figure 2.11: The 2D marginalised *forecasted* constraints with the proposed space-based Euclid survey. This corresponds to 1σ bounds of $\Omega_{\rm m} = 0.3 \pm 0.003$, $h = 0.7 \pm 0.0832$, $\sigma_8 = 0.8 \pm 0.0041$, $\Omega_{\rm b} = 0.05 \pm 0.0140$, $n_s = 1.0 \pm 0.0158$, $w_0 = -0.95 \pm 0.0357$ and $w_a = 0.0 \pm 0.1326$ from the fiducial input cosmology. This demonstrates that such a survey is a highly promising and worthwhile project with constraints being pushed towards the percent level for an *individual* late-time cosmological probe. The possible constraints on the equation of state in particular are thoroughly exciting, especially given there are no extra priors.

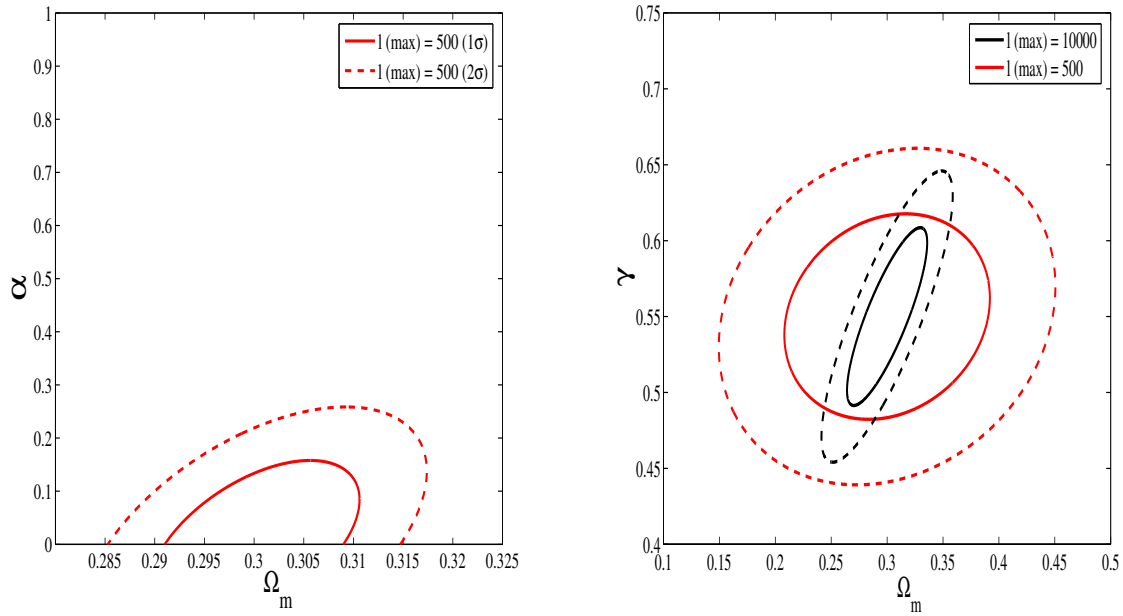

Figure 2.12: The left panel displays Euclid's potential constraining power with regards to the mDGP model in a lensing only analysis. Here the 1σ contour (all solid lines) is well within the $\alpha = 1$, or DGP, line and so it will be easily distinguishable from LCDM ($\alpha = 0$). In fact, this corresponds to an error of 0.104 on α with $l_{\rm max} = 500$ (all red contours) in stark contrast to today's constraint. The right panel shows the marginalised contours for the general growth parameterisation. Again, it seems that Euclid will provide excellent insight into any potential modified gravity signatures. Specifically it is found that it will be possible to constrain γ with an error of 0.045 (1σ). This is tightened further to 0.038 when $l_{\rm max} = 10000$ (black contours). The parameters h, σ_8, $\Omega_{\rm b}$ and n_s have been varied and marginalised over for both models considered here while in addition w_0, w_a and Σ_0 have been marginalised for the growth model.

within the $\alpha = 1$, or DGP, bound. In fact, Euclid will potentially constrain α to within an error of 0.104 at the 68% confidence level. This is in constrast to Figure 2.8 where no constraint was possible with a lensing-only study. Note that for this analysis *only* contributions from $l = 10$ to $l_{\rm max} = 500$ were considered such that the deeply non-linear regime could be neglected.

The right panel in Figure 2.12 again illustrates the expected constraining power of Euclid but now with regards to general modified gravity. For this general parameterisation I performed two runs with one corresponding to contributions from $l = 10$ to $l_{\rm max} = 500$ (red contours) and the other with contributions from $l = 10$ to $l_{\rm max} = 10000$ (black contours). Here one can see that Euclid will be able to extract the growth characteristic thus allowing a strong cosmological test of our gravitational framework. Indeed, it will be able to constrain the fiducial $\gamma = 0.55$ (LCDM) to within an error of 0.0446 at 1σ with $l_{\rm max} = 500$. This is further tightened to 0.038

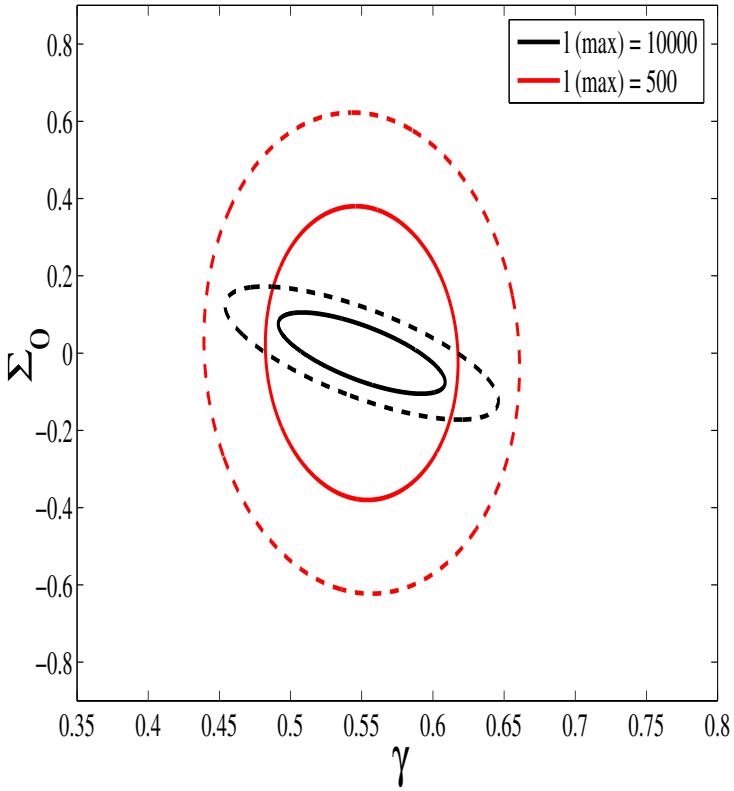

Figure 2.13: The above plot shows the marginalised $\gamma - \Sigma_0$ forecast for a weak lensing only analysis with Euclid. These two parameters, which could represent modified gravity or generic dark energy signatures, demonstrate how this future weak lensing probe will potentially place firm constrains on any model of late-time acceleration. The black contours correspond to $l_{\rm max} = 10000$, demonstrating an error of 0.069(1σ) on Σ_0, whereas the red contours correspond to $l_{\rm max} = 500$ giving instead an error of 0.25. In both cases the inner and outer contours are 1σ and 2σ, respectively.

with $l_{\rm max} = 10000$. The other 7 cosmological parameters (h, σ_8, $\Omega_{\rm b}$, w_0, w_a, n_s and Σ_0) have been varied and marginalised over in the plot. Again, this forecast is in contrast to Figure 2.10 where even the combined probes of weak lensing, BAOs and Supernovae were incapable of any constraint.

Finally, I include in Figure 2.13 a marginalised contour for γ against Σ_0 which further highlights how modified gravity or very generic dark energy signatures can be constrained, consistently, with weak lensing. I find that with $l_{\rm max} = 500$ (red contours) this survey could constrain alterations in the power spectrum with an error in Σ_0 of 0.25 at 1σ. This parameter is more sensitive to the range of scales used than γ, however, with $l_{\rm max} = 10000$ (black contours) confining Σ_0 to within 0.069 of the fiducial value $\Sigma_0 = 0$.

The two sets of modified gravity forecast figures reveal interesting degeneracies between the

new parameters, with both α and γ having the same degeneracy with respect to Ω_m. This can easily be understood by considering the compensation of one physical quantity for another in order to keep the magnitude of the weak lensing signal, and its corresponding statistic, constant. In each case an increase in the modified gravity parameter gives rise to a suppression in the growth of structure resulting from the force law (remembering Figure 2.2 and Figure 2.3). A less inhomogeneous and clustered intervening mass distribution naturally gives rise to less statistical weak lensing. This effect is simply offset by having more mass in the Universe, i.e. increasing Ω_m. Therefore, given the correlation between γ and Σ_0 it is evident that these bounds can be significantly improved with complementary constraints on the mass density, perhaps provided by a distance indicator.

It should also be emphasised that the spectroscopic element of Euclid (Cimatti *et al.* 2009) will also be able to constrain growth and therefore modified gravity via redshift space distortions (Peacock (2002) and Guzzo *et al.* (2008)).

2.7 Discussion and Conclusion

To summarise, I have noted that the surprising, but well confirmed, late-time acceleration of the universe *could* be the result of a modification to gravity. I then, in Section 2.2, reviewed the concept of modified gravity detailing in the process a model that is motivated by a large extra dimension (mDGP). Interpolating between LCDM ($\alpha = 0$) and DGP ($\alpha = 1$) it can be tested as a model in its own right and/or used as an example to demonstrate the rich set of observational signatures that are likely to arise for a modified gravity model in cosmology. These signatures include the expansion history, and rather interestingly, the growth of structure (Section 2.3) and a modification to the relationship between the potential power spectrum and the matter power spectrum (Section 2.3.1). With these characteristics in mind I then examined attempts to parameterise modified gravity in this way. This included a growth parameter γ and a power spectrum parameter Σ.

In Section 2.4 I introduced weak lensing and related its attributes to modified gravity given that it is sensitive to the expansion history, the growth of structure and the power spectrum. A severe caveat was described in the use of non-linear scales and therefore, in Section 2.4.2, I described the appropriate choice of survey (CFHTLS-wide) and data ($\theta > 30$ arcminutes) used in the cosmological analyses. The subsequent lensing only constraints were given in Section 2.5.1 where I showed that one could not yet constrain meaningful values of α or γ with the current data. It was

then demonstrated, by adding BAO and Supernovae data, that weak lensing was highly beneficial in aiding the constraint of mDGP in combination. Without the inclusion of the lensing data the expansion-only probes were incapable of constraining $\alpha = 1$ when varying Ω_m, α, h *and* Ω_b. I found however that the combined probes disfavoured the DGP model with over a 95% confidence level where specifically $\alpha < 0.58$ at 1σ and $\alpha < 0.91$ at 2σ.

I then showed that a constraint on the subtle, yet important, growth signature is beyond the current weak lensing, BAO and Supernovae data. Almost total cosmological freedom was allowed in all these analyses, varying parameters: Ω_m, h, σ_8, $\Omega_{\rm b}$, a, b and c for both models, in addition to α for mDGP and w_0 and γ for the growth model. Furthermore, I used the ξ_E two point statistic while analytically marginalising over the residual offset c'. It was also demonstrated in Section 2.5.3 that my results are insensitive to over or underestimation of the CFHTLS shear at high redshift.

Finally in Section 2.6 I looked towards the future space based weak lensing survey Euclid and discovered that it will have significant ability to discriminate the standard cosmological model. This was illustrated most clearly in Figure 2.11 and highlights that with the addition of a few simple priors we will soon be pushing towards percent level constraints with an individual late-time cosmological probe. This was followed by showing that Euclid will go further and be able distinguish between modified gravity and LCDM. I included a forecast for the mDGP model finding that even for a lensing only analysis Euclid could restrict α to within 0.104 of the fiducial $\alpha = 0$ at 1σ, even when the deeply non-linear regime has been removed ($l_{\rm max} = 500$). In addition, a complete and consistent forecast was included for generalised modified gravity demonstrating that deviations from a fiducial $\Sigma_0 = 0$ of $\Delta\Sigma_0 = 0.25$ at the 68% confidence level will be possible with $l_{\rm max} = 500$. When $l_{\rm max} = 10000$ this gets further restricted to $\Delta\Sigma_0 = 0.069$. It will also confine γ to within 0.045 ($l_{\rm max} = 500$) and 0.038 ($l_{\rm max} = 10000$) of the fiducial $\gamma = 0.55$ at 1σ, where a full 9 cosmological parameters were varied.

In the analyses with data I have, except as an example case, actively removed angular scales less than 30 arcminutes. This was to remove the contribution from the unknown non-linear regime in modified gravity. This clearly does not utilise the available information especially over scales for which weak lensing is particularly sensitive. In addition, one might also expect that non-linear physics will act to emphasise any difference in gravitational theory as an additional signature. This is analogous to the early studies of non-linearities with neutrinos where there is an *extra* suppression in the non-linear regime relative to a model mapped naively from the linear (E.g Saito *et al.* 2008). However, for a potential viable theory of gravity it is necessary for it to match the

stringent observations of solar system tests that are satisfied most closely by GR. In this way such a theory should actually tend to the non-linear behaviour of GR with the same expansion history. I elaborate on this idea in the discussion of Chapter 5 and how it is leading to developments that will benefit this study.

Even though I have detailed the advantages of weak lensing in a modified gravity study, and even though Euclid in particular will be deeply insightful it is obvious that a collected and coordinated assault on our gravitational framework will prove more advantageous. This might exist in the form of a combination of probes as discussed in Jain & Zhang (2007), for example, where ideally the four perturbation variables ϕ, ψ, δ and θ are independently targeted. This in principle would allow us unprecedented experimental scrutiny on the structure of our gravitational theory over large scales.

CHAPTER 3

THE ANGULAR POWER SPECTRUM OF PHOTOMETRIC SDSS LRGS

Abstract

I construct a new galaxy angular power spectrum C_ℓ based on the extended, updated and final SDSS II Luminous Red Galaxy *photometric* redshift survey–MegaZ LRG (DR7). Encapsulating $7746\ \mathrm{deg}^2$ (30% more area than the previous photometric SDSS power spectrum) I utilise 723,556 photometrically determined LRGs between $0.45 < z < 0.65$ in a spherical harmonic analysis of the galaxy distribution. By combining four photometric redshift bins I find parameter constraints of $f_b \equiv \Omega_b/\Omega_m = 0.173 \pm 0.046$ and $\Omega_m = 0.260 \pm 0.035$, consistent with and independent of the CMB. This survey is not only one of the largest to date but is one of the most competitive currently available. The robustness of the power spectra with respect to a number of potential systematics are discussed. Finally, this composed galaxy clustering data is combined with the CMB (WMAP 5-year) to examine the complementarity of these early and late-time probes.

This work is presented originally in Thomas, S.A., Abdalla, F.B. & Lahav, O., 2009a (In prep.).

3.1 Introduction

The analysis of the statistical distribution of fluctuations in the Universe is a potent method for constraining theories or components within Cosmology. In fact, the power spectrum will fully describe these variations, which are predicted by theory, if they are given by a Gaussian random field. The Cosmic Microwave Background (CMB) has been a great example of this principle in action with recent high precision measurements (Dunkley *et al.* (2009) and Komatsu *et al.* (2009)) confirming that a clear and consistent picture of cosmology is emerging. It is desirable however to test this picture with additional and independent data that explores a contrasting epoch of cosmic evolution and breaks the parameter degeneracies that exist from a single probe of the early Universe. A galaxy redshift survey is therefore a powerful tool in Cosmology (Peebles 1973). In addition, this late-time distribution is sensitive to the emergence of dark energy (Riess *et al.* (1998) and Perlmutter *et al.* (1999)) and arising through the growth of structure enables a test of gravity (Jain & Zhang (2007), Huterer & Linder (2007), Thomas *et al.* (2009) and Chapter 2) and the mass of the neutrino (Hu *et al.* 1998). I tackle this last topic in Chapter 4 with a combined constraint on the absolute mass.

The structure and aim of this Chapter is as follows: To construct and present the angular power spectrum C_ℓ of the new SDSS Luminous Red Galaxy (LRG) photometric survey (Section 3.2), along with the associated error and cosmological constraints.

Specifically, I determine the colour, redshift and angular selection functions that define the survey in Section 3.2.1. The spherical harmonic analysis is described in Section 3.3 and Section 3.4. The cosmological constraints inferred and the potential systematics of the data set are discussed in Section 3.5 and Section 3.6, respectively. Finally, I combine this data set with an analysis of the 5-year WMAP data in Section 3.7.

3.2 The LRG Angular Power Spectrum

3.2.1 Data

The development of galaxy surveys over the past few years reflects the balance between observational technology and gains in cosmological parameter estimation. This has at present culminated in the impressive 2-degree Field Galaxy Redshift Survey (2dFGRS - Colless *et al.* (2001)) and the Sloan Digital Sky Survey (SDSS - York *et al.* (2000)). However, the acquisition of a vast number of precise redshifts through spectroscopy is an expensive, challenging and time consuming task.

An alternative method is to use photometric redshifts (E.g. Csabai *et al.* (2003)) resulting from observations of broadband galaxy colours through a series of filters (see also Figure 3.1). The motivation is that a decrease in redshift accuracy is outweighed by measurements of a vast number of galaxies over a wide area of the sky, therefore encompassing a large cosmic volume. Photometric redshift surveys have been shown to be competitive (Blake *et al.* (2007) and Padmanabhan *et al.* (2007)) and upcoming surveys, such as the Dark Energy Survey (The Dark Energy Survey Collaboration (2005)), are heavily based on this efficiency principle.

I therefore aim to analyse the clustering of the latest and final SDSS II photometry given by Data Release 7 (DR7). The ≈ 1.5 million LRG catalogue (MegaZ-LRG DR7) is produced as an updated version of MegaZ-LRG (Collister *et al.* 2007). These LRGs are old red elliptical galaxies that provide a clean and consistent galaxy sample. With a stable spectral energy distribution (SED) and a sharp $4000\mathring{A}$ break (Figure 3.1) they therefore provide good photometric redshift estimates. Furthermore, they are known to strongly trace the underlying mass density; a distribution we are striving to quantify. Also, being among the brightest galaxies in the Universe they allow detailed studies over a large cosmic volume. This is highly desirable for a cosmological study given that it diminishes the effect of sample variance.

3.2.1.1 Redshift Selection

The redshift estimates for this above sample were constructed by using the redshift output as given by ANNz (Collister & Lahav 2004) an Artificial Neural Network code. This empirical photometric redshift estimator learns an effective parameterisation of redshift with varying galaxy magnitudes by working on a representative training set. The 13,000 spectroscopic redshifts from the 2dF-SDSS LRG and Quasar (2SLAQ) survey (Cannon *et al.* 2006), a $\delta \approx 0^\circ$ (declination) stripe within the DR7 imaging area, is one such training set. For this reason and for this specific galaxy sample over the range of redshifts of interest ($0.45 < z < 0.65$) Abdalla *et al.* (2008) found the ANNz training method to have the best performance on an evaluation LRG sample compared with other redshift estimation codes, with average scatter $\sigma_z = 0.0575$ and σ_z defined by,

$$\sigma_z = < (z_{\rm phot} - z_{\rm spec})^2 >^{\frac{1}{2}} . \tag{3.1}$$

The reliability of the neural network training procedure depends on the training set being completely representative of the target galaxy sample. It is noted that by applying this 2SLAQ stripe to the wider photometric LRGs there is an extrapolation of the training set with sky position. The discussion of this potential systematic, however, is left to Section 3.6.

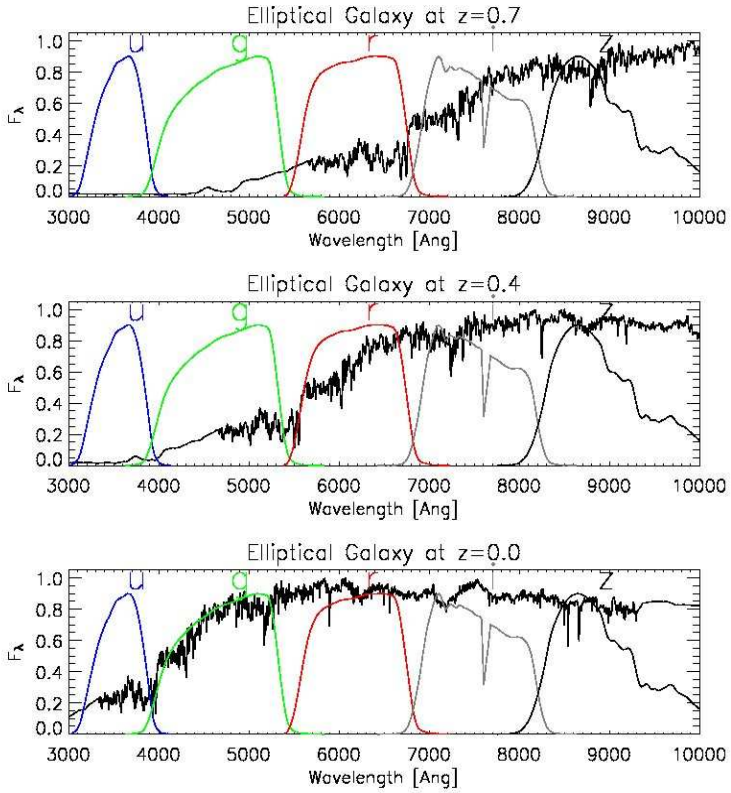

Figure 3.1: An example LRG spectrum is plotted over the SDSS filters (u, g, r, i and z) for varying redshifts. The $4000\mathring{A}$ break, which is clearly evident in the relatively stable SED, underlies the LRG photometric accuracy. The redshifting of the spectrum from the boundary of the g and r filters, through the r filter and up to the boundary of the r and i filters describes the high redshift galaxy sample that I utilise ($0.44 < z < 0.65$). To reiterate, it is from the flux through the different filters that allows one to estimate the redshift for the galaxy. CREDIT: *Padmanabhan* et al. *(2007)*.

3.2.1.2 The Colour Selection

At the start of the 2SLAQ survey there was an alteration in the selection criteria used to extract the homogeneous LRG sample from the overall galaxy population. This is associated with the de Vaucouleurs magnitude $i_{\rm deV}$ and also $d_{\rm perp}$, a colour cut which is related to the g, r and i magnitudes via,

$$d_{\rm perp} \equiv (r - i) - (g - r)/8.0. \tag{3.2}$$

I prefer to act cautiously in order to analyse a galaxy sample that most represents the training set used to infer its properties. Therefore, I introduce the additional colour cuts $i_{\rm deV} \leq 19.8$ and $d_{\rm perp} \geq 0.55$ to select the LRG population given that these were the selection criteria used in the strict majority of 2SLAQ. These cuts were also introduced in the analysis of the earlier MegaZ-LRG catalogue (Blake *et al.* 2007).

3.2.1.3 M-star Contamination

The presence of M-stars represent the main source of object contamination ($\approx 5\%$) within the remaining sample owing to similar broadband colours. Generally, an uncorrelated sample of stars will act to suppress the power of fluctuations (Huterer *et al.* 2001). One would expect a slightly correlated variation of stellar material through the galactic plane and hence our survey area. I therefore remove a large proportion of these contaminants with a cut in star-galaxy separation. The ANNz code has a star-galaxy parameter δ_{sg} as an additional optional output (Collister & Lahav 2004). The parameter varies continuously from 'guaranteed' star $\delta_{sg} = 0$ to 'certain' galaxy $\delta_{sg} = 1$. I remove all objects with $\delta_{sg} < 0.2$, in the processes decreasing the contamination fraction to $\approx 1.5\%$ with minimum loss of bona fide galaxies (Collister *et al.* (2007) and Blake *et al.* (2007)).

3.2.1.4 The Angular Selection Function

The angular selection function was obtained, which is used to determine the boundaries of the survey in the plane of the sky, from `tsChunk.dr7.best.par` downloaded at `www.sdss.org/dr7/coverage`. I converted the provided great circle coordinates (μ,ν) and the survey's stripe numbers to declination and right ascension before undergoing a HEALPix pixelisation on a sphere (Górski *et al.* 2005). I used a total of 3,145,728 pixels ($12 \times \mathrm{n_{side}} \times \mathrm{n_{side}}$ where $\mathrm{n_{side}} = 512$) over the entire sky, placing a zero in pixels corresponding to holes, gaps or regions not surveyed and a one in genuinely surveyed pixels. This discrete survey mask was then overlaid with the aforementioned LRG catalogue to leave the final galaxy map. I further tested this with $\mathrm{n_{side}} = 1024$ to examine the effects of a pixelised space. After appropriately adjusting the estimated C_ℓ (found in the next subsection), by dividing by the square of the HEALPix window function w_ℓ^2, the pixelisation effect was found to be negligible.

I imposed an additional constraint on the mask/map by excluding the survey stripes 76, 82 and 86, which are widely separated from the rest of the contiguous region. These segments act to increase the complexity of the survey window function and contribute relatively little extra galaxies. The resulting survey used for the primary angular power spectrum analysis spans $7746\ \mathrm{deg}^2$ and $723,556$ galaxies over a redshift $0.4 < z < 0.7$. This is a 30% larger area for analysis than the first and previous MegaZ-LRG survey (Blake *et al.* (2007) and Collister *et al.* (2007)). Likewise, it is significantly more expansive than the earlier Padmanabhan *et al.* (2005), which covering $3,528\mathrm{deg}^2$ and $0.2 < z < 0.6$ represents a slightly different LRG population and analysis method.

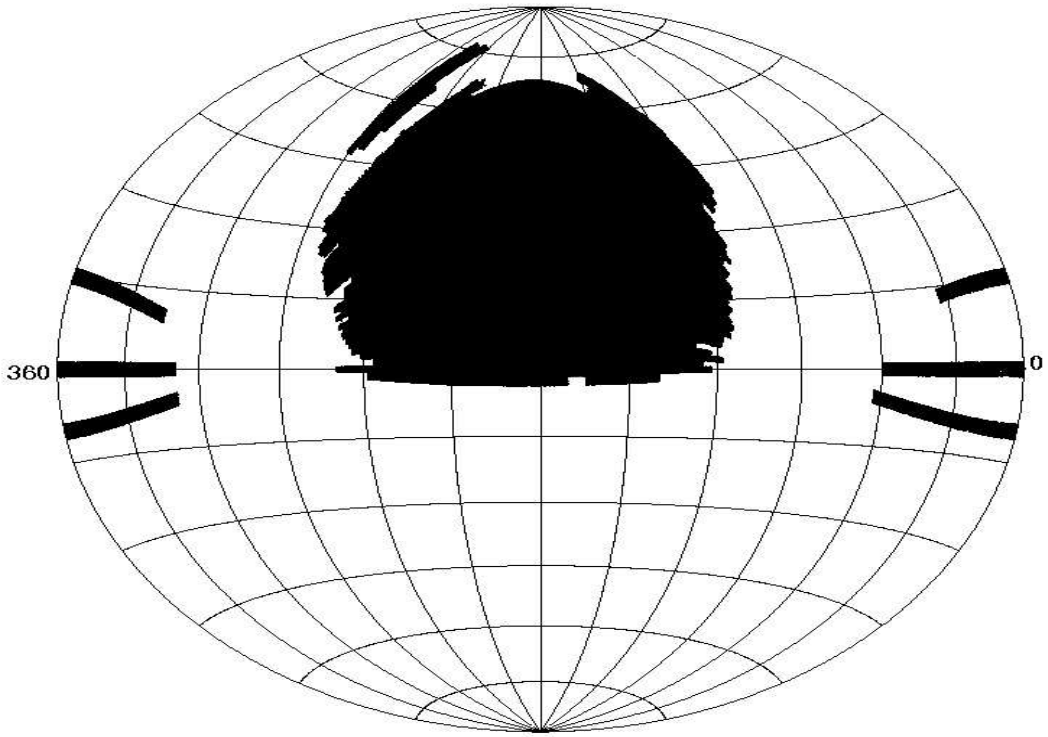

Figure 3.2: The SDSS Data Release 7 (DR7) photometric LRG coverage. At $7746\ \mathrm{deg}^2$ it covers $723,556$ galaxies over a redshift $0.4 < z < 0.7$. The three excluded stripes (76, 82 and 86) are visible towards the boundary of the plot. The 2dF SDSS LRG and Quasar (2SLAQ) survey and training set constitute a narrow stripe ($\delta \approx 0\,^\circ$) that passes approximately through the middle of the coordinate system and the bottom of the defined survey.

The final sky coverage is shown in Figure 3.2.

3.3 The Power Spectrum Measurement

The measurement of the angular power spectrum is performed by undertaking a spherical harmonic analysis (Peebles 1973). By explicitly summing the discrete galaxies over the incomplete sky I follow the derivation, methodology and/or notation of Peebles (1973), Wright *et al.* (1994), Blake *et al.* (2004) and Blake *et al.* (2007).

One connects the underlying density field in a redshift band to the relevant statistical entities by first projecting the mass distribution onto a plane in the sky $\sigma(\theta, \phi)$. This distribution is then decomposed into a series of spherical harmonics $Y_{l,m}$ and their corresponding coefficients $a_{l,m}$,

$$\sigma(\theta,\phi) = \sum_{l=0}^{\infty} \sum_{m=-l}^{l} a_{l,m} Y_{l,m}(\theta,\phi). \tag{3.3}$$

The statistical distribution–the angular power spectrum C_ℓ–is then given by the multi-realisation expectation of these $a_{l,m}$ coefficients, $< |a_{l,m}|^2 >$. For a full sky survey these coefficients represent an orthogonal and normalised basis and are thus found by a summation of the spherical harmonic conjugate over the galaxy catalogue,

$$A_{l,m} = \sum_{i=1}^{N} Y^*_{l,m}(\theta_i,\phi_i). \tag{3.4}$$

However, in reality one will observe a masked and therefore incomplete sky. This effectively correlates the spherical harmonic coefficients and induces the correction and adjustment for loss of power given by,

$$C^{\rm psky}_{l,m} = \frac{|A_{l,m} - \frac{N}{\Delta\Omega} I_{l,m}|^2}{J_{l,m}} - \frac{\Delta\Omega}{N} \tag{3.5}$$

where the $I_{l,m}$ and $J_{l,m}$ integrals in Equations 3.6 and 3.7 are evaluated over the geometry of the discrete survey area. I.e., $\delta\Omega = 1$ for a surveyed pixel and $\delta\Omega = 0$ for an unsurveyed pixel. The last subtracted term is a correction for the statistical distribution of shot noise and is equivalent to the expectation of the corresponding harmonic coefficient for a random unclustered sample.

$$I_{l,m} = \int_{\Delta\Omega} Y^*_{l,m}\, {\rm d}\Omega \tag{3.6}$$

$$J_{l,m} = \int_{\Delta\Omega} |Y_{l,m}|^2\, {\rm d}\Omega \tag{3.7}$$

One can then obtain the resulting angular power spectrum for a given multipole ℓ via an averaging of $C_{l,m}$ over the $(2\ell+1)$ $a_{l,m}$ values,

$$C^{\rm obs}_\ell = \frac{\sum_{m=-l}^{l} C^{\rm psky}_{l,m}}{2l+1}. \tag{3.8}$$

The angular power spectrum is independent of m for statistical isotropy. The C_ℓ values are further averaged into bins of width $\Delta\ell = 10$. I weight this average by the corresponding number of $a_{l,m}$s,

$$C^{\Delta\ell}_\ell = \frac{\sum_{\ell'}^{\ell'+\Delta\ell} (2\ell+1) C^{\rm obs}_\ell}{\sum_{\ell'}^{\ell'+\Delta\ell} (2\ell+1)}. \tag{3.9}$$

The angular power spectrum in these $\Delta\ell$ bands is measured up to $\ell = 500$. One can therefore use these statistics for each redshift bin within the survey volume. I measure the clustering distribution in four such photometric redshift bins, each having width $\Delta z = 0.05$ from $z = 0.45$ to $z = 0.65$. These procedures are in line with Blake *et al.* (2007) and therefore a direct MegaZ-LRG comparison and consistency check can be made.

The aforementioned redshift bins are correlated, however, as photometric errors scatter galaxies throughout the bins. A small modification to the angular power spectrum,

$$C_\ell^{i,j} = \frac{1}{2\ell+1} \sum_{m=-\ell}^{\ell} (A_{l,m}^i)^* A_{l,m}^j \tag{3.10}$$

enables a measurement where the harmonic coefficients in bin i and bin j have been adjusted for incomplete sky coverage as detailed above. The results are displayed in Section 3.3.2.

Note there exist other analogous procedures for the analysis of galaxy clustering including, for example, quadratic estimators, maximum likelihood methods and explicit reconstructions of the power spectrum (E.g. Huterer *et al.* (2001), Tegmark *et al.* (2002), Seo & Eisenstein (2003), Tegmark *et al.* (2004), Blake & Bridle (2005), Tegmark *et al.* (2006), Padmanabhan *et al.* (2007), Blake *et al.* (2007) and Reid *et al.* (2009)).

3.3.1 Simulations, the Covariance and Gaussian error

The methodology described above in Section 3.3, for the measurement of the angular power spectrum, was applied to simulated data in order to test the procedure and the code. This was performed by first constructing a Gaussian random field for some input cosmology, using best fit WMAP5 parameters (Dunkley *et al.* 2009), and subsequently reconstructing this cosmology for each of the four galaxy clustering redshift bins to be measured. I *randomly* selected the full set of spherical harmonic coefficients $a_{\ell',m}$ from Gaussian distributions with widths given by the underlying known cosmology [$(C_{\ell'})^{\frac{1}{2}}$]. The relation between the underlying matter power spectrum and the theoretical angular power spectrum is described in Section 3.4. Then, using the HEALPIX function `alm2map` (Górski *et al.* 2005) I simulated a pixelised galaxy map from these quantities and sampled objects as a Poisson realisation of the field. The full angular selection function of the survey (Section 3.2.1; Figure 3.2) was imposed on the simulated map and the number of galaxies sampled in each bin were matched to those present in the observed catalogue. This mock data was then analysed with my code in the same manner as the real data and averaged over 1000 simulated realisations. The accuracy and reliability of the code and the power spectrum measurement procedure is evident in Figure 3.3.

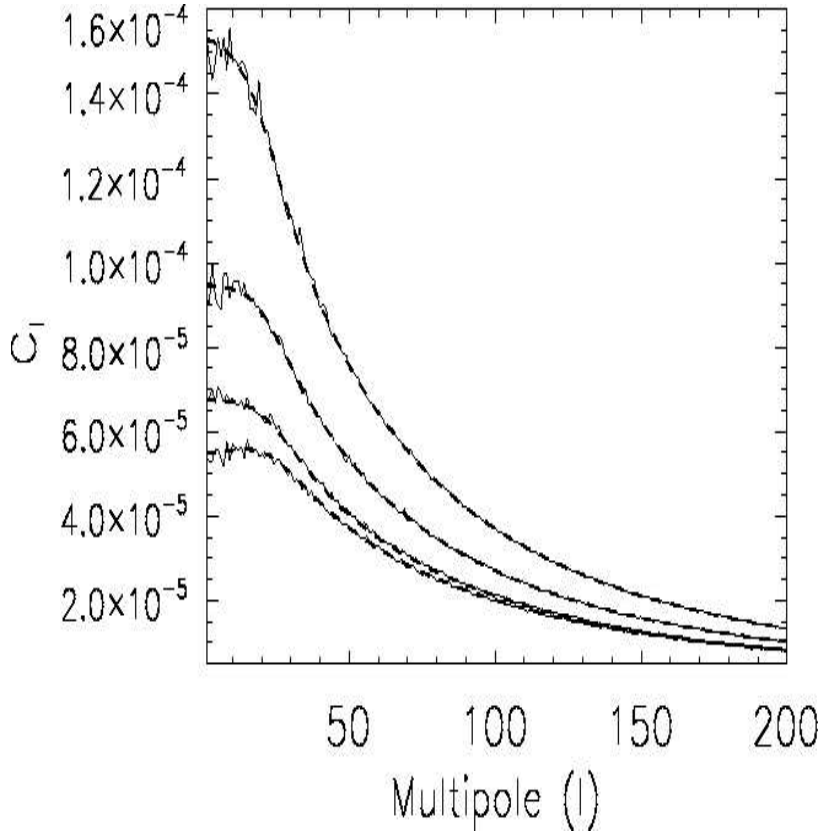

Figure 3.3: The averaged reconstruction of the input C_ℓ field for 1000 simulated realisations. The thick dashed lines represent the input cosmology for the four redshift bins between $0.45 < z < 0.65$ and the thinner solid lines are the recovered averages. The plot has been truncated at $\ell = 200$ as a visual aid to see the agreement. The behaviour beyond this point continues in an identical fashion and so the accuracy and consistency of the code and the measurement procedure is clear.

Interestingly one can also use these simulations to derive the statistical error in the galaxy clustering measurements $\sigma(C_\ell)$. This is extracted from the standard deviation over the 1000 mock realisations at each ℓ. An alternative estimate of the error is to use the simple analytic Gaussian expression (E.g. Dodelson (2003) and Blake *et al.* (2007)),

$$\sigma(C_l) = \sqrt{\frac{2}{f_{\rm sky}(2l+1)}}\Big(C_l + \frac{\Delta\Omega}{N}\Big) \tag{3.11}$$

where $\rm f_{sky}$ is the fraction of sky surveyed, $\Delta\Omega$ is the area, N is the measured number of galaxies in the bin and C_ℓ is the observed or theoretical angular power spectrum. The first and second terms in Equation 3.11 include the necessary error contributions from both cosmic variance and shot noise, respectively. It also accounts for the reduced error given the combination of $2\ell + 1$ $C_{\ell,m}$ values into the determination of each C_ℓ. For the statistical error in the cross power spectrum this

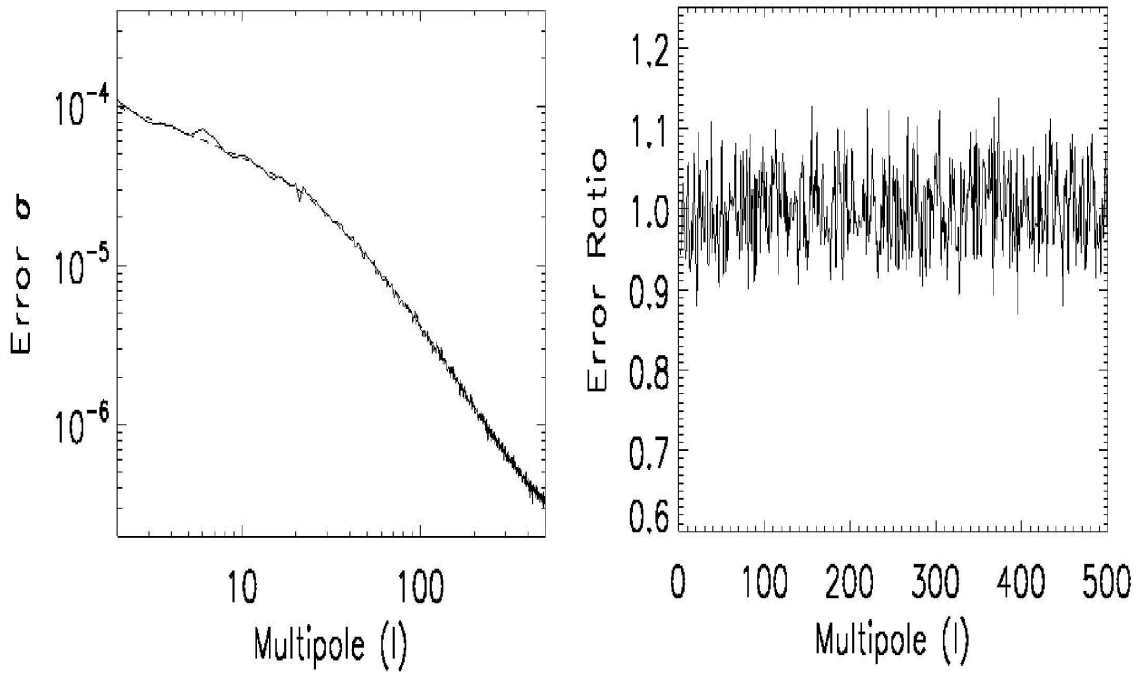

Figure 3.4: Left Panel: The analytic Gaussian expression (Equation 3.11; dashed line) is accurately traced by the 1000 realisation simulated error in a redshift band (solid line), shown here for bin 1 ($0.45 \leq z \leq 0.5$). This demonstrates the approximate validity of the Gaussian expression. Right Panel: The agreement is further highlighted by the ratio of the analytic and numerical estimations of the statistical error, where the overall behaviour is consistent with unity. The two panels are shown for the first bin only but are representative of all other bin combinations.

generalises to,

$$\sigma^2(C_l^{i,j}) = \frac{2}{f_{\rm sky}(2\ell+1)}\Big(C_\ell^i + \frac{1}{N_i/\Delta\Omega}\Big)\Big(C_\ell^j + \frac{1}{N_j/\Delta\Omega}\Big). \tag{3.12}$$

However, the expression for the error is potentially invalid for non-Gaussian statistics and non-linear growth and does not capture the full effects of a complex survey geometry. By earlier including the survey mask in the Monte Carlo realisations/simulations and accounting for the observed number density of galaxies in each redshift bin the simulated error has no such limitations. In addition, the variance between the simulated $C_\ell^{i,j}$ will incorporate the full covariance between redshift bins and $\Delta\ell$ bands. I therefore use the mock errors as a testbed for the Gaussian expression's validity.

I find the expression reconstructs the simulated error accurately in each of the four redshift bins and across the entire range of ℓ. This is easily seen in the left panel of Figure 3.4. The error ratio, typified by the first redshift bin, is displayed in the right panel.

3.3.2 Results

I have constructed the galaxy clustering angular power spectrum C_ℓ for SDSS MegaZ-LRG (DR7), an extension to the earlier analysis (Blake *et al.* 2007) of the original MegaZ-LRG catalogue (Collister *et al.* 2007). Including $723,556$ photometrically determined LRGs and encapsulating $7746\ \mathrm{deg}^2$ the measured values in four redshift bins extending $\Delta z = 0.05$ in redshift, from 0.45 to 0.65, are recorded in Table 3.1. These are illustrated further in Figure 3.5. The full measurement procedure was detailed in Section 3.3. In addition, the measured cross power spectra between bins are described and listed in Section 3.6.2.

Table 3.1 also includes the statistical errors $\sigma(C_\ell)$ on each power spectrum measurement as given by Equation 3.11, but calculated with the *measured* C_ℓ. They have been further weighted over the $\Delta\ell = 10$ band. This was shown in Figure 3.4 to be a good approximation. Note that for the cosmological parameter estimation in Section 3.5 I utilise the Gaussian expression but evaluated with *model* C_ℓs.

In addition to the simulations described previously I also test the measurement pipeline by reconstructing the observed C_ℓ as found in the DR4 catalogue. I find these values to be identical to Blake *et al.* (2007). As in the DR4 results I find that DR7 also exhibits an excess of power over the largest scale ($\ell = 6$ band) in the furthest redshift bin. There is slight relief from this tension however as the DR4 point is found to have a further 40% more amplitude. The effects and potential cause of this are discussed later in the chapter.

Table 3.1: The angular power spectrum C_ℓ for SDSS MegaZ-LRG (DR7), an extension to the first MegaZ-LRG analysis (Blake *et al.* (2007) and Collister *et al.* (2007)). The Gaussian statistical error on the measurement is also included, which has been weighted over each $\Delta\ell$ band. Each bin extends $\Delta z = 0.05$ in redshift from $z = 0.45$ to 0.65 and covering $7746\ \mathrm{deg}^2$ contain $259,498$; $237,564$; $155,293$ and $71,201$ galaxies, respectively. With the exception of the multipole values (ℓ) all quantities have been multiplied by 10^5. Note that for the main cosmological analyses the model C_ℓs are used to deduce $\sigma(C_\ell)$, except where explicitly stated for comparison.

ℓ	$C_\ell^{\mathrm{Bin}\,1}$	$\sigma(C_\ell^1)$	$C_\ell^{\mathrm{Bin}\,2}$	$\sigma(C_\ell^2)$	$C_\ell^{\mathrm{Bin}\,3}$	$\sigma(C_\ell^3)$	$C_\ell^{\mathrm{Bin}\,4}$	$\sigma(C_\ell^4)$
6	24.757	7.646	16.307	5.154	18.944	6.096	26.380	8.846
16	15.685	3.027	9.702	1.951	13.501	2.740	10.512	2.522
26	10.917	1.692	7.708	1.245	9.893	1.633	7.230	1.509
36	9.865	1.310	7.481	1.030	6.803	1.012	5.686	1.094
46	7.613	0.916	6.980	0.857	5.979	0.806	5.602	0.959
56	5.447	0.619	3.900	0.477	5.192	0.654	4.574	0.769

ℓ	$C_\ell^{\mathrm{Bin}\,1}$	$\sigma(C_\ell^1)$	$C_\ell^{\mathrm{Bin}\,2}$	$\sigma(C_\ell^2)$	$C_\ell^{\mathrm{Bin}\,3}$	$\sigma(C_\ell^3)$	$C_\ell^{\mathrm{Bin}\,4}$	$\sigma(C_\ell^4)$
66	5.293	0.557	5.072	0.544	4.177	0.511	4.408	0.693
76	5.088	0.501	4.872	0.491	3.802	0.445	3.165	0.542
86	3.817	0.371	3.945	0.388	3.936	0.429	3.636	0.546
96	3.675	0.341	3.068	0.302	3.368	0.364	2.728	0.450
106	3.358	0.302	3.141	0.293	3.313	0.342	2.944	0.443
116	2.987	0.264	2.947	0.266	2.736	0.288	2.966	0.425
126	2.570	0.226	2.333	0.216	2.056	0.232	2.052	0.348
136	2.426	0.208	2.064	0.191	2.310	0.239	1.817	0.321
146	2.375	0.198	1.847	0.171	2.069	0.216	1.690	0.302
156	2.162	0.179	1.860	0.166	1.683	0.187	1.888	0.303
166	1.878	0.157	1.342	0.132	1.390	0.164	1.504	0.272
176	1.579	0.136	1.647	0.145	1.569	0.169	1.561	0.268
186	1.842	0.147	1.552	0.136	1.310	0.151	1.497	0.257
196	1.507	0.125	1.152	0.111	1.356	0.149	1.050	0.227
206	1.358	0.115	1.140	0.108	1.267	0.141	0.992	0.218
216	1.159	0.102	1.203	0.109	1.302	0.140	1.345	0.231
226	1.163	0.100	1.244	0.108	1.191	0.131	0.844	0.201
236	1.149	0.097	1.036	0.096	1.237	0.130	0.712	0.191
246	0.906	0.084	0.943	0.090	0.933	0.114	0.959	0.198
256	1.025	0.088	0.872	0.085	0.984	0.114	1.038	0.198
266	0.998	0.085	0.875	0.083	0.888	0.107	0.713	0.180
276	0.853	0.077	0.955	0.085	0.794	0.101	0.745	0.178
286	0.824	0.074	0.724	0.074	0.855	0.102	0.949	0.183
296	0.738	0.069	0.657	0.070	0.796	0.098	0.795	0.174
306	0.754	0.069	0.707	0.070	0.639	0.090	0.582	0.162
316	0.780	0.069	0.717	0.070	0.571	0.085	0.764	0.167
326	0.784	0.068	0.654	0.066	0.611	0.086	0.635	0.159
336	0.727	0.065	0.634	0.064	0.612	0.084	0.689	0.159
346	0.756	0.065	0.626	0.063	0.700	0.087	0.728	0.158
356	0.686	0.061	0.690	0.065	0.586	0.081	0.589	0.150

ℓ	$C_\ell^{\mathrm{Bin}\,1}$	$\sigma(C_\ell^1)$	$C_\ell^{\mathrm{Bin}\,2}$	$\sigma(C_\ell^2)$	$C_\ell^{\mathrm{Bin}\,3}$	$\sigma(C_\ell^3)$	$C_\ell^{\mathrm{Bin}\,4}$	$\sigma(C_\ell^4)$
366	0.667	0.060	0.519	0.057	0.589	0.080	0.553	0.147
376	0.681	0.059	0.632	0.061	0.485	0.075	0.532	0.144
386	0.611	0.056	0.517	0.056	0.569	0.077	0.432	0.139
396	0.617	0.055	0.525	0.055	0.599	0.077	0.307	0.132
406	0.561	0.053	0.559	0.056	0.540	0.074	0.592	0.141
416	0.427	0.047	0.489	0.053	0.510	0.072	0.545	0.138
426	0.625	0.054	0.515	0.053	0.511	0.071	0.257	0.126
436	0.558	0.051	0.509	0.052	0.502	0.070	0.376	0.128
446	0.521	0.049	0.459	0.050	0.332	0.063	0.541	0.133
456	0.539	0.049	0.459	0.049	0.482	0.068	0.398	0.126
466	0.488	0.047	0.447	0.048	0.446	0.066	0.419	0.126
476	0.438	0.045	0.453	0.048	0.403	0.064	0.425	0.125
486	0.429	0.044	0.364	0.044	0.419	0.064	0.153	0.114
496	0.493	0.045	0.356	0.044	0.330	0.060	0.410	0.122

3.4 Theoretical Power Spectrum

In order to deduce the cosmology to match the measured angular distribution above one must first have a method for connecting the underlying 3D mass distribution to C_ℓ. The outline description below simply follows the approach and notation of Huterer *et al.* (2001), Tegmark *et al.* (2002), Blake *et al.* (2007) and, most clearly, Padmanabhan *et al.* (2007).

One starts by noting that before the statistical decomposition of the density field into spherical harmonics in Section 3.3 the field was projected onto the plane of the sky. The same procedure is initially followed for the theoretical angular power spectrum with the 3D mass distribution δ projected along the line-of-sight δ^{2D}. This gives,

$$\delta^{2D} = i^l \int \frac{\mathrm{d}^3 k}{(2\pi)^3}\, \delta(\mathbf{k}) W_l(k), \tag{3.13}$$

where δ has also undergone a Fourier transformation. The resulting spherical Bessel function $j(kz)$ and the projection's weight $f(z)$ have been absorbed into the window function given by,

$$W_l(k) = \int f(z) j_l(kz)\, \mathrm{d}z. \tag{3.14}$$

The weight naturally depends on the normalised redshift distribution of the objects under consideration $\int n(z)\, \mathrm{d}z = 1$ and the linear growth factor $D(z)$,

$$f(z) = n(z) D(z) \Big(\frac{\mathrm{d}z}{\mathrm{d}x} \Big) \tag{3.15}$$

with the Jacobian relating to the radial comoving coordinate x. Using the definition of the power spectrum $P(k)$ for the 3D density field $\delta(\mathbf{k})$,

$$< \delta(\mathbf{k}) \delta^*(\mathbf{k}') >= (2\pi)^3 \delta^3(\mathbf{k} - \mathbf{k}') P(k) \tag{3.16}$$

the angular power spectrum C_ℓ is found and similarly defined to be,

$$C_\ell \equiv < \delta^{2D} \delta^{*2D} >= 4\pi \int \Delta^2(k) W_\ell^2(k) \frac{\mathrm{d}k}{k}. \tag{3.17}$$

The power spectrum has been recast into the dimensionless power spectrum defined in Equation 3.18. This power spectrum describes the variance of the matter field in logarithmic bands and so the equation for C_ℓ is subsequently a weighted integral of this quantity over logarithmic intervals ($\mathrm{d}k/k = \mathrm{d}\ln\, k$).

$$\Delta^2(k) \equiv \frac{4\pi k^3 P(k)}{(2\pi)^3} \tag{3.18}$$

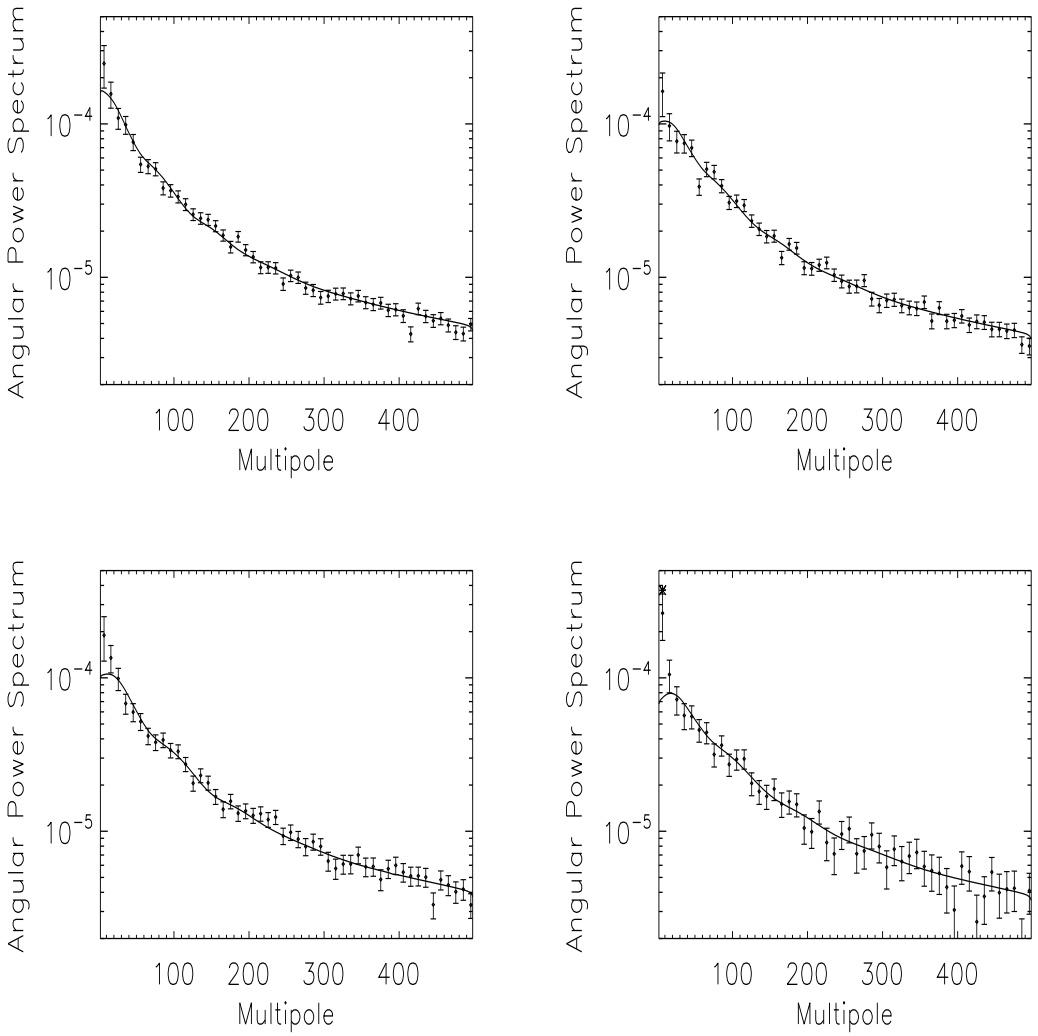

Figure 3.5: The measured Angular Power Spectra (C_ℓ) for the photometric SDSS MegaZ-LRG (DR7) population as presented in Table 3.1. The error bars correspond to those calculated with Equation 3.11 using the measured power spectrum. These include contributions from cosmic variance and shot noise, while accounting for the fraction of the sky surveyed. The solid line is evaluated for the the best fit parameters found in Section 3.5 using the Smith *et al.* (2003) non-linear prescription. The panels are: Bin 1 (top left), Bin 2 (top right), Bin 3 (bottom left) and Bin 4 (bottom right). In the furthest redshift bin an excess of power is observed over the largest scale. This was found similarly in DR4 but in that earlier case with an additional 40% more amplitude. The DR4 point is shown by the cross in the top left corner of the panel.

This can be further written in terms on the galaxy power spectrum with the addition of the linear galaxy bias b,

$$P_g(k) = b^2 P(k). \tag{3.19}$$

For $\ell \gtrsim 60$ the exact expression (Equation 3.17) can be simplified by the small angle approximation (e.g. Blake *et al.* (2007)),

$$C_\ell = b^2 \int P(k,z) \frac{n(z)^2}{x(z)^2} \Big(\frac{\mathrm{d}x}{\mathrm{d}z} \Big)^{-1} \mathrm{d}z. \tag{3.20}$$

On larger scales (smaller ℓ) this approximation becomes invalid as it seriously underestimates the power in C_ℓ. In fact, even the exact expression does not capture the shape of the true power spectrum below $\ell \sim 60$. The main reason is because of redshift space distortions, which lead to a significant boost in the angular power spectrum.

3.4.1 Redshift Space Distortions

The peculiar velocity of a galaxy will cause it to appear shifted along the line-of-sight in redshift coordinates (E.g. Sargent & Turner (1977), Peebles (1980), Kaiser (1987), Fisher *et al.* (1994), Heavens & Taylor (1995), Hamilton (1998) and Guzzo *et al.* (2008)). This is relative to the same galaxy carried along only by the background Hubble flow. That is, the redshift distance s of a body will be altered from its true distance r, by its own peculiar velocity $v \equiv \hat{\mathbf{r}}.\mathbf{v}$, radially from the observer,

$$s = r + \hat{\mathbf{r}}.\mathbf{v} \equiv r + v. \tag{3.21}$$

In redshift space this deviation alters the apparent clustering of galaxies and collectively the effect is said to be the result of *redshift space distortions*.

Over large scales the gravitational collapse of some spherically symmetric (in real space) overdensity will cause it to appear narrower along the line-of-sight (in the observed redshift space). As alluded to above this is because the matter nearest to the observer is redshift distorted towards the overdensity's centre, giving the impression that it is located closer to the origin. Matter on the other side of the structure will have projected peculiar velocities towards the observer such as to make them also appear closer to the origin. The object therefore seems flatter in the radial direction. Naturally the object is not deformed along the plane of the sky as the inferred redshift is not affected by its transverse motion.

Over smaller scales the peculiar velocity tends to increase through infall. In addition to this, the velocity is larger relative to the distance from the test matter to the centre of the structure. In redshift space the distorted object subsequently becomes ever more flat. Eventually, over sufficiently small scales or within a viralised object, the peculiar velocity will be high enough such that visible objects appear on the *other* side of the overdensity. This gives rise to a tendency of long, thin, column-like structures to appear radially in a galaxy survey. These particular objects, resulting from the redshift space distortions, are grandiosely referred to as ***fingers-of-God***.

To include redshift space distortions in the angular power spectrum the window function $W_\ell(k)$ in Equation 3.17 is modified such that $W_\ell(k) \rightarrow W_\ell(k) + W_\ell^R(k)$ (E.g. Fisher *et al.* (1994) and Padmanabhan *et al.* (2007)). This is a result of writing the weight properly as a function of redshift distance $f(s)$ and assuming that the magnitude of the peculiar velocities are small. This is because with this assumption one can perform a Taylor expansion of the weight,

$$f(s) \approx f(r) + \frac{\mathrm{d}f}{\mathrm{d}r}(\mathbf{v}(r\hat{\mathbf{r}}).\hat{\mathbf{r}}). \tag{3.22}$$

The subsequent window function (remembering Equation 3.14) therefore now has the two components, $W_\ell(k)+W_\ell^R(k)$, with the latter currently a function of $\mathbf{v}$ from above. The Fourier transform of $\mathbf{v}$ is in turn related to the density perturbation through the linear continuity equation,

$$\mathbf{v}(\mathbf{k}) = -i\beta\delta_g(\mathbf{k})\frac{\mathbf{k}}{k^2} \tag{3.23}$$

with the constant of proportionality β known as the redshift distortion parameter. This is commonly approximated by $\beta \approx \Omega_m^{0.6}/b$. Substituting this into the expression for the window function and Legendre transforming (see Padmanabhan *et al.* (2007) for further details) eventually leaves one with,

$$W_l^R(k) = \beta \int f(y)\Big[\frac{(2l^2+2l-1)}{(2l+3)(2l-1)}j_l(ky) - \frac{l(l-1)}{(2l-1)(2l+1)}j_{l-2}(ky) - \frac{(l+1)(l+2)}{(2l+1)(1l+3)}j_{l+2}(ky)\Big]\,\mathrm{d}y. \tag{3.24}$$

For large values of ℓ the integral within Equation 3.24 tends to zero and so the total window function is reduced to the previous form. In this way, even with the inclusion of redshift distortions, the small angle approximation is an efficient and accurate estimate of the angular power spectrum at small scales. The behaviour of this approximation and the effects of the redshift space distortions on the power spectrum are illustrated further in Figure 3.6.

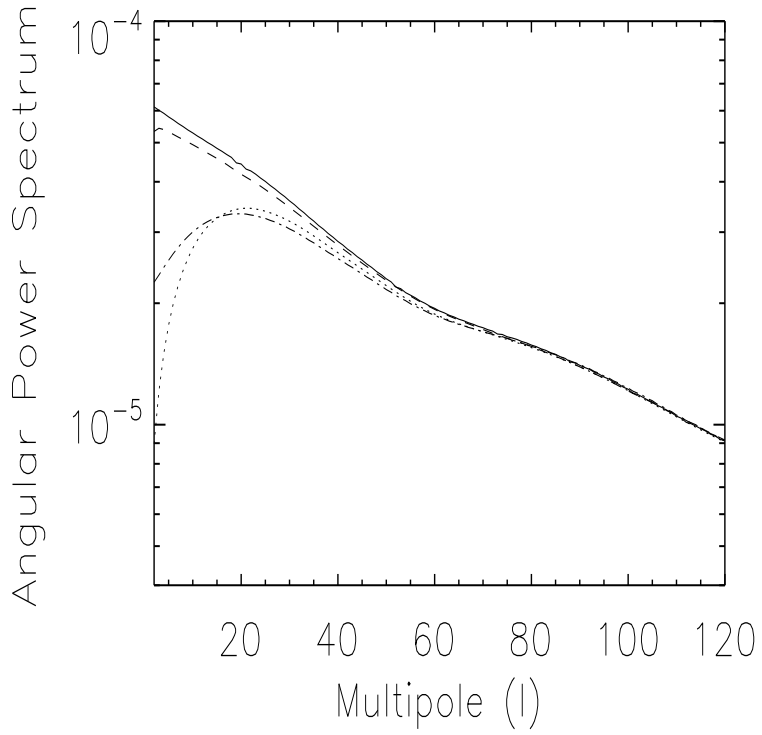

Figure 3.6: A range of theoretical angular power spectra for the lowest redshift bin used in this survey ($0.45 \leq z \leq 0.5$). This includes the small angle approximation (Equation 3.20; dotted line), the exact expression with no redshift space distortions (Equation 3.17; dot-dashed line), the exact expression including redshift space distortions (Equation 3.24; solid line) and also with the addition of the partial sky mixing matrix convolution (Section 3.4.2; Equation 3.26; dashed line). The input parameters are taken to be: $\Omega_b = 0.05$, $\Omega_m = 0.3$, $h = 0.75$, $\sigma_8 = 0.8$ and $b = 1$ for all four profiles. The small angle approximation is used for multipole scales $\ell \gtrsim 60$ for faster computation in the cosmological analyses.

For an analysis between redshift bins the above outline can be easily extended. The cross correlation of two distinct projected mass distributions $< \delta_i^{2D} \delta_j^{*2D} >$ leads simply to a slight modification in Equation 3.17; with the window function for each bin treated separately,

$$C_\ell^{ij} = 4\pi \int \Delta^2(k) W_i(k) W_j(k) \frac{\mathrm{d}k}{k}. \tag{3.25}$$

3.4.2 The Mixing Matrix: Partial Sky Convolution

An additional alteration in the shape of C_ℓ at large scales is to account for the partial sky coverage of the real survey. As stated in Section 3.3 this correlates the usually orthonormal spherical harmonic coefficients, effectively creating a dependency on neighbouring scales. The net effect

is to slightly suppress the shape of the power spectrum C_ℓ below $\ell \sim 60$ as seen in Figure 3.6. The effect can be calculated by convolving with the *mixing matrix* $R_{l,l'}$ (Hauser & Peebles (1973), Hivon *et al.* (2002) and Blake *et al.* (2007)),

$$C_l = \sum_{l'} R_{l,l'} C_{l'}. \tag{3.26}$$

The mixing matrix can be pre-calculated and depends purely on the survey geometry. It is described by,

$$R_{l,l'} = \frac{2l'+1}{4\pi} \sum_{l''} (2l''+1) W_{l''} \begin{pmatrix} l & l' & l'' \\ 0 & 0 & 0 \end{pmatrix}^2 \tag{3.27}$$

with W_l, the power spectrum of the survey's mask, calculated using Equation 3.28. The 2×3 matrix within $R_{l,l'}$ is a Wigner coefficient. For a full sky survey the convolution should have no effect on the angular power spectrum and accordingly the mixing matrix reduces to the identity matrix $R_{\ell,\ell'} \rightarrow \delta_{\ell\ell'}$.

$$W_l = \frac{\sum_{m=-l}^{l} |I_{l,m}|^2}{2l+1} \tag{3.28}$$

For the DR7 survey geometry the mixing matrix at a given ℓ is seen to be heavily peaked as a function of ℓ' about that multipole value. The profile rapidly falls within the chosen $\Delta\ell$ bin, implying only a small correlation between the ℓ bands is introduced by the mask. This is illustrated in Figure 3.7 for two different multipole scales.

3.5 The Cosmological Analysis

I calculate $P(k)$ for the angular power spectrum C_ℓ using CAMB (Lewis *et al.* 2000). The HALOFIT fitting function (Smith *et al.* 2003) is then used to map the linear power spectrum into the non-linear regime (large ℓ). To increase the speed of calculation I use the small angle approximation (Equation 3.20) for $\ell \gtrsim 60$ and the full and exact window function, including redshift distortions (Equation 3.17 and Equation 3.24), otherwise. This is all convolved with the mixing matrix $R_{\ell,\ell'}$ as described in the previous subsection.

3.5.1 The Redshift Distribution

The model redshift distribution $n(z)$ in each redshift slice is taken to be the form of the spectroscopic 2SLAQ evaluation set, with the same LRG selection criteria, in that *photometric* bin.

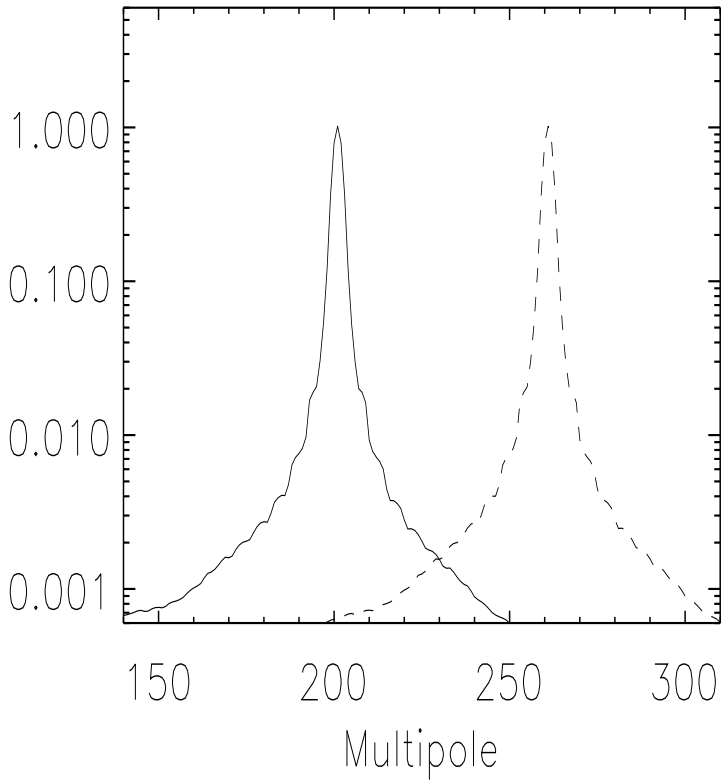

Figure 3.7: A slice through the mixing matrix $R_{\ell,\ell'}$ is plotted for two fixed multipole values given by $\ell' = 200$ (solid curve) and $\ell' = 260$ (dashed curve). The amplitude of the matrix peaks at those fixed values and decays rapidly within the size of a $\Delta\ell$ band. This establishes how little correlation is induced by the survey's window function. Furthermore, the behaviour is observed similarly across all angular scales. Note that the matrix profiles have been normalised to unity at their peaks and the vertical axis is in logarithmic space.

This is possible because the 2SLAQ evaluation objects have both a spectroscopic and photometric redshift. These $n(z)$ were fit with a Gaussian function given by,

$$n(z) \propto \exp\Big[-\frac{(z-\mu)^2}{2\sigma^2}\Big]. \tag{3.29}$$

For the cosmological analyses μ and σ are fixed to their best fit values in each bin. I address this assumption as a potential calibration systematic in Section 3.5.3 and Section 3.6.2. The best fit quantities are summarised in Table 3.2 for the current (DR7) and previous data release (DR4). In addition, the Gaussian fits to the spectroscopic distributions are illustrated in Figure 3.8. The vertical axis represents the number of spectroscopic 2SLAQ objects within a small histogram band (δz).

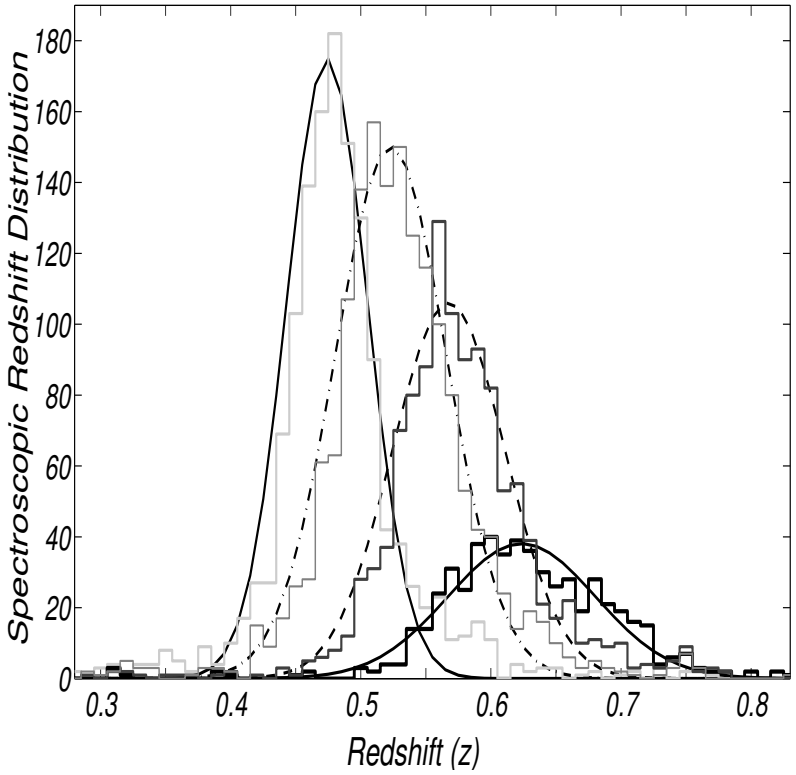

Figure 3.8: The spectroscopic redshift distribution $n(z)$ for each photometric bin in DR7 is illustrated as a series of histograms. Each redshift distribution is fit by a Gaussian function $\exp[-(z-\mu)^2/2\sigma^2]$, where μ and σ are specified in Table 3.2. The associated Gaussian fits are represented by the smooth and continuous curves.

3.5.2 Parameter Constraints: The Single Redshift Bins

I start by undertaking a cosmological analysis in each of the four separate redshift bins described previously. A conservative choice of parameters is studied such that I can test for consistency against the previous MegaZ LRG analysis (Blake *et al.* 2007). I therefore vary four quantities: $f_b = \Omega_b/\Omega_m$, Ω_m, σ_8 and b; the baryon-to-matter density ratio, the matter density, the normalisation of the power spectrum and the galaxy bias, respectively. The bias is assumed to be scale independent ($b \neq b(k)$). Along with the earlier MegaZ paper the Hubble constant is fixed to $H_0 = 75$ km s^{-1} Mpc^{-1} and the spectral index to $n_s = 1$. Both σ_8 and the bias control the amplitude of the power spectrum and are thus degenerate with one another. A flat prior is therefore enforced on the former such that $0.7 \leq \sigma_8 \leq 1.1$. The Universe is assumed to be flat throughout with the equation of state fixed to $w_0 = -1$. Again, to compare directly to the first MegaZ analysis I use all the multipole values up to $\ell = 300$. This is the scale at which the non-linear corrections become

μ	σ	Redshift Bin	Photometric Range
0.474	0.035	Bin 1	$0.45 < z < 0.50$
0.525	0.042	Bin 2	$0.50 < z < 0.55$
0.572	0.044	Bin 3	$0.55 < z < 0.60$
0.625	0.053	Bin 4	$0.60 < z < 0.65$
0.474	0.0312	Bin 1	$0.45 < z < 0.50$
0.523	0.0428	Bin 2	$0.50 < z < 0.55$
0.568	0.0433	Bin 3	$0.55 < z < 0.60$
0.624	0.0568	Bin 4	$0.60 < z < 0.65$

Table 3.2: The mean μ and deviation σ of the Gaussian fitting to the spectroscopic redshift distribution $n(z)$ in each photometric bin. The top segment is the fit corresponding to the previous DR4 release as found in Blake *et al.* (2007) and similarly in Collister *et al.* (2007). The bottom segment is for the new DR7 release. This is highlighted in Figure 3.8.

increasingly significant. For the parameter exploration I use the publicly available COSMOMC package (Lewis & Bridle 2002).

3.5.2.1 Data Release 4

To test for consistency I first perform the cosmological analysis on the previous DR4 angular power spectra, which are then compared to those found in Blake *et al.* (2007). I find a remarkably similar agreement to the previous study in the first three redshift bins over a redshift range $0.45 \leq z \leq 0.6$. However, for the final and furthest redshift bin ($0.6 < z \leq 0.65$) a large discrepancy is discovered when all angular scales to $l_{\max} = 300$ are utilised. It is interesting that for this particular redshift bin a large excess of power was detected in the measurement of the C_ℓ on the largest angular scale ($\ell = 6$ band). Even though this is approximately at the turnover scale of the power spectrum, where one might expect the power to start decreasing, the excess was found to be just over 1σ from the best fit C_ℓ profile. One might not therefore expect this anomalous point to cause any significant alteration in the cosmological analysis. It is important to remember, however, that the error on this data point, assigned in the previous study, was the error given by the Gaussian expression (Equation 3.11) using the *data* value for the C_ℓ. As the magnitude of this point is so much larger than the C_ℓ corresponding to a smooth fit through the other data points, the associated data error bar is made to appear much larger also. In the parameter estimation performed here

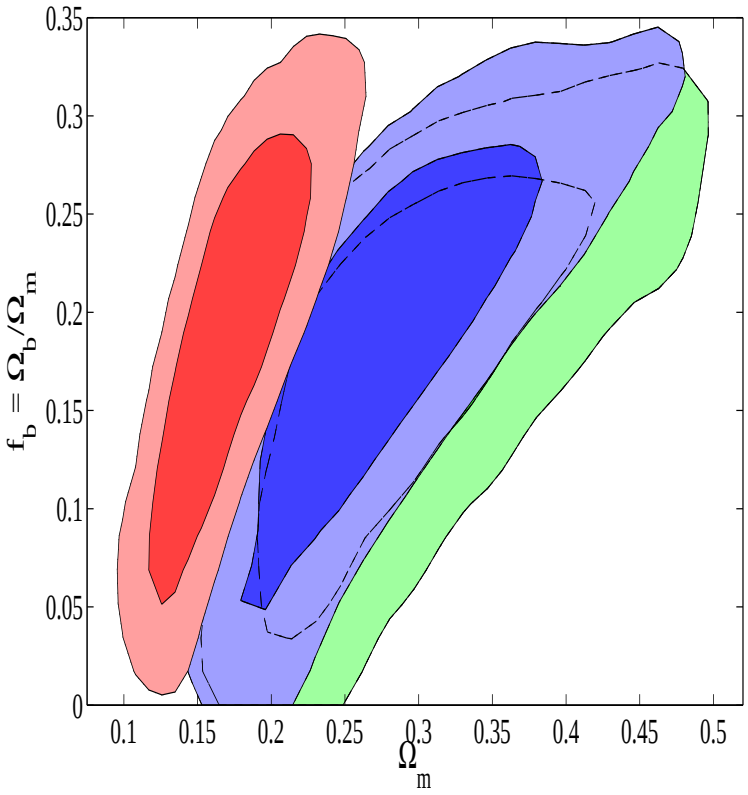

Figure 3.9: Constraints on the MegaZ LRG (DR4) highest redshift bin ($0.6 < z \leq 0.65$) using model errors (red contour), data errors (green contour) and model errors with the lowest multipole removed (blue contour). The last analysis gives constraints consistent with the previous Blake *et al.* (2007) study. Otherwise the excess power on large scales acts to alter the constraints; in the process favouring a much lower matter density.

and in Blake *et al.* (2007) the error and therefore covariance matrix are evaluated using the *model* errors. This is because in a Bayesian analysis one implicitly assumes the model to be true. Any model spectrum attempting to fit the other data points will assign a theoretical value at the largest angular scales much lower than that measured and subsequently the error bar will be much smaller. The excess power is therefore a much poorer fit than is first thought. In order to try and replicate the original DR4 constraint for this furthest bin I remove this irregular point. In addition, I also follow an analysis using the data errors in the covariance matrix while *including* the excess power quantity. The resulting contours are shown in Figure 3.9.

The plot highlights that the excess power at low multipoles is indeed significant, with the inclusion of the lowest point dragging the constraint to much lower values of Ω_m (red contour). Also, the figure reiterates the notion that the data error (green contour) acts to buffer against this anomaly given that the contour is similar to the model analysis that excludes the excess power

(blue contour). When fitting with the model errors and no excess power I find the constraints to be identical to those in Blake *et al.* (2007) and also consistent with the three other redshift bins. These are all plotted in Figure 3.10 along with analyses using the data error in each bin.

3.5.2.2 Data Release 7

The angular power spectrum for the last redshift bin was measured for DR7 in Section 3.3.2 and shown in Figure 3.5. Once again an excess of power is detected at this high redshift. However, there seems to be a slight hint of an ease in tension as the magnitude of the DR4 point is found to be 40% higher than the newly measured DR7 value. I therefore undertake a cosmological run for this bin using the excess power point and also with it removed to test the effects. I find that despite the more recent decrement in the C_ℓ on these large scales the inclusion of the quantity still significantly affects the parameter constraints found with the bin. This is illustrated clearly in Figure 3.11. Again, with this point excluded the fourth redshift bin is found to be consistent with the other three slices.

I therefore choose to continue the galaxy clustering study by excluding the anomalous excess power in the $\ell = 6$ band for the furthest redshift bin. It is intriguing that excess power has also been detected in Padmanabhan *et al.* (2007) and, most recently, in the study of the maxBCG cluster power spectrum by Huetsi (2009). I discuss the possible origin of this signal further in Section 3.6.1.

For the new DR7 release the associated constraints for every redshift bin are displayed as the yellow contours in Figure 3.12 and Figure 3.13. Also included, for direct comparison and consistency, is my analysis of the previous SDSS release (DR4) as described above. This is illustrated in each panel by the blue contours.

The increase in survey area and thus galaxy number does not seem to particularly aid the joint constraint of Ω_m and f_b along the direction of their mutual degeneracy, except perhaps in the highest redshift bin. Perpendicular to the degeneracy, however, there is a slight restriction in the parameter space. Also, the new DR7 sample predicts a modest shift in the value of the bias in each bin. Even though this is much less than a significance level it could reflect the fact that the continually updated SDSS pipeline gives rise to different photometry values even for the same objects as before. In this way galaxies near the selection criteria (as discussed in Section 3.2.1) might be scattered into/out of the new analysis, resulting in a slightly different galaxy sample. This can be a moderate effect for LRGs and is discussed, along with other systematics that might affect the samples, also in Section 3.6. Irrespective of the changes inherent in the samples there is

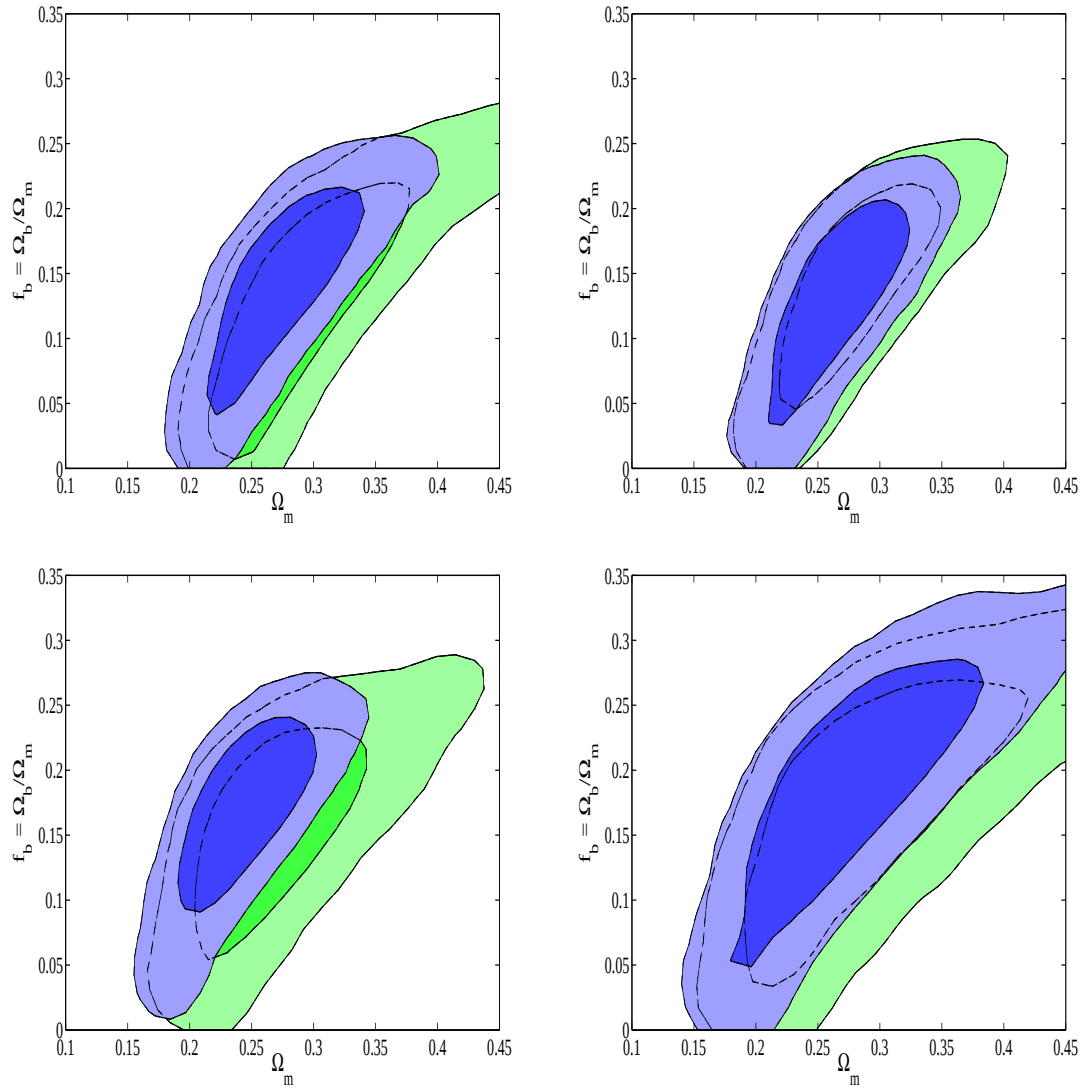

Figure 3.10: MegaZ LRG DR4 constraints on $f_b = \Omega_b/\Omega_m$ and Ω_m for four redshift bins using model errors (blue contours) and data errors (green contours) in the covariance matrix. b and σ_8 have been marginalised over and H_0 and n_s are fixed to 75 km s^{-1} Mpc^{-1} and 1, respectively. This release has been analysed to test for consistency with Blake *et al.* (2007). All the bins are remarkably compatible except for the fourth redshift bin. Here an excess of power at the lowest multipole must be removed for an agreement (see text). The panels are: Bin 1 (top left), Bin 2 (top right), Bin 3 (bottom left) and Bin 4 (bottom right). The inner and outer contours are the 68% and 95% confidence levels, respectively.

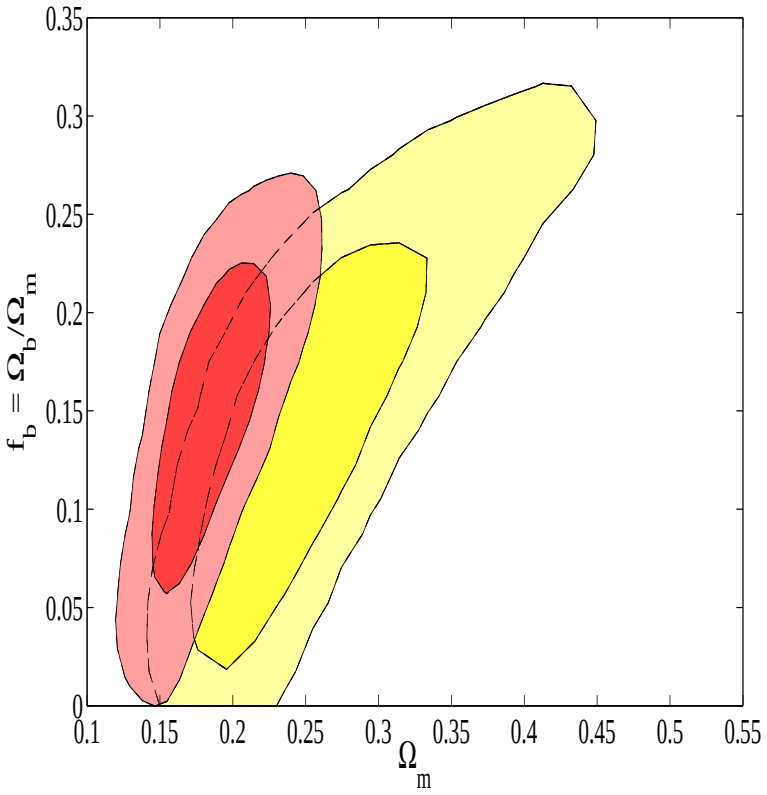

Figure 3.11: Constraints on the MegaZ LRG (DR7) highest redshift bin ($0.6 < z \leq 0.65$) using model errors and all data points to $\ell_{\rm max} = 300$ (red contour) and model errors with the lowest multipole band removed (yellow contour). Despite a decrease in the excess power in DR7, relative to the previous DR4 release, the observed shift in constraints above show the contribution from the anomalous low band to still be significant. The yellow contour analysis is consistent with the other three redshift bins (Figures 3.12 and 3.13) and as such this point is removed from all subsequent analyses as before.

a comfortable consistency between the two releases and all four bins within the releases. All the inferred constraints are summarised in Table 3.3.

When obtaining f_b, Ω_m or b all the other parameters are marginalised over. The bias is subsequently seen to enlarge with an increase in redshift. This is partially due to the observed galaxies in the furthest redshift bin necessarily being more luminous, resulting from the pseudo-magnitude limit in the survey. They are therefore observed to be more highly clustered (Blake *et al.* 2007).

3.5.3 Parameter Constraints: The Combined Redshift Bins

I now combine the data from each of the four redshift bins. These bins are not independent, however, as photometric redshift errors act to disperse galaxies throughout the bins. Another way of noting this is to observe that the Gaussian redshift distributions, as seen in Figure 3.8,

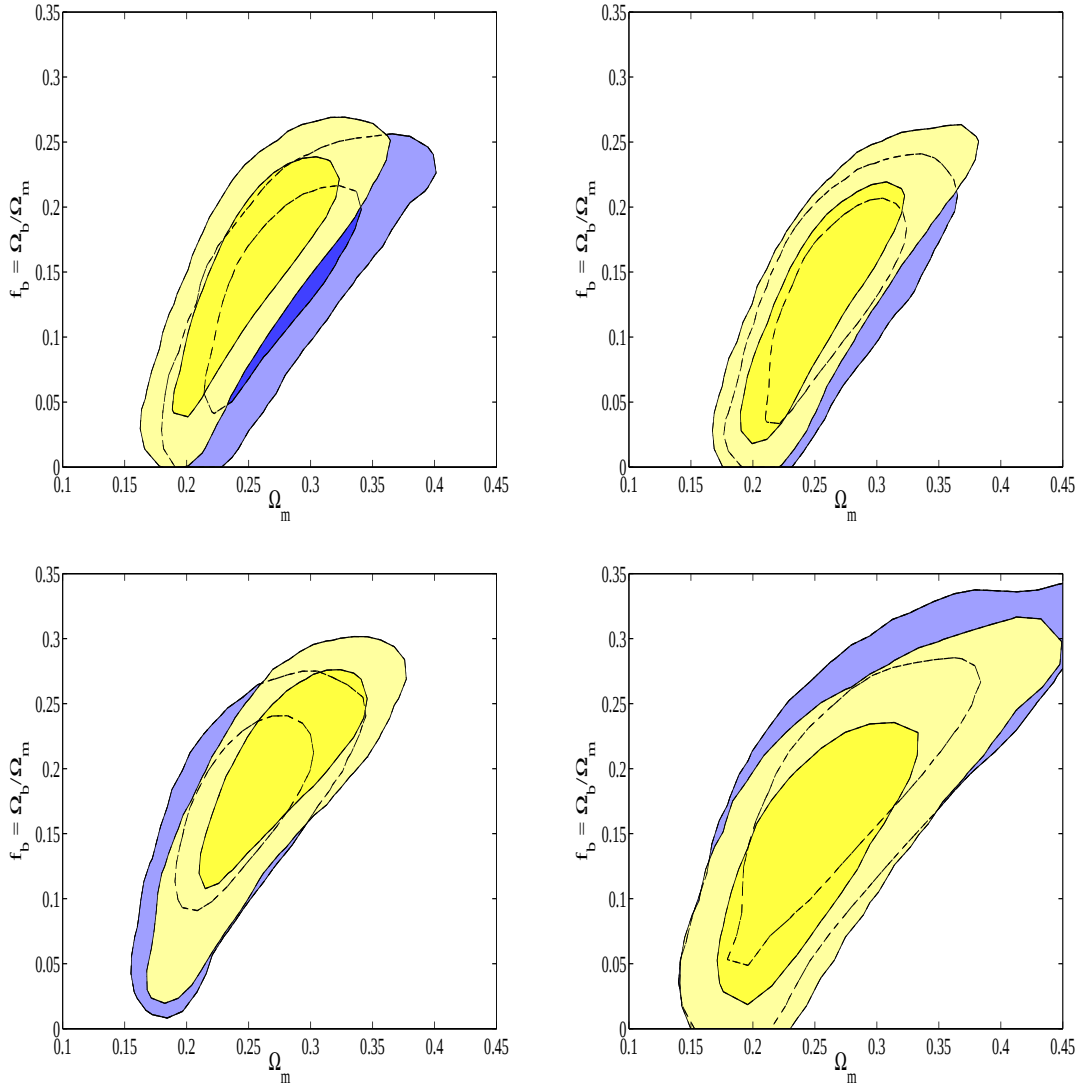

Figure 3.12: MegaZ LRG DR7 constraints on $f_b = \Omega_b/\Omega_m$ and Ω_m for four redshift bins (yellow contours). b and σ_8 have been marginalised over and H_0 and n_s are fixed to 75 km s^{-1} Mpc^{-1} and 1, respectively. The previous MegaZ LRG DR4 release has been reevaluated to test against Blake *et al.* (2007) (blue contours). The panels are: Bin 1 (top left), Bin 2 (top right), Bin 3 (bottom left) and Bin 4 (bottom right). The inner and outer contours are the 68% and 95% confidence levels, respectively.

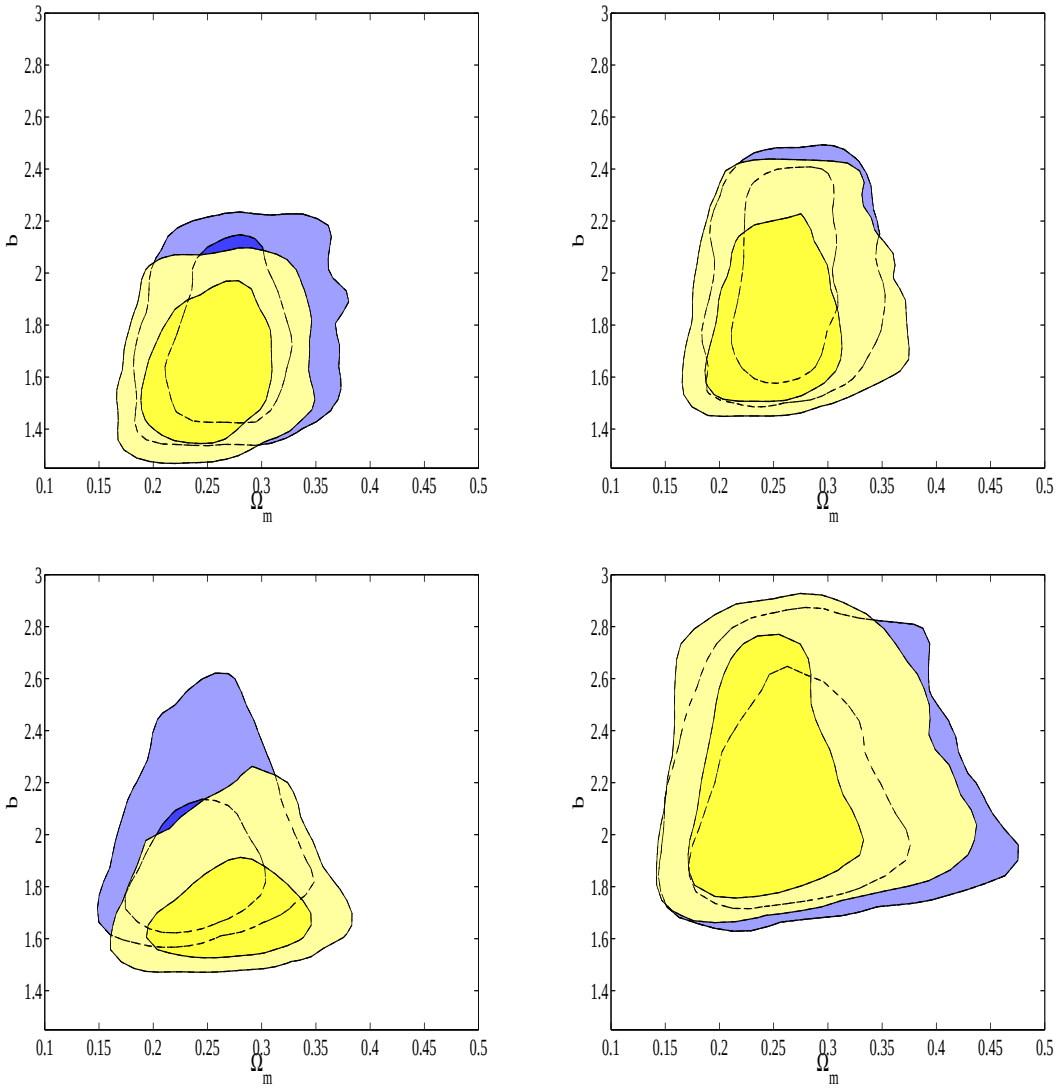

Figure 3.13: MegaZ LRG DR7 constraints on Ω_m and the bias b for four redshift bins (yellow contours). $f_b = \Omega_b/\Omega_m$ and σ_8 have been marginalised over and H_0 and n_s are fixed to 75 km s^{-1} Mpc^{-1} and 1, respectively. The previous MegaZ LRG DR4 release has been reevaluated to test against Blake *et al.* (2007) (blue contours). The panels are: Bin 1 (top left), Bin 2 (top right), Bin 3 (bottom left) and Bin 4 (bottom right). The inner and outer contours are the 68% and 95% confidence levels, respectively.

f_b	Ω_m	Redshift Slice	Photometric Range
0.152 ± 0.055	0.271 ± 0.0430	Bin 1 (DR4)	$0.45 \leq z < 0.5$
0.139 ± 0.053	0.262 ± 0.040	Bin 2 (DR4)	$0.5 \leq z < 0.55$
0.175 ± 0.051	0.240 ± 0.038	Bin 3 (DR4)	$0.55 \leq z < 0.6$
0.199 ± 0.072	0.268 ± 0.0655	Bin 4 (DR4)	$0.6 \leq z < 0.65$
0.166 ± 0.066	0.253 ± 0.049	Bin 1 (DR7)	$0.45 \leq z < 0.5$
0.136 ± 0.069	0.251 ± 0.051	Bin 2 (DR7)	$0.5 \leq z < 0.55$
0.206 ± 0.062	0.274 ± 0.052	Bin 3 (DR7)	$0.55 \leq z < 0.6$
0.146 ± 0.076	0.248 ± 0.067	Bin 4 (DR7)	$0.6 \leq z < 0.65$
0.163 ± 0.0373	0.263 ± 0.0270	All bins (DR4)	$0.45 \leq z \leq 0.65$
0.173 ± 0.0462	0.260 ± 0.0351	All bins (DR7)	$0.45 \leq z \leq 0.65$
0.163 ± 0.0480	0.234 ± 0.0309	All bins (DR7)*	$0.45 \leq z \leq 0.65$

Table 3.3: The marginalised mean values obtained from the analyses of the galaxy clustering angular power spectra C_ℓ. $f_b = \Omega_b/\Omega_m$, Ω_m, σ_8 and b are varied for each single bin run. The values for the previous release (DR4) were recalculated and shown to be entirely consistent with Blake *et al.* (2007). In the last three runs all the bins were combined together using the full covariance matrix and a bias parameter for each bin (b_1, b_2, b_3, b_4). *In this analysis the lowest multipole band in the highest redshift slice is included.

overlap for each bin. I therefore use the full covariance matrix in the analysis. The variance element corresponding to the same redshift bin (e.g. between C_ℓ^i and C_ℓ^i) is given by the square of Equation 3.11 using the *theoretical* expression for C_ℓ as before. The covariance elements between different bins are described by,

$$\mathrm{Cov}(C_\ell^i, C_\ell^j) = \frac{2}{f_{\mathrm{sky}}(2\ell+1)}\left(C_\ell^{i,j}\right)^2. \tag{3.30}$$

In this way the whole matrix allows for the covariance between all bin combinations but not multipole bands. This is a good approximation given our earlier discussion of the highly peaked mixing matrix $R_{l,l'}$ (Figure 3.7).

I include a redshift dependence in the galaxy bias, to the extent that each redshift bin is assigned a separate bias parameter (b_1, b_2, b_3 and b_4) in the cosmological run.

The marginalised best fit parameters are again listed in Table 3.3, with the corresponding contours displayed in Figure 3.14. The updated DR7 release (yellow contours) demonstrate consistent

constraints with the previous DR4 study (blue contours). For the four bias parameters (b_1, b_2, b_3 and b_4) this analysis gives noticeably tighter bounds. As found with the individual bins the contours can be seen to visibly rise along the bias axis with an increase in redshift. Moreover, the four bias quantities are seen to be relatively high implying that the LRGs strongly trace the underlying mass distribution.

Again, due to the degeneracy between f_b and Ω_m the new data does not reduce the contour or resultant constraints on either parameter. In fact, despite a minor narrowing of the degeneracy's width the distribution is seen to slightly elongate. This could be the consequence of having a different fixed best fit Gaussian redshift distribution (μ, σ) for each of the four redshift bins compared to DR4. In this way each analysis might represent a different slice through the parameter hyper-volume for which the matter densities have a different local curvature. Furthermore, these parameters could be naturally degenerate with the other parameters, such as the matter density, given that a displacement in μ alters the effective comoving distance to the sources and σ alters the degree of predicted anisotropy.

Additional tests on the redshift distribution are needed to probe this potential calibration and, as well as a suggestion for future work, is discussed further in Section 3.6. It is worth reiterating, however, that the constraints are similar and have been analysed using the redshift distribution that most corresponds to their spectroscopic-photometric bins with the most recent SDSS photometry.

Finally, in the top left hand panel I include a calculation of the combined bins with (red contour) and without (all yellow contours) the lowest multipole band measured in redshift bin 4. As with the individual bin the excess power is seen to systematically displace the marginalised distribution and once again is removed from all other constraints.

3.5.3.1 Other Studies

In as much as other analyses can be compared, with varying parameter choices and assumptions, these results are concordant but competitive with respect to recent studies of SDSS galaxy clustering. These often include alternate or earlier data sets and at different redshifts. This includes Padmanabhan *et al.* (2007), an analogous *photometric* study to Blake *et al.* (2007), that instead reconstructs the 3D real space power spectrum. Apart from these two works, studies have tended to focus on the spectroscopic samples, such as Tegmark *et al.* (2004), Tegmark *et al.* (2006) (DR4), Cabré & Gaztañaga (2009) and Sanchez *et al.* (2009) (DR6) (with a measurement of the correlation function) and most recently Reid *et al.* (2009) (DR7). A more direct numerical comparison is made with this latest release in Section 3.7.

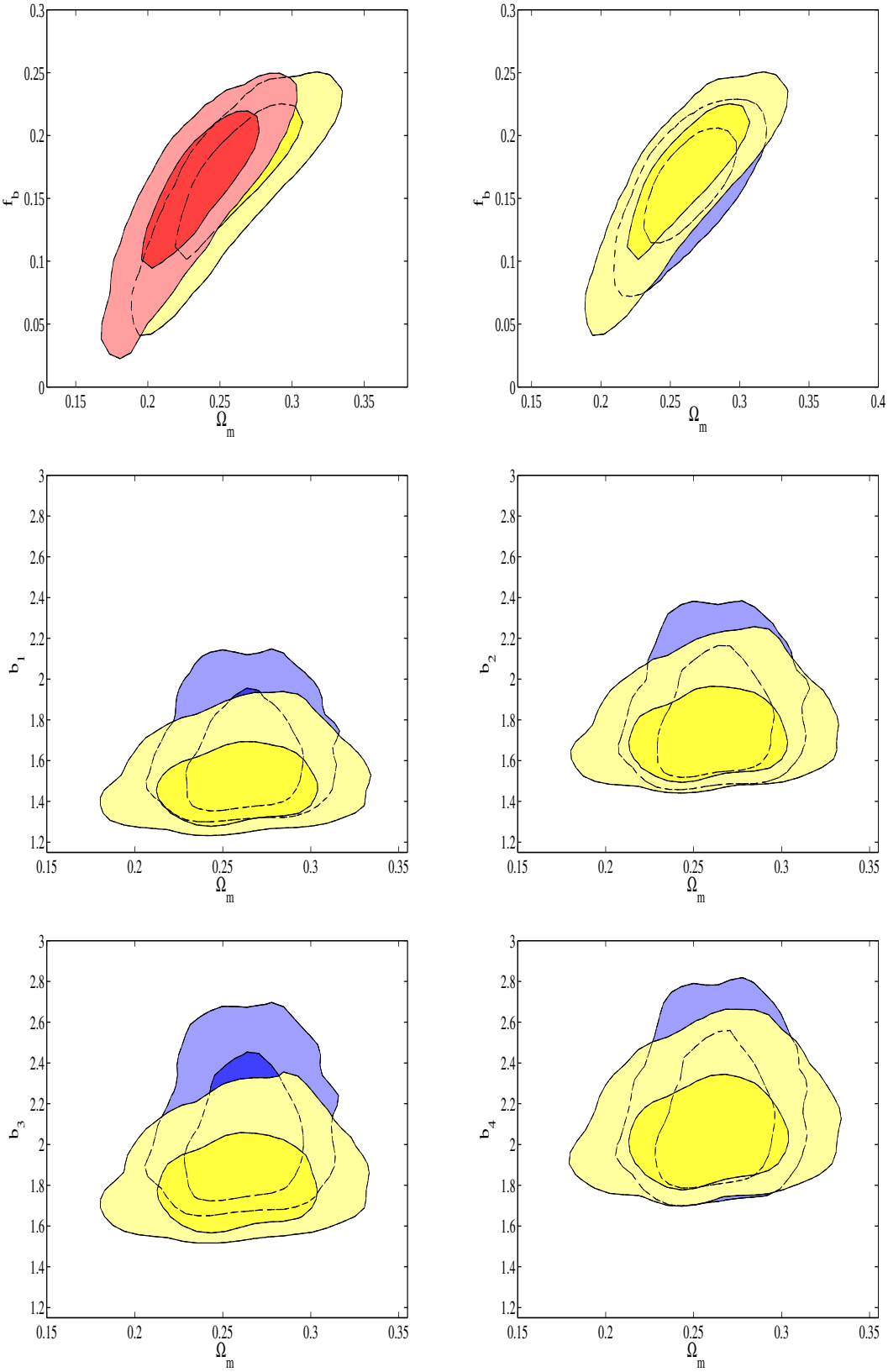

Figure 3.14: Cosmological constraints given by the combination of four redshift bins between $0.45 < z < 0.65$. The earlier DR4 (Blake *et al.* 2007) analysis, which has been recalculated as a consistency check, is illustrated by the series of blue contours. The DR7 bounds are displayed by the yellow contours. The red 2D distribution in the top left panel shows the systematic shift induced by including the excess power measured over large scales in the highest redshift bin, whereas the normal yellow contours have this anomalous point removed. The bottom four panels demonstrate the additional constraining power of DR7 on the bias where b_1, b_2, b_3 and b_4 are the bias parameters in sequentially higher redshift bins.

Furthermore, the SDSS galaxies have permitted measurements of the Baryon Acoustic Oscillations with Percival *et al.* (2007), Gaztanaga *et al.* (2008) and Percival *et al.* (2009).

3.6 Systematics and Further Tests

The earlier MegaZ release (Blake *et al.* 2007) performed a series of systematic tests based naturally on examining variations across the plane of the sky. This included astronomical seeing, overlapping survey stripes, regions of low galactic latitude, varying completeness and variations in star-galaxy separation. The aforementioned paper also highlighted the impact of photometric errors for LRGs given their location on the galaxy luminosity function. This function $\phi(M)$ describes the *number* of galaxies that have absolute magnitudes M within an interval $M + \mathrm{d}M$. The position of the galaxy sample under consideration is one where the gradient of this function is high. Therefore, any slight systematic shift in M will impart a large systematic shift in the number of galaxies. If this systematic shift were some function of sky position, for example, it could contribute significantly (and artificially) to the galaxy clustering signal at that scale. All of the separate tests run for DR4 were found to produce no significant change in the galaxy clustering data.

Even though I have demonstrated the impact of the large scale excess power on the cosmological parameters there has yet been no solution to the cause of the effect in the literature. Considering this and also the caveat discussed above I therefore continue with a discussion of potential systematics in the analysis and consider and suggest further tests for the work.

3.6.1 Excess Power

With the earlier Blake *et al.* (2007) and Padmanabhan *et al.* (2007) studies it might be tempting to assume that the excess power is related to an analysis using two disconnected angular selection functions. This is because for these two papers the power spectra were estimated using both a separate northern and southern region of galaxies. This could introduce a difficulty in the relative photometric calibration between the bands, for example. DR7, on the other hand, presents a fully contigious region for C_ℓ estimation. However, despite a diminished amplitude in the excess of the power it still persists and has a significant effect on the cosmological parameters. This is approximately consistent with the preliminary tests performed in each DR4 paper–in that the two separate regions do not appear to significantly shift the C_ℓs. Irrespective of this, the fully connected region and updated SDSS pipeline are expected to produce more robust photometric estimates for

DR7.

Alternatively, the origin of this data point could be the result of something more physical and radical, such as a dark energy fluid with low sound speed that induces further clustering. This would suggest that dark energy is not some form of cosmological constant. Or, it could be the first evidence for some large scale inhomogeneity or over density that opposes our very core assumptions in cosmology: the cosmological principle. Another possibility is a severe change (increase) in the galaxy biasing process over these large scales or even a consequence of cosmic variance. While these are interesting and potential avenues for future work there also remain some more mundane, but pernicious, systematics; such as the effects of extinction and the extrapolation of the 2SLAQ training set with sky position.

3.6.2 Redshift Bin Cross Correlations

A useful test of any known or unknown systematic present in the study is the cross angular power spectra (Equation 3.25). A signal in these quantities should be the result of photometric errors scattering galaxies between bins as *predicted* by the spectroscopic redshift distribution defined earlier and the best fit auto-correlation functions. Any significant alteration in the measurement relative to the theoretical $C_\ell^{i,j}$ could indicate an additional systematic in the photometry, extinction correction or an ill-calibrated redshift distribution, for example.

I measure the cross power spectra in each of the six cross-bin combinations (note that $C_\ell^{i,j} = C_\ell^{j,i}$) in multipole bands of $\Delta\ell = 10$ up until $l_{\max} = 500$ as performed previously for the auto power spectra. The observed values are listed in Table 3.4 and Table 3.5 and are plotted in Figure 3.15 along with their associated error bars. The solid lines in these plots show the predicted theoretical spectra using the best fit values from the DR7 combined bins run and the corresponding Gaussian redshift distributions. For nearby bins there is excellent agreement in the values. However, the anticipated cross spectrum between bin 1 and bin 4 (middle left panel) suffers from a lack of amplitude and consequently does not fit the mean profile of the data well. This is most likely the result of the Gaussian redshift distributions being weak fits to the spectroscopic profiles far from the mean of the distribution. As can be seen in Figure 3.8 the Gaussian underestimates the number of galaxies far from the bin centre. This will lead to an under prediction in the cross term. Less dramatic is the apparent marginal overestimation of the cross spectrum between bins 2 and 3 (middle right panel). This might be the result of the Gaussian smoothing adding slightly more galaxies in the overlap region between the redshift slices.

To test this hypothesis I interpolated the spectroscopic distribution with a spline through the

$n(z)$ histogram. Then using this more 'realistic' profile I re-evaluated the theoretical cross power spectra in the bin. These are shown as the dashed lines in the cross spectrum panels. For the most physically separated bins (1 and 4) this is seen to give, as predicted, a significant boost in amplitude and a better fit to the data points. It is worth noting the presence of the log scale in the plot which acts to disguise the 40% increase in amplitude. Once again this hints that the use of a fixed μ and σ in a Gaussian is not optimal with regards to the data. When I calculated the cross power spectrum for the DR4 release it was intriguing to see that the quoted best fit Gaussian was a much worse fit than is seen in DR7. In this case the interpolated redshift, for that catalogue, gave rise to $\sim 100\%$ boost in power. Meanwhile, back in DR7, the splined distribution is also seen to give a slightly better fit between bins 2 and 3 with a modest decrement in power (dashed line to solid line–middle right panel). Finally, with the redshift function now accounted for in the cross correlation measurement it is interesting to see that in several of the bins there does exist an excess of power. This could point towards a residual systematic in the catalogue.

While beyond the scope of this work it would be interesting to see the effect on the inferred constraints in using the spline interpolated redshift distribution in the cosmological analysis. However, it is important to note that this could introduce errors of its own. For example, it might propagate inherent fluctuations in the profile, that are particular to that bin in that patch of the sky, into the analysis. This was the reason why the fitting function from Fu *et al.* (2008) was used in Section 2.4.2 for the CFHTLS weak lensing redshift distribution (Equation 2.29).

Another suggestion for the future would be to include μ and σ as extra parameters with an additional likelihood associated with the spectroscopic redshift distribution. By varying these quantities one could calculate the effects of a more flexible distribution but smooth the more noisy spectroscopic interpolation.

Table 3.4: The observed *cross* angular power spectra $C_\ell^{i,j}$ for SDSS MegaZ-LRG (DR7), an extension to the first MegaZ-LRG analysis (Blake *et al.* (2007) and Collister *et al.* (2007)). The Gaussian statistical error on the measurement is also included, which has been weighted over each $\Delta\ell$ band. Each bin extends $\Delta z = 0.05$ in redshift from $z = 0.45$ to 0.65 and covering $7746\mathrm{deg}^2$ contain $259,498$; $237,564$; $155,293$ and $71,201$ galaxies, respectively. With the exception of ℓ all quantities have been multiplied by 10^5.

ℓ	$C_\ell^{\mathrm{Bin1,2}}$	$\sigma(C_\ell^{1,2})$	$C_\ell^{\mathrm{Bin1,3}}$	$\sigma(C_\ell^{1,3})$	$C_\ell^{\mathrm{Bin1,4}}$	$\sigma(C_\ell^{1,4})$
6	13.249	6.278	3.220	6.828	-2.846	8.224
16	8.783	2.430	1.892	2.880	2.923	2.763
26	6.449	1.452	3.738	1.663	2.713	1.598

ℓ	$C_\ell^{\mathrm{Bin1,2}}$	$\sigma(C_\ell^{1,2})$	$C_\ell^{\mathrm{Bin1,3}}$	$\sigma(C_\ell^{1,3})$	$C_\ell^{\mathrm{Bin1,4}}$	$\sigma(C_\ell^{1,4})$
36	6.674	1.162	3.119	1.152	2.630	1.197
46	4.552	0.887	1.638	0.860	0.688	0.938
56	2.461	0.544	0.580	0.637	0.322	0.691
66	3.270	0.551	1.312	0.534	0.504	0.622
76	3.486	0.496	1.408	0.473	0.153	0.522
86	2.550	0.380	1.053	0.400	0.564	0.451
96	2.064	0.321	0.837	0.353	0.284	0.392
106	2.056	0.298	0.893	0.322	0.542	0.366
116	1.860	0.266	0.600	0.276	0.294	0.335
126	1.619	0.221	0.722	0.229	0.241	0.281
136	1.530	0.199	0.621	0.224	0.532	0.259
146	1.264	0.184	0.511	0.207	0.140	0.245
156	1.372	0.173	0.519	0.183	0.359	0.234
166	0.989	0.145	0.325	0.161	0.447	0.208
176	1.058	0.141	0.342	0.152	0.172	0.192
186	1.190	0.142	0.313	0.149	-0.0868	0.195
196	0.877	0.119	0.364	0.137	0.0336	0.169
206	0.763	0.112	0.293	0.128	0.0406	0.159
216	0.764	0.106	0.215	0.120	-0.0144	0.154
226	0.856	0.105	0.371	0.115	0.211	0.142
236	0.698	0.0971	0.308	0.113	0.191	0.137
246	0.612	0.0872	0.180	0.0982	0.0328	0.130
256	0.606	0.0867	0.203	0.100	0.0949	0.132
266	0.574	0.0845	0.259	0.0959	0.179	0.124
276	0.518	0.0814	0.145	0.0887	-0.0396	0.117
286	0.550	0.0744	0.327	0.0875	0.197	0.117
296	0.392	0.0699	0.258	0.0829	0.113	0.110
306	0.512	0.0702	0.097	0.0791	0.142	0.106
316	0.506	0.0698	0.193	0.0772	0.0520	0.108
326	0.461	0.0675	0.233	0.0768	0.0764	0.105

ℓ	$C_\ell^{\mathrm{Bin1,2}}$	$\sigma(C_\ell^{1,2})$	$C_\ell^{\mathrm{Bin1,3}}$	$\sigma(C_\ell^{1,3})$	$C_\ell^{\mathrm{Bin1,4}}$	$\sigma(C_\ell^{1,4})$
336	0.451	0.0649	0.152	0.0744	-0.0201	0.102
346	0.426	0.0645	0.119	0.0754	0.242	0.102
356	0.402	0.0634	0.117	0.0709	0.0258	0.0965
366	0.325	0.0589	0.103	0.0695	-0.0632	0.0942
376	0.339	0.0605	0.0916	0.0672	0.0740	0.0931
386	0.345	0.0563	0.159	0.0662	0.124	0.0886
396	0.346	0.0558	0.149	0.0660	0.00243	0.0862
406	0.361	0.0547	0.125	0.0630	0.0432	0.0868
416	0.242	0.0504	0.0560	0.0589	-0.0303	0.0813
426	0.328	0.0538	0.139	0.0624	0.00808	0.0828
436	0.339	0.0519	0.170	0.0602	0.0270	0.0813
446	0.335	0.0498	0.0636	0.0562	0.0365	0.0812
456	0.300	0.0496	0.130	0.0582	0.000687	0.0793
466	0.290	0.0479	0.101	0.0560	0.0505	0.0772
476	0.297	0.0467	0.0643	0.0538	0.0655	0.0751
486	0.323	0.0446	0.134	0.0533	0.0629	0.0713
496	0.277	0.0451	0.0731	0.0528	0.0519	0.0749

Table 3.5: The observed *cross* angular power spectra $C_\ell^{i,j}$ for SDSS MegaZ-LRG (DR7), an extension to the first MegaZ-LRG analysis (Blake *et al.* (2007) and Collister *et al.* (2007)). The Gaussian statistical error on the measurement is also included, which has been weighted over each $\Delta\ell$ band. Each bin extends $\Delta z = 0.05$ in redshift from $z = 0.45$ to 0.65 and covering $7746\mathrm{deg}^2$ contain $259,498$; $237,564$; $155,293$ and $71,201$ galaxies, respectively. With the exception of ℓ all quantities have been multiplied by 10^5.

ℓ	$C_\ell^{\mathrm{Bin2,3}}$	$\sigma(C_\ell^{2,3})$	$C_\ell^{\mathrm{Bin2,4}}$	$\sigma(C_\ell^{2,4})$	$C_\ell^{\mathrm{Bin3,4}}$	$\sigma(C_\ell^{3,4})$
6	11.687	5.605	8.670	6.752	18.705	7.343
16	6.354	2.312	3.313	2.218	10.076	2.629
26	5.887	1.426	3.206	1.370	6.577	1.570
36	4.801	1.021	3.115	1.062	5.210	1.052
46	4.398	0.832	2.280	0.907	4.193	0.879
56	2.457	0.558	1.217	0.605	3.857	0.709
66	3.342	0.528	2.201	0.614	3.336	0.595
76	2.978	0.467	0.915	0.516	2.106	0.491
86	2.809	0.408	1.156	0.461	2.342	0.484
96	2.315	0.331	0.887	0.369	2.172	0.404
106	2.288	0.316	1.160	0.360	2.061	0.389
116	2.071	0.277	1.008	0.337	1.846	0.350
126	1.725	0.224	0.572	0.274	1.567	0.284
136	1.602	0.214	0.649	0.247	1.495	0.277
146	1.538	0.192	0.410	0.227	1.131	0.255
156	1.237	0.176	0.432	0.225	1.267	0.238
166	0.934	0.147	0.739	0.190	1.156	0.212
176	1.210	0.157	0.406	0.197	0.904	0.213
186	0.917	0.143	0.343	0.187	0.871	0.197
196	0.925	0.129	0.344	0.159	0.827	0.184
206	0.892	0.124	0.411	0.154	0.882	0.176
216	0.928	0.123	0.347	0.158	0.940	0.180
226	0.813	0.119	0.336	0.148	0.800	0.163
236	0.722	0.112	0.358	0.135	0.743	0.158
246	0.628	0.101	0.253	0.133	0.657	0.150

ℓ	$C_\ell^{\mathrm{Bin2,3}}$	$\sigma(C_\ell^{2,3})$	$C_\ell^{\mathrm{Bin2,4}}$	$\sigma(C_\ell^{2,4})$	$C_\ell^{\mathrm{Bin3,4}}$	$\sigma(C_\ell^{3,4})$
256	0.677	0.0985	0.228	0.129	0.491	0.150
266	0.594	0.0949	0.338	0.122	0.610	0.139
276	0.558	0.0932	0.234	0.123	0.561	0.134
286	0.632	0.0871	0.225	0.116	0.631	0.137
296	0.476	0.0829	0.165	0.110	0.439	0.130
306	0.441	0.0799	0.248	0.107	0.426	0.121
316	0.500	0.0776	0.164	0.108	0.350	0.119
326	0.460	0.0757	0.154	0.103	0.492	0.117
336	0.354	0.0741	0.132	0.101	0.525	0.116
346	0.449	0.0744	0.221	0.100	0.646	0.117
356	0.458	0.0728	0.141	0.0991	0.471	0.110
366	0.390	0.0681	0.0715	0.0922	0.418	0.108
376	0.340	0.0679	0.142	0.0941	0.359	0.104
386	0.329	0.0659	0.0718	0.0883	0.228	0.103
396	0.355	0.0657	0.144	0.0860	0.570	0.101
406	0.372	0.0647	0.168	0.0892	0.567	0.102
416	0.298	0.0620	0.173	0.0856	0.233	0.100
426	0.308	0.0618	0.0122	0.0820	0.204	0.0952
436	0.327	0.0609	0.135	0.0823	0.300	0.0954
446	0.253	0.0566	0.167	0.0817	0.234	0.0923
456	0.283	0.0582	0.140	0.0793	0.308	0.0931
466	0.267	0.0568	0.140	0.0784	0.373	0.0916
476	0.330	0.0557	0.194	0.0777	0.382	0.0896
486	0.260	0.0537	0.131	0.0718	0.302	0.0858
496	0.241	0.0517	0.116	0.0734	0.258	0.0860

3.6.3 Extinction

Light from more distant galaxies is potentially absorbed, scattered or re-emitted by the dust and gas within our own galaxy. This *galactic extinction* has the capacity to be one of the dominant systematics in a galaxy survey such as this. For example, extinction can preferentially absorb light at the blue end of a galaxy's spectral energy distribution thus making it appear redder and more LRG-like. Alternatively, it can have the effect of scattering faint galaxies from the sample. As the contribution from our own galaxy changes as a function of position this is a cause for concern given that we are interested in inferring cosmological quantities through statistical variations across the sky. Worse still, it could act to further systematically bias our redshift estimates given that the ANNz derived galaxy catalogue is a spatial extrapolation of the 2SLAQ *training set*, which confined to a stripe at $\delta \approx 0\,^{\circ}$, covers a limited region of galactic extinction.

Fortunately detailed maps of galactic extinction are available (Schlegel *et al.* (1998); see also Figure 3.16) and subsequently the u, g, r, i and z bands used are dereddened model magnitudes, i.e. they are extinction corrected. Figure 3.17 shows the exaggerated effect that is the result of not adjusting properly for the presence of dust. In this plot the angular power spectrum is evaluated for the catalogue when the $i_{\rm dev}$ magnitude/colour cut is not extinction corrected. This causes extra galaxies to be scattered from the sample in different regions of the survey area and a large boost of power is observed. Although the values used for galaxy clustering statistics *are* corrected for extinction it could be that there are errors in the correction map. If these errors were related to the magnitude of extinction or again varied with position, then they too would propagate into the LRG sample.

To test for extinction correction errors I repeat the measurement of the angular power spectrum with regions of high extinction removed (> 0.1 mag). This constitutes a removal 15% of the survey area. The resulting values are plotted in Figure 3.18 as solid lines against the previous data points and error. It is clear that the profiles are not significantly affected. This result is consistent with the preliminary examination in Blake *et al.* (2007) and Abdalla *et al.* (2008). In the latter paper a comparison of the ANNz catalogue was made with a template based photometric method (SDSS-Padmanabhan *et al.* (2005)) in regions of varying extinction. The template based procedure does not utilise a spatially confined training set and is effectively blind to the extinction with regards to calibration. Given that they found no resultant bias or additional scatter in the photometric redshifts between the procedures the extinction error is expected to be partially subdominant, *at least* with respect to the extrapolation of the 2SLAQ calibration.

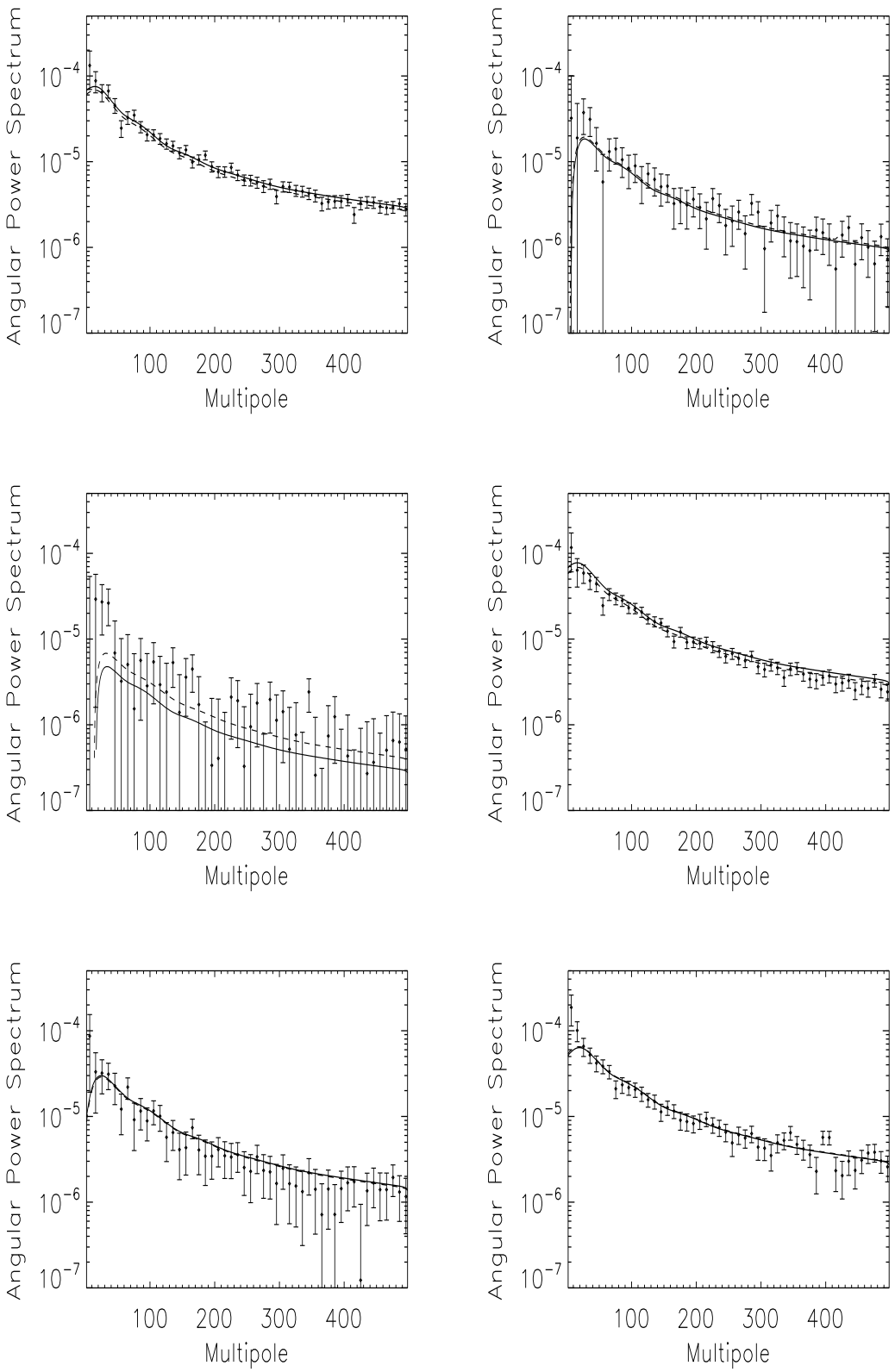

Figure 3.15: The measured cross Angular Power Spectra ($C_\ell^{i,j}$) for the photometric SDSS MegaZ-LRG (DR7) population as presented in Table 3.4 and Table 3.5. The error bars correspond to those calculated with Equation 3.12 using the measured power spectrum. The solid lines are evaluated for the the best fit parameters found in Section 3.5.3 using the the Gaussian redshift distributions. The dashed lines are the theoretical power spectra using a spline interpolation of the spectroscopic distribution. The panels are: Bin 1,2 (top left), Bin 1,3 (top right), Bin 1,4 (middle left), Bin 2,3 (middle right), Bin 2,4 (bottom left) and Bin 3,4 (bottom right).

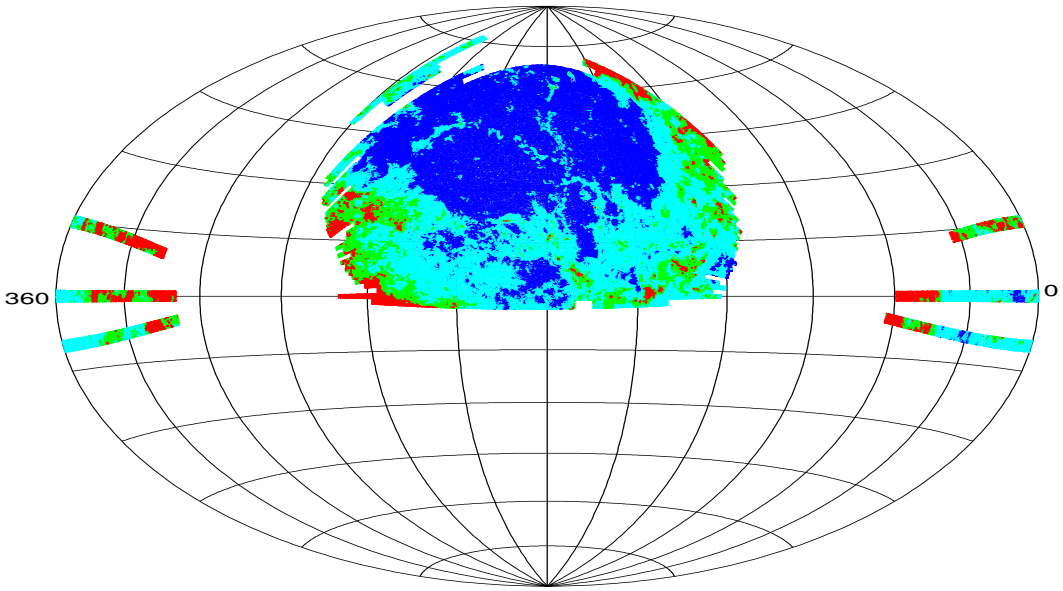

Figure 3.16: The fluctuations in galactic extinction are shown as a function of sky position across the DR7 survey area. The magnitude values are represented by dark blue ($0.0 - 0.05$), light blue ($0.05 - 0.1$), green ($0.1 - 0.15$) and red (> 015). The dust is particularly abundant near the edges of the survey indicating the outer boundaries of the Galaxy.

3.6.3.1 Photometric Codes

The previous Abdalla *et al.* (2008) work also evaluated the SDSS DR6 LRG catalogue with six different photometric codes: ANNZ (Collister & Lahav 2004), HyperZ (Bolzonella *et al.* 2000), SDSS (Padmanabhan *et al.* 2005), Le PHARE (Ilbert *et al.* 2006), BPZ (Benítez 2000) and ZEBRA (Feldmann *et al.* 2006). The survey area corresponding to this release is remarkably similar to that in this study. For future work and tests on the analysis it would be interesting to repeat the combined bins study with each of the six different catalogues. Once again, as a number of the methods have different mechanisms for producing the photometric redshift estimates it would help to quantify or reveal any remaining systematic. This also includes a cosmological comparison of the photometric codes as naturally one would expect their cosmology to be photometric-code invariant.

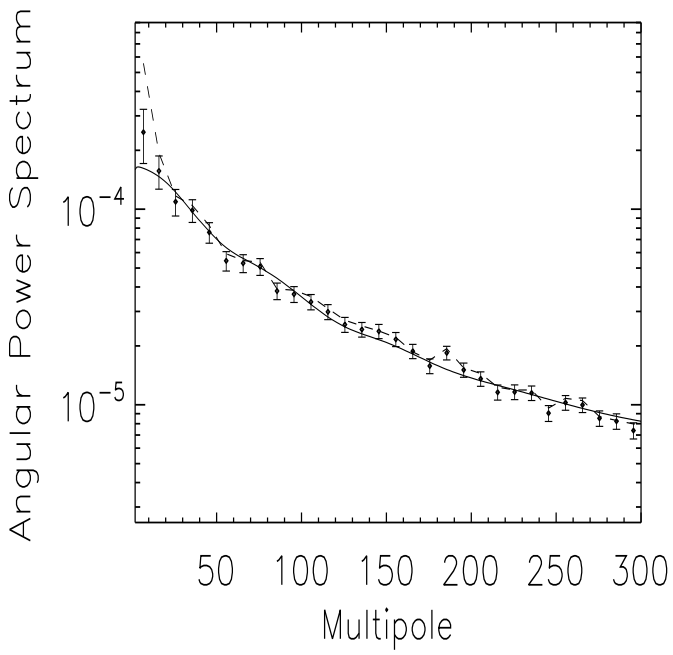

Figure 3.17: The exaggerated effect caused by neglecting the extinction correction for the $i_{\rm dev}$ colour cut (dashed line). Although this is not used in the study it highlights how any systematic error in the correction *could* affect the C_ℓ over various scales. The extinction corrected spectrum is shown by the solid points with associated error bars. The solid line is a best fit profile for comparison.

3.7 Complementarity with WMAP5

It is reassuring that the galaxy clustering results are consistent with the most recent WMAP analysis (Dunkley *et al.* 2009). This is a crucial consistency check as the two surveys probe vastly contrasting cosmic epochs and are subject to different systematics. In addition, each tool in isolation is subject to degeneracies given that a variation in one parameter can often be compensated with a change in another for the same physical process. It is therefore also highly advantageous to combine the two data sets. Hence I add the MegaZ LRG (DR7) data to WMAP5 in order to examine the complementarity of a joint analysis and further push the current parameter bounds. Furthermore, I repeat the study with the DR4 galaxy clustering data.

I study six ΛCDM parameters in all ($\Omega_b h^2$, $\Omega_c h^2$, Ω_Λ, n_s, τ and A_s), in addition to a bias parameter for each of the four combined redshift bins (b_1, b_2, b_3 and b_4). I also include and marginalise over A_{SZ}, the normalisation of the Sunyaev-Zeldovich template fluctuations. The CMB power spectrum is evaluated using CAMB (Lewis *et al.* 2000). Further details of these parameters and my WMAP methodology are described in Section 4.2.

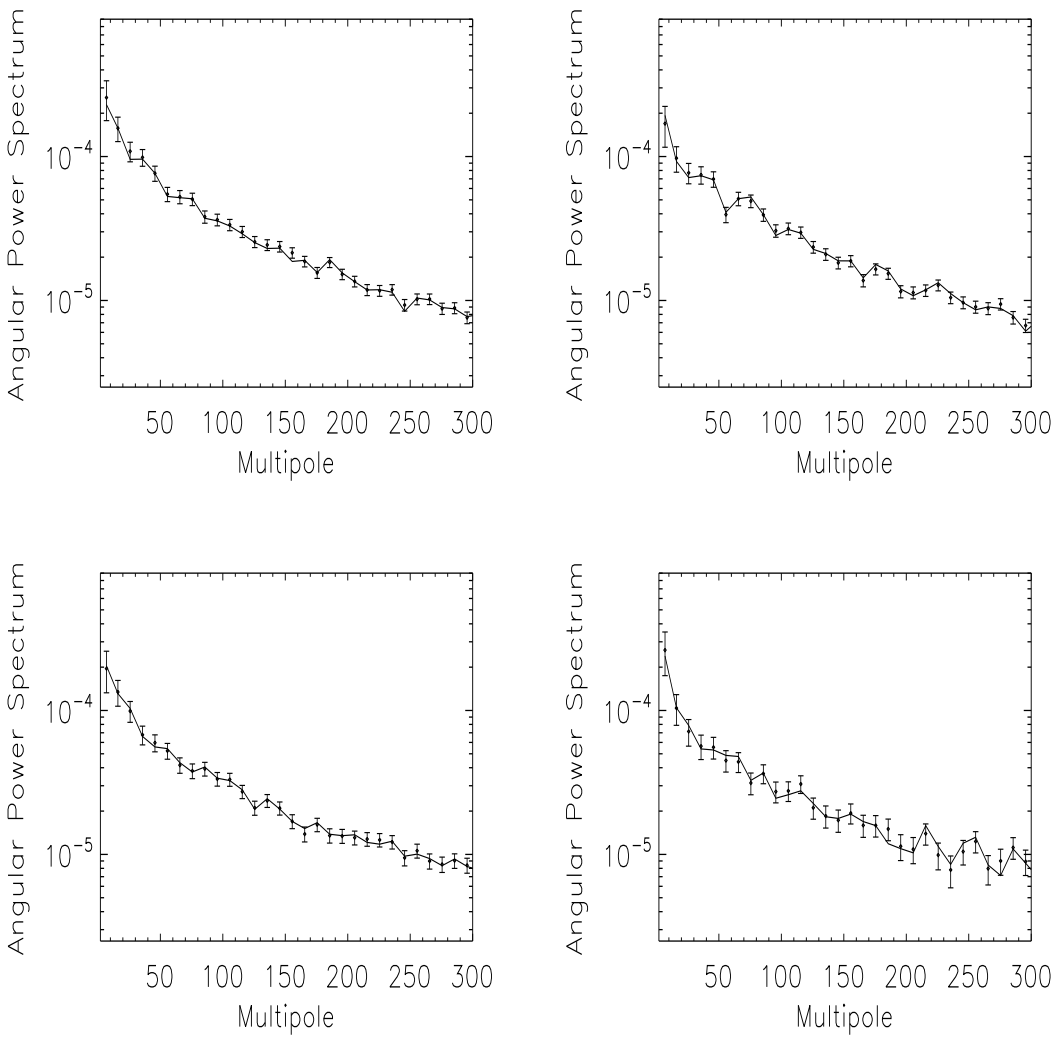

Figure 3.18: The Angular Power Spectrum in all four bins are measured with regions of high galactic extinction removed (> 0.1 mag; solid lines). This is to test for possible extinction correction errors propagating into the analysis. The spectra deduced earlier in the Chapter are included as data points with error bars. There does not seem to be a discrepancy between the two calculations.

$100\Omega_b h^2$	$\Omega_c h^2$	Ω_Λ	n_s	τ	$\ln(10^{10}A_s)$
1) 2.269 ± 0.067	0.1101 ± 0.00643	0.746 ± 0.0297	0.962 ± 0.015	0.0891 ± 0.0191	3.197 ± 0.05116
2) 2.296 ± 0.064	0.1192 ± 0.00346	0.711 ± 0.0183	0.962 ± 0.0139	0.0882 ± 0.0189	3.223 ± 0.0436
3) 2.276 ± 0.065	0.1191 ± 0.00324	0.706 ± 0.0184	0.958 ± 0.0144	0.0880 ± 0.0187	3.234 ± 0.0450
4) 2.272 ± 0.058	0.1161 ± 0.0039	0.711 ± 0.019	0.961 ± 0.013	0.084 ± 0.016	$3.080 \pm 0.037*$

Table 3.6: Constraints on the WMAP5 analysis and with the addition of various cosmological data: 1) WMAP5 2) WMAP5 + MegaZ DR4 3) WMAP5 + MegaZ DR7 4) WMAP5 + SDSS (Reid *et al.* 2009). The introduction of the constructed MegaZ LRG angular power spectra significantly reduces the bounds on $\Omega_c h^2$ and Ω_Λ due to a break in the Ω_m-h degeneracy. A similar analysis was performed by Reid *et al.* (2009), with the inclusion of the spectroscopic DR7 galaxy clustering data. * It should be noted that A_s corresponds to a slightly different parameter between the studies. For the first three cosmological runs this is actually Δ^2_R, the amplitude of curvature perturbations, at $k = 0.002\mathrm{Mpc}^{-1}$. In Reid *et al.* (2009) the corresponding scale is defined at $k = 0.05\mathrm{Mpc}^{-1}$.

The improvement relative to a CMB-only study is evident in Figure 3.19 and Figure 3.20. The black contours illustrate the individual WMAP5 result, whereas the tighter red contours represents the joint constraint: WMAP5 + MegaZ DR7 and WMAP5 + MegaZ DR4. A similar combination of data and cosmological parameters was investigated in the *spectroscopic* DR7 release by Reid *et al.* (2009). A comparison of all these results are summarised in Table 3.6.

It is found that the addition of galaxy clustering data not only improves constraints through the presence of more raw data, but acts to break the degeneracy between Ω_m and h that exists in the CMB alone. This subsequently leads to significantly tighter constraints in Ω_Λ and $\Omega_c h^2$ with a factor ~ 1.6 and ~ 2 improvement in the error on the former and latter, respectively. This was found similarly and compatibly in Reid *et al.* (2009). Moreover, through this complementary comparison it seems the photometric approach to modern cosmological surveys is justifiable with equally competitive and consistent results compared to the spectroscopic survey. The tight constraints on the matter densities show there is now overwhelming and precision evidence for some dark energy-like component to the cosmos when including photometric data from the late-time Universe. However, along with this optimism it has been shown in the preceding few subsections, for example, that there are potentially still residual systematics to be examined.

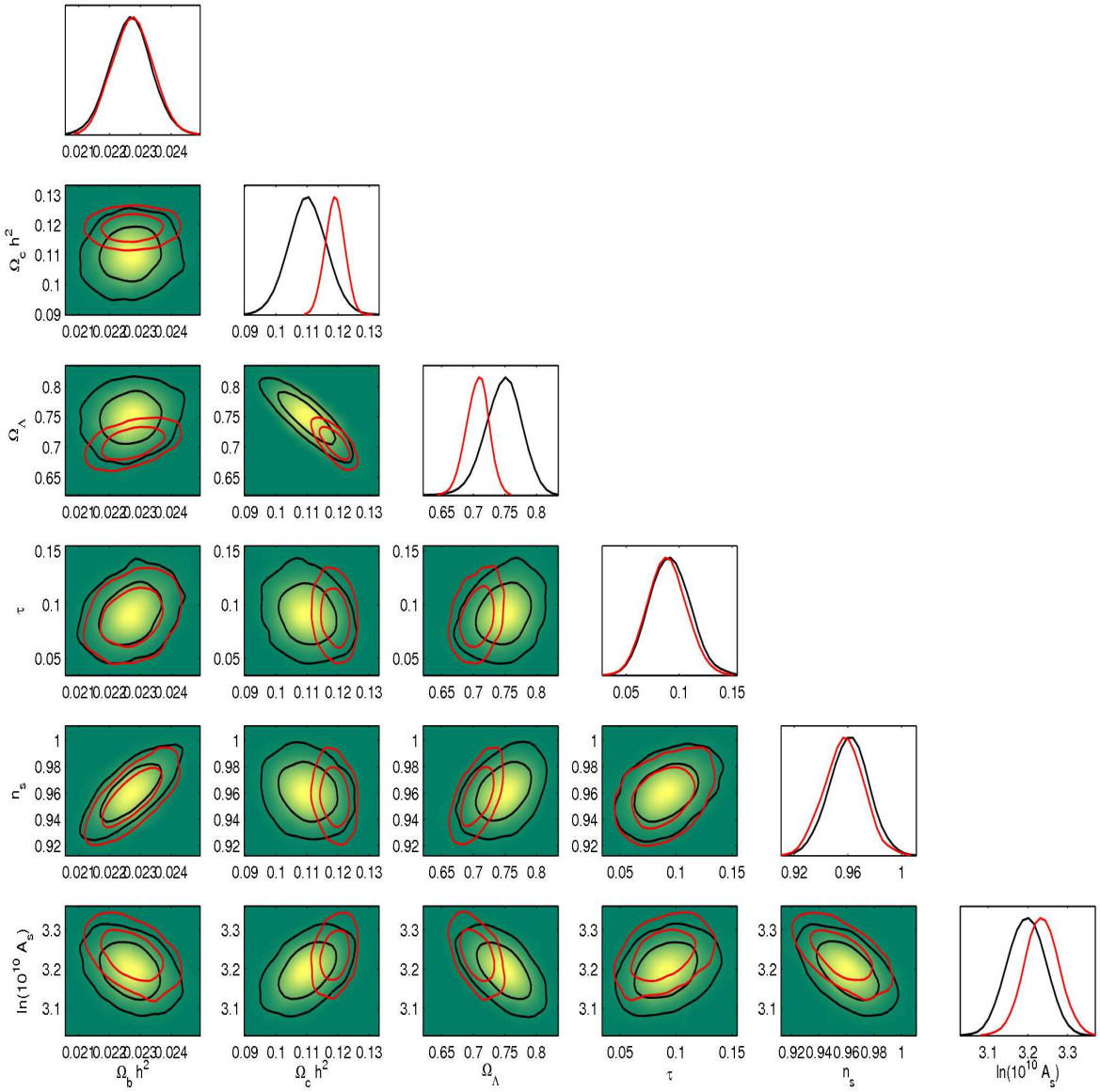

Figure 3.19: The two dimensional 68% and 95% contours and marginalised one dimensional distributions for 6 ΛCDM parameters ($\Omega_b h^2$, $\Omega_c h^2$, Ω_Λ, n_s, τ and $\ln(10^{10}A_s)$) and the amplitude of the Sunyaev-Zeldovich fluctuations A_{SZ} (not shown). The black contours are given by a WMAP-only analysis, whereas the red constraints are with the addition of MegaZ DR7. For the latter analysis four bias parameters have been implicitely marginalised over. The data is incapable of constraining A_{SZ} consistent with Dunkley *et al.* (2009). Note that n_s and A_s are defined at $k = 0.002\mathrm{Mpc}^{-1}$ (E.g. Komatsu *et al.* (2009)).

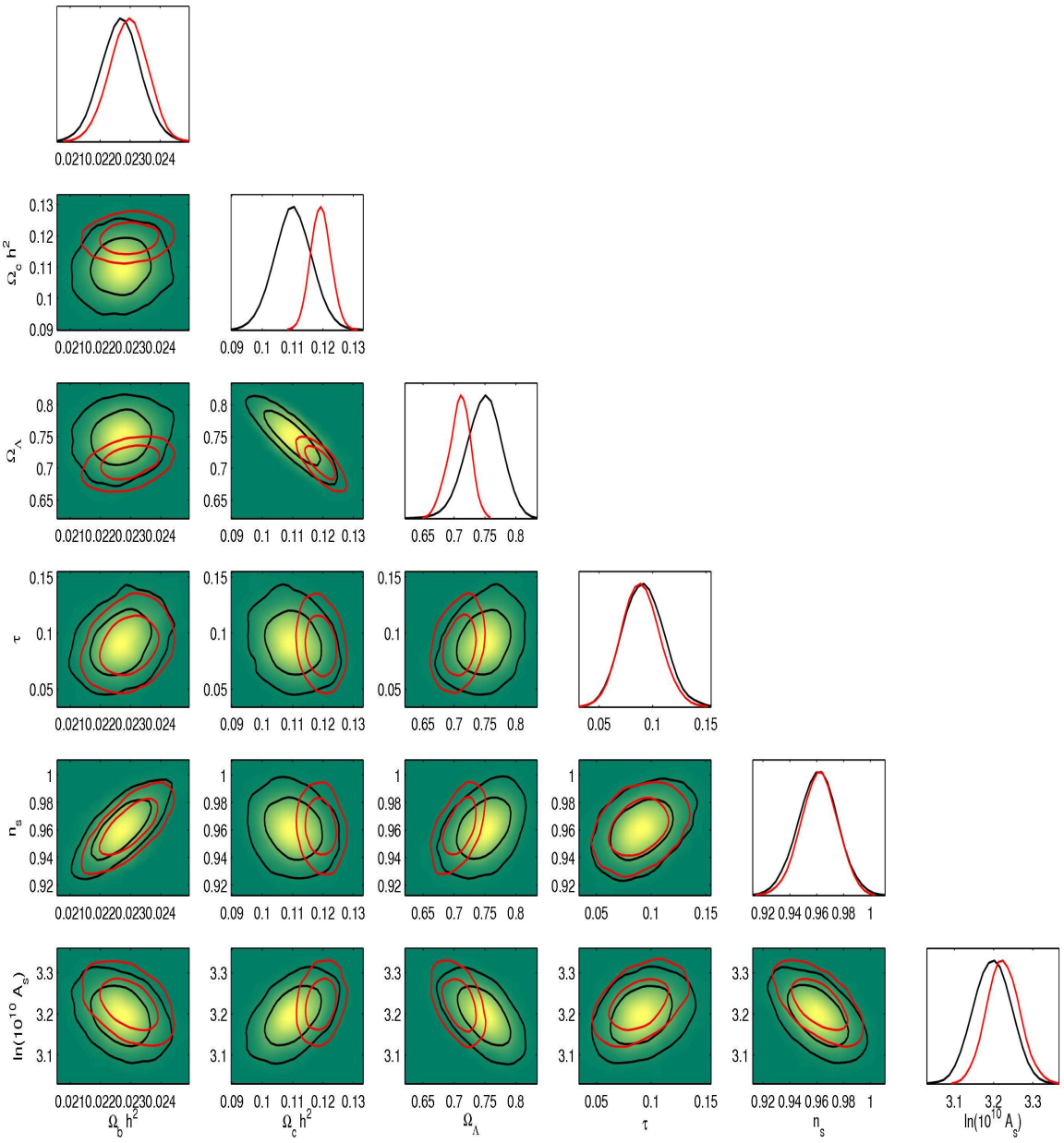

Figure 3.20: The two dimensional 68% and 95% contours and marginalised one dimensional distributions for 6 ΛCDM parameters ($\Omega_b h^2$, $\Omega_c h^2$, Ω_Λ, n_s, τ and $\ln(10^{10} A_s)$) and the amplitude of the Sunyaev-Zeldovich fluctuations A_{SZ} (not shown). The black contours are given by a WMAP-only analysis, whereas the red constraints are with the addition of MegaZ DR4. For the latter analysis four bias parameters have been implicitely marginalised over. Once again the data is incapable of constraining A_{SZ} consistent with Dunkley *et al.* (2009). Note that n_s and A_s are defined at $k = 0.002\mathrm{Mpc}^{-1}$ (E.g. Komatsu *et al.* (2009)).

CHAPTER 4

A COMBINED CONSTRAINT ON THE NEUTRINO MASS

Abstract

The neutrinos are not only unimaginably elusive particles but, with the presence of mass, are an extension to the standard model of particle physics. Most surprising therefore is its measurable effects on physics of the comparatively large scale. I discuss these effects and then pursue a combined constraint on the sum of the species' mass. Firstly, I use data from the 5-year WMAP CMB temperature and polarisation fluctuations. I then add information from Baryon Acoustic Oscillations (BAO) and type 1a Supernovae (SNe) to reduce the degenerate parameter space. The neutrinos' physical effects are also measurable in the pattern of galaxy clustering and with this in mind I combine the MegaZ LRG data from Chapter 3 with the aforementioned analyses. Finally, using an HST prior on the Hubble parameter, I find the collective bound of $\sum m_\nu \leq 0.281$ eV at the 95% CL for a flat ΛCDM cosmology–one of the tightest current constraints. Other studies are also discussed in addition to the potential systematics that might affect such a calculation.

This work is presented originally in Thomas, S.A., Abdalla, F.B. & Lahav, O., 2009b.

4.1 Introduction

4.1.1 The Neutrino: Particle Physics

Studies of the neutrino have traditionally been the realm of particle physics experiments, with Super-Kamiokande (Fukuda *et al.* 1998) first detecting the presence of mass. In this experiment the neutrinos were shown to oscillate between the known flavors (ν_e, ν_μ, ν_τ) solving, in the process, the long standing solar neutrino problem. This was the observed discrepancy between the number of predicted and detected neutrinos thought to originate from the sun. The detectors were measuring far fewer electron neutrinos ν_e (for which they were sensitive to) given that they had *changed* flavor[1]. This implied the neutrinos have non-zero mass eigenstates (m_1, m_2, m_3) because the flavor mixing depends on the differences between their masses squared. Subsequently, bounds have been placed on the splitting between the neutrino mass eigenstates from a host of solar, accelerator and atmospheric experiments; $|\Delta m^2_{31}| \approx 2.4 \times 10^{-3}\mathrm{eV}^2$ and $|\Delta m^2_{21}| \approx 7.7 \times 10^{-5}\mathrm{eV}^2$ (E.g. Schwetz *et al.* (2008)). However, currently both the absolute scale and the hierarchy of the masses remain hidden. KATRIN, a kinematic tritium beta decay experiment (Wolf *et al.* 2008), aims to provide such a constraint. This will be performed by looking at the end region of the β energetic spectrum where the finite mass electron neutrino is expected to cause a decrement in energy.

4.1.2 The Neutrino: Cosmology

Cosmology not only probes the absolute mass scale of the neutrino but is a completely independent method for which to test against (E.g. Elgarøy & Lahav (2005), Lesgourgues & Pastor (2006) and references therein). In any case, it is imperative to include an accurate prescription for the neutrino in cosmology, as any failure to do so can bias the other cosmological parameters.

A cosmological constraint on the sum of the neutrino masses is primarily a constraint on the relic Big-Bang neutrino density Ω_ν, i.e. the energy budget consumed by the cosmic neutrino background. This background was initially in equilibrium with the very early cosmic plasma but subsequently decoupled after t $\sim$ 1 sec as a result of its weak interaction. Despite electron-positron annihilations later heating the photon distribution it is still possible to associate the temperature of the two particle populations by equating their entropy densities. From this one can then relate the cosmic neutrino density to the sum of the individual mass eigenstates $\sum m_\nu$ (E.g. Dodelson

[1]With other models such as neutrino decay less favoured by the data.

(2003)) as given[2] by,

$$\Omega_\nu = \frac{\sum m_\nu}{93.14\mathrm{h}^2\mathrm{eV}}. \tag{4.1}$$

It is this relation that helps us to probe the sum of the neutrino masses and the absolute scale. Even with the most extreme conservativeness the above relation immediately enables a hard upper bound of $\sum m_\nu \lesssim 94\mathrm{h}^2\ \mathrm{eV}$ given that we live in a Universe that is at least close to flat (Komatsu *et al.* 2009).

The more direct effects of the neutrino depend on whether they are relativistic, non-relativistic and also over what scale one is considering. In the early Universe these particles will naturally behave like radiation and at some point, depending on their mass, will make a transition to become matter-like. Specifically, the massive neutrino species start to become non-relativistic at a redshift given by,

$$1 + z_{\mathrm{NR}} \approx 2/3 \times 10^3 \Big(\frac{\sum m_\nu}{\mathrm{eV}}\Big). \tag{4.2}$$

I therefore combine a series of probes in the following sections that might be sensitive to these different regimes or restrict the degenerate parameter space.

Explicitly, the layout of the Chapter is as follows: I start with preliminary bounds given by WMAP5 CMB data in Section 4.2, while adding both Supernovae and Baryon Acoustic Oscillations in Section 4.3. The influence of the particle on this cosmology and the subsequent degeneracies are discussed. Following this, the MegaZ LRG (DR4/DR7) clustering data measured in Chapter 3 is combined with the previous analyses to place one of the most stringent combined constraints available on the total mass of the neutrino species (Section 4.4). Finally, I finish with a discussion of other neutrino studies, the potential systematics that might affect such works and conclude in Section 4.5.

4.1.2.1 Assumptions

For the parameter analyses and subsequent constraints I use the COSMOMC parameter estimation package (Lewis & Bridle 2002). I assume a flat Universe with Gaussian and adiabatic primordial fluctuations and no running of the spectral index ($\alpha_s = 0$) throughout. The effective number of neutrinos are fixed to $\mathrm{N_{eff}} = 3.04$ (E.g. Mangano *et al.* (2002) and Yao *et al.* (2006)), thereby assuming there are no sterile neutrinos or other relativistic degrees of freedom. The equation of state

[2] *If* massive.

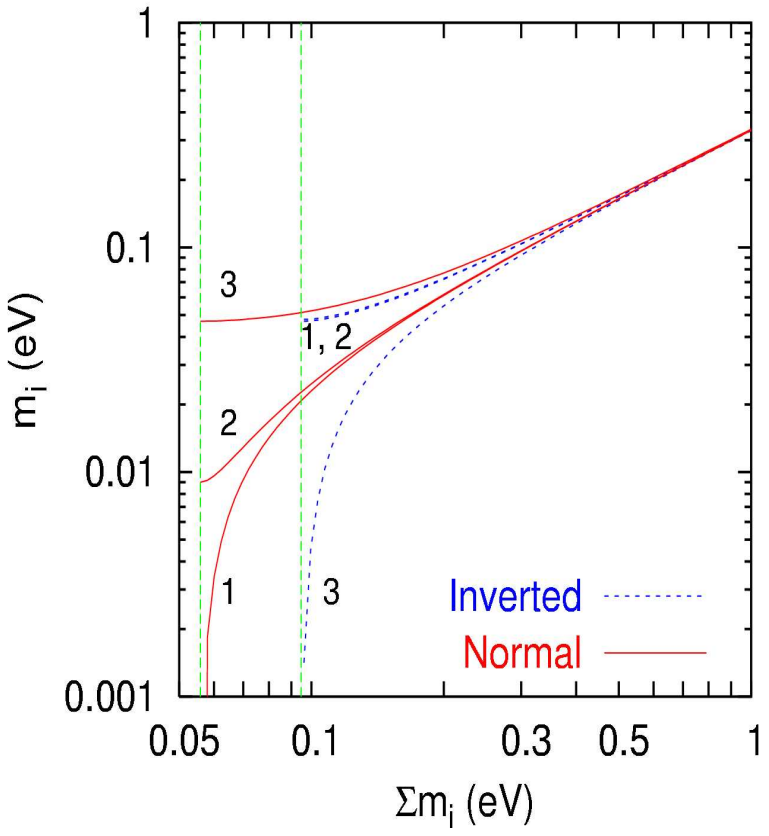

Figure 4.1: The relationship between the individual and sum of three non-degenerate neutrino mass eigenstates is highlighted for the two possible hierarchies. These hierarchies are a consequence of knowing the absolute differences ($|\Delta m^2_{31}|$ and $|\Delta m^2_{21}|$) between two sets of mass eigenstates but not the *sign*. These are known as the normal ($m_3 \gg m_2 > m_1$; solid lines) and inverted ($m_2 > m_1 \gg m_3$; dashed lines) hierarchies. Current bounds of $\sim$ sub $1\mathrm{eV}$ imply the assumption of degenerate masses to be valid. CREDIT: Lesgourgues & Pastor (2006).

for dark energy is set to $w_0 = -1$ for a ΛCDM cosmology. Finally, I consider the three standard neutrinos to be completely degenerate in mass given that the current inferred bounds are much greater than the splitting hierarchies. The relation between the individual states, the hierarchies and the total mass are highlighted in Figure 4.1. It should be noted that if the mass degeneracy approximation is relaxed then Equation 4.1 remains a valid approximation (Lesgourgues & Pastor 2006). The potential of future surveys to discriminate this mass hierarchy and the encapsulated mass splittings has been discussed in Abdalla & Rawlings (2007), Kitching *et al.* (2008) and De Bernardis *et al.* (2009). Any possible limitations imposed on the study from these assumptions are discussed in Section 4.5.1.

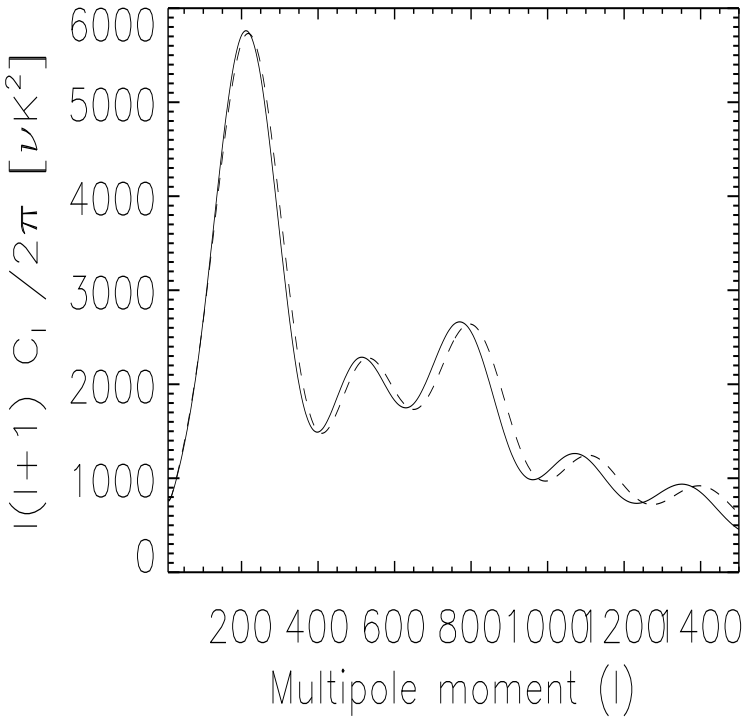

Figure 4.2: The effect of massive neutrinos is shown to alter the predicted CMB pattern. The dashed line represents a flat ΛCDM cosmology with massless neutrinos only. While fixing $\Omega_c h^2$, $\Omega_b h^2$ and h, three massive species are introduced with an increase in the neutrino fraction $f_\nu = 0.1$ (solid line). The CMB angular power spectrum has been calculated using CAMB.

4.2 Cosmic Microwave Background

The abundance of neutrinos in the Universe can have a *direct* effect on the primary CMB anisotropies if non-relativistic before the time of decoupling (i.e. when sufficiently massive). Otherwise, if lighter, they act as a collisionless radiation-like fluid and have little impact. However, one of the most clear effects at this epoch is a displacement in the time of matter-radiation equality. This is a consequence of potentially having neutrinos either side of the relativistic/non-relativistic boundary at decoupling; in the process changing the early ISW effect. In addition, as energy constituents, the neutrinos can affect the observed CMB pattern through the background expansion, by altering the angular diameter distance to last scattering. The overall effects are illustrated in Figure 4.2. Although parameter degeneracies and a mild insensitivity to relativistic (lighter) neutrinos therefore limit the upper bounds one can place on $\sum m_\nu$ (Ichikawa *et al.* 2005), the CMB represents a relatively clean and systematic-less cosmological tool whose high statistical discrimination of the

remaining cosmological model facilitates a competitive combination of probes.

4.2.1 The WMAP Analysis

I therefore start by using the latest 5-year WMAP data (WMAP5) and the full likelihood as described in Dunkley *et al.* (2009)[3] to vary six core ΛCDM parameters: $\Omega_b h^2$, $\Omega_c h^2$, Ω_Λ, n_s, τ and $\ln(10^{10} A_s)$, plus $\sum m_\nu$– the sum of the neutrino masses. τ, n_s and A_s represent the optical depth to reionisation, the scalar spectral index and the amplitude of curvature perturbations defined at $k = 0.002/\mathrm{Mpc}$, respectively.

I also include contributions from the Sunyaev-Zeldovich fluctuations by adding a template spectrum C_ℓ^{SZ} to the overall power spectrum. The template is approximately insensitive to the bulk of cosmological parameters except for a $\sim (\Omega_b h)^2 (\sigma_8)^7$ dependence (Komatsu & Seljak 2002). The amplitude of C_ℓ^{SZ} is moderated with a pre-factor A_{SZ} that I include in the cosmological analyses. It is allowed to vary from $0 < A_{SZ} < 2$ as in Dunkley *et al.* (2009) and Spergel *et al.* (2007). This inclusion was found to gently alter the cosmological parameters, including a slight decrease in n_s and increase in $\Omega_b h^2$ (Dunkley *et al.* 2009). As in the aforementioned analysis I use the pre-March 2008 version of CAMB (Lewis *et al.* 2000) to produce the CMB power spectra. The reionisation is therefore treated as an instantaneous process by shifting from neutral to ionised in a redshift of $\Delta z = 0.5$.

Due to the high statistical power of the new data I also include the gravitational lensing effect on the CMB, e.g. Seljak (1996) and Lewis & Challinor (2006). To test for consistency with the original 5-year analysis a primary run is performed based on the six core (plus A_{SZ}) ΛCDM parameters described above. I find: $100\Omega_b h^2 = 2.269 \pm 0.067$, $\Omega_c h^2 = 0.1101 \pm 0.00643$, $\Omega_\Lambda = 0.746 \pm 0.0297$, $n_s = 0.962 \pm 0.015$, $\tau = 0.0891 \pm 0.0191$, $\ln(10^{10} A_s) = 3.197 \pm 0.0512$ and no constraint on the amplitude of the Sunyaev-Zeldovich template spectrum. The contours and one dimensional marginalised distributions for each parameter were illustrated previously in Figure 3.19 as the WMAP-only run (black contours).

4.2.2 CMB constraints

I now extend the above analysis to include 3 degenerate massive neutrinos via $\sum m_\nu$. I subsequently find $\sum m_\nu < 1.271$ eV at the 95% confidence level. This is completely consistent with Komatsu *et al.* (2009), who find $\sum m_\nu < 1.3$ eV. The result is shown further in Figure 4.3 where

[3]Publicly available at: http://lambda.gsfc.nasa.gov/product/map/

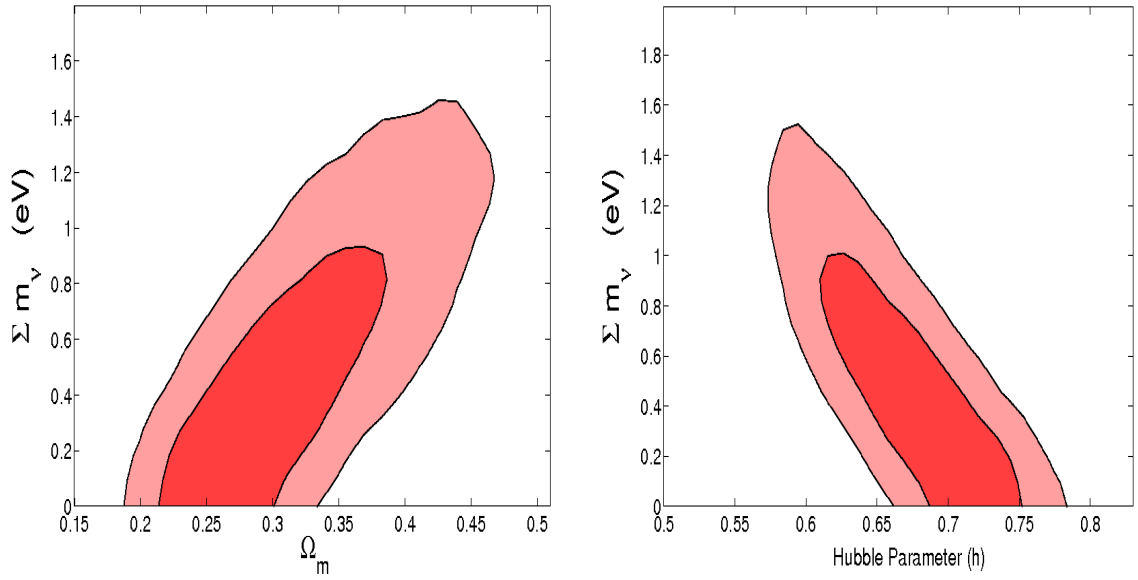

Figure 4.3: For an isolated analysis of the neutrino mass with the CMB I find $\sum m_\nu < 1.271\mathrm{eV}$ consistent with Komatsu *et al.* (2009). The corresponding 2D marginalised constraints are shown above with the matter density (Ω_m) and the Hubble parameter (h) degeneracy clear. The derived constraint implies that the neutrinos were indeed relativistic at the time of decoupling and that the assumed degeneracy of the neutrino masses is valid.

the inner and outer contours represent 68% and 95% confidence levels, respectively.

The inferred bounds imply that the neutrinos were relativistic at decoupling ($z \approx 1090$) as can be seen with reference to Equation (4.2). Therefore, as alluded to above, they will make a significant contribution by delaying the matter-radiation equality. This explains the observed degeneracy with Ω_m for one can counteract the delay by adding more matter. Furthermore, the early ISW effect resulting from the extra relativistic material causes a shift in the low ℓ part of the CMB spectrum. This can be partially mimicked with a change in h, which is again degenerate with $\sum m_\nu$. Finally, for increasing neutrino mass the distance to last scattering is reduced. This induces a shift in the multipole scale and again can be compensated by a decrease in the Hubble parameter. These have been found and described similarly in Ichikawa *et al.* (2005), Komatsu *et al.* (2009) and Ichiki *et al.* (2009). Hence I now look to adding probes of the expansion history in order to reduce these issues and the upper bound.

4.3 Supernovae and Baryon Acoustic Oscillations

It is reasonable to assume that further constraining either the matter density (Ω_m) and/or the Hubble parameter (h) will break the degeneracies seen in the previous section, even if those probes are not directly sensitive to the neutrino species. I therefore add information from the distance measures provided by both supernovae and baryon acoustic oscillations. This was shown in Ichikawa *et al.* (2005), Komatsu *et al.* (2009), Tereno *et al.* (2009) and Ichiki *et al.* (2009), for example, to be a particularly fruitful avenue.

I use 71 type 1a Supernovae from the first year Supernova Legacy Survey (SNLS; Astier *et al.* 2006) to initially probe the luminosity distance-redshift relation. A measure of this luminosity distance $d_L(z)$ is the distance modulus μ_0 given by,

$$\mu_0 = 5\mathrm{log}10(d_L(z)) + 25. \tag{4.3}$$

This is shown in the log-likelihood in Equation (4.4), where μ_B is the observed value. The contributions to the error are the intrinsic dispersion of the absolute magnitudes $\sigma_{\rm int}$ and the peculiar velocity and light curve parameter information $\sigma(\mu_B)$.

$$\chi^2 = \sum_{\rm SN} \frac{(\mu_B - 5\mathrm{log}_{10}(d_L(\theta, z)) - 25)^2}{\sigma^2(\mu_B) + \sigma^2_{\rm int}}. \tag{4.4}$$

The oscillations set up in the early photon-baryon fluid are observable in the late-time galaxy distribution. These baryon acoustic oscillations (BAOs) can be used as standard rulers and aim to test our cosmology through the angular diameter distance-redshift relation. Using the data and notation of Percival *et al.* (2007) I look to utilise the distance measure described by,

$$D_V(z) = [(1+z)^2 D_A^2 cz/H(z)]^{\frac{1}{3}} \tag{4.5}$$

where D_A is the angular diameter distance and $H(z)$ is the Hubble parameter. Specifically, it is the ratio $r_s/D_V(z)$ that is examined where r_s is the comoving sound horizon at recombination. Percival *et al.* (2007) detects the BAO in the clustering of 2dFGRS and SDSS galaxy samples and the clustering of SDSS LRGs to quantify this measure at $z = 0.2$ and $z = 0.35$, respectively. For each likelihood evaluation I compare this data to $r_s/D_V(z)$ calculated with $D_V(z)$ from Equation (4.5) and the varying comoving sound horizon r_s evaluated using the formulae in Eisenstein & Hu (1998).

Combining these two probes with the CMB data I find a substantial improvement with $\sum m_\nu < 0.695$ eV at the 95% confidence level. This is similar to both Komatsu *et al.* (2009) ($\sum_\nu < 0.67$

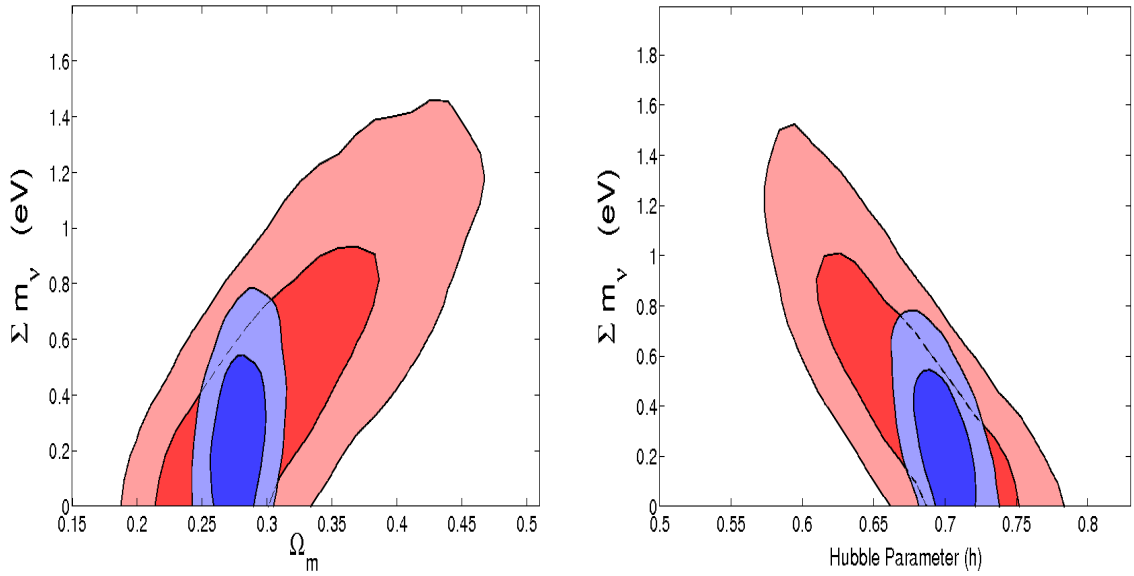

Figure 4.4: Targeting the the degenerate parameter space of the CMB-only study (red/lighter contours) is shown to be highly beneficial with the inclusion of both BAO and SN data (blue/darker contours). With this configuration I find $\sum m_\nu < 0.695$ eV at the 95% confidence level, consistent with Komatsu *et al.* (2009).

eV) and Ichiki *et al.* (2009) ($\sum_\nu < 0.76$ eV). The former analysis also highlights an additional gain from using these two geometric probes. This results from the highly complementary limits that they place on the equation of state (as a consequence of their constrasting correlation in Ω_m-w_0). In this way the bounds on the mass are not seen to degrade substantially when the parameter space is extended to include dark energy. It is also worth mentioning that the slight variation in neutrino mass quoted between the other two studies is most likely a result of different data sets being used. Both utilise the *Union* supernovae (Kowalski *et al.* 2008) but Ichiki *et al.* (2009) uses the BAO measurements from Eisenstein *et al.* (2005).

The bounds measured in this study are highlighted in Figure 4.4 with the degeneracy breaking particularly evident.

4.4 Galaxy Clustering

4.4.1 Galaxy Clustering Signatures

Statistical galaxy clustering is an effective tool for breaking some of the parameter degeneracies implicit in a CMB-centric study. This is demonstrated clearly in Figure 3.19 and Figure 3.20

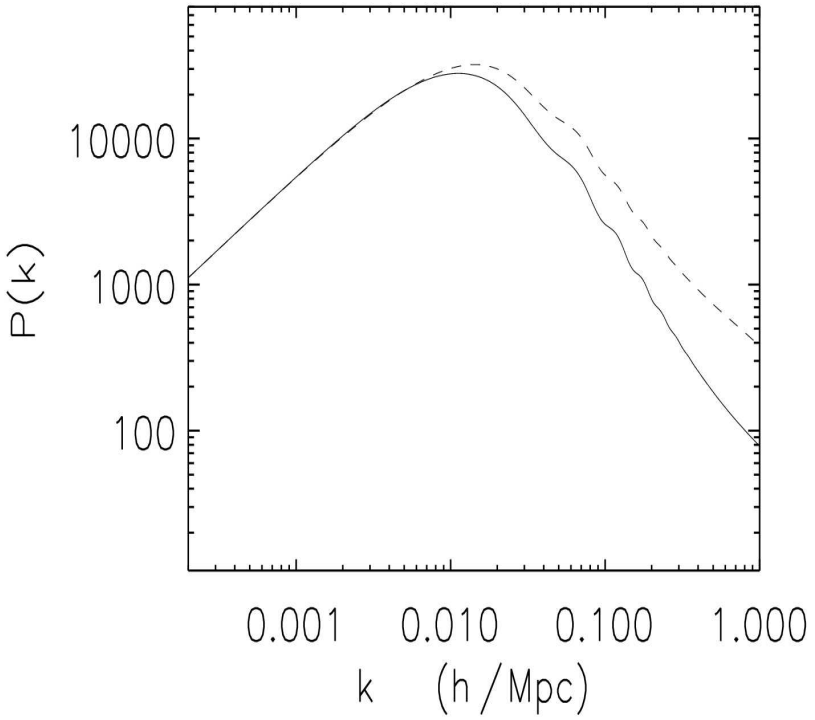

Figure 4.5: The impact of finite mass neutrinos on the matter power spectrum is demonstrated above. The dashed line represents a standard flat ΛCDM cosmology with three massless neutrinos $f_\nu \approx 0$. While fixing $\Omega_b h^2$, $\Omega_m h^2$ and Ω_Λ, three massive species are introduced with an increase in the neutrino fraction $f_\nu = 0.1$ (solid line). It is clear that massive neutrinos act to suppress the power of fluctuations over smaller scales. The power spectrum $P(k)$ is calculated using CAMB and the Smith *et al.* (2003) non-linear prescription.

with MegaZ Luminous Red Galaxies (LRGs) in the previous Chapter. In order to reduce the current bounds on the neutrino mass it seems reasonable therefore to amalgamate these with the preceding data. While this would naturally give better constraints there is also a far greater physical motivation for utilising the galaxy power spectrum: neutrinos *directly* alter the clustering of a galaxy survey (E.g. Hu *et al.* (1998), Lesgourgues & Pastor (2006) and references therein.).

The neutrinos have a large thermal velocity as a result of their low mass and subsequently erase their own perturbations on scales smaller than what is known as the *free streaming* length. They impart this suppression on the perturbations of other species through a gravitational backreaction. However, while relativistic the neutrinos propagate at the speed of light and consequently their free-streaming scale is equal to the Hubble radius. This is why they only had an indirect effect on the CMB. After this period any neutrino with an individual mass given by m_ν will suppress

scales in Fourier space smaller than the free-streaming wave vector $k_{\rm fs}$ (Hu & Eisenstein (1998) and Lesgourgues & Pastor (2006)) where,

$$k_{\rm fs} = 0.82\,\frac{\sqrt{\Omega_\Lambda + \Omega_m(1+z)^3}}{(1+z)^2}\Big(\frac{m_\nu}{1\ {\rm eV}}\Big)\ h{\rm Mpc}^{-1}. \tag{4.6}$$

Implicit within this reasoning is also the fact that all the perturbations are affected by the neutrinos' contribution to the Friedmann equation and therefore background expansion. The effects of expansion on the growth of structure are discussed in detail in Section 2.2.2. The equation of state of the neutrinos naturally evolve from that of radiation to matter and can be approximated by the function,

$$w_\nu^{\rm eff}(z) = \frac{1}{3}\Big(1 + \Big(\frac{m_\nu}{(1+z)\times 0.058\ {\rm eV}}\Big)^a\Big)^{-b} \tag{4.7}$$

with values $a = 1.652$ and $b = 0.561$ (E.g. Tereno *et al.* (2009)). In this way the neutrino density is included within the total matter density: $\Omega_m = \Omega_b + \Omega_c + \Omega_\nu$.

The net behaviour for a study of the late-time Universe is a clustering of the particles on the largest of scales, similar to ordinary cold Dark Matter. Alternatively, on the smallest scales there is a uniform and therefore scale independent suppression of growth. Between these regions the corresponding suppression is scale dependent. Thus statistically, the overall effect of massive neutrino species is a damping of the power spectrum over larger k and is shown clearly in Figure 4.5. These signatures have been exploited with previous studies of galaxy clustering including, for example, Elgarøy *et al.* (2002), Tegmark *et al.* (2006) and Reid *et al.* (2009).

4.4.2 Galaxy Clustering Analysis

4.4.2.1 LRG data

Considering the aforementioned effects I therefore look to use the most recent galaxy clustering measurement, MegaZ LRG DR7 (Chapter 3), to aid the bounds from the previous subsections. This catalogue is composed of 723,556 Luminous Red Galaxies (LRGs) and spanning $7746\ {\rm deg}^2$ on the sky represents the final SDSS II *photometric* release. These objects are old, stable systems that provide reliable photometric redshift estimates and, due to their high luminosity, probe a large region of cosmic volume.

I analyse the angular power spectrum C_ℓ of the LRGs in four equally spaced redshift bins ($\Delta z = 0.05$) between $z = 0.45$ and $z = 0.65$ up until a maximum multipole $\ell_{\rm max} = 300$. The likelihood combines the four bins and includes the full covariance as a result of photometric errors scattering galaxies between slices. There are four additional parameters included in the study as a

result of the galaxy bias in each of the four bins (b_1, b_2, b_3 and b_4), i.e., modestly accounting for the redshift dependence in each slice. By marginalising over these values only information from the shape of the power spectrum is therefore utilised. Including a scale dependence in these biases is beyond the scope of this work. Finally, the theoretical angular power spectra (Equation 3.17 and Equation 3.25) have been adjusted to include the effects of redshift space distortions (Equation 3.24). These allow an additional measure for the bias parameters through a change in shape at low ℓ. For more specific information pertaining to the galaxy clustering study the finer details of the galaxy catalogue, measurement, power spectrum and systematics are described thoroughly in Section 3.2.1, Section 3.3, Section 3.4 and Section 3.6, respectively.

In addition to their sensitivity of the neutrino signatures and the breaking of degeneracies present in the CMB, the MegaZ power spectra are particularly beneficial to this combined measurement. This is because the BAOs, which were shown to be so advantageous in the previous section, can be used in conjunction to MegaZ with no cross-covariance. The BAO data is extracted at $z = 0.2$ and $z = 0.35$, whereas MegaZ is defined from $z = 0.45$ to $z = 0.65$. They therefore constitute two independent data sets and can be used both simply and *simultaneously*.

4.4.2.2 The Linear and Non-linear Power Spectrum

In a linear ΛCDM Universe the matter densities give rise to a scale independent growth of structure. In this way the shape of the power spectrum is redshift independent, with the amplitude moderated by the linear growth factor $g(z)$. In this regime one can therefore directly decompose the power spectrum into scale and redshift terms ($P(k, z) = P_0(k)g(z)^2$). The introduction of neutrinos into the late-time cosmology introduces a scale dependence that changes with cosmological epoch and therefore redshift (E.g. Equation 4.6). It is interesting to note therefore that the decomposition into k and z is technically invalid. However, it is found that the inaccuracy introduced by this decomposition is small compared to the discriminatory power of the current galaxy clustering data (Lesgourgues & Pastor (2006) and Lahav *et al.* (2009)). Regardless of this the matter power spectrum used here is calculated using CAMB (Lewis *et al.* 2000).

As in the original MegaZ *DR4* release (Blake *et al.* 2007) the maximum multipole scale is limited to $l_{\max} = 300$ at which point the non-linear regime starts to become significantly different from the linear prediction. However, even for multipoles below this (i.e. larger scales) the non-linear regime is still important due to a slight increase in power and should still be included. Therefore in this study the HALOFIT (Smith *et al.* 2003) non-linear prescription is implemented. Even though this fitting function is a good approximation for normal ΛCDM cosmology and even

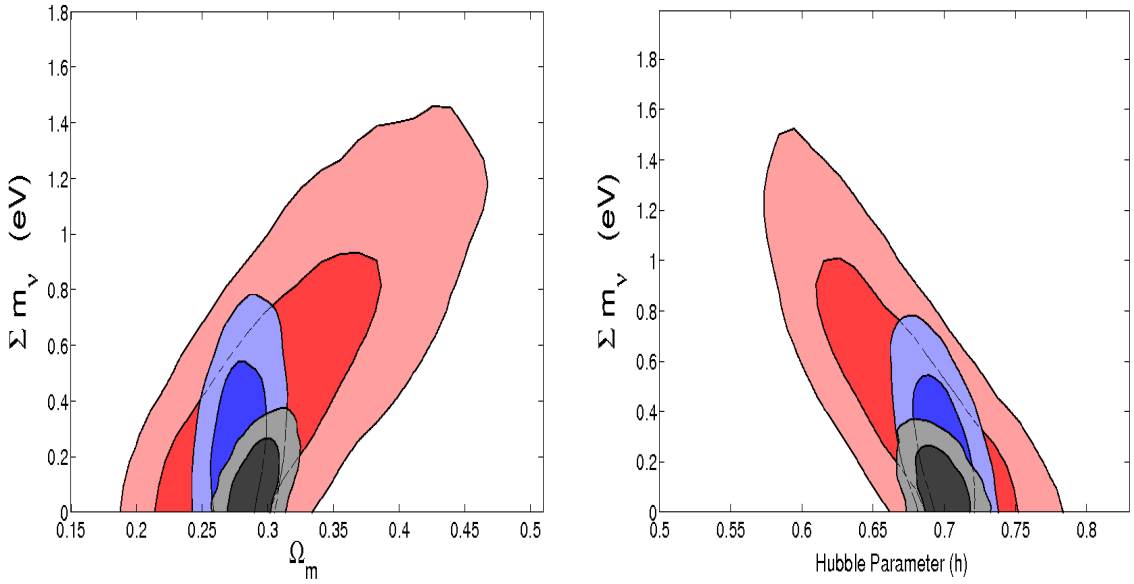

Figure 4.6: Marginalised constraints on the sum of the neutrino mass from a complete joint analysis against the matter density Ω_m and the Hubble parameter h. Each successive addition of data gives a factor of 2 improvement from the CMB (red/lighter contours); with the inclusion of SN + BAO (blue/darker contours) and finally the DR7 LRGs (grey/darkest contours). The overall bound is found to be $\sum m_\nu < 0.325$ eV at the 95% confidence level.

though it is widely used in that context the effects of the neutrino in this regime are ill-understood. It should be noted therefore that non-linearities could represent a systematic and limitation to a study such as this. However, very recently tests of the non-linear power spectrum in the presence of neutrinos and new approaches to the regime have started to emerge in order tackle this difficult issue, e.g., Hannestad *et al.* (2006), Brandbyge *et al.* (2008), Saito *et al.* (2008), Brandbyge & Hannestad (2009) and Saito *et al.* (2009). While the implementation and further testing of these procedures is very much the subject of future work, I reduce the reliance on the non-linear regime in this study by repeating the full combined analysis but truncating the maximum multipole to $\ell_{\rm max} = 200$.

4.4.2.3 Combined Results

I start by combining the MegaZ LRGs as described above with the previous CMB, SN and BAO data in a complete joint analysis. I subsequently find a significantly lower bound of $\sum m_\nu < 0.325$ eV at the 95% confidence level. Again, this is roughly a factor 2 improvement in the sum of the neutrino masses with the addition of the LRGs and is shown clearly against the matter density and

Hubble parameter in Figure 4.6. A plot of all parameter combinations compared to the CMB-only study is displayed in Figure 4.7. Furthermore, the cosmology corresponding to the best fit values is plotted in Figure 4.9 compared to the data used. The improvement in the 1D marginalised distribution is illustrated further in Figure 4.10. No evidence for massive neutrinos is found in the data.

For interest I also repeat this analysis using instead the MegaZ DR4 galaxy clustering data. The differences and subtleties in this catalogue are discussed thoroughly in Section 3.5.2.1 and Section 3.5.3. Using this data set gives a slight further improvement in constraint with $\sum m_\nu < 0.2996$ eV. This could be the result of the slightly stricter errors on Ω_m and $f_b = \Omega_b/\Omega_m$ between the releases (Section 3.5.3).

As stated before the information on the growth of structure is paramount to the improvement seen in the neutrino study. However, part of this information originates from the non-linear regime and could systematically bias the inferred constraint. While work continues into the effects of the neutrino on these scales I repeat the primary combined analysis (DR7) with the most non-linear of scales removed. By truncating the multipoles at $\ell_{\rm max} = 200$ the more conservative approach is seen to give a similar but slightly relaxed limit of $\sum m_\nu < 0.393$ eV. While this highlights the importance of understanding non-linearities for obtaining the most stringent constraints, it is reassuring that there is still a marked improvement on the previous study (CMB+SN+BAO) with the linear LRGs.

It is also intriguing to examine the input of the LRGs to the constraint with the two distance measures (SN+BAO) removed. These have previously been highly beneficial to the uncertainty. I therefore perform a joint analysis using just the WMAP5 and LRG (DR7) data. I subsequently obtain the limit $\sum m_\nu < 0.651$ eV at the 95% confidence level. This is comparable with the *spectroscopic* DR7 galaxy clustering addition to the CMB in Reid *et al.* (2009) with $\sum m_\nu < 0.62$ eV. These are both comparable but naturally tighter than the earlier data analysis provided by Tegmark *et al.* (2006) where $\sum m_\nu < 0.9$ eV.

I conclude the combined constraint on the neutrino by adding the new HST prior on the Hubble parameter to the original WMAP5 + SN + BAO + MegaZ LRG DR7 run. The improved prior was recently found to be: $H_0 = 74.2 \pm 3.6\ {\rm km\ s^{-1} Mpc^{-1}}$ by Riess *et al.* (2009). With this information added the final limit in this study is reduced to $\sum m_\nu < 0.281$ eV at the 95% confidence level. The constraint is one of the tightest current bounds available without the use of data from Lyman-α (E.g. Seljak *et al.* (2006)) or a complicated modelling of the bias (de Bernardis *et al.* 2008). However, I leave a more complete discussion of other works for the following subsection.

The parameter distributions for the last three additional cosmological analyses are displayed in Figure 4.8.

4.5 Discussion and Conclusion

4.5.1 Systematics and further work

4.5.1.1 Non-linearities

It is clear from the incredibly tight bounds placed on the neutrino in the previous subsections and from the complementary analysis with the CMB in Section 3.7 that the LRG spectrum is a powerful addition to any cosmological constraint. However, despite the possible gain this often comes with information extracted in the non-linear regime. As alluded to before, this regime is tested in the ΛCDM framework (E.g. Smith *et al.* (2003)) but any deviations from this represent an extrapolation.

A recent method to probe into the mildly non-linear regime with neutrinos is through standard perturbation theory (SPT). This next order correction or *one-loop* correction has been highlighted by e.g. Saito *et al.* (2008) and Saito *et al.* (2009). An alternative suggestion is the use of nuisance parameters including a non-linear correction parameter $Q_{\rm nl}$ (Cole *et al.* 2005). This has been used also in Tegmark *et al.* (2006). Alternatively, Hannestad *et al.* (2006) has suggested the power spectrum to be taken as a weighted average of the neutrino and baryon and cold dark matter power spectra (Equation 4.8). This has been used, for example, in Tereno *et al.* (2009).

$$P_m(k) = [f_\nu \sqrt{P\nu^L(k)} + (f_b + f_c)\sqrt{P^{NL}_{b+c}(k)}]^2 \tag{4.8}$$

Given the lack of testing, range of validity or recent emergence of some these methods the approach taken here is to use the Smith *et al.* (2003) fitting function with the most non-linear scales removed ($\ell > 300$). A more conservative bound was inferred by placing a strict cut in multipole space $\ell = 200$. This still gave a significant improvement in the sum of the masses from a CMB+SN+BAO calculation ($\sum m_\nu = 0.695 \rightarrow 0.393$ eV).

In the future it would be interesting to test the effect of these new procedures on the data and previous constraints and see if there is any bias induced by neglecting them (or between them). Early work in Saito *et al.* (2009) implies this could bias the equation of state parameter w_0. This might be more severe for future large scale structure surveys where the direct contribution from the galaxy clustering or weak lensing is not as statistically limited. One could examine the predictions

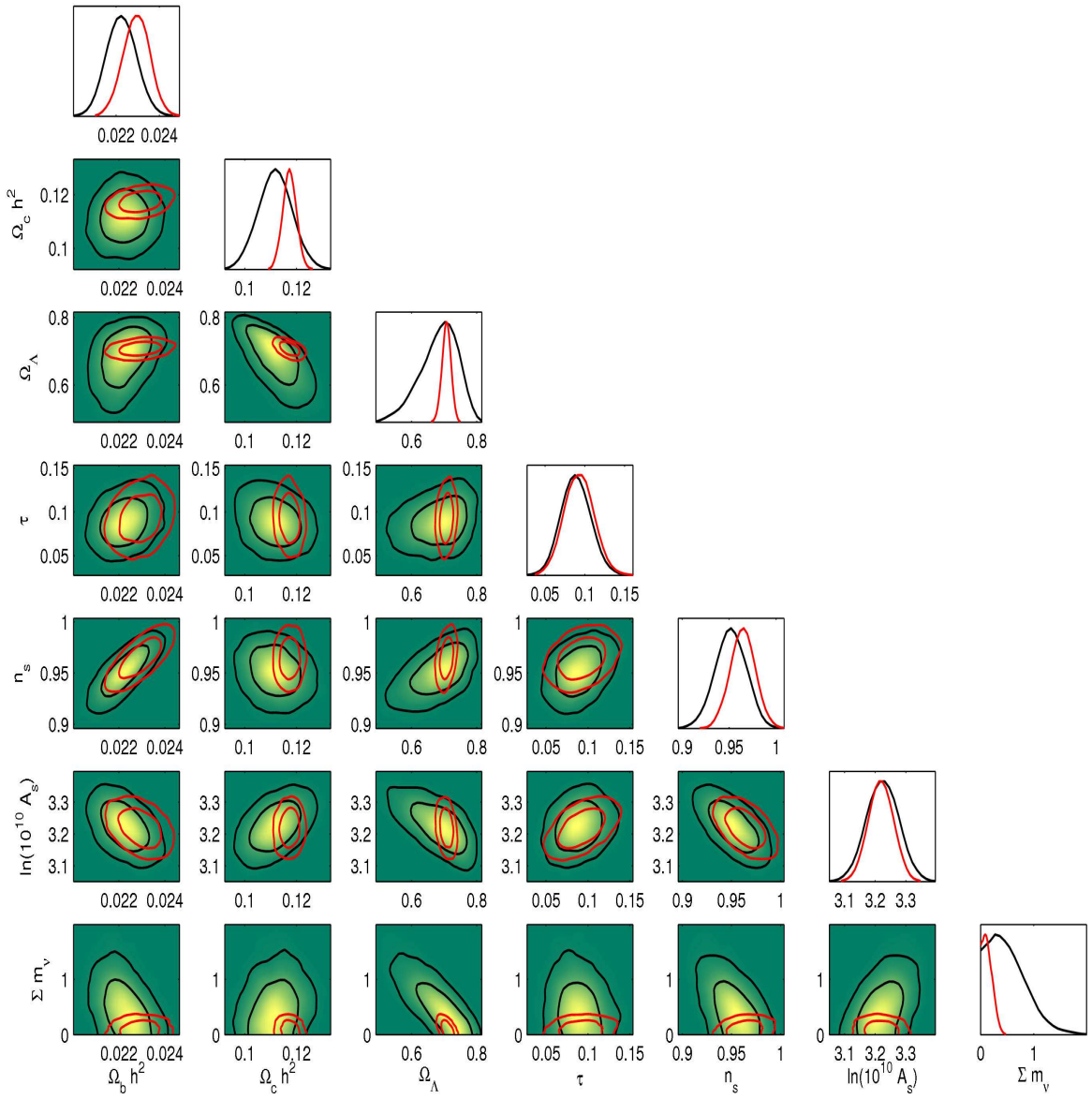

Figure 4.7: The two dimensional 68% and 95% contours and marginalised one dimensional distributions for 7 cosmological parameters ($\Omega_b h^2$, $\Omega_c h^2$, Ω_Λ, n_s, τ, $\ln(10^{10} A_s)$ and $\sum m_\nu$) in a WMAP5 + SN + BAO + MegaZ DR7 combined constraint. The amplitude of the Sunyaev-Zeldovich fluctuations (A_{SZ}) is included in the analysis but is not plotted. The black contours are given by a WMAP-only analysis, whereas the red constraints are with the addition of MegaZ DR7. For the latter analysis four bias parameters have been marginalised. The data constrains the sum of the neutrino masses to $\sum m_\nu < 0.325$ eV (95% CL).

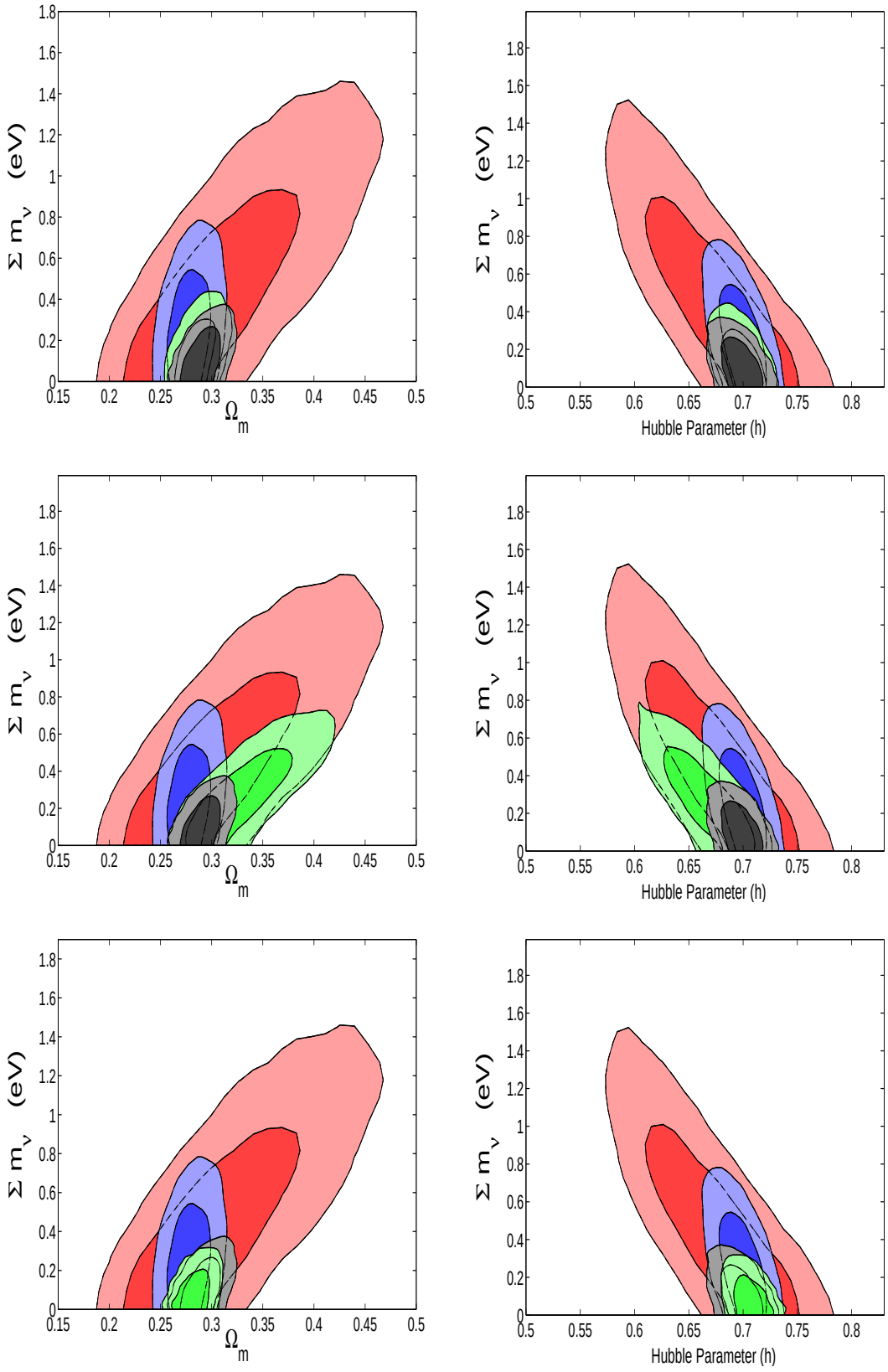

Figure 4.8: The marginalised distributions for three additional cosmological analyses (green contours) are plotted against the previous neutrino bounds. Upper Panels: The contribution from the more non-linear regime is removed by truncating the MegaZ multipole scale at $l_{\max} = 200$ ($\sum m_\nu < 0.393$ eV). Middle Panels: The LRGs are seen to provide approximately equal gain to the CMB as the SN and BAOs when the distance measures are removed ($\sum m_\nu < 0.651$ eV). Bottom Panels: The addition of the new HST prior restricts the parameter space further still, rendering one of the tightest current constraints ($\sum m_\nu < 0.281$ eV).

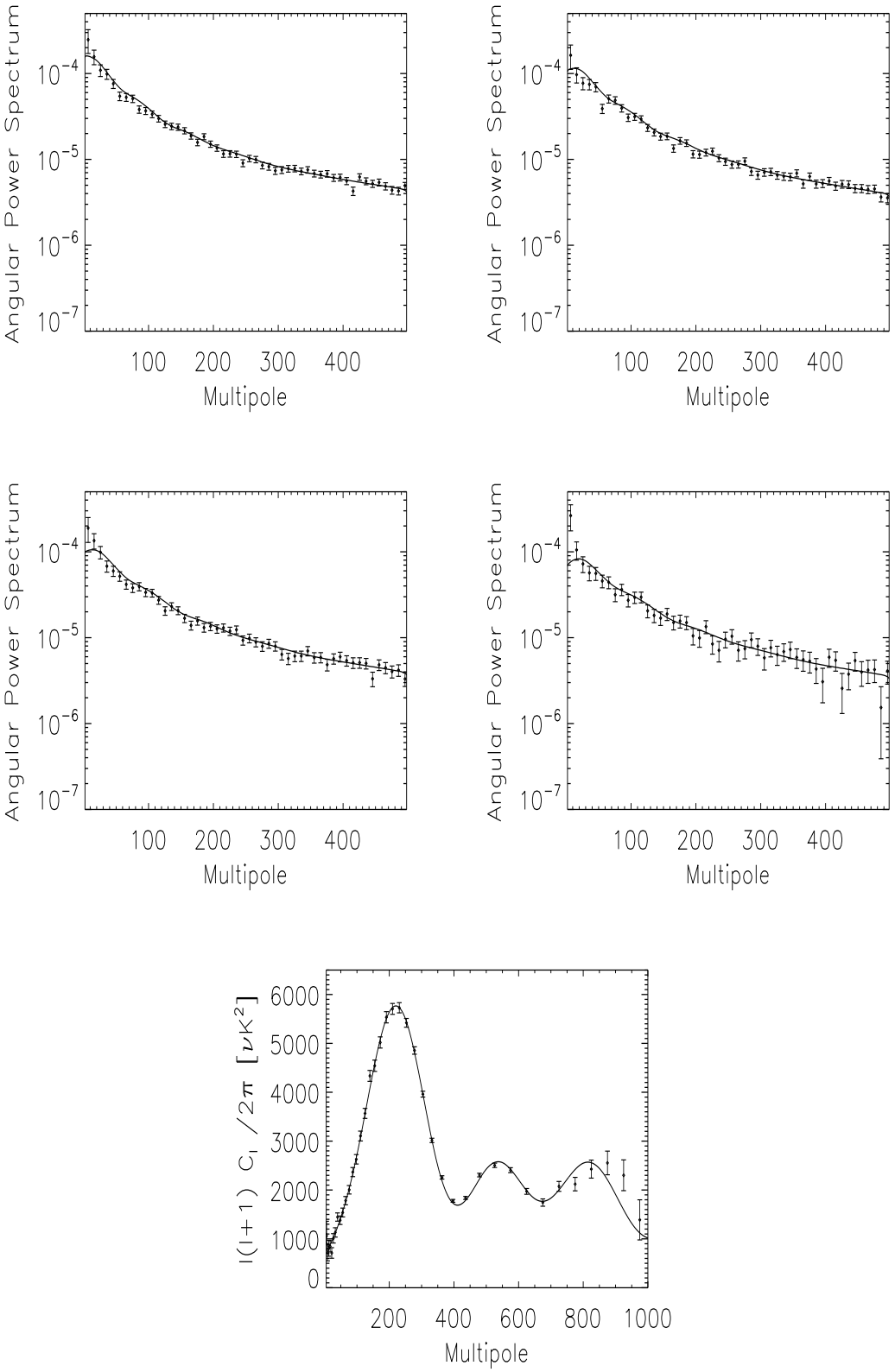

Figure 4.9: The theoretical galaxy angular power spectra (top four panels) and theoretical CMB power spectrum (bottom panel) are plotted for the best fit values found in the CMB+SN+BAO+MegaZ LRG DR7 analysis (solid lines). These are compared to the data points in MegaZ DR7 and WMAP5, respectively. There is no observed discrepancy between the best fit models and the data. The top four panels correspond to redshift bin 1 (top left; $0.45 < z < 0.5$), bin 2 (top right; $0.5 < z < 0.55$), bin 3 (middle left; $0.55 < z < 0.6$) and bin 4 (middle right; $0.6 < z < 0.65$).

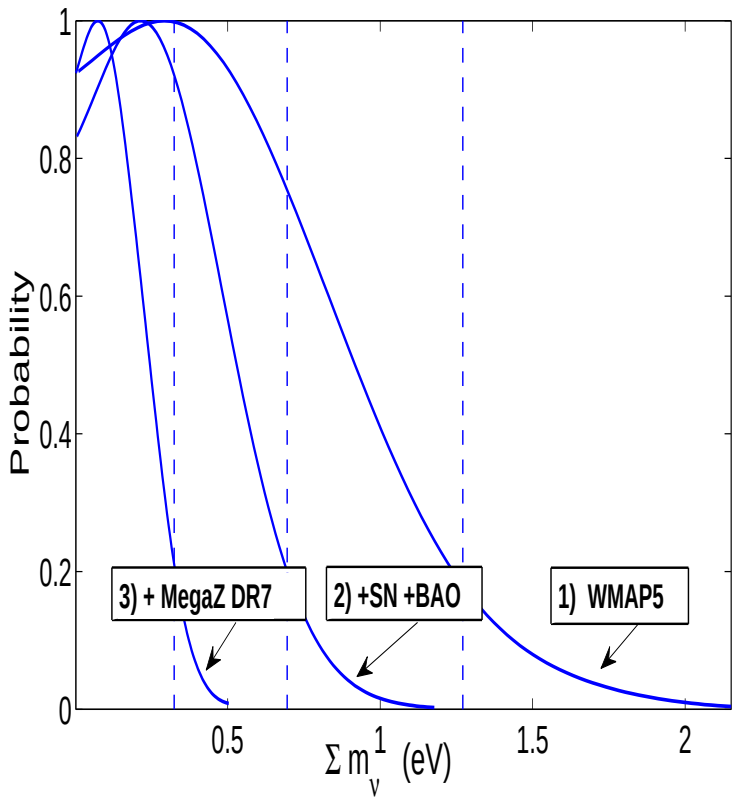

Figure 4.10: The 1D marginalised distributions for the sum of the neutrino mass $\sum m_\nu$ are highlighted above (solid lines). The bounds displayed are the result of a WMAP5 analysis ($\sum m_\nu < 1.271$ eV) that is shown to decrease dramatically with the inclusion of SN and BAOs ($\sum m_\nu < 0.695$ eV) and also with the further addition of MegaZ DR7 ($\sum m_\nu < 0.325$ eV). No evidence for massive neutrinos is observed and so all constraints correspond to *upper bounds*. These levels and the vertical dashed lines denote 95% confidence levels.

separately with a Fisher matrix forecast. In addition, a greater number of N-body simulations must be performed with the presence of neutrinos to probe the regime fully. Early work on such simulations include e.g. Brandbyge *et al.* (2008) and Brandbyge & Hannestad (2009).

4.5.1.2 Extended Parameter Space

The combined constraints have been derived by varying a total of 12 parameters, including the normalisation of SZ fluctuations in the CMB and four bias parameters in the galaxy survey. While a substantial sample of parameter space there are potentially extensions that could degrade or shift the results of the previous sections.

Effective Number of Species

The number of massive neutrinos has been fixed to 3.04 in this study. This assumes there

are no sterile neutrinos or other relativistic degrees of freedom. These potential species are often parameterised in terms of the *effective* number of neutrinos $N_{\rm eff}$. Variations in this quantity allow a displacement in the time of matter and radiation equality in the early Universe. Subsequently it is degenerate with the matter density and can weaken the best possible constraint. The effective number of species has been analysed previously in a number of papers, including Goobar *et al.* (2006), Ichikawa *et al.* (2007), Komatsu *et al.* (2009), Dunkley *et al.* (2009), Reid *et al.* (2009) and references therein. In future work I intend to extend the previous parameter space to account for $N_{\rm eff}$ as a free parameter.

Equation of State

As described earlier allowing for a more general dark energy model $w \neq -1$ does not significantly alter the neutrino constraint for a combination of WMAP+SN+BAO (Komatsu *et al.* 2009). However, the sum of the neutrino masses has been shown to be degenerate with the equation of state in the presence of data from the late time Universe (Hannestad 2005). This can be understood by considering that an increase in the expansion history (less negative w_0) will suppress the growth of matter fluctuations, similar to the effect of the free-streaming particles. As for the other studies highlighted in Figure 4.1 the results quoted here are for a ΛCDM cosmology and similarly represent the benchmark of a more stringent restriction of parameters. It will be interesting to see how the complete joint analysis will change with this extra parameter freedom and is the subject of future work.

The Galaxy Bias

By marginalising over the four bias parameters information mainly on the shape of the power spectrum was used. However, the exact relationship between galaxies and their tracing of the underlying mass distribution is unknown. It could be that the bias is some function of scale $b(k)$ (E.g. Swanson *et al.* (2008) and Cresswell & Percival (2009)). In this case the biasing mechanism could act to mimic (oppose) the neutrino signature in the galaxy clustering measurement by suppressing (boosting) the power of fluctuations over smaller scales. This is similar to allowing for a running of the spectral index but in this case would be seen in the CMB as well as the galaxy survey. Testing for a more extended bias model is beyond the scope of this work but could be an interesting avenue for future work. Moreover, it would also be interesting to examine the constraints using various galaxy types in order to get a measure on the *relative* biasing of the galaxies. The motivation is that if one expects the galaxy field to be correlated with the dark matter field then all the galaxy fields should be directly correlated with each other. This will be possible with future/upcoming projects such as the Square Kilometre Array (SKA; Abdalla & Rawlings (2007)), DES or Pan-Starrs.

$\sum m_\nu$ 95% CL	Analysis	Comments
< 1.3 eV	Komatsu *et al.* (2009)	WMAP5
< 0.9 eV	Tegmark *et al.* (2006)	WMAP3 + SDSS
< 0.67 eV	Komatsu *et al.* (2009)	WMAP5 + SN + BAO
< 0.62 eV	Reid *et al.* (2009)	WMAP5 + SDSS (DR7)
< 0.54 eV	Ichiki *et al.* (2009)	WMAP5 + SN + BAO + CFHTLS WL
< 0.54 eV	Tereno *et al.* (2009)	WMAP5 + SN + BAO + CFHTLS WL
< 0.471 eV	Li *et al.* (2009)	CMB + WL + SDSS + SN
< 0.28 eV	de Bernardis *et al.* (2008)	WMAP5 + SDSS + bias $b_g(L)$
< 0.17 eV	Seljak *et al.* (2006)	CMB + SDSS + 2dF +SN + Lyα

Table 4.1: A brief list of other recent cosmological studies on the absolute mass scale is included above. All the bounds quoted are for ΛCDM cosmologies at the 95% confidence level. 'CMB' and 'WL' denote an analysis that contains a range of CMB or Weak Lensing data, respectively. $b_g(L)$ corresponds to a luminosity dependent bias measurement. For a detailed breakdown of the analyses the reader is referred to the papers themselves.

4.5.2 Other Studies

At the present the addition of LRGs are far more effective for constraining the absolute mass scale than current weak lensing data. The preliminary studies by Tereno *et al.* (2009) and Ichiki *et al.* (2009) with CFHTLS data (Section 2.4.2) both find $\sum_\nu < 0.54\mathrm{eV}$ at the 95% confidence level for a CMB+SN+BAO+CFHTLS joint analysis. The lack of substantial improvement with the lensing data is a result of a similar degeneracy between the neutrinos and Ω_m, where the neutrinos' suppression of the inhomogeneities can be compensated by an increase in Ω_m (or σ_8). It is also mainly a property of the probe being a *developing* tool, as the prospects for the addition of weak lensing to the mass determination are promising. Interestingly, weak lensing does not suffer any unknown biasing that is present in the galaxy clustering measurement. This is because the lensing signal responds to the entire mass distribution. It does, however, probe matter fluctuations on non-linear scales. The optimism seems well justified as it has been shown that a future probe such as Euclid (Refregier *et al.* 2008) could even be sensitive to the neutrino mass hierarchy with the addition of Planck data (De Bernardis *et al.* 2009).

The $\sum m_\nu < 0.281$ eV limit found in this Chapter represents one of the most stringent constraints placed in the literature. A small list of some of the most recent and competitive studies is

therefore given in Table 4.1. Within this table two papers have constraints that are similar to the one mentioned above. The de Bernardis *et al.* (2008) study uses a measurement of the luminosity-dependent bias $b_g(L)$ at various redshifts for three different surveys and adds this information to a WMAP5 and SDSS LRG constraint. They find $\sum m_\nu < 0.28\mathrm{eV}$ for a ΛCDM Universe, which relaxes to $\sum m_\nu < 0.59\mathrm{eV}$ in the presence of a general dark energy model ($w_0 \neq -1$). The Seljak *et al.* (2006) analysis represents the tightest bound placed on the neutrino to date $\sum m_\nu < 0.17\mathrm{eV}$. This uses a range of CMB surveys in addition to SDSS galaxy clustering and supernovae data. However, the main gain in parameter uncertainty arises from use of Lyman-α. This cosmological tool probes the underlying mass distribution by looking at quasar absorption in intervening hydrogen. There is great uncertainty, however, as to how this gas traces the distribution. This could be subject to unknown winds or complex local physics, for example. There appears to be tension at around 2σ in the amplitude of the power spectrum between the Lyman-α and CMB data. To compound this issue Seljak *et al.* (2006) also find evidence at 2.5σ for more than 3 effective neutrino species.

Considering the above the $\sum m_\nu < 0.281$ eV limit in this work is the tightest constraint on the sum of the neutrino masses without the need for higher knowledge on complex biasing or higher knowledge of complex gas physics. However, in the future we are not only interested in tight neutrino constraints, but also trustworthy neutrino constraints. This is why the previous suggestions for further work necessarily involve working on the associated systematics and extensions to the cosmological model. Despite this, preliminary work on neutrino forecasts for future surveys, such as the Dark Energy Survey (Lahav *et al.* 2009), Euclid (De Bernardis *et al.* 2009) and the SKA (Abdalla & Rawlings 2007) highlight that the gain in statistical information will be substantial.

CHAPTER 5

FUTURE WORK AND CONCLUSION

This chapter discusses some of the issues pertaining to the previous three chapters. This includes the limitations and applicability of the methods and developments relating to these on the horizon. The following therefore represents suggestions for *future work*. However, it should be noted that this does not consist of all the suggestions for future work, given that segments will have been discussed while relevant in the preceding chapters.

I finish by summarising the work in this thesis in Section 5.4.

5.1 The Non-linear Regime

The work examined in Chapters 2 and 4 have both been affected or limited by the non-linear regime with current data. As stated previously this is usually tackled by using the fitting functions of Peacock & Dodds (1996) and Smith *et al.* (2003) found with detailed N-body simulations. This was the procedure followed in Chapter 3 where I used my constructed SDSS II angular power spectra to place constraints on the *standard* cosmological model. The other chapters are studies of deviations from this model and so such an application is an extrapolation of validity. Brute force application could systematically bias the inferred parameters or fail to encapsulate any subtle signatures at this scale. With the advent of high precision probes such as the Dark Energy Survey (DES) or Euclid (Section 2.6) and consequently higher statistical discrimination, the need for a correct treatment or a quantification of the systematic error induced is even more vital.

5.1.1 Modified Gravity

The most obvious concern for using any available prescription for the non-linearities in modified gravity is that they have been evaluated using general relativity. Any use is therefore an extrapolation of the framework especially given that the clustering is a gravitational effect.

A more pernicious problem concerns the potential scale or environmental dependence of the modifications. Some theories, such as f(R), include an extra scalar degree of freedom that behaves as an additional field. The extent over which this field acts depends on the local curvature and density. The current fitting functions, such as Smith *et al.* (2003), determine the non-linear regime from a mapping of the linear spectrum. For any theory where the extra field is suppressed at high curvature there will be a change in the behaviour of the gravity when non-linear. This is *not* encapsulated by the linear range of scales. It is this scale dependence that eludes the aforementioned prescriptions.

In fact, due to the stringent constraints on gravity from solar system tests (E.g. Will (1993), Chiba *et al.* (2006) and Erickcek *et al.* (2006)) any viable theory *must* degrade the extra field in the high density environment and subsequently tend to a 'general relativity-like' gravity. This non-linear process is often referred to as the chameleon mechanism (Khoury & Weltman 2004).

Some progress can be made with the use of perturbation theory (E.g. Koyama *et al.* 2009) but this has a limited range of validity to quasi-linear scales $k \sim 0.1\ \mathrm{h\ Mpc^{-1}}$. In this way the *deeply* non-linear regime remains beyond the scope of conventional methods and the application of such data is suspect.

The Interpolation Function

Despite the fact that this appears to be a dire situation there is a subtlety above that has led to recent developments. This concerns the idea that the actual power spectrum (including the *fully* non-linear) must therefore be an interpolation between modified gravity, with the extra field and no chameleon suppression, and normal general relativity with the same expansion history as the new theory at small scales. Hu & Sawicki (2007) found such an interpolating function and it is described by,

$$P(k,z) = \frac{P_{MG}(k,z) + c_{nl}\Sigma^2(k,z)P_{GR}(k,z)}{1 + c_{nl}(z)\Sigma^2(k,z)}. \tag{5.1}$$

In this equation c_{nl} determines the scale for the interpolation to general relativity; $\Sigma^2(k,z)$ details the degree of non-linearity at a given scale; $P_{MG}(k,z)$ is the power spectrum for the environment independent modified gravity and $P_{GR}(k,z)$ is standard general relativity with the same expansion history. For each of the two $P(k,z)$ a fitting function such as that from Smith *et al.* (2003) can be

used.

Hu & Sawicki (2007) also proposed a parameterised form for the degree of non-linearity, which is given by,

$$\Sigma^2(k,z) = \left(\frac{k^3}{2\pi^2}P_{\rm linear}(k,z)\right)^a \tag{5.2}$$

and Koyama *et al.* (2009) have suggested a general expression for the possible redshift dependence of c_{nl} expressed as,

$$c_{nl} = A(1+z)^b. \tag{5.3}$$

For the DGP model these expressions were calibrated with perturbation theory (Koyama *et al.* 2009) in the quasi-linear regime and checked for consistency and extrapolation against the N-body simulations of Oyaizu *et al.* (2008). They subsequently found $a = 1$, $A = 0.3$ and $b = 0.16$ to be good fits.

It would be interesting to see how this new non-linear treatment affects the constraints on mDGP from lensing given in Section 2.5.2 and in particular the analysis with all angular scales in Figure 2.10. However, due to the lower statistical power of the current weak lensing data it might prove more insightful to examine how this would alter the forecasts for Euclid. One could use this as an example to quantify how an incorrect prescription for the regime will bias the inferred constraining power relative to the brute force application of the usual scaling relation. Preliminary work in this area has already started to appear very recently, e.g., Beynon *et al.* (2009).

Furthermore, despite the early work of Oyaizu (2008), Oyaizu *et al.* (2008) and Schmidt *et al.* (2009) it is imperative that further N-body simulations are carried out for a range of models to high resolution (large k). It will be interesting to apply this interpolating function to simulated cosmologies in order to test the accuracy of any reconstructed power spectrum and the range of validity. If it does describe the deeply non-linear regime well and if one quantifies the systematic uncertainty it induces, it might have a role to play in the search for modified gravity in the next generation of data.

5.1.2 Neutrinos

Like the interpolation model described above several fitting functions or approximate methods exist to describe the impact of neutrinos on the non-linear power spectrum. This includes the weighted average of the neutrino, baryon and cold dark matter power spectra proposed by Hannestad *et al.* (2006) and shown previously in Equation 4.8. A more technical approach is through the

use of higher order perturbations (or *one loop corrections*) that probe the mildly non-linear regime. See Saito *et al.* (2008), Saito *et al.* (2009) and references therein.

While the deeply and quasi-linear regimes were removed in the combined constraint on the neutrinos in Section 4.4.2.3 it would be interesting to test these approaches on the data given its high discriminatory power. This would allow a more robust measurement at the tightest end of the constraint and, furthermore, the potential to quantify the biasing induced on any parameters by neglecting it. Naturally this reasoning can be extended to forecasts for future probes such as Euclid or the Dark Energy Survey. In addition, a comparison between the methods and to continuing N-body simulations would allow the most thorough test. N-body simulations with neutrino components have begun to emerge with e.g., Brandbyge *et al.* (2008) and Brandbyge & Hannestad (2009).

5.2 The Extended Neutrino Parameter Space

The neutrino bounds found in Chapter 4 were evaluated and compared to other studies in a flat ΛCDM cosmology. A natural extension of this work is to extend the parameter space to other potential physical phenomena.

5.2.1 The Equation of State

An example of the aforementioned extension is to relax the restriction placed on the equation of state ($w_0 \neq -1$). A change in the expansion history can act to either suppress or boost the power of fluctuations relative to a cosmological constant (see Chapter 2) and thus partially mimic the effects of the neutrino. In this way the equation of state can be degenerate with the sum of the neutrino masses. Allowing this freedom is an intention for future work.

5.2.2 The Effective Number of Neutrinos

In addition, the effective number of neutrinos $N_{\rm eff}$ was fixed to 3.04 for all cosmological analyses. Allowing for a variation in this parameter can also degrade the neutrinos' constraint but gives a more realistic and robust measurement. Again, including this for the combined constraint analysis is an aim of future work.

These extensions of the parameter space are discussed in more detail in Section 4.5.1.2.

5.3 A Cosmological Comparison of Photometric Codes

The galaxy clustering constraint on the cosmological model in Chapter 3 was the consequence of a photometric redshift survey (SDSS DR7). The redshift estimates were assigned to the galaxy objects using ANNz (Collister & Lahav 2004) an Artificial Neural Network code. For future work I intend to use the catalogues produced for Data Release 6 (DR6; Abdalla *et al.* (2008)) to test the effect of photometric codes on cosmological bounds. This is possible for DR6 because the corresponding catalogue was evaluated using six different photometric codes: ANNZ (Collister & Lahav 2004), HyperZ (Bolzonella *et al.* 2000), SDSS (Padmanabhan *et al.* 2005), Le PHARE (Ilbert *et al.* 2006), BPZ (Benítez 2000) and ZEBRA (Feldmann *et al.* 2006). Performing cosmological runs for each code would constitute a cosmological comparison of the codes and test the influence of any particular code on the galaxy clustering measurement of MegaZ DR7. This is feasible because the survey areas for DR6 and DR7 are remarkably similar.

The Redshift Distribution

Continuing with the galaxy clustering analysis it is important to evaluate the role of the redshift distribution on the inferred parameters. This could be performed by including the Gaussian redshift parameters (μ, σ) as free variables or using the interpolated spectroscopic redshift distribution. This is discussed more thoroughly in Section 3.6.2.

Extra Likelihood Details

Finally, it would be intriguing to examine what extra information is gained by actually including the cross correlation C_ℓ^{ij} data in the galaxy clustering likelihood. Likewise, a cosmological constraint could easily be run including a larger range of multipole scales ($\ell > 300$). This would test the information present at highly non-linear scales.

5.4 Conclusion

This Thesis is related mainly to the growth of structure in the late-time Universe. Specifically, it addresses both the active measurement of this structure, through a galaxy survey, and the use of late-time data in constraining more fundamental underlying physics. This includes the gravitational framework and the sum of massive neutrino species. These themes were directly related to three main science chapters:

1. Constraining Modified Gravity and Growth with Weak Lensing
2. The Angular Power Spectrum of Photometric SDSS LRGs
3. A Combined Constraint on the Neutrino Mass

The conclusions of the Thesis are as follows:

- In the first chapter I performed one of the first studies on modified gravity with weak gravitational lensing data. A phenomenological model that interpolates with a parameter α between a 5D DGP braneworld model ($\alpha = 1$) and ΛCDM ($\alpha = 0$) was constrained at $\alpha < 0.58$ (1σ) and $\alpha < 0.91$ (2σ) using supernovae, baryon acoustic oscillation and linear CFHTLS lensing data. I showed this to be insensitive to potential systematics in the lensing data. The role of weak lensing in a modified gravity study was discussed and the growth of structure γ and power spectrum parameters Σ are highlighted. I subsequently found that the current data (SN+BAO+CFHTLS) is incapable of a constraint on this growth signature.

- I also looked beyond the present bounds and showed that Euclid, a future weak lensing survey, will deeply probe the nature of gravity. I predicted potential 1σ constraints of $\Delta\gamma = 0.045$ and $\Delta\Sigma = 0.25$ for a maximum multipole of $\ell_{\rm max} = 500$ (linear regime). This is tightened to $\Delta\gamma = 0.038$ and $\Delta\Sigma = 0.069$ for $\ell_{\rm max} = 10,000$ (linear and non-linear scales). Forecasted bounds are also shown for the standard cosmological framework.

- In the second chapter I constructed a new galaxy power spectrum based on the extended SDSS II Data Release 7 (DR7) *photometric* Luminous Red Galaxies (LRGs): MegaZ DR7. This encapsulated $7746\ \deg^2$ and $723,556$ LRGs between $0.45 < z < 0.65$ in a spherical harmonic analysis of the galaxy distribution. An excess of power was detected on the largest scales in the highest redshift slice similar to the previous DR4 data release, but with a reduced tension to the best fit cosmology.

- The cosmological constraints were then derived based on the newly constructed MegaZ power spectra. The excess power in the high redshift bin was demonstrated to have a substantial effect on the calculation and was therefore removed from subsequent analyses. Including the effects of the survey window function, redshift space distortions and correlations between the redshift bands I found the combined bin analysis to give cosmological limits of $f_b \equiv \Omega_b/\Omega_m = 0.173 \pm 0.046$ and $\Omega_m = 0.260 \pm 0.035$. Finally, I demonstrate the LRGs to be highly complementary to the CMB with the photometric analysis comparable to the spectroscopic DR7 release.

- In the last chapter I highlighted the degeneracies present in a combined constraint on the sum of the neutrino masses with the CMB, SN and BAOs. By then combining these probes with the earlier MegaZ DR7 data I discovered a further reduction on the previous limit by a factor of 2 ($\sum m_\nu < 0.325$ eV). With an additional HST prior this bound dropped to $\sum m_\nu < 0.281$ eV–one of the tightest constraints in the literature. Additional runs without the distance measures or the non-linear contribution were also performed, illustrating the stringent and more conservative gains available with LRGs.

Bibliography

Abate, A. & Lahav, O., 2008, *MNRAS*, L81+

Abdalla, F. B., Banerji, M., Lahav, O. & Rashkov, V., 2008, *ArXiv e-prints*

Abdalla, F. B. & Rawlings, S., 2007, *MNRAS*, **381**, 1313

Albrecht, A. & Skordis, C., 2000, *Phys. Rev. Letters*, **84**, 2076

Amendola, L., Kunz, M. & Sapone, D., 2007, *ArXiv e-prints*

Astier, P., Guy, J., Regnault, N., Pain, R., Aubourg, E., Balam, D., Basa, S., Carlberg, R. G., Fabbro, S., Fouchez, D., Hook, I. M., Howell, D. A., Lafoux, H., Neill, J. D., Palanque-Delabrouille, N., Perrett, K., Pritchet, C. J., Rich, J., Sullivan, M., Taillet, R., Aldering, G., Antilogus, P., Arsenijevic, V., Balland, C., Baumont, S., Bronder, J., Courtois, H., Ellis, R. S., Filiol, M., Gonçalves, A. C., Goobar, A., Guide, D., Hardin, D., Lusset, V., Lidman, C., McMahon, R., Mouchet, M., Mourao, A., Perlmutter, S., Ripoche, P., Tao, C. & Walton, N., 2006, *A&A*, **447**, 31

Bacon, D., Refregier, A. & Ellis, R., 2000, *MNRAS*, **318**, 625

Bartelmann, M. & Schneider, P., 2001, , **340**, 291

Benítez, N., 2000, *ApJ*, **536**, 571

Benjamin, J., Heymans, C., Semboloni, E., van Waerbeke, L., Hoekstra, H., Erben, T., Gladders, M. D., Hetterscheidt, M., Mellier, Y. & Yee, H. K. C., 2007, *MNRAS*, **381**, 702

Bertschinger, E. & Zukin, P., 2008, *ArXiv e-prints*, **801**

Beynon, E., Bacon, D. J. & Koyama, K., 2009, *ArXiv e-prints*

Blackman, R. B. & Tukey, J. W., 1959

Blake, C. & Bridle, S., 2005, *MNRAS*, **363**, 1329

Blake, C., Collister, A., Bridle, S. & Lahav, O., 2007, *MNRAS*, **374**, 1527

Blake, C., Ferreira, P. G. & Borrill, J., 2004, *MNRAS*, **351**, 923

Bolzonella, M., Miralles, J. M. & Pelló, R., 2000, *A&A*, **363**, 476

Brandbyge, J. & Hannestad, S., 2009, *Journal of Cosmology and Astro-Particle Physics*, **5**, 2

Brandbyge, J., Hannestad, S., Haugbølle, T. & Thomsen, B., 2008, *Journal of Cosmology and Astro-Particle Physics*, **8**, 20

Bridle, S., Balan, S. T., Bethge, M., Gentile, M., Harmeling, S., Heymans, C., Hirsch, M., Hosseini, R., Jarvis, M., Kirk, D., Kitching, T., Kuijken, K., Lewis, A., Paulin-Henriksson, S., Scholkopf, B., Velander, M., Voigt, L., Witherick, D., Amara, A., Bernstein, G., Courbin, F., Gill, M., Heavens, A., Mandelbaum, R., Massey, R., Moghaddam, B., Rassat, A., Refregier, A., Rhodes, J., Schrabback, T., Shawe-Taylor, J., Shmakova, M., van Waerbeke, L. & Wittman, D., 2009, *ArXiv e-prints*

Bridle, S., Shawe-Taylor, J., Amara, A., Applegate, D., Balan, S. T., Berge, J., Bernstein, G., Dahle, H., Erben, T., Gill, M., Heavens, A., Heymans, C., High, F. W., Hoekstra, H., Jarvis, M., Kirk, D., Kitching, T., Kneib, J., Kuijken, K., Lagatutta, D., Mandelbaum, R., Massey, R., Mellier, Y., Moghaddam, B., Moudden, Y., Nakajima, R., Paulin-Henriksson, S., Pires, S., Rassat, A., Refregier, A., Rhodes, J., Schrabback, T., Semboloni, E., Shmakova, M., van Waerbeke, L., Witherick, D., Voigt, L. & Wittman, D., 2008, *ArXiv e-prints*

Cabré, A. & Gaztañaga, E., 2009, *MNRAS*, **393**, 1183

Cannon, R., Drinkwater, M., Edge, A., Eisenstein, D., Nichol, R., Outram, P., Pimbblet, K., de Propris, R., Roseboom, I., Wake, D., Allen, P., Bland-Hawthorn, J., Bridges, T., Carson, D., Chiu, K., Colless, M., Couch, W., Croom, S., Driver, S., Fine, S., Hewett, P., Loveday, J., Ross, N., Sadler, E. M., Shanks, T., Sharp, R., Smith, J. A., Stoughton, C., Weilbacher, P., Brunner, R. J., Meiksin, A. & Schneider, D. P., 2006, *MNRAS*, **372**, 425

Carroll, S. M., Duvvuri, V., Trodden, M. & Turner, M. S., 2004, , **70**(4), 043528

Chiba, T., Smith, T. L. & Erickcek, A. L., 2006, *ArXiv e-prints*

Cimatti, A., Robberto, M., Baugh, C., Beckwith, S. V. W., Content, R., Daddi, E., De Lucia, G., Garilli, B., Guzzo, L., Kauffmann, G., Lehnert, M., Maccagni, D., Martínez-Sansigre, A., Pasian, F., Reid, I. N., Rosati, P., Salvaterra, R., Stiavelli, M., Wang, Y., Osorio, M. Z., Balcells, M., Bersanelli, M., Bertoldi, F., Blaizot, J., Bottini, D., Bower, R., Bulgarelli, A., Burgasser, A., Burigana, C., Butler, R. C., Casertano, S., Ciardi, B., Cirasuolo, M., Clampin, M., Cole, S., Comastri, A., Cristiani, S., Cuby, J., Cuttaia, F., de Rosa, A., Sanchez, A. D., di Capua, M., Dunlop, J., Fan, X., Ferrara, A., Finelli, F., Franceschini, A., Franx, M., Franzetti, P., Frenk, C., Gardner, J. P., Gianotti, F., Grange, R., Gruppioni, C., Gruppuso, A., Hammer, F., Hillenbrand, L., Jacobsen, A., Jarvis, M., Kennicutt, R., Kimble, R., Kriek, M., Kurk, J., Kneib, J., Le Fevre, O., Macchetto, D., MacKenty, J., Madau, P., Magliocchetti, M., Maino, D., Mandolesi, N., Masetti, N., McLure, R., Mennella, A., Meyer, M., Mignoli, M., Mobasher, B., Molinari, E., Morgante, G., Morris, S., Nicastro, L., Oliva, E., Padovani, P., Palazzi, E., Paresce, F., Perez Garrido, A., Pian, E., Popa, L., Postman, M., Pozzetti, L., Rayner, J., Rebolo, R., Renzini, A., Röttgering, H., Schinnerer, E., Scodeggio, M., Saisse, M., Shanks, T., Shapley, A., Sharples, R., Shea, H., Silk, J., Smail, I., Spanó, P., Steinacker, J., Stringhetti, L., Szalay, A., Tresse, L., Trifoglio, M., Urry, M., Valenziano, L., Villa, F., Villo Perez, I., Walter, F., Ward, M., White, R., White, S., Wright, E., Wyse, R., Zamorani, G., Zacchei, A., Zeilinger, W. W. & Zerbi, F., 2009, *Experimental Astronomy*, **23**, 39

Clowe, D., Bradač, M., Gonzalez, A. H., Markevitch, M., Randall, S. W., Jones, C. & Zaritsky, D., 2006, *ApJL*, **648**, L109

Cole, S., Percival, W. J., Peacock, J. A., Norberg, P., Baugh, C. M., Frenk, C. S., Baldry, I., Bland-Hawthorn, J., Bridges, T., Cannon, R., Colless, M., Collins, C., Couch, W., Cross, N. J. G., Dalton, G., Eke, V. R., De Propris, R., Driver, S. P., Efstathiou, G., Ellis, R. S., Glazebrook, K., Jackson, C., Jenkins, A., Lahav, O., Lewis, I., Lumsden, S., Maddox, S., Madgwick, D., Peterson, B. A., Sutherland, W. & Taylor, K., 2005, *MNRAS*, **362**, 505

Colless, M., Dalton, G., Maddox, S., Sutherland, W., Norberg, P., Cole, S., Bland-Hawthorn, J., Bridges, T., Cannon, R., Collins, C., Couch, W., Cross, N., Deeley, K., De Propris, R., Driver, S. P., Efstathiou, G., Ellis, R. S., Frenk, C. S., Glazebrook, K., Jackson, C., Lahav, O., Lewis, I., Lumsden, S., Madgwick, D., Peacock, J. A., Peterson, B. A., Price, I., Seaborne, M. & Taylor, K., 2001, *MNRAS*, **328**, 1039

Collister, A., Lahav, O., Blake, C., Cannon, R., Croom, S., Drinkwater, M., Edge, A., Eisenstein,

D., Loveday, J., Nichol, R., Pimbblet, K., de Propris, R., Roseboom, I., Ross, N., Schneider, D. P., Shanks, T. & Wake, D., 2007, *MNRAS*, **375**, 68

Collister, A. A. & Lahav, O., 2004, *PASP*, **116**, 345

Cresswell, J. G. & Percival, W. J., 2009, *MNRAS*, **392**, 682

Crittenden, R. G., Natarajan, P., Pen, U. & Theuns, T., 2002, *ApJ*, **568**, 20

Crittenden, R. G., Natarajan, P., Pen, U.-L. & Theuns, T., 2001, *ApJ*, **559**, 552

Csabai, I., Budavári, T., Connolly, A. J., Szalay, A. S., Győry, Z., Benítez, N., Annis, J., Brinkmann, J., Eisenstein, D., Fukugita, M., Gunn, J., Kent, S., Lupton, R., Nichol, R. C. & Stoughton, C., 2003, *AJ*, **125**, 580

Daniel, S. F., Caldwell, R. R., Cooray, A. & Melchiorri, A., 2008, , **77**(10), 103513

De Bernardis, F., Kitching, T. D., Heavens, A. & Melchiorri, A., 2009, *ArXiv e-prints*

de Bernardis, F., Serra, P., Cooray, A. & Melchiorri, A., 2008, , **78**(8), 083535

Deffayet, C., 2001, *Phys. Lett.*, **B502**, 199

Dodelson, S., 2003, *Modern cosmology*

Doré, O., Martig, M., Mellier, Y., Kilbinger, M., Benjamin, J., Fu, L., Hoekstra, H., Schultheis, M., Semboloni, E. & Tereno, I., 2007, *ArXiv e-prints*

Dunkley, J., Komatsu, E., Nolta, M. R., Spergel, D. N., Larson, D., Hinshaw, G., Page, L., Bennett, C. L., Gold, B., Jarosik, N., Weiland, J. L., Halpern, M., Hill, R. S., Kogut, A., Limon, M., Meyer, S. S., Tucker, G. S., Wollack, E. & Wright, E. L., 2009, *ApJS*, **180**, 306

Durrer, R. & Maartens, R., 2007, *ArXiv e-prints*, **711**

Durrer, R. & Maartens, R., 2008, *ArXiv e-prints*

Dvali, G., Gabadadze, G. & Porrati, M., 2000, *Physics Letters B*, **484**, 112

Dvali, G. & Turner, M. S., 2003, *ArXiv e-prints*

Eisenstein, D. J. & Hu, W., 1998, *Astrophys. J.*, **496**, 605

Eisenstein, D. J., Zehavi, I., Hogg, D. W., Scoccimarro, R., Blanton, M. R., Nichol, R. C., Scranton, R., Seo, H., Tegmark, M., Zheng, Z., Anderson, S. F., Annis, J., Bahcall, N., Brinkmann, J., Burles, S., Castander, F. J., Connolly, A., Csabai, I., Doi, M., Fukugita, M., Frieman, J. A., Glazebrook, K., Gunn, J. E., Hendry, J. S., Hennessy, G., Ivezić, Z., Kent, S., Knapp, G. R., Lin, H., Loh, Y., Lupton, R. H., Margon, B., McKay, T. A., Meiksin, A., Munn, J. A., Pope, A., Richmond, M. W., Schlegel, D., Schneider, D. P., Shimasaku, K., Stoughton, C., Strauss, M. A., SubbaRao, M., Szalay, A. S., Szapudi, I., Tucker, D. L., Yanny, B. & York, D. G., 2005, *ApJ*, **633**, 560

Elgarøy, Ø. & Lahav, O., 2005, *New Journal of Physics*, **7**, 61

Elgarøy, Ø., Lahav, O., Percival, W. J., Peacock, J. A., Madgwick, D. S., Bridle, S. L., Baugh, C. M., Baldry, I. K., Bland-Hawthorn, J., Bridges, T., Cannon, R., Cole, S., Colless, M., Collins, C., Couch, W., Dalton, G., de Propris, R., Driver, S. P., Efstathiou, G. P., Ellis, R. S., Frenk, C. S., Glazebrook, K., Jackson, C., Lewis, I., Lumsden, S., Maddox, S., Norberg, P., Peterson, B. A., Sutherland, W. & Taylor, K., 2002, *Physical Review Letters*, **89**(6), 061301

Erickcek, A. L., Smith, T. L. & Kamionkowski, M., 2006, , **74**(12), 121501

Fairbairn, M. & Goobar, A., 2006, *Physics Letters B*, **642**, 432

Fang, W., Wang, S., Hu, W., Haiman, Z., Hui, L. & May, M., 2008, , **78**(10), 103509

Feldmann, R., Carollo, C. M., Porciani, C., Lilly, S. J., Capak, P., Taniguchi, Y., Le Fèvre, O., Renzini, A., Scoville, N., Ajiki, M., Aussel, H., Contini, T., McCracken, H., Mobasher, B., Murayama, T., Sanders, D., Sasaki, S., Scarlata, C., Scodeggio, M., Shioya, Y., Silverman, J., Takahashi, M., Thompson, D. & Zamorani, G., 2006, *MNRAS*, **372**, 565

Ferreira, P. G. & Joyce, M., 1998, *Phys. Rev D*, **58**(2), 023503

Fisher, K. B., Scharf, C. A. & Lahav, O., 1994, *MNRAS*, **266**, 219

Freedman, W. L., Madore, B. F., Gibson, B. K., Ferrarese, L., Kelson, D. D., Sakai, S., Mould, J. R., Kennicutt, Jr., R. C., Ford, H. C., Graham, J. A., Huchra, J. P., Hughes, S. M. G., Illingworth, G. D., Macri, L. M. & Stetson, P. B., 2001, *ApJ*, **553**, 47

Frieman, J. *et al.*, 1995, *Physical Review Letters*, **75**, 2077

Fu, L., Semboloni, E., Hoekstra, H., Kilbinger, M., van Waerbeke, L., Tereno, I., Mellier, Y., Heymans, C., Coupon, J., Benabed, K., Benjamin, J., Bertin, E., Doré, O., Hudson, M. J., Ilbert, O., Maoli, R., Marmo, C., McCracken, H. J. & Ménard, B., 2008, *A&A*, **479**, 9

Fukuda, Y. *et al.*, 1998, *Phys. Rev. Lett.*, **81**(6), 1158

Gannouji, R., Moraes, B. & Polarski, D., 2008, *ArXiv e-prints*

Gaztanaga, E., Cabre, A. & Hui, L., 2008, *ArXiv e-prints*

Goobar, A., Hannestad, S., Mörtsell, E. & Tu, H., 2006, *Journal of Cosmology and Astro-Particle Physics*, **6**, 19

Gorbunov, D., Koyama, K. & Sibiryakov, S., 2006, , **73**(4), 044016

Górski, K. M., Hivon, E., Banday, A. J., Wandelt, B. D., Hansen, F. K., Reinecke, M. & Bartelmann, M., 2005, *ApJ*, **622**, 759

Guzzo, L., Pierleoni, M., Meneux, B., Branchini, E., Le Fèvre, O., Marinoni, C., Garilli, B., Blaizot, J., De Lucia, G., Pollo, A., McCracken, H. J., Bottini, D., Le Brun, V., Maccagni, D., Picat, J. P., Scaramella, R., Scodeggio, M., Tresse, L., Vettolani, G., Zanichelli, A., Adami, C., Arnouts, S., Bardelli, S., Bolzonella, M., Bongiorno, A., Cappi, A., Charlot, S., Ciliegi, P., Contini, T., Cucciati, O., de la Torre, S., Dolag, K., Foucaud, S., Franzetti, P., Gavignaud, I., Ilbert, O., Iovino, A., Lamareille, F., Marano, B., Mazure, A., Memeo, P., Merighi, R., Moscardini, L., Paltani, S., Pellò, R., Perez-Montero, E., Pozzetti, L., Radovich, M., Vergani, D., Zamorani, G. & Zucca, E., 2008, *Nature*, **451**, 541

Hamilton, A. J. S., 1998, in D. Hamilton (ed.), *The Evolving Universe*, volume 231 of *Astrophysics and Space Science Library*, pp. 185–+

Hannestad, S., 2005, *Physical Review Letters*, **95**(22), 221301

Hannestad, S., Tu, H. & Wong, Y. Y., 2006, *Journal of Cosmology and Astro-Particle Physics*, **6**, 25

Hauser, M. G. & Peebles, P. J. E., 1973, *ApJ*, **185**, 757

Heavens, A., Kitching, T. & Verde, L., 2007, *MNRAS*, **380**, 1029

Heavens, A. F. & Taylor, A. N., 1995, *MNRAS*, **275**, 483

Heymans, C., Van Waerbeke, L., Bacon, D., Berge, J., Bernstein, G., Bertin, E., Bridle, S., Brown, M. L., Clowe, D., Dahle, H., Erben, T., Gray, M., Hetterscheidt, M., Hoekstra, H., Hudelot, P., Jarvis, M., Kuijken, K., Margoniner, V., Massey, R., Mellier, Y., Nakajima, R., Refregier, A., Rhodes, J., Schrabback, T. & Wittman, D., 2006, *MNRAS*, **368**, 1323

Hirata, C. M. & Seljak, U., 2004, , **70**(6), 063526

Hivon, E., Górski, K. M., Netterfield, C. B., Crill, B. P., Prunet, S. & Hansen, F., 2002, *ApJ*, **567**, 2

Hoekstra, H., Mellier, Y., van Waerbeke, L., Semboloni, E., Fu, L., Hudson, M. J., Parker, L. C., Tereno, I. & Benabed, K., 2006, *ApJ*, **647**, 116

Hu, W. & Eisenstein, D. J., 1998, *ApJ*, **498**, 497

Hu, W., Eisenstein, D. J. & Tegmark, M., 1998, *Physical Review Letters*, **80**, 5255

Hu, W. & Sawicki, I., 2007, *Phys. Rev. D*, **76**(10), 104043

Hubble, E., 1929, *Proceedings of the National Academy of Science*, **15**, 168

Huetsi, G., 2009, *ArXiv e-prints*

Huterer, D., Knox, L. & Nichol, R. C., 2001, *ApJ*, **555**, 547

Huterer, D. & Linder, E. V., 2007, *Phys. Rev. D*, **75**(2), 023519

Ichikawa, K., Fukugita, M. & Kawasaki, M., 2005, , **71**(4), 043001

Ichikawa, K., Kawasaki, M. & Takahashi, F., 2007, *Journal of Cosmology and Astro-Particle Physics*, **5**, 7

Ichiki, K., Takada, M. & Takahashi, T., 2009, , **79**(2), 023520

Ilbert, O. *et al.*, 2006, *ArXiv e-prints*

Ilbert, O., Arnouts, S., McCracken, H. J., Bolzonella, M., Bertin, E., Le Fèvre, O., Mellier, Y., Zamorani, G., Pellò, R., Iovino, A., Tresse, L., Le Brun, V., Bottini, D., Garilli, B., Maccagni, D., Picat, J. P., Scaramella, R., Scodeggio, M., Vettolani, G., Zanichelli, A., Adami, C., Bardelli, S., Cappi, A., Charlot, S., Ciliegi, P., Contini, T., Cucciati, O., Foucaud, S., Franzetti, P., Gavignaud, I., Guzzo, L., Marano, B., Marinoni, C., Mazure, A., Meneux, B., Merighi, R., Paltani,

S., Pollo, A., Pozzetti, L., Radovich, M., Zucca, E., Bondi, M., Bongiorno, A., Busarello, G., de La Torre, S., Gregorini, L., Lamareille, F., Mathez, G., Merluzzi, P., Ripepi, V., Rizzo, D. & Vergani, D., 2006, *A&A*, **457**, 841

Ishak, M., Upadhye, A. & Spergel, D. N., 2006, , **74**(4), 043513

Jain, B. & Zhang, P., 2007, *ArXiv e-prints*, **709**

Kaiser, N., 1987, *MNRAS*, **227**, 1

Kaiser, N., Wilson, G. & Luppino, G. A., 2000, *ArXiv e-prints*

Khoury, J. & Weltman, A., 2004, , **69**(4), 044026

Kilbinger, M., Benabed, K., Guy, J., Astier, P., Tereno, I., Fu, L., Wraith, D., Coupon, J., Mellier, Y., Balland, C., Bouchet, F. R., Hamana, T., Hardin, D., McCracken, H. J., Pain, R., Regnault, N., Schultheis, M. & Yahagi, H., 2009, *A&A*, **497**, 677

Kilbinger, M., Schneider, P. & Eifler, T., 2006, *A&A*, **457**, 15

Kitching, T. D., Heavens, A. F., Verde, L., Serra, P. & Melchiorri, A., 2008, , **77**(10), 103008

Komatsu, E., Dunkley, J., Nolta, M. R., Bennett, C. L., Gold, B., Hinshaw, G., Jarosik, N., Larson, D., Limon, M., Page, L., Spergel, D. N., Halpern, M., Hill, R. S., Kogut, A., Meyer, S. S., Tucker, G. S., Weiland, J. L., Wollack, E. & Wright, E. L., 2009, *ApJS*, **180**, 330

Komatsu, E. & Seljak, U., 2002, *MNRAS*, **336**, 1256

Kowalski, M., Rubin, D., Aldering, G., Agostinho, R. J., Amadon, A., Amanullah, R., Balland, C., Barbary, K., Blanc, G., Challis, P. J., Conley, A., Connolly, N. V., Covarrubias, R., Dawson, K. S., Deustua, S. E., Ellis, R., Fabbro, S., Fadeyev, V., Fan, X., Farris, B., Folatelli, G., Frye, B. L., Garavini, G., Gates, E. L., Germany, L., Goldhaber, G., Goldman, B., Goobar, A., Groom, D. E., Haissinski, J., Hardin, D., Hook, I., Kent, S., Kim, A. G., Knop, R. A., Lidman, C., Linder, E. V., Mendez, J., Meyers, J., Miller, G. J., Moniez, M., Mourão, A. M., Newberg, H., Nobili, S., Nugent, P. E., Pain, R., Perdereau, O., Perlmutter, S., Phillips, M. M., Prasad, V., Quimby, R., Regnault, N., Rich, J., Rubenstein, E. P., Ruiz-Lapuente, P., Santos, F. D., Schaefer, B. E., Schommer, R. A., Smith, R. C., Soderberg, A. M., Spadafora, A. L., Strolger, L., Strovink, M., Suntzeff, N. B., Suzuki, N., Thomas, R. C., Walton, N. A., Wang, L., Wood-Vasey, W. M. & Yun, J. L., 2008, *ApJ*, **686**, 749

Koyama, K., 2005, *Phys. Rev. D*, **72**(12), 123511

Koyama, K., 2006, *JCAP*, **3**, 17

Koyama, K. & Maartens, R., 2006, *JCAP*, **1**, 16

Koyama, K., Taruya, A. & Hiramatsu, T., 2009, , **79**(12), 123512

Kunz, M. & Sapone, D., 2007, *Phys. Rev. Letters*, **98**(12), 121301

Lahav, O. *et al.*, 1991, *MNRAS*, **251**, 128

Lahav, O., Kiakotou, A., Abdalla, F. B. & Blake, C., 2009, *ArXiv e-prints*

Laszlo, I. & Bean, R., 2008, *Phys. Rev. D*, **77**(2), 024048

Lesgourgues, J. & Pastor, S., 2006, , **429**, 307

Lewis, A. & Bridle, S., 2002, *Phys. Rev.*, **D66**, 103511

Lewis, A. & Challinor, A., 2006, , **429**, 1

Lewis, A., Challinor, A. & Lasenby, A., 2000, *ApJ*, **538**, 473

Li, H., Liu, J., Xia, J.-Q., Sun, L., Fan, Z.-H., Tao, C., Tilquin, A. & Zhang, X., 2009, *Physics Letters B*, **675**, 164

Linder, E. V., 2005, *Phys. Rev. D*, **72**(4), 043529

Linder, E. V. & Cahn, R. N., 2007, *ArXiv e-prints*

Lue, A., 2006, , **423**, 1

Lue, A., Scoccimarro, R. & Starkman, G. D., 2004, , **69**(12), 124015

Maartens, R. & Majerotto, E., 2006, *Phys. Rev. D*, **74**(2), 023004

Mangano, G., Miele, G., Pastor, S. & Peloso, M., 2002, *Physics Letters B*, **534**, 8

Massey, R., Heymans, C., Bergé, J., Bernstein, G., Bridle, S., Clowe, D., Dahle, H., Ellis, R., Erben, T., Hetterscheidt, M., High, F. W., Hirata, C., Hoekstra, H., Hudelot, P., Jarvis, M., Johnston, D., Kuijken, K., Margoniner, V., Mandelbaum, R., Mellier, Y., Nakajima, R., Paulin-Henriksson, S., Peeples, M., Roat, C., Refregier, A., Rhodes, J., Schrabback, T., Schirmer, M., Seljak, U., Semboloni, E. & van Waerbeke, L., 2007, *MNRAS*, **376**, 13

Milgrom, M., 1983, *ApJ*, **270**, 365

Oyaizu, H., 2008, , **78**(12), 123523

Oyaizu, H., Lima, M. & Hu, W., 2008, *ArXiv e-prints*

Padmanabhan, N., Budavári, T., Schlegel, D. J., Bridges, T., Brinkmann, J., Cannon, R., Connolly, A. J., Croom, S. M., Csabai, I., Drinkwater, M., Eisenstein, D. J., Hewett, P. C., Loveday, J., Nichol, R. C., Pimbblet, K. A., De Propris, R., Schneider, D. P., Scranton, R., Seljak, U., Shanks, T., Szapudi, I., Szalay, A. S. & Wake, D., 2005, *MNRAS*, **359**, 237

Padmanabhan, N., Schlegel, D. J., Seljak, U., Makarov, A., Bahcall, N. A., Blanton, M. R., Brinkmann, J., Eisenstein, D. J., Finkbeiner, D. P., Gunn, J. E., Hogg, D. W., Ivezić, Ž., Knapp, G. R., Loveday, J., Lupton, R. H., Nichol, R. C., Schneider, D. P., Strauss, M. A., Tegmark, M. & York, D. G., 2007, *MNRAS*, **378**, 852

Peacock, J. A., 2002, in N. Metcalfe & T. Shanks (ed.), *A New Era in Cosmology*, volume 283 of *Astronomical Society of the Pacific Conference Series*, pp. 19–+

Peacock, J. A. & Dodds, S. J., 1996, *MNRAS*, **280**, L19

Peebles, P. J. E., 1973, *ApJ*, **185**, 413

Peebles, P. J. E., 1980, *The large-scale structure of the universe* (Princeton University Press, 1980. 435 p.)

Peebles, P. J. E. & Ratra, B., 1988, *ApJ*, **325**, L17

Percival, W. J., Cole, S., Eisenstein, D. J., Nichol, R. C., Peacock, J. A., Pope, A. C. & Szalay, A. S., 2007, *MNRAS*, **381**, 1053

Percival, W. J., Reid, B. A., Eisenstein, D. J., Bahcall, N. A., Budavari, T., Frieman, J. A., Fukugita, M., Gunn, J. E., Ivezic, Z., Knapp, G. R., Kron, R. G., Loveday, J., Lupton, R. H., McKay, T. A., Meiksin, A., Nichol, R. C., Pope, A. C., Schlegel, D. J., Schneider, D. P., Spergel, D. N., Stoughton, C., Strauss, M. A., Szalay, A. S., Tegmark, M., Vogeley, M. S., Weinberg, D. H., York, D. G. & Zehavi, I., 2009, *ArXiv e-prints*

Perlmutter, S., Aldering, G., Goldhaber, G., Knop, R. A., Nugent, P., Castro, P. G., Deustua, S., Fabbro, S., Goobar, A., Groom, D. E., Hook, I. M., Kim, A. G., Kim, M. Y., Lee, J. C., Nunes, N. J., Pain, R., Pennypacker, C. R., Quimby, R., Lidman, C., Ellis, R. S., Irwin, M., McMahon,

R. G., Ruiz-Lapuente, P., Walton, N., Schaefer, B., Boyle, B. J., Filippenko, A. V., Matheson, T., Fruchter, A. S., Panagia, N., Newberg, H. J. M., Couch, W. J. & The Supernova Cosmology Project, 1999, *ApJ*, **517**, 565

Rassat, A., Land, K., Lahav, O. & Abdalla, F. B., 2007, *MNRAS*, **377**, 1085

Refregier, A., 2003, *ArA&A*, **41**, 645

Refregier, A. *et al.*, 2008, *ArXiv e-prints*

Reid, B. A., Percival, W. J., Eisenstein, D. J., Verde, L., Spergel, D. N., Skibba, R. A., Bahcall, N. A., Budavari, T., Fukugita, M., Gott, J. R., Gunn, J. E., Ivezic, Z., Knapp, G. R., Kron, R. G., Lupton, R. H., McKay, T. A., Meiksin, A., Nichol, R. C., Pope, A. C., Schlegel, D. J., Schneider, D. P., Strauss, M. A., Stoughton, C., Szalay, A. S., Tegmark, M., Weinberg, D. H., York, D. G. & Zehavi, I., 2009, *ArXiv e-prints*

Riess, A. G., Filippenko, A. V., Challis, P., Clocchiatti, A., Diercks, A., Garnavich, P. M., Gilliland, R. L., Hogan, C. J., Jha, S., Kirshner, R. P., Leibundgut, B., Phillips, M. M., Reiss, D., Schmidt, B. P., Schommer, R. A., Smith, R. C., Spyromilio, J., Stubbs, C., Suntzeff, N. B. & Tonry, J., 1998, *AJ*, **116**, 1009

Riess, A. G., Macri, L., Casertano, S., Sosey, M., Lampeitl, H., Ferguson, H. C., Filippenko, A. V., Jha, S. W., Li, W., Chornock, R. & Sarkar, D., 2009, *ApJ*, **699**, 539

Rubakov, V. A., 2003, *ArXiv e-prints*

Saito, S., Takada, M. & Taruya, A., 2008, *Physical Review Letters*, **100**(19), 191301

Saito, S., Takada, M. & Taruya, A., 2009, *ArXiv e-prints*

Sanchez, A. G., Crocce, M., Cabre, A., Baugh, C. M. & Gaztanaga, E., 2009, *ArXiv e-prints*

Sargent, W. L. W. & Turner, E. L., 1977, *ApJL*, **212**, L3

Schimd, C., Tereno, I., Uzan, J., Mellier, Y., van Waerbeke, L., Semboloni, E., Hoekstra, H., Fu, L. & Riazuelo, A., 2007, *A&A*, **463**, 405

Schimd, C., Uzan, J.-P. & Riazuelo, A., 2005, , **71**(8), 083512

Schlegel, D. J., Finkbeiner, D. P. & Davis, M., 1998, *ApJ*, **500**, 525

Schmidt, F., Lima, M., Oyaizu, H. & Hu, W., 2009, , **79**(8), 083518

Schwetz, T., Tórtola, M. & Valle, J. W. F., 2008, *New Journal of Physics*, **10**(11), 113011

Seljak, U., 1996, *ApJ*, **463**, 1

Seljak, U., Slosar, A. & McDonald, P., 2006, *Journal of Cosmology and Astro-Particle Physics*, **10**, 14

Semboloni, E., Mellier, Y., van Waerbeke, L., Hoekstra, H., Tereno, I., Benabed, K., Gwyn, S. D. J., Fu, L., Hudson, M. J., Maoli, R. & Parker, L. C., 2006, *A&A*, **452**, 51

Semboloni, E., van Waerbeke, L., Heymans, C., Hamana, T., Colombi, S., White, M. & Mellier, Y., 2007, *MNRAS*, **375**, L6

Seo, H.-J. & Eisenstein, D. J., 2003, *ApJ*, **598**, 720

Smith, R. E., Peacock, J. A., Jenkins, A., White, S. D. M., Frenk, C. S., Pearce, F. R., Thomas, P. A., Efstathiou, G. & Couchman, H. M. P., 2003, *MNRAS*, **341**, 1311

Song, Y.-S., Sawicki, I. & Hu, W., 2007, , **75**(6), 064003

Spergel, D. N., Bean, R., Doré, O., Nolta, M. R., Bennett, C. L., Dunkley, J., Hinshaw, G., Jarosik, N., Komatsu, E., Page, L., Peiris, H. V., Verde, L., Halpern, M., Hill, R. S., Kogut, A., Limon, M., Meyer, S. S., Odegard, N., Tucker, G. S., Weiland, J. L., Wollack, E. & Wright, E. L., 2007, *ApJS*, **170**, 377

Starobinskii, A. A., 1980, *Physics Letters B*, **91**, 99

Swanson, M. E. C., Tegmark, M., Blanton, M. & Zehavi, I., 2008, *MNRAS*, **385**, 1635

Tegmark, M., Blanton, M. R., Strauss, M. A., Hoyle, F., Schlegel, D., Scoccimarro, R., Vogeley, M. S., Weinberg, D. H., Zehavi, I., Berlind, A., Budavari, T., Connolly, A., Eisenstein, D. J., Finkbeiner, D., Frieman, J. A., Gunn, J. E., Hamilton, A. J. S., Hui, L., Jain, B., Johnston, D., Kent, S., Lin, H., Nakajima, R., Nichol, R. C., Ostriker, J. P., Pope, A., Scranton, R., Seljak, U., Sheth, R. K., Stebbins, A., Szalay, A. S., Szapudi, I., Verde, L., Xu, Y., Annis, J., Bahcall, N. A., Brinkmann, J., Burles, S., Castander, F. J., Csabai, I., Loveday, J., Doi, M., Fukugita, M., Gott, J. R. I., Hennessy, G., Hogg, D. W., Ivezić, Ž., Knapp, G. R., Lamb, D. Q., Lee, B. C., Lupton, R. H., McKay, T. A., Kunszt, P., Munn, J. A., O'Connell, L., Peoples, J., Pier, J. R., Richmond, M., Rockosi, C., Schneider, D. P., Stoughton, C., Tucker, D. L., Vanden Berk, D. E., Yanny, B. & York, D. G., 2004, *ApJ*, **606**, 702

Tegmark, M., Dodelson, S., Eisenstein, D. J., Narayanan, V., Scoccimarro, R., Scranton, R., Strauss, M. A., Connolly, A., Frieman, J. A., Gunn, J. E., Hui, L., Jain, B., Johnston, D., Kent, S., Loveday, J., Nichol, R. C., O'Connell, L., Sheth, R. K., Stebbins, A., Szalay, A. S., Szapudi, I., Vogeley, M. S., Zehavi, I., Annis, J., Bahcall, N. A., Brinkmann, J., Csabai, I., Doi, M., Fukugita, M., Hennessy, G., Ivezíc, Ž., Knapp, G. R., Lamb, D. Q., Lee, B. C., Lupton, R. H., McKay, T. A., Kunszt, P., Munn, J. A., Peoples, J., Pier, J. R., Richmond, M., Rockosi, C., Schlegel, D., Stoughton, C., Tucker, D. L., Yanny, B. & York, D. G., 2002, *ApJ*, **571**, 191

Tegmark, M., Eisenstein, D. J., Strauss, M. A., Weinberg, D. H., Blanton, M. R., Frieman, J. A., Fukugita, M., Gunn, J. E., Hamilton, A. J. S., Knapp, G. R., Nichol, R. C., Ostriker, J. P., Padmanabhan, N., Percival, W. J., Schlegel, D. J., Schneider, D. P., Scoccimarro, R., Seljak, U., Seo, H., Swanson, M., Szalay, A. S., Vogeley, M. S., Yoo, J., Zehavi, I., Abazajian, K., Anderson, S. F., Annis, J., Bahcall, N. A., Bassett, B., Berlind, A., Brinkmann, J., Budavari, T., Castander, F., Connolly, A., Csabai, I., Doi, M., Finkbeiner, D. P., Gillespie, B., Glazebrook, K., Hennessy, G. S., Hogg, D. W., Ivezić, Ž., Jain, B., Johnston, D., Kent, S., Lamb, D. Q., Lee, B. C., Lin, H., Loveday, J., Lupton, R. H., Munn, J. A., Pan, K., Park, C., Peoples, J., Pier, J. R., Pope, A., Richmond, M., Rockosi, C., Scranton, R., Sheth, R. K., Stebbins, A., Stoughton, C., Szapudi, I., Tucker, D. L., vanden Berk, D. E., Yanny, B. & York, D. G., 2006, , **74**(12), 123507

Tereno, I., Schimd, C., Uzan, J., Kilbinger, M., Vincent, F. H. & Fu, L., 2009, *A&A*, **500**, 657

The Dark Energy Survey Collaboration, 2005, *ArXiv Astrophysics e-prints*

Thomas, S. A., Abdalla, F. B. & Weller, J., 2009, *MNRAS*, **395**, 197

Tsujikawa, S. & Tatekawa, T., 2008, *ArXiv e-prints*, **804**

Uzan, J.-P. & Bernardeau, F., 2001, *Phys. Rev. D*, **64**(8), 083004

Van Waerbeke, L., Mellier, Y., Erben, T., Cuillandre, J. C., Bernardeau, F., Maoli, R., Bertin, E., Mc Cracken, H. J., Le Fèvre, O., Fort, B., Dantel-Fort, M., Jain, B. & Schneider, P., 2000, *A&A*, **358**, 30

Wang, L. & Steinhardt, P. J., 1998, *ApJ*, **508**, 483

Wetterich, C., 1988, *Nucl. Phys.*, **B302**, 668

Will, C. M., 1993, *Theory and Experiment in Gravitational Physics* (Cambridge University Press, March 1993.)

Wittman, D. M., Tyson, J. A., Kirkman, D., Dell'Antonio, I. & Bernstein, G., 2000, *Nature*, **405**, 143

Wolf, J. *et al.*, 2008, *The KATRIN Neutrino Mass Experiment*
URL: *http://www.citebase.org/abstract?id=oai:arXiv.org:0810.3281*

Woodard, R., 2007, in *The Invisible Universe:*

Wright, E. L., Smoot, G. F., Bennett, C. L. & Lubin, P. M., 1994, *ApJ*, **436**, 443

Yamamoto, K., Bassett, B. A., Nichol, R. C., Suto, Y. & Yahata, K., 2006, , **74**(6), 063525

Yao, W. M. *et al.*, 2006, *J. Phys.*, **G33**, 1

York, D. *et al.*, 2000, *AJ*, **120**, 1579

Yu, J. T. & Peebles, P. J. E., 1969, *ApJ*, **158**, 103

ACKNOWLEDGEMENTS

I feel exceptionally lucky to have enjoyed my time at school. This was without doubt a major influence on me as a person and my desire to become a scientist. I am so grateful to have had some truly fantastic teachers during this time, from Watford Fields Junior to Watford Boys Grammar school. I don't have the space or time to acknowledge each teacher but I just want to say I am indebted to every single one of you. In addition, I simply have to note the importance of having had such exceptional peers. I still feel the benefit and inspiration from working, thinking and competing with all of you[1]!

I would like to thank my two supervisors Jochen Weller and Ofer Lahav for allowing me to work on such interesting areas of cosmology–I really really appreciate it. Thanks also to Ofer for giving me the chance to continue and Jochen for some great trips to Munich! I would also like to say a big thank you to Filipe Abdalla, my mentor, for being there, answering my questions and guiding me through the three years. However, sometimes you can be wrong...!

This time has on occasions been busy and stressful but I've been fortunate enough to know some great friends that have made this period one of the best. Thanks to my recent flatmates Perran and Dan (the boys), Sanaz and Poppy for many great nights out. I include in this some great mates that have provided so much entertainment, inspiration and also support when needed: Stuart, Tobin, Nick, Dee, Ed, Manda, Bethan, Jamie, Jeff, Carolyn, Minoo and Jafar. The last three years have been a great time in my life. A big shout out also for my office *G15*. Thanks to *everyone* that has worked in there and made it a great work environment. I should also mention G18 - my party office - for making the department so much fun. Thank you to everyone that is, or was, a part of that office and to those who regularly played football. PTO :)

[1] Particularly *that* further maths set...

Thank you to my family for helping me along each step of the journey and for contributing so much: Auntie Jo, Daniel, David, Molly, George and Bernadette. I love you all every single day. In particular I would like to thank Sanaz for all your support and encouragement. It has meant so much and I could not have done it without you. I'll never forget your contribution to this PhD time...

Finally, I would like recognise the efforts of my mum through all these years. I simply can't thank you enough. This thesis is yours.